INTERNET DOCUMENT INFORMATION FORM

A. **Report Title: Naval Research Lab Review 1998**
B. **Report downloaded From the Internet: May 21, 2002**
C. **Report's Point of Contact: (Name, Organization, Address, Office Symbol, & Ph #): - Naval Research Lab, Washington, DC 20375-5320**

D. **Currently Applicable Classification Level**: Unclassified

E. **Distribution Statement A**: Approved for Public Release

F. **The foregoing information was compiled and provided by:**
DTIC-OCA Initials: __LL__ **Preparation Date May 21, 2002**

The foregoing information should exactly correspond to the Title, Report Number, and the Date on the accompanying report document. If there are mismatches, or other questions, contact the above OCA Representative for resolution.

20020522 134

NRL Review

This *1998 NRL Review* introduces you to the Naval Research Laboratory—the Navy's Corporate Laboratory—and focuses on research highlights from fiscal year 1997. In addition, it presents the special honors awarded to NRL employees and describes the programs available to NRL and non-NRL employees. This publication offers an exchange of information among scientists, engineers, scholars, and managers, and it is used as a recruiting tool.

As you read the *NRL Review*, you will become even more aware that the Naval Research Laboratory comprises a dynamic team of scientists, engineers, and support personnel working together to promote the programs that will continue to foster discoveries and scientific advances for the Navy of the future.

General information on the research described in this *NRL Review* may be obtained from the Public Affairs Office, Code 1230, (202) 767-2541. Information concerning Technology Transfer is available from Dr. Richard Rein, head of the Technology Transfer Office, Code 1004, (202) 767-7230. The sources of information on the various nonresearch programs at NRL are listed in the chapter entitled "Programs for Professional Development."

For additional information about NRL, the *Fact Book* lists the organization, key personnel, and major facilities for each division. Further, it contains information about Laboratory funding, programs, and field sites. A copy of the *Fact Book* may be obtained by contacting the Technical Information Division, Publications Branch, Code 5230, (202) 767-2782.

NRL's URL: http://www.nrl.navy.mil/

1923 - 1998

Celebrating 75 Years

1998 NRL Review

Contents

MISSION

REFLECTIONS

75 YEARS OF RESEARCH

THE NAVAL RESEARCH LABORATORY

FEATURED RESEARCH

ACOUSTICS

CHEMICAL/BIOCHEMICAL RESEARCH

OPTICAL SCIENCE

REMOTE SENSING

SIMULATION, COMPUTING, AND MODELING

SPACE RESEARCH AND SATELLITE TECHNOLOGY

SPECIAL AWARDS AND RECOGNITION

PROGRAMS FOR PROFESSIONAL DEVELOPMENT

GENERAL INFORMATION

Mission

To conduct a broadly based multidisciplinary program of scientific research and advanced technological development directed toward maritime applications of new and improved materials, techniques, equipment, systems, and ocean, atmospheric, and space sciences and related technologies.

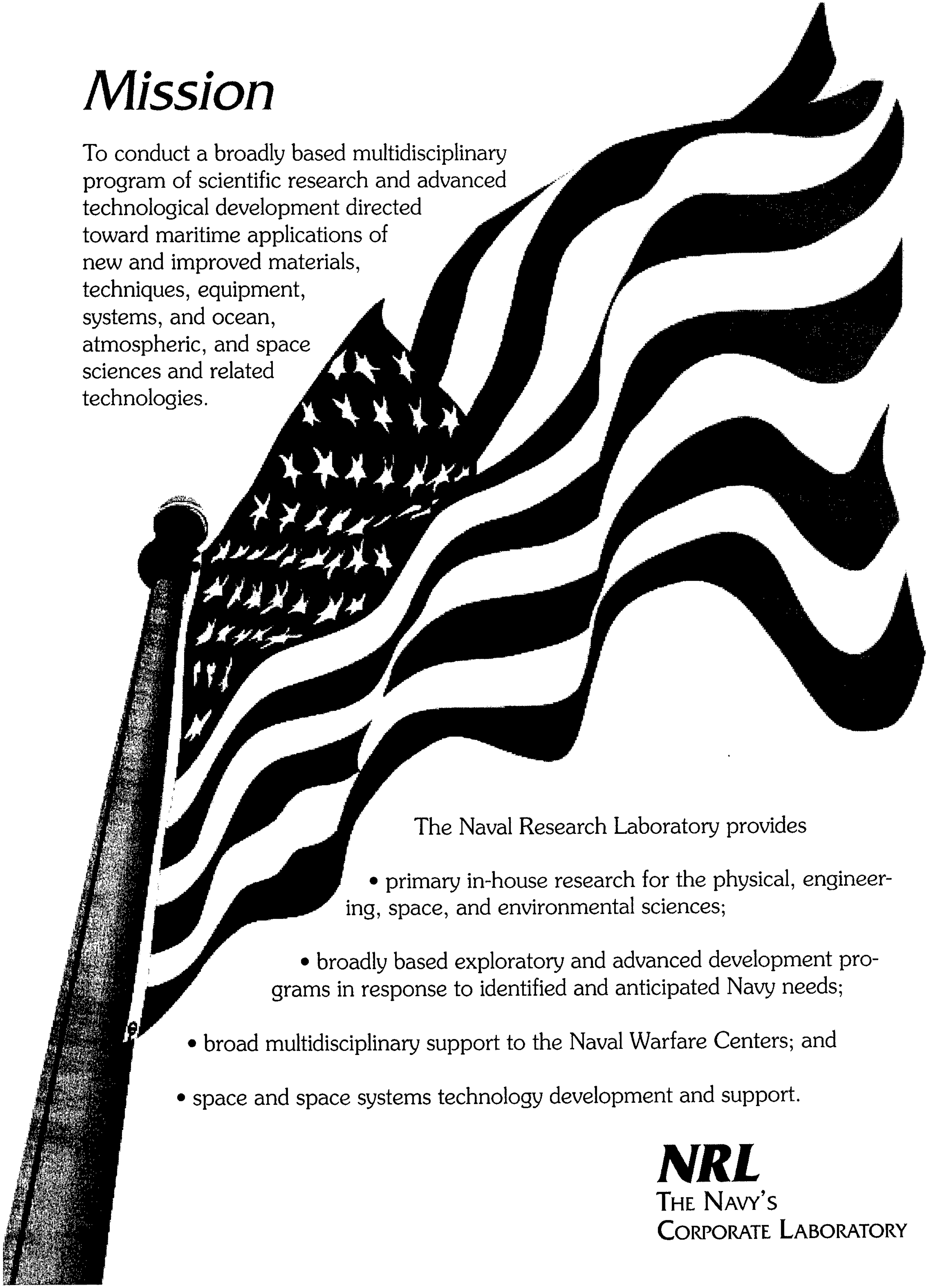

The Naval Research Laboratory provides

- primary in-house research for the physical, engineering, space, and environmental sciences;
- broadly based exploratory and advanced development programs in response to identified and anticipated Navy needs;
- broad multidisciplinary support to the Naval Warfare Centers; and
- space and space systems technology development and support.

NRL
THE NAVY'S
CORPORATE LABORATORY

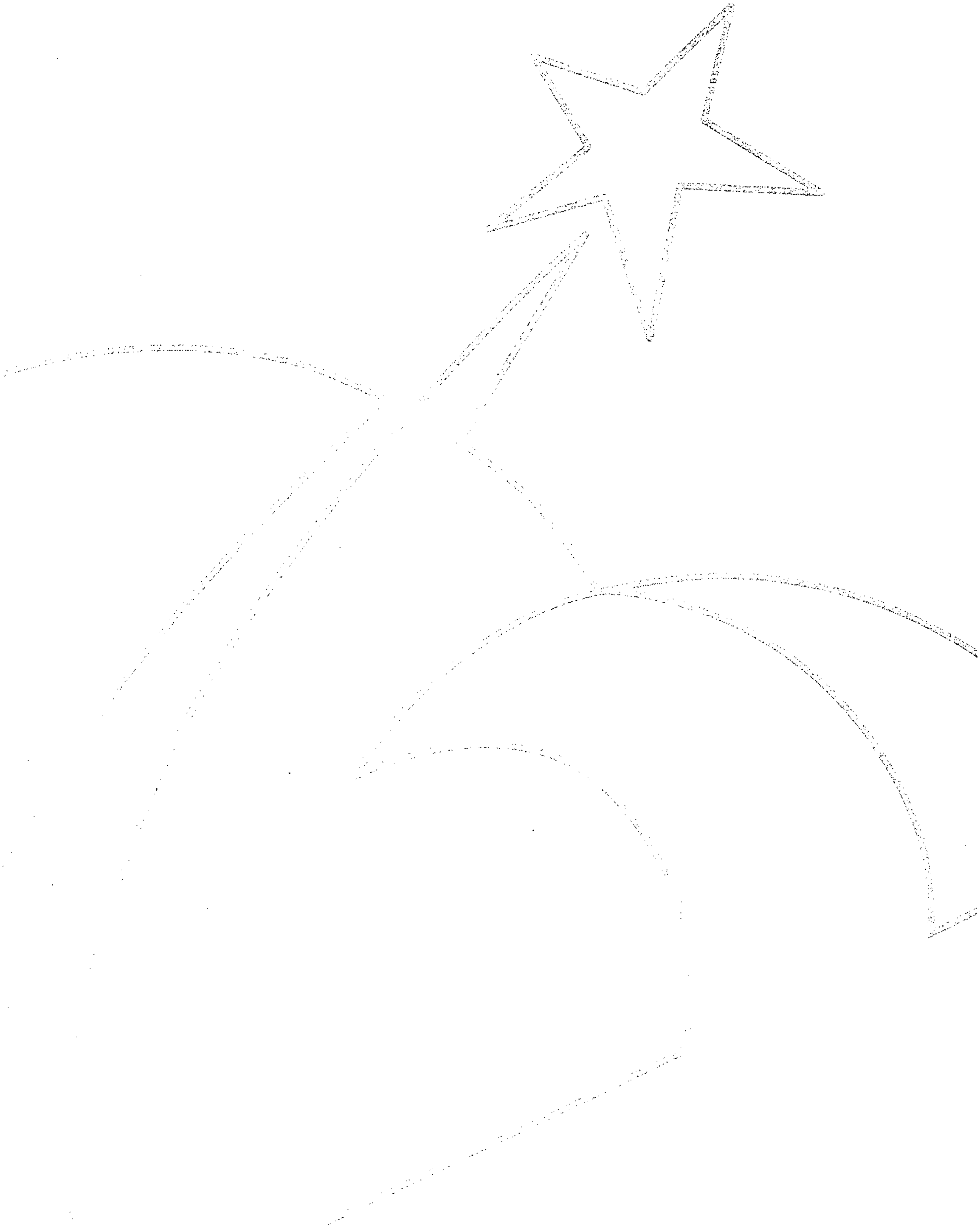

...the Commanding Officer and the Director of Research

that the 21st-century will be characterized not by technical advances in any single technology or discipline but by a coming together of many technologies and disciplines in a complementary fashion to allow one to do things that would not be achievable by any single technology.

We are at present well positioned to enter the next century with a strong technical program and all of the tools necessary to prosecute it. There are, of course, many important discussions currently underway, that will impact the future of NRL. The environment in which science and technology must justify itself has changed. The matter of the government's role in science and technology and in the development of military systems is the subject of active debate. While the specifics of today's discussions are unique to the current time, discussion and debate on these matters is not at all unique. Indeed, if one reads the early history of the establishment of NRL, one will find that the topics of the federal role in support of research and the roles of government and industry in the development of military systems were very actively debated within the context of the establishment of the Naval Research Laboratory. The intensity of these discussions has varied over time, usually driven by political events such as the beginning and the end of World War II, the entry into the Cold War, and the end of the Cold War. Such discussions are very proper and necessary, both for our Nation to chart its course and for the Laboratory to sort out its proper role. Therefore, while we need to pay careful attention to these discussions and, as appropriate, be an active participant in the discussions, we should not be alarmed that such discussions are underway. If past is prologue, then when the dust settles, the Laboratory will emerge as a strong player in the Naval Science and Technology of the early 21st-century.

Dr. Timothy Coffey
Director of Research

CAPT Bruce W. Buckley, USN
Commanding Officer

A Message from ...

As the *1998 NRL Review* goes to press, the Laboratory is preparing to recognize its 75th anniversary. Much time will be spent remembering and recognizing past accomplishments. These accomplishments are quite remarkable both for their impact and the span of disciplines that they cover. To make this point, consider just a few: the discovery and early development of radar; the first operational fathometer; seminal contributions to understanding the physics of radiowave propagation in the ionosphere; major contributions to rocketry and space science and technology through the Viking and Vanguard programs; the molecular structure analysis methods developed by Jerome and Isabella Karle and Herbert Hauptman (resulting in the Nobel Prize in Chemistry); development of the concept of fracture toughness; key contributions to navigation technology leading to the Global Positioning System; discovery of the X-ray universe; historic contributions to understanding the Sun (and its impact on the environment that naval systems must operate in), of which NRL's currently operating LASCO instrument is the latest; the development of fiber-optic sensors; the development of the rare earth permanent magnets; optical interferometry; the development of the Navy's global ocean and atmospheric models; the paradigm shift in spacecraft development caused by the Clementine program.

These remarkable achievements have contributed to shaping the 20th-century and have enabled our Navy and Marine Corps to be the most technologically superior force afloat. While it is proper to marvel at these accomplishments, the real focus during this year of celebration must be on the future. NRL today is well positioned to continue to make contributions in the 21st-century of the same impact as those made by the Laboratory during the 20th-century. It is always risky to speculate where future revolutionary developments will actually occur. We suggest, however,

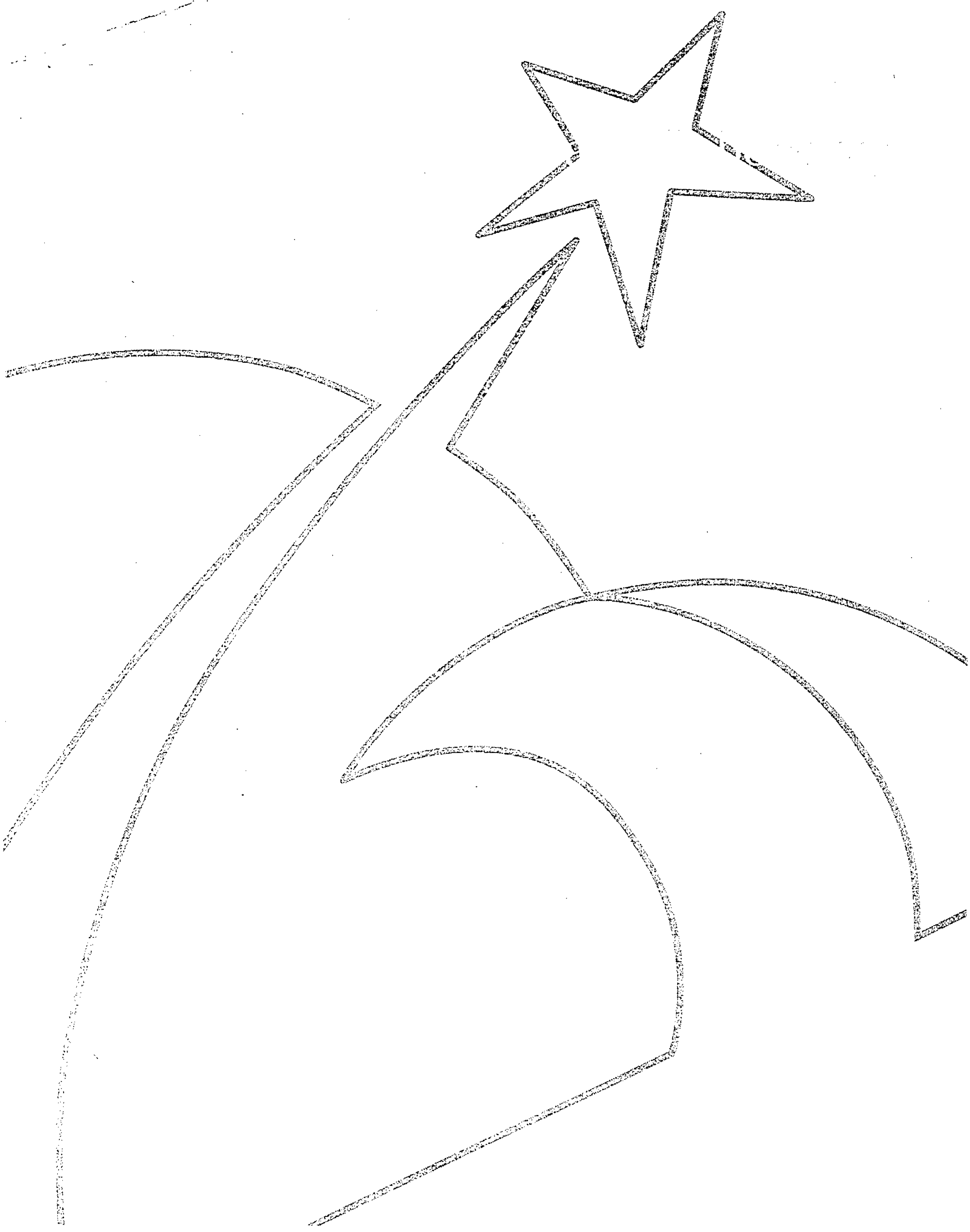

1964 — The USNS *Mizar* was built in 1957 as a supply ship for U.S. Arctic forces and was converted to serve as a support vessel in Navy deep-ocean research missions. NRL scientists used the *Mizar* in their discovery of the wreck of the USS *Thresher* (1964), the USS *Scorpion* (1968), the submersible *Alvin* (1969), the French submarine *Eurydice* (1970), and in locating an American H-bomb that was lost off of Palomares, Spain (1966).

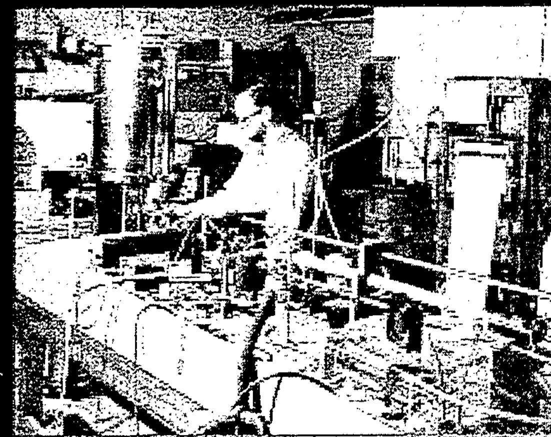

1971 — The first purely chemical CO_2 laser developed by NRL researchers. Laser research began at NRL in 1968, and the Laboratory quickly became a national leader in the field. Among NRL's many accomplishments was the development of the first successful glass laser disc amplifier. NRL is currently a national center for research in laser fusion.

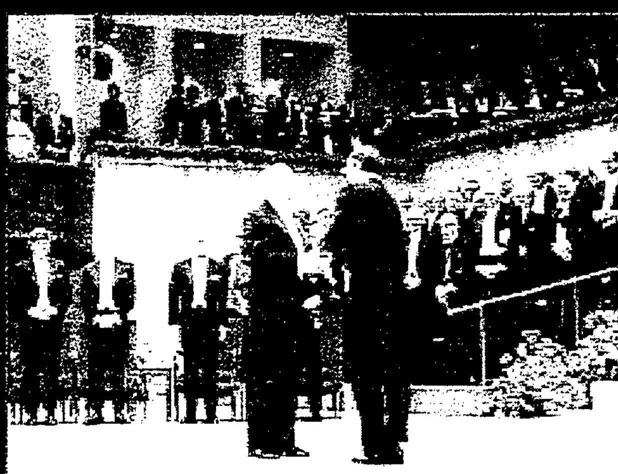

1986 — Dr. Jerome Karle receives the 1985 Nobel Prize in Chemistry from King Carl Gustav XVI of Sweden. Dr. Karle and his colleague, Dr. Herbert Hauptman, shared the prize for their path-breaking work in crystal structure analysis.

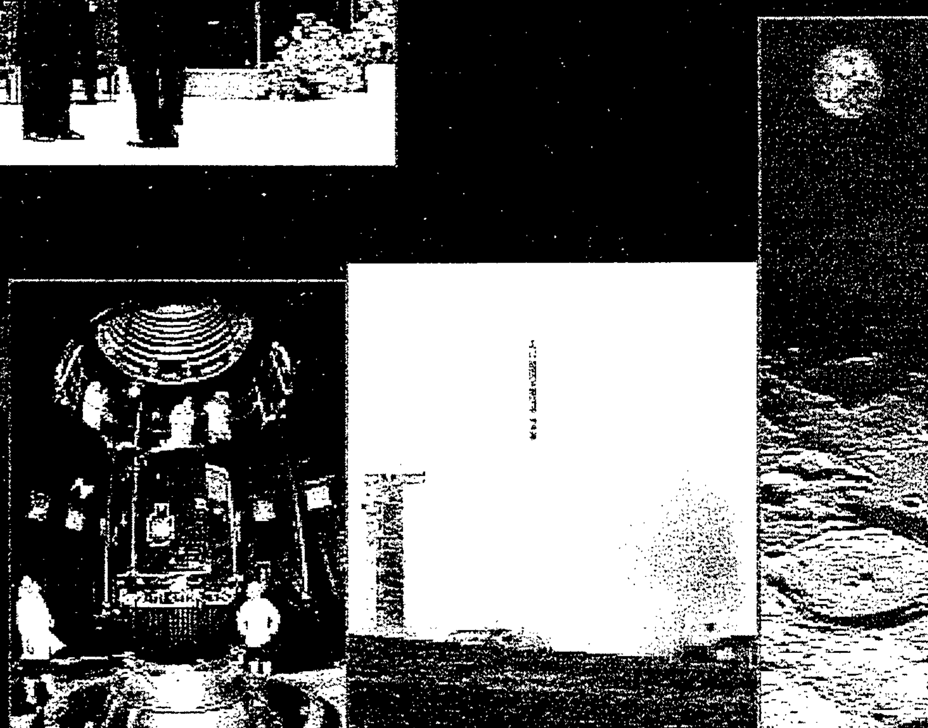

1994 — A final look at the *Clementine* spacecraft, which is mated to its launch vehicle, the Titan IIG (left). *Clementine* was launched on January 25, 1994, at 8:34 a.m. PST, from Vandenberg Air Force Base (center). A colorized image showing the full Earth over the lunar north pole as *Clementine* completes mapping orbit 102 on March 13, 1994 (right).

75 Years of Research

1920s - 1990s

1923 — Assistant Secretary of the Navy, Theodore Roosevelt, Jr., delivering the principal address at the dedication of NRL on July 1, 1923.

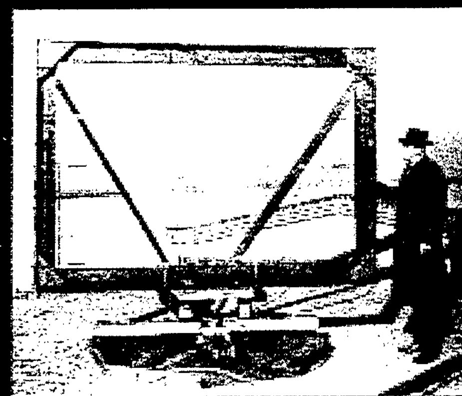

1937 — Radar researcher and later Director of Research, Dr. Robert Page, standing on the roof of Building 1 with an antenna developed for performance comparison with the experimental 200 MHz radar installed on the USS *Leary*. The USS *Leary* served as a test platform for radar before its general introduction into the Fleet.

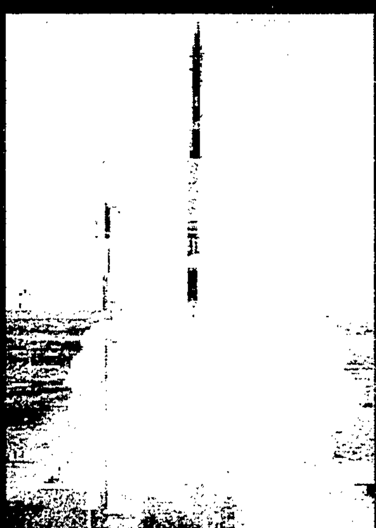

1958 — Launch of NRL's Vanguard rocket from Cape Canaveral. In 1955, NRL had been selected to develop and launch the first U.S. space satellite in conjunction with the International Geophysical Year. Vanguard I (TV-4) was successfully launched on March 17, 1958, after two earlier attempts to reach orbit failed during the preceding December and February.

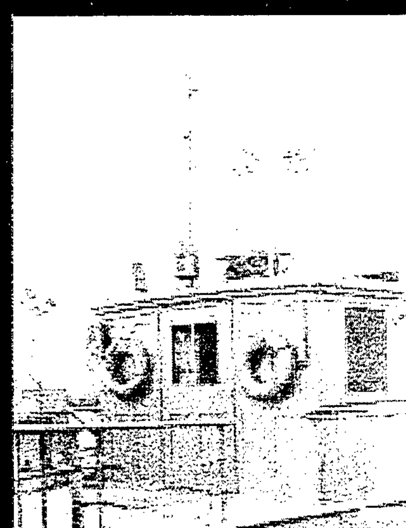

1944 — The U.S. model TDY radar jammer (designed and developed by NRL) included a beam antenna and a transmitter. Shown here is an antenna that covered a range of 116 to 770 kHz. During World War II, no ship equipped with a radar jammer was hit by enemy fire .

1958 — NRL scientists inspect the satellite in Vanguard II's nosecone. Pictured from left is Roger Easton, Marty Votaw, Robert Baumann, and Joe Schwartz of the NRL Vanguard team. The first successful Vanguard satellite remains in Earth orbit and is the oldest surviving artificial satellite.

NRL — Our Heritage

Today, when government and science seem inextricably linked, when virtually no one questions the dependence of national defense on the excellence of national technical capabilities, it is noteworthy that in-house defense research is relatively new in our Nation's history. The Naval Research Laboratory (NRL), the first modern research institution created within the United States Navy, began operations in 1923.

Thomas Edison's Vision: The first step came in May 1915, a time when Americans were deeply worried about the great European war. Thomas Edison, when asked by a New York Times correspondent to comment on the conflict, argued that the Nation should look to science. "The Government," he proposed in a published interview, "should maintain a great research laboratory....In this could be developed...all the technique of military and naval progression without any vast expense." Secretary of the Navy Josephus Daniels seized the opportunity created by Edison's public comments to enlist Edison's support. He agreed to serve as the head of a new body of civilian experts—the Naval Consulting Board—to advise the Navy on science and technology. The Board's most ambitious plan was the creation of a modern research facility for the Navy. Congress allocated $1.5 million for the institution in 1916, but wartime delays and disagreements within the Naval Consulting Board postponed construction until 1920.

The Laboratory's two original divisions—Radio and Sound—pioneered in the fields of high-frequency radio and underwater sound propagation. They produced communications equipment, direction-finding devices, sonar sets, and perhaps most significant of all, the first practical radar equipment built in this country. They also performed basic research, participating, for example, in the discovery and early exploration of the ionosphere. Moreover, the Laboratory was able to work gradually toward its goal of becoming a broadly based research facility. By the beginning of World War II, five new divisions had been added: Physical Optics, Chemistry, Metallurgy, Mechanics and Electricity, and Internal Communications.

The War Years and Growth: Total employment at the Laboratory jumped from 396 in 1941 to 4400 in 1946, expenditures from $1.7 million to $13.7 million, the number of buildings from 23 to 67, and the number of projects from 200 to about 900. During WWII, scientific activities necessarily were concentrated almost entirely on applied research. New electronics equipment—radio, radar, sonar—was developed. Countermeasures were devised. New lubricants were produced, as were antifouling paints, luminous identification tapes, and a sea marker to help save survivors of disasters at sea. A thermal diffusion process was conceived and used to supply some of the ^{235}U isotope needed for one of the first atomic bombs. Also many new devices that developed from booming wartime industry were type tested and then certified as reliable for the Fleet.

NRL Reorganizes for Peace: Because of the major scientific accomplishments of the war years, the United States emerged into the postwar era determined to consolidate its wartime gains in science and technology and to preserve the working relationship between its armed forces and the scientific community. While the Navy was establishing its Office of Naval Research (ONR) as a liaison with and supporter of basic and applied scientific research, it was also encouraging NRL to broaden its scope and become, in effect, its corporate research laboratory. There was a transfer of NRL to the administrative oversight of ONR and a parallel shift of the Laboratory's research emphasis to one of long-range basic and applied investigation in a broad range of the physical sciences.

However, rapid expansion during the war had left NRL improperly structured to address long-term Navy requirements. One major task—neither easily nor rapidly accomplished—was that of reshaping and coordinating research. This was achieved by transforming a group of largely autonomous scientific divisions into a unified institution with a clear mission and a fully coordinated research program. The first attempt at reorganization vested power in an executive committee composed of all the division superintendents. This committee was impracticably large, so

in 1949, a civilian director of research was named and given full authority over the program. Positions for associate directors were added in 1954.

The Breadth of NRL: During the years since the war, the areas of study at the Laboratory have included basic research concerning the Navy's environments of Earth, sea, sky, and space. Investigations have ranged widely from monitoring the Sun's behavior to analyzing marine atmospheric conditions to measuring parameters of the deep oceans. Detection and communication capabilities have benefitted by research that has exploited new portions of the electromagnetic spectrum, extended ranges to outer space, and provided a means of transferring information reliably and securely, even through massive jamming. Submarine habitability, lubricants, shipbuilding materials, fire fighting, and the study of sound in the sea have remained steadfast concerns, to which have been added recent explorations within the fields of virtual reality, superconductivity, and biomolecular science and engineering.

The Laboratory has pioneered naval research into space from atmospheric probes with captured V-2 rockets through direction of the *Vanguard* project — America's first satellite program — to involvement in such projects as the Navy's Global Positioning System. Today NRL is the Navy's lead laboratory in space systems research, fire research, tactical electronic warfare, microelectronic devices, and artificial intelligence.

The consolidation in 1992 of NRL and the Naval Oceanic and Atmospheric Laboratory, with centers at Bay St. Louis, Mississippi, and Monterey, California, added critical new strengths to the Laboratory. NRL now is additionally the lead Navy center for research in ocean and atmospheric sciences, with special strengths in physical oceanography, marine geosciences, ocean acoustics, marine meteorology, and remote oceanic and atmospheric sensing. The expanded Laboratory is focusing its research efforts on new Navy strategic interests and needs in the post-Cold War world. Although not abandoning its interests in blue-water operations and research, the Navy is also focusing on defending American interests in the world's littoral regions. NRL scientists and engineers are working to give the Navy the special knowledge and capabilities it needs to operate in these waters.

1997 in Review

NRL scientists and engineers continue to find new opportunities for cooperative research with their colleagues in the former Soviet republics. In a possible Navy Department first, members of NRL's Patuxent Flight Support Detachment flew an NP-3 aircraft into Kazakstan during June of 1997. The object of the joint U.S.-Kazakstani mission was to conduct several remote-sensing experiments using the Airborne Multisensor Pod System. The NP-3 carried a Sandia National Laboratories synthetic aperture radar pod, a Bechtel Remote Sensing Laboratory multispectral imaging pod, and an Earth Sciences, Inc. hyperspectral sensor. The sensors collected unclassified mineral, geological, and environmental data.

In other environmental studies, NRL's Middle Atmosphere High Resolution Spectrograph Investigation (MAHRSI) remote-sensing instrument concluded its second data-collecting mission. The scientific objective of MAHRSI was to map the distribution of two important gases in the middle polar atmosphere believed to be important in determining its natural balance of ozone. After deployment from the space shuttle *Discovery* during NASA's STS-85 mission, MAHRSI measured OH and nitric oxide in the atmosphere above 35 km through analysis of atmospheric emission and scattering of ultraviolet radiation.

Scientists from NRL's Surface Chemistry Branch have applied atomic-force microscopy (AFM) to measure forces between single pairs of molecules, such as complementary DNA strands, streptavidin-biotin, and antibodies and their antigens. The ability to measure these intermolecular forces is helpful in allowing scientists to understand the physical basis of biochemical mechanisms. NRL is using AFM in its attempt to develop ultrasensitive diagnostics for understanding the molecular mechanisms responsible for biofouling and for measuring the forces necessary for DNA replication.

NRL researchers also have been active in the realm of space science. Using the Rossi X-ray Timing Explorer satellite, Laboratory investigators have discovered that the eclipsing binary star system EXO0748-676 may be slowing down

On June 18, 1997, members of NRL's Patuxent River Flight Support Detachment (FSD) flew an NP-3 aircraft into Kazakstan to conduct Department of Energy-sponsored missions for the Airborne Multisensor Pod System (AMPS) program over a three-week period.

through the mechanism of gas ejection. Eclipse timing measurements from the binary system indicate that the eclipses are arriving later and later. The NRL researchers speculate that large amounts of matter are being ejected at irregular intervals, increasing the time required for one member of the pair to orbit the other. Studies of the star system may help us understand the formation and ultimate fate of X-ray binaries.

In a startling discovery, NRL scientists have found evidence of a previously unknown cloud of positrons 3,000 light years above the center of our galaxy. This cloud of positrons is in addition to the discovery of an expected belt of antimatter at the galactic core and along its plane. Maps were produced by NASA's Compton Gamma Ray Observatory. The NRL-developed Oriented Scintillation Spectrometer Experiment (OSSE) aboard the observatory is sensitive to gamma rays produced by the annihilation of positrons, the antimatter counterpart of the electron. This NRL discovery points to the existence of a hot fountain of gas filled with antimatter electrons rising from a region that surrounds the galactic center.

Closer to home, scientists using instruments on the Solar Heliospheric satellite (SOHO) have produced movies that show the origin and propagation of large solar explosions in new detail. The coronal mass ejections can cause large geomagnetic storms on Earth. One of the contributing SOHO instruments was the Large-Angle Spectrometric Coronagraph built by a consortium of American and European scientists under the direction of NRL's Dr. Guenter Brueckner. The SOHO is a joint effort of NASA and the European Space Agency.

The Naval Center for Space Technology is revamping its Shuttle Launch Dispenser, first flown on a Titan IV rocket, for use as the back-up Interim Control Module (ICM) for the International Space Station (ISS). If necessary, the ICM will be mated with the Space Station via the space shuttle and will reboost the ISS to higher orbits and provide attitude and guidance control for the positioning of the spacecraft. The ICM may also provide a refueling capability that could extend ISS operations for up to three years.

In other research, NRL scientists within the Laboratory for Computational Physics and Fluid Dynamics are participating in a collaborative effort with NASA and other investigators to develop Grand Challenge supercomputer applications. The applications are expected to provide a new understanding of the fundamental problems in the Earth and space sciences. The eventual goal of the NRL effort is to reach 100 Gflops of sustained performance. The NRL group is one of nine different research teams developing Grand Challenge applications.

An NRL research team has developed and demonstrated a fiber-optic beamformer for true time-delay steering of a two-dimensional transmitter array. The beamformer serves as a cost-effective method for distributing microwave signals and for providing a true time-delay function to antenna subarrays. Phased-array antennas are being increasingly applied to modern commercial and military radar and communication systems. Array antennas permit the implementation of such functions as dynamic beam steering and shaping.

Researchers at NRL's Virtual Reality Lab have designed and developed a three-dimensional (3-D) interactive terrain battlefield map for the Marine Corps. The virtual map was developed to help the command visualize the battle space during the Marines' "Hunter-Warrior Advanced Warfighting Experiment." The map was created for use with a Responsive Workbench, a graphics system that displays computer-generated images that can be seen by the user in 3-D with lightweight stereoscopic glasses. The image simulates an actual situation and can be manipulated by the operator through the use of a flight stick, special "tracking" glove, or some other handheld input device.

Work done within the Electronics Science and Technology Division has resulted in a way of precisely measuring individual quantum dots formed of the semiconductor gallium arsenide. The

dots have a diameter of approximately 10 nm. It is anticipated that quantum dots will eventually increase the performance of devices such as lasers, electro-optical devices and optical memories, and recent improvements in growth techniques. Current types of quantum dots suffer from large fluctuations in size, and the NRL work is part of a broad scientific effort to resolve and study individual quantum dots optically.

In other work, NRL researchers have developed and flight tested the first prototype *Eager* (Electric Preferential Acquisition Decoy) vehicle. The decoy is a recoverable, tethered, electric-powered rotary wing vehicle with an RF repeater payload. The *Eager* is considered a breakthrough for affordable, effective ship defense. It is designed for littoral warfare and will have an operational life of 1000 hours, instead of the minutes now standard for existing electronic decoys of comparable cost. The decoy is launched without pyrotechnics from a ship or ground platform and can be recovered and redeployed.

Technology Transfer: During 1997, NRL's Technology Transfer Office continued its successful pattern of facilitating the implementation of NRL technology by the commercial sector through means of Cooperative Research and Development Agreements (CRADAs) and licensing of NRL patents. The patent-licensing agreement among NRL, the Shipley Company, and GEO-Centers, Inc., concerning NRL's liquid crystal display (LCD) optical alignment technology is an example of this activity. This exclusive license is the result of inventions originating, in part, from work performed under a CRADA.

CAPT Buckley and Mr. Richard Carroll, of Digital System Resources, Inc., sign the cooperative research and development agreement.

NRL and the Diamond Microelectronics Corporation (DMC) established a CRADA to develop cost-effective, diamond-based, high-power/high-frequency switches and assorted vacuum electronics. DMC acquired access to the basic technology by licensing an NRL patent and then supported additional research at the Laboratory to further develop the technology.

In the area of electronic warfare, NRL and Digital System Resources, Inc. (DSR), signed a CRADA to design and develop techniques and technology required for the production of Advanced Integrated Electronic Warfare Systems (AIEWS). NRL and DSR cooperatively will conduct electronic warfare (EW) research for naval surface ship applications and evaluate innovative concepts for adaptation of commercial-off-the-shelf digital equipment and operating systems in support of the AIEWS and similar advanced EW systems. Additionally, NRL and the Lockheed Martin Corporation signed a CRADA focused on the simulation and visualization of surface-ship missile-blast and ship structural response dynamics to support the DARPA Simulation-based Design Program.

Two CRADAs take advantage of NRL's unique testing capabilities in the radiation effects field—one with Essential Research, Inc., and the other with International Stellar Technology, Inc., to study radiation effects in advanced solar cell devices. These new cell technologies are being developed for their potentially high radiation resistance. These are expected to be enabling technologies that will allow future Navy space missions to have significantly longer operational lifetimes and will allow access to high-radiation orbits inaccessible with present cell technologies. The combination of analysis capabilities and expertise in space-radiation effects makes NRL unique in the nation.

The Technology Transfer Office, working with the University of Maryland and the Mid-Atlantic Technology Applications Center under the ONR sponsored mini-CRADA program, transferred technology to 16 small businesses located in the mid-Atlantic region. Through these mini-CRADAs, NRL is able to develop interactions with many organizations by partnering a company and its technical problem with an NRL researcher who assists the company in finding a solution. Listed are several of this year's successfully completed mini-CRADAs: Plymouth Tube Co., Salisbury, Maryland; Sterling Semiconductor, Herndon, Virginia; and Gulden Opthalmics, Elkins Park, Pennsylvania.

NRL Today

ORGANIZATION AND ADMINISTRATION

The Naval Research Laboratory is a field command under the Chief of Naval Research, who reports to the Secretary of the Navy via the Assistant Secretary of the Navy for Research, Development and Acquisition.

Heading the Laboratory with joint responsibilities are CAPT Bruce W. Buckley, USN, Commanding Officer, and Dr. Timothy Coffey, Director of Research. Line authority passes from the Commanding Officer and the Director of Research to three Associate Directors of Research, a Director of the Naval Center for Space Technology, and an Associate Director for Business Operations. Research is performed in the following areas:

- Systems
- Materials Science and Component Technology
- Ocean and Atmospheric Science and Technology
- Naval Center for Space Technology.

NRL operates as a Navy Working Capital Fund (NWCF). All costs, including overhead, are charged to various research projects. Funding in FY 97 came from the Chief of Naval Research, the Naval Systems Commands, and other Navy sources; government agencies, such as the U.S. Air Force, Advanced Research Projects Agency, the Department of Energy, and the National Aeronautics and Space Administration; and several nongovernment activities.

PERSONNEL DEVELOPMENT

At the end of FY 97, NRL employed 3460 personnel—53 officers, 131 enlisted, and 3276 civilians. In the research staff, there are 869 employees with doctorate degrees, 423 with masters degrees, and 560 with bachelors degrees. The support staff assists the research staff by providing administrative, computer-aided design, machining, fabrication, electronic construction, publication, personnel development, information retrieval, large mainframe computer support, and contracting and supply management services.

Opportunities for higher education and other professional training for NRL employees are available through several programs offered by the Employee Development Branch. These programs provide for graduate work leading to advanced degrees, advanced training, college course work, short courses, continuing education, and career

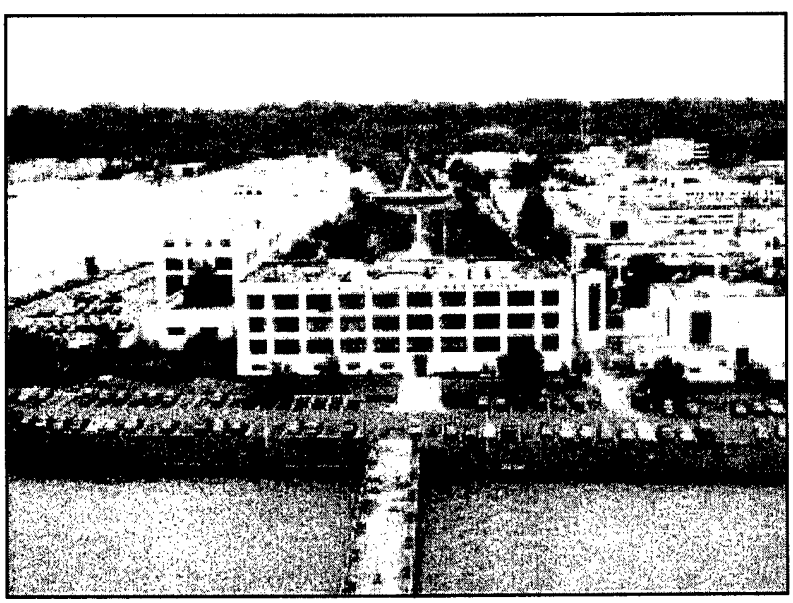

NRL headquarters, located off Interstate 295 in S.W. Washington, D.C., as viewed from the Potomac River.

radar-imaging data collection. There is a space-time adaptive processing (STAP) array and associated processors for the airborne early warning (AEW) area. In connection with ship-based radar, the division operates a Radar Test Bed Facility at the Chesapeake Bay Detachment (CBD), Randle Cliffs, Maryland. Represented are radars for long-range air search, point defense, and surface search functions. The point defense and surface search systems are designed to be mobile so that testing is not limited to this specific environment. A new capability for investigating backscatter from surface and volumetric clutter is now operational, and a millimeter wave radar system is currently being developed. Concepts and engineering developments in connection with target identification are explored by using an experimental Cooperative Aircraft Identification (CAI) System. Other installations operated by the division include an Electromagnetic Compatibility (EMC) Facility supported by a mode-stirred chamber, a Radar Signature Calculation Facility for complex electromagnetic radar target modeling, a Compact Antenna Range (operated jointly with the Space Systems Development Department) for antenna design and development, and a Computer-aided Engineering (CAE) Facility.

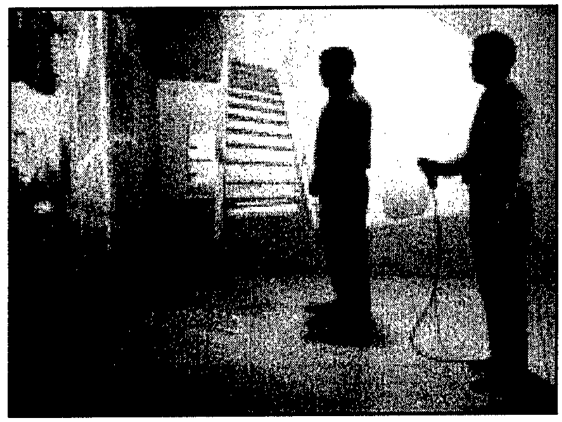

The Information Technology Division's surround-screen Virtual Reality Immersive Room provides a unique 3-D environment in which to perform scientific research and development investigations.

Information Technology

The Information Technology Division (ITD) is at the forefront of DoD research and development in artificial intelligence, telecommunications, computer networking, human-computer interaction, information security, parallel computation, and computer science.

The division maintains local area computer networks to support its research and hosts test-beds for advanced high-performance fiber-optic network research. These networks make available hundreds of high-performance computers to local and remote users. The ITD research networks connect to NRL's internal network via DS-3 (45 Mbps) links to NSI and via ATM to the ATDnet and AAI. The ATDnet is a metropolitan ATM network with OC-3 (155 Mbps) and OC-12 (622 Mbps) links at NRL. AAI is a CONUS-wide ATM network.

Major shared resources include the systems and networks available in ITD's Center for Computational Science (CCS). The systems include an SGI/CRAY Origin2000 with 128 processors; an HP/Convex Exemplar SPP-2000 with 64 processors; two CM-500e Connection Machines, one with 256 processors, 32 Gbytes of memory, and rated at 40 Gflops, and the other with 32 processors, 4 Gbytes of memory, and rated at 5 Gflops; a 43 Tbyte robotic D2 tape storage archiver; a 6 Tbyte file server and archiver; and the Scientific Visualization Laboratory. The CCS manages NICEnet, NRL's local area network, which runs FDDI on the backbone and to some desktops and includes ATM support. NICEnet provides external connections to other networks and the worldwide Internet.

The division facilities also include an Information Security Engineering Laboratory, a high-data-rate multimedia satellite transmission facility, and an experimental facility with special displays, eye and gesture trackers, and speech I/O devices for research in human computer interaction.

The Virtual Reality (VR) Laboratory provides the facilities and expertise to allow NRL scientists to use virtual reality in a variety of scientific investigations. Research areas include shipboard firefighting, simulation-based design, command and control, and scientific visualization. A number of high-speed graphics workstations, including Onyx Reality Engine 2 and Infinite Reality computers, and a variety of VR peripherals comprise the VR Lab computer equipment inventory.

Current VR technologies available include desktop VR systems, head-mounted displays (HMDs), the Responsive Workbench, and the surround-screen Immersive Room. The Responsive Workbench is an interactive 3-D tabletop environment that displays computer-generated, stereographic images on the workbench surface for use in battlespace situation awareness, simulation-based design, and other applications. The surround-screen

Immersive Room is a multiuser, high-resolution 3-D visual and audio environment that projects computer-generated images onto three walls and the floor to create an immersive, large-scale, shared virtual environment.

Optical Sciences

The Optical Sciences Division has a broad program of basic and applied research in optics and electro-optics. Areas of concentration include fiber optics, integrated optical devices, signal processing, optical information processing, fiber-optic and infrared sensors, high-power diode lasers, and diode-pumped solid-state lasers.

The division occupies some of the most modern optical facilities in the country. This includes an Ultralow-loss, Fiber-Optic Waveguide Facility using high-temperature infrared glass technology. There is also a Focal-Plane Evaluation Facility to measure the optical and electrical characteristics of infrared focal-plane arrays being developed for advanced Navy sensors. The IR Missile-Seeker Evaluation Facility performs open-loop measurements of the susceptibilities of IR tracking sensors to optical countermeasures. The Large-Optic, High-Precision Tracker system is used for atmospheric transmission and target signature measurements. The High-Energy Pulsed Hydrogen Fluoride, Deuterium Fluoride Laser is used for investigation into a wide variety of research areas including stimulated Brillouin scattering, optical-phase conjugation, and pulsed laser amplification.

There are several Fiber-Optic Sensor Facilities with fiber splicers, an acoustic test cell, a three-axis magnetic sensor test cell, equipment for evaluating optical fiber coatings, and various computers for concept analysis. The Digital Processing Facility is used to collect, process, analyze, and manipulate infrared data and imagery from several sources. The Emittance Measurements Facility performs measurements of directional hemispherical reflectance. Diode-pumped solid-state lasers operate in an eye-safe region of the optical spectrum.

The newest facility is the Infrared Test Chamber, or IR Range, which is an ultradry test chamber used to measure the IR signatures of new surface treatments, scale models, and components used for observables control on ships, aircraft, and missiles.

Electronic Warfare

The scope of research and development at NRL in the field of electronic warfare covers the entire electromagnetic spectrum—from basic technology research, component, and subsystem development—to system design and effectiveness evaluation. Major emphasis is placed on providing the methods and means to counter enemy hostile actions in all battle phases, from the beginning—when enemy forces are mobilized for an attack—through the final engagement stages. For this purpose, NRL has constructed special research and development laboratories, anechoic chambers, and facilities for modeling and simulation. NRL has also added extensive new facilities where scientists can focus on the coordinated use of all organic defensive and offensive resources now present in the Fleet.

Laboratory for Structure of Matter

The laboratory investigates the atomic arrangements in materials to improve them or facilitate the development of new substances. Various diffraction methodologies are used to make these investigations. Subjects of interest include the structural and functional aspects of energy conversion, ion transport, device materials, and physiologically active substances such as drugs, antibiotics, and antiviral agents. Theoretical chemistry calculations are used to complement the structural research. A real-time graphics system aids in modeling and molecular dynamics studies.

Chemistry

NRL has been a major center for chemical research in support of naval operational requirements since the late 1920s. The Chemistry Division continues its tradition with a broad spectrum of basic and applied research programs concerned with controlled energy release (fuels, fire, combustion, countermeasure decoys, explosives), surface chemistry (corrosion, adhesion, tribology, adsorbents, film growth/etch), advanced polymeric materials (high-strength/low-weight structures, drag reduction, damping, special function), and advanced detection techniques (environment, chemical/biological, surveillance). Facilities for research include a wide range of the modern photon/electron, magnetic- and ion-based spectroscopic/microscopic techniques for bulk and surface analysis; nanometer-scale fabrication and characterization; multiple facilities for materials synthesis and physical/chemical characterization; an 11,400 ft^3 fire-research chamber (Fire I); and a 475-ft ex-USS *Shadwell* (LSD-15) advanced fire-research ship.

The Chemistry Division has been involved in environmental quality studies for many years; some of these efforts have recently coalesced into an Environmental Quality Sciences Section whose mission includes characterization of chemically polluted environments, remediation technologies and evaluations, pollution-prevention strategies for Fleet and shore-side operations, environmental security, and disposal of chemical-warfare agents. Facilities in support of this research are laboratories for molecular biology, microbiology, biodegradation assessment, environmental biosensors, and geochemistry. In addition, a mesocosm facility has been established to bridge between laboratory and field work, with controlled scale-up of environmental systems. Located at the Aberdeen Proving Ground (APG), Edgewood, Maryland, it is currently configured to mimic a vertical circulation cell induced in an aquifer by a specific groundwater circulation technology. With that technology, a vertical circular flow pattern in the groundwater is created that transports dissolved contaminants around the circulation well for treatment directly in the well. The mesocosm facility is available for a variety of scientific endeavors. It enables (1) the controlled study of relationships between the effects of an environmental process and the high degree of spatial variability found in natural systems and (2) the development/validation of hypotheses and/or mathematical models that describe biogeochemical processes. In addition, the Chemistry Division maintains scientific and technical liaison with the Chemical and Biological Defense Command at APG, to promote interchange of information between the Navy and the Army in the areas of chemical and biological defense.

Materials Science and Technology

NRL has capabilities for X-ray and electron-diffraction analyses and for electron and Auger spectroscopy. Scanning, transmission, and combined scanning-transmission electron microscopes are used to study surface and/or internal microstructures. The division has a secondary ion mass spectrometer for surface analysis that significantly extends the diagnostic capability of the technique. A high-resolution, reverse-geometry mass spectrometer is used to probe reactions between ions and molecules. The Laboratory has a fully equipped fatigue and fracture laboratory, a modern vacuum arc-melting furnace for reactive metals, an ultrasonic gas-atomization system for making metal powders, and hot isostatic press facilities. The Laboratory's cryogenic facilities include dilution refrigerators and superconducting magnetic sensors for measuring ultrasmall magnetic fields. Also available are two molecular beam epitaxy devices for growing thin films.

Laboratory for Computational Physics and Fluid Dynamics

The Laboratory for Computational Physics and Fluid Dynamics is in round-the-clock production for computational studies in the fields of compressible and incompressible fluid dynamics, reactive flows, fluid-structure interaction (including submarine, ship, and aerospace applications), atmospheric and solar magnetoplasma dynamics, application of parallel processing to large-scale problems, such as unstructured grid generation for complex flows, target tracking and correlations for battle management, and other disciplines of continuum and quantum computational physics. The facility is used to develop and maintain state-of-the-art analytical and computational capabilities in fluid dynamics and related fields of physics, to establish in-house expertise in parallel processing and on-line graphical rendering for large-scale scientific computing, to perform analyses and computational experiments on specific relevant problems, and to transfer this technology to new and ongoing projects through cooperative programs.

The Parallel High Performance Computer/Graphics Facility is a heterogeneous high-performance computer system composed of a number of autonomous computers with a composite peak speed equivalent to about 15 Cray 90 processors. The system is coupled directly to the advanced video recording center described below. The main computational engine comprises of three Intel iPSC/860 Touchstone Gamma parallel supercomputers supported by the hardware and software environment necessary to develop, debug, and benchmark parallel simulations. With multi-Mflop processors as building blocks, the Intel iPSC/860 is a MIMD-distributed memory machine configured as a hypercube. These three machines comprise a block of 224 parallel nodes with a peak computational speed of 18 Gflops with a cross-connected disk farm file system and network connections.

The facility's disk farm also supports three IBM RS/6000 and three DEC AXP high capacity compute-server computers, providing the facility with medium-to-large-scale memory and computational power enabling heterogeneous simulations

with a significant scalar component, algorithm development, and diagnostic and postprocessing for large simulations. Special software allows simultaneous use of these computers on a single problem. Access to various other HPCC capabilities around the United States is accomplished through this system by using the new DoD high-bandwidth communication networks. A six-processor, 5-Gbyte SGI Onyx provides the division with state-of-the-art high-performance visualization.

A high-quality video studio has been created around a Sony D2 digital recording system, with a coupled Lyon-Lamb animation controller and a large memory Silicon Graphics ONYX workstation. Through the network, other graphics stations, including the extensive resources of NRL's Visualization Laboratory, can create and record high-quality graphical images of simulation data for analysis and presentation by using digital recording techniques.

Scientists in the Condensed Matter and Radiation Sciences Division perform time-resolved nonlinear-optical experiments using a titanium:sapphire regenerative amplifier/optical parametric amplifier system that can generate optical pulses of less than 100 fs duration with wavelengths spanning the UV, visible, and infrared spectral regions.

Condensed Matter and Radiation Sciences

The Condensed Matter and Radiation Sciences Division is the primary Navy center studying the effects of radiation on materials, electronic equipment, satellites, etc., and the production of thin films on diverse objects. The facilities for production and employment of photons, ions, and hypervelocity projectiles available to the division include:

High-Power Microwave (HPM) Facility: The large anechoic chamber (4.9 m × 4.9 m × 9.8 m) can be used at frequencies ranging from 0.5 to 94 GHz. Effects, susceptibility, and survivability of systems are the major research areas of interest.

Laser Facilities: Pulses of up to several joules are available from one system, while time resolutions down to 30 femtoseconds are produced by another. Synchronized Q-switched oscillators are configured for pump-probe experiments.

Thin-Film Preparation Facilities: The division has several major capabilities for preparation of thin films of advanced materials, such as high-temperature superconductors and active dielectrics. These include ion-assisted evaporation (which produces dense, adherent films), various dc plasma sources (which can etch as well as deposit films), and pulsed laser deposition (for production of chemically complex films).

X-ray Facility: Laboratory X-ray sources, monochromators, detectors, and related equipment are available for X-ray energies from 0.7 to 25 keV and dose rates up to 10^5 rads/s.

Synchrotron Radiation Facility: Intense, monochromatic X-ray photon beams tunable from 10 eV to 12 keV are available from the three beam lines developed by NRL at the National Synchrotron Light Source at the Brookhaven National Laboratory. Environmental target chambers can span a pressure range from 10^{-12} to 10^5 atm and temperatures from 10 to 1500 K.

Ion Implantation Facility: The facility consists of a 200 keV ion implanter with specialized ultrahigh vacuum chambers and associated in situ specimen analysis instrumentation.

3-MeV Tandem Van de Graaff: This facility is used to study charged-particle radiation damage effects such as occur in space, to provide high-sensitivity analysis of materials, and to perform MeV energy implants in materials.

Plasma Physics

The Plasma Physics Division is the major center for in-house Navy and DoD plasma physics research. The division conducts a broad experimental and theoretical program in basic and applied research in plasma physics, which includes laboratory and space plasmas, pulsed-power sources, plasma discharges, intense electron and ion beams and photon sources, atomic physics, laser physics, advanced spectral diagnostics, plasma processing, nonlinear dynamics and chaos, and numerical simulations. The facilities include an

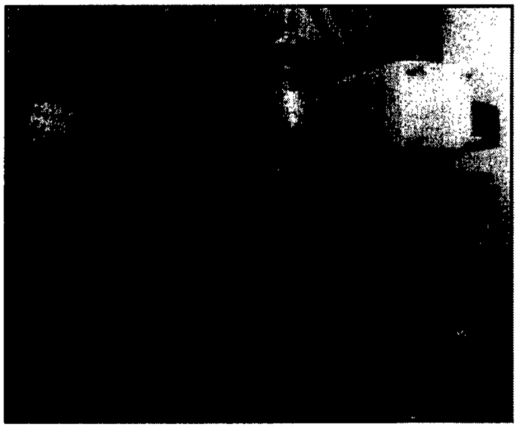

(a)

(b)

The Agile Mirror plasma (purple-colored region) (a) is contained within a low pressure (200 mTorr air) chamber. The mirror is formed by a multikilovolt one-dimensional electron beam driven between a linear cathode and a flat plate anode located inside the chamber. A 200-G vertical magnetic field is superimposed by magnetic field coils above and below the plasma. (b) The plasma is shown edge-on (left) and slightly rotated from a side view. The structure at the top is the linear cathode that produces a beam of kilovolt electrons. These electrons ionize the background gas as they stream from the cathode to the anode, forming the plasma sheet. The plasma is sufficiently dense to reflect high frequency microwaves, thereby acting like a plasma mirror.

extremely high-power laser—Pharos III—for the laboratory simulation of space plasmas and nuclear weapons effects studies and a short pulse, high-intensity Table-Top Terawatt (T^3) laser to study intense laser-plasma, laser-electron beam, and laser-matter interactions. The division also has an 11 m^3 space chamber capable of reproducing the near-Earth space plasma environment and a radar antenna laboratory where the interaction of high-frequency microwaves and a sheet plasma distribution (agile mirror) are studied. The division has developed a variety of pulsed-power sources to generate intense electron and ion beams, powerful discharges, and various types of radiation. The largest of these pulsers—GAMBLE II—is used to study the production of megampere electron and ion beams and to produce very hot, high-density plasmas. Other generators are used to produce particle beams that are injected into magnetic fields and/or cavities to generate intense microwave pulses (e.g., the Relativistic Klystron Amplifier (RKA), in the 1 to 10 GHz regime). A large array of high-frequency microwave sources (35 to 120 GHz) are available to conduct research on microwave processing of advanced ceramic materials.

A major 3 kJ KrF laser facility opened in June 1995. This facility is being initiated to provide intense radiation for studying inertial confinement fusion target heating at short wavelengths (0.25 microns) and high pressure physics.

Electronics Science and Technology

In addition to specific equipment and facilities to support individual science and technology programs, NRL operates the Nanoelectronics Processing Facility (NPF), the Penthouse Processing Facility (PPF), the Laboratory for Advanced Material Synthesis (LAMS), and the EPICENTER. The NPF's mission is to provide service to both NRL and external organizations requiring micro- and nanofabrication processing support. Lithography is a particular strength of the NPF, with definition of feature sizes down to 150 Å possible with an e-beam nanowriter. The NPF can supply items ranging from individual discrete structures and devices to circuits with very-large-scale integration complexity. The PPF is dedicated to processing III-V semiconductor devices and circuits in addition to serving the hands-on fabrication needs of individual NRL scientists. The PPF uses a single-pass air-ventilation system to minimize human risk to potentially hazardous III-V semiconductor processes and associated chemicals, thereby further meeting existing safety standards. The LAMS' mission is to support NRL programs that require thin-film III-V or refractory semiconductor technology. The LAMS employs organometallic vapor phase epitaxy to synthesize a wide range of thin films such as InSb, InGaP, InP, and GaN. The EPICENTER (a joint activity of the Electronics Science and

Technology, Materials Science and Technology, and Chemistry Divisions) is dedicated to the production of multilayer microstructures using in-situ surface analytical techniques in either of two ultrahigh vacuum, molecular-beam-epitaxy growth chambers—one for III-V semiconductors and the other for magnetic materials and II-VI semiconductors.

Bio/Molecular Science and Engineering

The Center for Bio/Molecular Science and Engineering conducts research and development using biotechnological approaches to solve problems for the Navy, DoD, and the nation at large. Problems currently being addressed include advanced material development (for electronic, biomedical, and structural applications), combat casualty care, environmental quality (including pollution cleanup and control), and biological warfare defense. The approach to these problems involves long-term research focused on the study of complex materials systems, coupled with integrated exploratory and advanced development programs. The staff of the center is an interdisciplinary team who performs basic and applied research and development in areas that require expertise in bio- and surface chemistry, biophysics, genetic engineering, cell biology, advanced organic synthesis, solid-state and theoretical physics, and electronics and materials engineering. In addition, the center has many collaborations throughout the Laboratory, at universities, and in industry to ensure that a broad base of the required expertise and critical evaluations are part of the research and development programs. Highlights of the program include the development of liposome-based blood substitutes, the manipulation of biologically derived structures on the nanometer scale, the development of ferroelectric liquid crystal systems with microsecond response times, discovery of an advanced resist system for high-speed, high-density integrated circuits, the patterning of neuronal cells to form neural networks, and the development of biosensors for environmental monitoring.

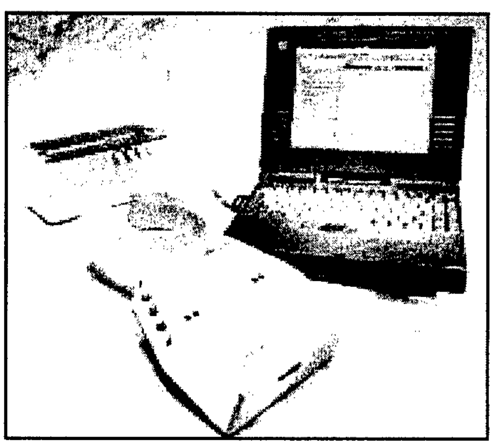

Portable field biosensor for environmental monitoring. The instrument was engineered by Research International (Woodinville, WA) based on NRL flow immunosensor technology.

In October 1994, the center occupied newly renovated laboratories and offices in Building 30. These modern facilities, designed to be used into the next century, include general laboratories for research in chemistry, biochemistry, molecular biology, and physics. Specialized areas include a 600-ft^2 Class 1000 clean room; an advanced Electron Microscope facility; and a Scanning Probe Microscope laboratory. Instrument rooms in the new building provide access to a variety of spectrophotometers (IR, GC-MS, NMR, and UV-Vis) and other equipment used in biochemical or physical analyses of biomaterials. Additional laboratories accommodate an X-ray diffraction instrument, a liquid crystal fabrication facility, and equipment for advanced electronics and biosensor programs.

Acoustics

The Acoustics Division has three integrated acoustic pool facilities supporting research in submarine target characteristics for ASW, submarine acoustic design and quieting, sensors for hull-mounted sonars, and structural acoustics for mine countermeasures. Scaled submarine targets, real mine structures, sensors mounted on hull simulators, and underwater buried objects can all be examined with advanced nearfield holographic and scanning 3-D laser vibrometer systems to measure and visualize the sound fields near a structure, the vibrations of the structure itself, the resulting farfield sound fields, and the physics of the sound-structure-fluid interactions.

The division operates several acoustic projectors and receive arrays for the generation and collection of experimental data. Source projectors include five towed XF4 flextensional transducers, two moored organ-pipe projectors, and a battery-operated arbitrary-waveform projector system. Receive systems include a moored, 32-element (up

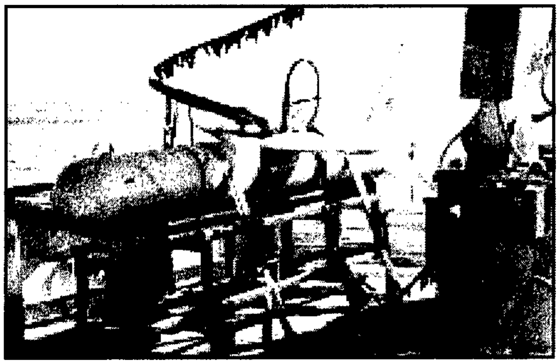

NRL's High-Frequency Acoustics Tow Body System is a high-speed, remotely operated vehicle with acoustic instrumentation to measure high-frequency acoustic properties in shallow water environments.

to 50 kHz) vertical-array with an RF telemetry system, a 64-element (25 Hz to 2 kHz) towed oil-filled seismic-type array, and a 64-element (25 Hz to 2 kHz) array that can either be deployed along the ocean bottom or moored vertically. The 64-element arrays use direct-link cabling to a 256-channel (expendable to 1024 channel), 50 kHz bandwidth data acquisition and processing system with a 330 Gbyte recording system. The division also has unique, self-recording digital acquisition buoy systems (DABS) that are used to obtain multichannel (up to 128) acoustic data in the 10 Hz to 5 kHz regime. These systems provide up to 250 Gbytes of data on a single 15-in. reel of 1-in. tape. The division has recently developed the Satellite-Linked Vertical Line Array (SLVA) system to collect acoustic and oceanographic data and transmit selected data to a remote shore station in real time. The buoy has a local-area network and computers on board to control the collection, preprocessing, and transmission of data. The multichannel data are sent via high-speed satellite channel at speeds in excess of 1 Mbit/s, using commercial Ku-band satellites.

The division operates high-frequency (up to 600 kHz) acoustic measurement systems to obtain scattering, target strength, and propagation data using bottom-moored instrumentation towers and a high-speed, remotely operated vehicle. These data are used to simulate the performance of weapons and mine countermeasure sonars (including advanced synthetic aperture sonars) in shallow and very shallow water environments.

The Tactical Oceanography Simulation Laboratory (TOSL) is a modeling and simulation architecture consisting of a set of tools for ingesting and processing climatological and real-time environmental data and applying energy propagation models to those data to determine acoustic and nonacoustic propagation loss. TOSL also contains tools to provide physical performance modeling using the available environmental data. TOSL is coupled with a storage repository of environmental data and a wide-area network (WAN), which allow full participation in a distributed simulation environment. TOSL features a high-performance computational capability for providing real or near-real-time calculations in support of training, war games, operations rehearsal, and other distributed simulation functions.

Remote Sensing

The Remote Sensing Division conducts a program of basic research, science, and applications to develop new concepts for sensors and imaging systems for objects and targets on the Earth, in the near-Earth environment, and in deep space. The research, both theoretical and experimental, leads to discovering and understanding the basic physical principles and mechanisms that give rise to the background environmental emissions and targets of interest and to absorption and emission mechanisms of the intervening medium. Accomplishing this research requires the development of sensor systems' technology. The developmental effort includes active and passive sensor systems used for the study and analysis of the physical characteristics of phenomena that evolve from naturally occurring background radiation, such as that caused by the Earth's atmosphere and oceans and man-made or induced phenomena, such as ship/submarine hydrodynamic effects. The research includes theory, laboratory, and field experiments leading to ground-based, airborne, or space systems for use in remote sensing, astrometry, astrophysics, surveillance, nonacoustic ASW, improved meteorological/oceanographic support systems for the operational Navy, and the environmental/global climate change initiatives. Special emphasis is given to developing space-based platforms and exploiting existing space systems.

The Navy Prototype Optical Interferometer (NPOI), a major new facility of the Remote Sensing Division, is actually two collocated instruments for making high-angular-resolution optical measurements of stars. Light from widely separated individual siderostats is combined simultaneously to synthesize the angular resolution of a telescope tens to hundreds of meters in diameter. Four

siderostats are placed in an array with extremely accurate metrology to enable very-high-precision measurements of stellar positions (wide-angle astrometry). These measurements are used by the U.S. Naval Observatory to refine the celestial reference frame, determine Earth rotation parameters, and thus satisfy Navy requirements for precise time and navigation data. They also provide determinations of basic astrophysical parameters, such as stellar masses and diameters. Additional relocatable siderostats can be placed out to distances of 250 m from the array center and used to construct very-high-resolution images of stars. These images provide fundamental astrophysical information on stellar structure and activity. When complete, the NPOI will be the most advanced high-resolution imaging optical interferometer in the world.

Oceanography

The Oceanography Division is the major center for in-house Navy research and development in oceanography. It is known nationally and internationally for its unique combination of theoretical, numerical, and experimental approaches to oceanographic problems. Researchers make extensive use of the Maury Oceanographic Library (jointly operated by NRL-Stennis Space Center (NRL-SSC) and the Naval Oceanographic Office), which is recognized as one of the best and most comprehensive oceanographic libraries in the world. The division numerically models the ocean and coastal areas of the world. This modeling is conducted on the Navy's and DoD's most powerful vector and parallel-processing machines. To study the results of this intense modeling effort, the division operates a number of highly sophisticated graphic systems to visualize ocean and coastal dynamic processes. The seagoing experimental programs of the division range worldwide. Unique measurement systems include towed sensor and advanced microstructure profiler systems for studying micro- and fine-scale ocean structures; an integrated absorption cavity, optical profiler system and towed optical hyperspectral towed array for studying ocean optical characteristics, and self-contained bottom-mounted upward-looking acoustic Doppler current profilers for measuring ocean variability. In the laboratory, the division operates an environmental scanning electron microscope and a laser confocal scanning microscope for detailed studies of biocorrosion in naval materials.

Marine Geosciences

The Marine Geosciences Division is the major center for in-house naval research and development in marine geology, geophysics, geoacoustics, and geotechnology. It is also the Navy's lead activity for mapping, charting, and geodesy research and development. The division has acquired unique instrumentation suites for studies of the seafloor and subseafloor. These include sidescan sonar systems; deep-towed, low-frequency acoustic-reflection systems; parametric acoustic-swath subbottom-mapping systems; remotely operated vehicles; and electromagnetic mapping sensors. These systems allow studies ranging from sediment classification to mapping of inclusions and changes in the seafloor subbottom structure. The division deploys ocean bottom and subbottom seismometer systems for use in studies ranging from tectonic noise to whale migration. Specialized seafloor probes allow measurement of the water pressure

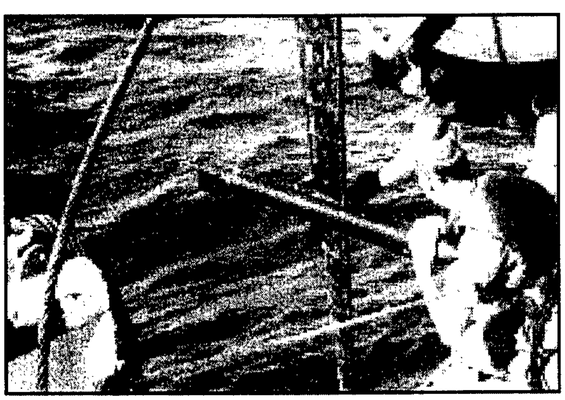

Oceanography Division's new Hyper-Spectral Towed Array (HYSTAR) shown being deployed in the Gulf of Mexico.

and pressure gradient in sediment pores, electrical conductivity, and acoustic compression and shear wave velocity and attenuation. Laboratory equipment includes a transmission electron microscope (100 and 300 kVa) with environmental cells to carry out sediment-fabric and sediment-pollutant adsorption studies.

The Moving-Map Composer Facility, a collection of computers and work stations with associated graphics manipulation software, is used to design mission specific map coverages for tactical fighter pilots and to compress map information onto a CD-ROM for Navy and Marine Corps aircraft digital moving maps. The division also operates the NRL Magnetic Observatory at SSC. This facility includes two specially built wooden buildings with minimal ferrous content and arrays of magnetometers that extend radially from the building. The Magnetic Observatory measures the Earth's ambient magnetic field, its changes, and other magnetic phenomena. The observatory is part of a worldwide observing system.

Marine Meteorology

The Marine Meteorology Division is located in Monterey, California. NRL-Monterey (NRL-MRY) performs basic and applied research in the atmospheric sciences relevant to both central-site and on-scene operations. Located adjacent to the Navy's operational weather forecasting center, Fleet Numerical Meteorology and Oceanography Center, NRL-MRY develops global and regional mesoscale data assimilation/forecast systems and other products that provide worldwide environmental support for Navy and joint operations.

NRL-MRY's access to a variety of computer resources, databases, and numerical prediction systems helps make this Division one of the premier centers for weather prediction and data application research and development. Large mainframes and databases at Fleet Numerical are used to develop and transition operational analysis and prediction systems. Secure terminal rooms located throughout NRL-MRY and Fleet Numerical allow for a direct link to classified computer resources. Furthermore, NRL-MRY is networked to the DoD High-Performance Computing Centers, which support research in atmospheric process studies and coupled air-ocean model development. Locally, high-performance workstations are used for on-scene system development, and the John B. Hovermale Visualization Center is designed for the display and interpretation of meteorological data and the development of briefing tools. State-of-the-art satellite receivers allow for local collection of data for applications research in support of the Joint Typhoon Warning Center and other Navy operations.

NRL-MRY has a long-standing tradition for participation in field projects. The Division has been involved in numerous fleet exercises to collect data and validate products for on-scene forecast systems development and weather-impact assessment. Recent participation in the Fronts and Atlantic Storm Track Experiment (FASTEX) provided a source of observations for testing hypotheses related to atmospheric predictability and sensitivity.

NRL-MRY is the lead laboratory for the Tactical Environmental Support System (TESS), a workstation-based environmental database and diagnostic/forecast system designed for on-scene use. Advanced technologies used in development include satellite meteorology, data analysis, advanced numerical modeling techniques, visualization, and artificial intelligence.

Space Science

NRL is the Navy's main laboratory for conducting basic research and development in the space sciences. The Space Science Division conducts and supports a number of space experiments in the areas of upper atmospheric, solar, and astronomical research aboard NASA, DoD, and other government-agency space platforms. Division scientists are involved in major research thrusts that include remote sensing of the upper and middle atmospheres, studies of the solar atmosphere, and astronomical radiation ranging from the ultraviolet through cosmic rays. In support of this work, the division maintains facilities to design, construct, assemble, and calibrate space experiments. A network of computers, workstations, image-processing hardware, and special processors is used to analyze and interpret space data. Among the division's space science data acquisition and analysis efforts are the following:

- mission operations and data analyses of NRL's Oriented Scintillation Spectrometer Experiment (OSSE) for NASA's Compton Observatory;

- observation of the Sun's interaction with the upper-Earth atmosphere through the Solar Ultraviolet Spectral Irradiance Monitor (SUSIM) experiment in support of NASA's Upper Atmosphere Research Satellite (UARS) and Atmospheric

Laboratory for Application and Science (ATLAS) missions; and

• observation and analysis of the evolution and structure of the solar corona from the disk to 0.14 AU. This effort involves acquiring and analyzing data from the Large-Angle Spectrometric Coronagraph and Extreme Ultraviolet Imaging Telescope on the Solar Heliospheric Observatory satellite.

• observation of selected celestial and atmospheric targets in the ultraviolet and X-ray bands by three Advanced Research and Geophysical Observation Satellite (ARGOS) experiments—Global Imaging of the Ionosphere (GIMI), High-Resolution Atmospheric and Auroral Spectroscopy (HIRAAS), and Unconventional Stellar Aspect (USA). ARGOS is scheduled to be launched in 1998.

The Space Science Division has established a major facility for the application of high spectral resolution ultraviolet (UV) spectroscopy to the satellite observations of Earth's middle atmosphere between the altitudes of 30 and 100 km. This highly successful facility has dramatically demonstrated the power of the technique. The Middle Atmosphere High Resolution Spectrograph Investigation, or MAHRSI, recently completed its second flight as part of the CRISTA-SPAS satellite, which was deployed and retrieved by the space shuttle. MAHRSI has a resolving power of 16,000 at a wavelength of 308 nm. On its first flight in November 1994, MAHRSI made the first-ever global maps of the distribution of hydroxyl (OH) in the middle atmosphere. It also measured a 7 1/2-hour snapshot of the distribution of nitric oxide (NO) between 55 South latitude and 63 North latitude. OH is important in the photochemistry of ozone throughout the atmosphere and is responsible for nearly all of the destruction of ozone at altitudes above 65 km. Despite its well known importance, the difficulty of measuring OH from space defied previous attempts; high spectral resolution was the key to the success of MAHRSI. Because OH is produced when UV sunlight dissociates water molecules, it is a sensitive indicator of the abundance of H_2O as well. Both flights of MAHRSI substantiate the view that the amounts of H_2O at these high altitudes are unexpectedly high and remain unexplained. The division is also developing a miniaturized UV imaging interferometer nearly 20 times smaller than MAHRSI with orders of magnitude more throughput, a resolving power of 53,000, and with no moving parts. This instrument is called the Spatial Heterodyne Imager for Mesospheric Radicals, or SHIMMER. The concept of SHIMMER is extremely powerful, with application to a wide range of DoD and scientific investigations.

Space Technology

In its role as a center of excellence for space systems research, the Naval Center for Space Technology (NCST) designs, builds, analyzes, tests, and operates spacecraft as well as identifies and conducts promising research to improve spacecraft and their support systems. NCST facilities that support this work include large and small anechoic radio frequency chambers, clean rooms, shock and vibration facilities, an acoustic reverberation chamber, large and small thermal/vacuum test chambers, a control system interaction laboratory, satellite command and control ground stations, a fuels test facility, and modal analysis test facilities. NCST has a facility for long-term testing of satellite clock time/frequency standards under thermal/vacuum conditions linked to the Naval Observatory; a 5-m optical bench laser laboratory; and a hologram research laboratory to conduct research in support of the development of space systems.

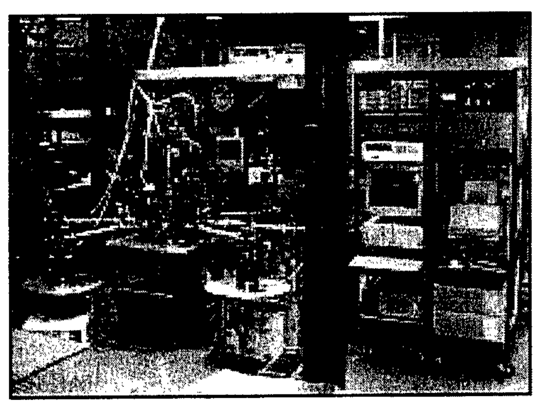

The NRL Life Cycle Crycooler Test Facility uses an automated vacuum and data acquisition system to monitor and control ten cryocoolers simultaneously.

Research Support Facilities

Technical Information Services

The Ruth H. Hooker Research Library supports the NRL mission through a comprehensive program of scientific information services available to NRL-DC employees, on-site contractors, and ONR Headquarters staff. The Library maintains a 50,000 volume research collection of technical books and scholarly monographs, a scientific journal collection with approximately 1,000 current subscriptions with extensive back files maintained as bound volumes or on microfilm, and a research reports collection of more than one million items stored in paper, microform, and digital format. In addition to providing such traditional library services as on-site materials circulation, interlibrary loan, literature searches, and a full range of reference and information services covering both open literature and classified information sources, the Library has initiated an aggressive program of delivering both bibliographic data and textual images directly to researchers. The Library's substantial digital efforts include Internet-based desktop availability of the Library catalog to all platforms at all sites of NRL and ONR Headquarters; major scientific and reference databases; page images of several hundred journal titles and thousands of research reports; and e-mail delivery of journal tables of contents. The Library also has formed cooperative research agreements with scientific publishers in electronic publishing/archiving and has joined other federal science libraries in co-founding the National Research Library Alliance (consisting of NRL, National Institutes of Standards and Technology, the National Science Foundation, and the NASA Goddard Space Flight Center) to build superior and cost-effective digital library infrastructures.

Publication services include writing, editing, composition, publications consultation and production, and printing management. Quick turnaround black and white as well as color copying services are provided. The primary focus is on using computer-assisted publishing technology to produce scientific and technical information containing complex artwork, equations, and tabular material.

The research conducted at NRL requires a diversity of graphic support from the Systems/Photographic Branch, such as technical and scientific illustrations, computer graphics, design services, photographic composites, calligraphy, display panels, sign making, and framing. A high-end workstation provides and delivers a new level of electronic airbrushing and photographic retouching. Photographic services include still-camera coverage for data documentation both at NRL and in the field. Photographic images can also be captured with state-of-the-art digital cameras and still video. A photographic laboratory offers custom processing and printing of black and white and color films. Quick-service color prints are also available. Video services include producing video reports of scientific and technical programs. A video studio and editing facility with high-quality Beta Cam and digital video editing equipment are available to support video production. The NRL Exhibits Program develops and produces displays, audio-visual material, and multimedia programs for presentation at technical meetings, conferences, and symposia. The Multimedia Center has the capability of authoring/producing multimedia programs. The Center uses two complete multimedia systems with Macromedia Director and Adobe Photoshop and a digital video editing system, the AVID Media Composer 1000. The Visual Design/Imaging Center offers high-quality output from computer-generated files in EPS, Postscript, PICT, TIFF, Photoshop, and PowerPoint. The Captivator film recorder produces high-resolution 35-mm slides, viewgraphs, and negatives. Photographic quality color prints and viewgraphs are available from Kodak dye-sublimation printers. High-resolution scanning to a Macintosh or PC disk is available. The Linotron imagesetter produces gray-scale prints and transparencies at 1693 dots per inch.

The Administrative Services Branch is responsible for collecting and preserving the archival documents that comprise NRL's corporate memory. Archival documents include personal papers and correspondence, laboratory notebooks, and work project files—documents that are appraised for their historical or informational value and considered to be permanently valuable. The Branch provides records management services, training, and support for the maintenance of active records as an important information resource, including electronic records and e-mail. The Administrative Services Branch is also responsible for NRL's postal mail services.

Center for Computational Science

The Center for Computational Science (CCS) conducts research and development to further the advancement of computing and communications systems to solve Navy problems. Promising technologies are transitioned to production systems. The CCS operates and maintains computer systems and networks that provide support for NRL, Navy, and DoD research. The CCS features two massively parallel processing (MPP) CM-500e Connection Machines: one with 256 processors, 32 Gbytes of memory, and rated at 40 Gflops, and the other with 32 processors, 4 Gbytes of memory, and rated at 5 Gflops; a 43 Tbytes robotic D2 tape storage system. The CCS operates high-performance network testbeds including an ATM/SONET experimental metropolitan area network. These leading-edge systems are being investigated and developed by the CCS.

The CCS also manages and operates production computer systems and networks. A Cray Y-MP EL provides support for vector computing. The CCS supplies lab-wide data storage support with NRL's File Server/Archiver (FS/A) system. The FS/A provides 70 Gbytes of on-line disk storage and 6 Tbytes of robotic tape storage.

The CCS Scientific Visualization Lab (Viz Lab) functions as an information center, video production unit, and training center for the latest tools in scientific visualization and visual supercomputing. By using powerful computational workstations, graphics workstations, and a networked digital video editor, researchers can turn the results of their computations into color prints, 35-mm slides, or animations on video tape. The Viz Lab has a "Responsive Workbench" developed by ITD's VR Lab, which uses an SGI Onyx RE2 so scientists can interact and control their supercomputing calculations in real time. The Viz Lab also provides assistance and training in high-performance computing and clustered workstation programming.

The CCS manages the NRL local area network, NICEnet, which provides access to all NRL computing assets including those of the CCS. NICEnet also has an FDDI backbone, FDDI to some desktops, and ATM support. NICEnet also has a lab-wide cable television network and provides external connections to DoD networks and the worldwide Internet. NICEnet also provides dial-in services including SLIP/PPP and ISDN.

The CCS provides site licenses, support contracts for most workstations and desktop computers as well as acquisition contracts, on-line software, consulting and e-mail support, and training. A help desk and software demonstration are provided to assist NRL researchers.

FIELD STATIONS

NRL has acquired or made arrangements over the years to use a number of major sites and facilities for research. The largest facility is located at the Stennis Space Center (NRL-SSC), in Bay St. Louis, Mississippi. Others include a facility at the Naval Postgraduate School in Monterey, California (NRL-MRY), and the Chesapeake Bay Detachment (CBD) in Maryland. Additional sites are located in Randall Cliffs, Maryland, Virginia, Alabama, and Florida.

Flight Support Detachment (NRL FSD)

Located aboard the Patuxent River Naval Air Station in Lexington Park, Maryland, NRL FSD operates and maintains five uniquely configured P-3 Orion turboprop aircraft as airborne research platforms. The FSD conducts single aircraft, worldwide detachments in support of a wide range of scientific research.

In FY 97, NRL FSD provided flight support for diverse research programs including: Airborne Multisensor Pod System (AMPS), a multisensor data collection system that made a first time detachment to Kazakstan, located in former USSR; Airborne Geographical Sensor Suite (AGSS), involving data and gravimeter testing to detect variations in the ocean floor; Fly's Eye, an infrared threat warning system; Real Aperture Radar (RAR); Integrated Electronic Warfare System (IEWS), a system that simulates radars of various surface and airborne platforms; Oceanographic Surveillance (OS); and Chaff, test and evaluation of air deployed chaff.

The NRL FSD aircraft are the sole airborne platforms for numerous projects, such as bathymetry, electronic countermeasures, gravity mapping, and radar development research. The detachment has an impressive safety record of over 54,000 accident-free flight hours amassed over a 34-year period.

Chesapeake Bay Detachment (CBD)

CBD occupies a 168-acre site near Chesapeake Beach, Maryland, and provides facilities and support services for research in radar, electronic

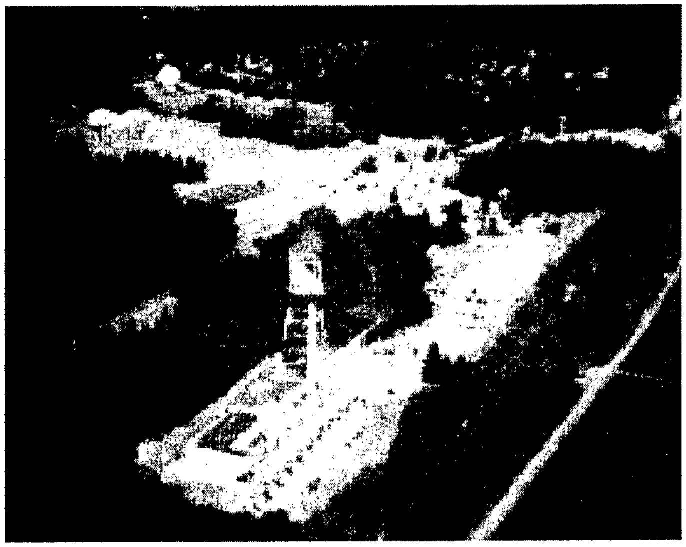

Aerial view of NRL's Chesapeake Bay facility located near Chesapeake Beach, Maryland.

warfare, optical devices, materials, communications, and fire research. Because of its location high above the Chesapeake Bay on the western shore, unique experiments can be performed in conjunction with the Tilghman Island site, 16 km across the bay from CBD. Some of these experiments include low clutter and generally low-background radar measurements. By using CBD's support vessels, experiments are performed that involve dispensing chaff over water and radar target characterizations of aircraft and ships. Basic research is also conducted in radar antenna properties, testing of radar remote-sensing concepts, use of radar to sensor ocean waves, and laser propagation. CBD also hosts facilities of the Navy Technology Center for Safety and Survivability, which conducts fire research on simulated carrier, surface, and submarine platforms.

Marine Corrosion Test Facility

Located on Fleming Key at Key West, Florida, this facility offers an ocean-air environment and clear, unpolluted, flowing seawater for studies of environmental effects on materials. Equipment is available for experiments involving weathering, general corrosion, fouling, and electrochemical phenomena as well as coatings, cathodic protection devices, and other means to combat environmental degradation.

Naval Research Laboratory-Stennis Space Center (NRL-SSC)

NRL-SSC, a tenant activity at NASA's Stennis Space Center, is located in the southwest corner of Mississippi, about 50 miles northeast of New Orleans, Louisiana, and 20 miles from the Mississippi Gulf Coast. The Center encompasses over 200 square miles of land area, including a perimeter buffer zone to insulate surrounding civilian communities from the noise of rocket-engine testing by NASA. Other Navy tenants at NRL-SSC include the Commander, Naval Meteorology and Oceanography Command and the Naval Oceanographic Office, who are major operational users of the oceanographic and atmospheric research and development performed by NRL. The Naval Oceanographic Office provides access for NRL researchers to one of the Navy's largest supercomputers. This unique concentration of operational and research oceanographers makes NRL-SSC the center of naval oceanography and the largest such grouping in the Western world.

NRL-SSC provides administrative and business operations support for entities of the Acoustics and Marine Geosciences Division, the Remote Sensing Applications Branch and the Oceanography Division. NRL-SSC occupies over 200,000 square feet of research, computation, laboratory, administrative, and warehouse space. Facilities include the

new microscopy center, a visualization laboratory, numerous large antennas to receive available oceanographic and meteorological satellite data, the Magnetic Observatory—part of a worldwide observing system, the Pattern Analysis Laboratory, a Map Data Formatting Facility, a water-wave channel, and numerous laboratories for acoustic and oceanographic computation, instrumentation, analysis, and testing. Special areas are available for constructing, staging, refurbishing, and storing sea-going equipment.

Marine Meteorology Division Monterey, California (NRL-MRY)

Located in Monterey, California, as a tenant activity of the Naval Support Activity, Monterey Bay, this facility is collocated with the Navy's operational Fleet Numerical Meteorology and Oceanography Center to support development of numerical atmospheric prediction systems and related user products. NRL-MRY's mission has broadened considerably in recent years to include basic research and development and to provide support to other customers. Collocation with Fleet Numerical allows NRL-MRY easy access to a large classified vector supercomputer mainframe. This access provides real-time global atmospheric and oceanographic databases for research on-site and at other NRL locations. Interfaces to the Defense Research and Engineering Network has also been established. Locally, NRL-MRY has multiprocessing Digital Equipment Corporation and Silicon Graphics Inc. workstations and data archives that allow in-house researchers to conduct numerical weather-prediction experiments, data processing, simulation, and visualization studies.

NRL-MRY's experience extends to mesoscale and on-scene atmospheric prediction systems. The Navy's Tactical Environmental Support System (TESS), developed for the Space and Naval Warfare Systems Command, is installed on-site and has undergone various upgrades to provide substantial improvements in system performance and capability and automatic product generation and display. TESS is functioning as an R&D testbed for new tactical/environmental decision aids, database management systems, and WindowsNT/X Windows-user interfaces. State-of-the-art graphics workstations (SGIs), network file-servers (Suns), and tactical (HP) systems have been acquired for use by researchers. Environmental components of future on-scene systems are currently being developed. In addition, the effects of the atmosphere on weapons, sensors, and platforms are being evaluated with primary emphasis on electromagnetic/electro-optic aerosols, and modeling and simulation impacts.

Midway Research Center

The Midway Research Center (MRC) is located on a 158-acre site in Stafford County, Virginia. Located adjacent to the Quantico Marine Corps' Combat Development Command, the MRC has 10,000 square feet of operations and administration area and three precision 18.5-m-diameter parabolic antennas housed in 100-ft radomes. The MRC, under the auspices of the Naval Center for Space Technology, provides NRL with state-of-the-art facilities dedicated solely to space-related applications in naval communications, navigation, and basic research.

Other Sites

Some field sites have been chosen primarily because they provide favorable conditions to operate specific antennas and electronic subsystems and are close to NRL's main site. Pomonkey, Maryland, a field site south of NRL, has a free-space antenna range to develop and test a variety of antennas. The antenna model measurement range in Brandywine, Maryland, has a 4.6-m diameter turntable in the center of a 305-m-diameter ground plane for conducting measurements on scale-model shipboard and other antenna designs. A site on the cliffs overlooking the Chesapeake Bay provides an over-the-water range of approximately 10 miles to Tilghman Island.

Research Platforms

Mobile research platforms contribute greatly to NRL's research. These include five P-3 Orion turboprop aircraft and one ship, the ex-USS *Shadwell* (LSD-15), berthed in Mobile Bay, Alabama. The ex-*Shadwell* is used for research on fire-suppression techniques on-board ship.

Looking Ahead

To provide preeminent research for tomorrow's Navy, NRL must maintain and upgrade its scientific and technological equipment to keep it at the forefront of modern research facilities. The physical plant to house this equipment must also be state of the art. NRL has embarked on a Corporate Facilities Plan to accomplish these goals. This plan and future facility plans are described below.

THE CORPORATE FACILITIES INVESTMENT PLAN (CFIP)

The CFIP is a financial spending plan to provide modern research facilities at NRL by the year 2000. The plan calls for both Congressional and Laboratory investment and is updated and altered as changes occur in scientific emphasis and Congressional attitude. During the past five years, Congressionally approved military construction (MILCON) funds were used to construct the new Electro-Optics Laboratory and a high-bay facility for the Naval Center for Space Technology. MILCON funds were approved in the FY 97 Congressional budget for the construction of an Ocean Acoustics Research Laboratory building at NRL-SSC. Future MILCON funds have also been requested for the construction of a Nano Science Research building at NRL-DC.

To complement these efforts, overhead funds have been used to renovate and upgrade laboratory and support areas in several existing buildings. Modern laboratory facilities have recently been provided for the Center for Bio/Molecular Science and Engineering, the Materials Science and Technology Division, the Remote Sensing Division, and the Acoustics Division. Work that is currently in progress will provide new facilities for the Information Technology Division and the Radar Division.

In parallel with efforts to upgrade laboratory buildings to the most modern standards, those buildings that were built during World War II and do not lend themselves to renovation are being demolished. This will provide space for the construction of future MILCON buildings, and it will also reduce the Laboratory's overhead costs.

Information Technology

The Information Technology Division's Center for Computational Science received two scalable, multiple-instruction multiple-data (MIMD) computer systems, which have Global Shared Memory (GSM) and Nonuniform Memory Access (NUMA) architectures. They are an SGI/CRAY Origin2000 with 128 processors and an HP/Convex Exemplar SPP-2000 with 64 processors. These systems are part of the Distributed Center (DC) at NRL that is funded by the DoD High Performance Computing Modernization Program (HPCMP). The systems will be used to continue innovative exploration and evaluation of massively parallel processing (MPP) technology for the solution of significant military-relevant problems relating to computational and information science. The systems will allow for continuing research into heterogeneous parallel processing with the NRL Thinking Machines Corporation CM-500e systems and other computational assets.

ITD's satellite transmission capability will expand to include high-data-rate Code Division Multiple Access (CDMA) spread spectrum systems that will allow networking with NRL-developed very small aperture terminals (VSATs) having apertures of 1 meter or less. This capability will permit experimentation with networked communications to small combatants that do not currently have high-data-rate access to land-based wide-area networks.

Plasma Physics

The division has established a new facility for research on high-frequency microwave processing of advanced ceramic materials. It features 35 and 94 GHz fixed-frequency gyrotrons, a 6 kW, 2.45 GHz industrial microwave source, and a unique tunable 60-120 GHz quasioptical gyrotron, which is under development. The facility is being used to investigate the scientific basis for understanding and controlling microwave processes, such as sintering/densification, coating, and joining for low-loss, refractory, ultrafine-grain polycrystalline ceramic materials.

Electronics Science and Technology

Important division emphasis is focused on the continual upgrading of the Nanoelectronics Processing Facility (NPF) and the Penthouse Processing Facility (PPF) and expanding activities in the nanoelectronics, heterostructures, and vacuum

electronics science and technology programs. The Laboratory for Advanced Material Synthesis Facility will continue to upgrade its organometallic vapor-phase epitaxy equipment for thin-film semiconductors and provide safer and more environmentally benign processing and waste-disposal techniques. The EPICENTER (a joint activity of the Electronics Science and Technology, Materials Science and Technology, and Chemistry Divisions) will continue to provide new insight into epitaxial semiconductor growth processes. Knowledge of these growth processes will be used for improved control of film properties for use in the electronic devices of tomorrow. These facilities will be enhanced with the creation of the Joint Laboratory for proximal probe nanofabrication. Completion of this facility is expected to occur by the end of 1998. It will serve as a resource for characterization patterning and defining the processes necessary for advanced nanodevice fabrication.

Acoustics

NRL's Salt Water Tank Facility was designed to provide a controlled environment for studying complex bubble-related processes found in the ocean. It is an experimental facility for studies of underwater acoustics, fluid dynamics, and air-sea interface environmental topics where saline conditions are an issue. This facility is used to study the acoustics of bubbly media, including bubble entrainment and ambient noise generation, scattering from bubbly structures, and propagation through bubbly media. Related studies include the interaction of bubbles with turbulent flows, bubble coalescence and dissolution, effects of surfactants and contaminants, and bubble-related gas exchange across the air-sea interface.

The heart of this facility is a 27,000 gallon tank containing saltwater. This tank is entirely above ground, with a 20-ft^2 by 20-ft^2 footprint. Each vertical face affords a high degree of optical access into the tank interior by means of a 12-ft wide by 8-ft high window. High-capacity water and air chillers are available, capable of lowering the water and air temperatures down to near the freezing point. Equipment can be lowered into the tank by means of a 2000-lb crane that covers the entire tank footprint plus the staging area alongside. A separate laboratory area (with it's own heating/cooling controls to provide normal working conditions) within the tank room is available for housing equipment and instrumentation. The facility is instrumented with a full suite of appropriate environmental sensors, hydrophones, amplifiers, filters, a data acquisition system, and an array of software and hardware for image acquisition and analysis.

Ocean Research Laboratory

NRL's Ocean Acoustics Research Laboratory (MILCON Project P-006) is a 52,000 square-foot building that will house the Oceanography Division of the Ocean and Atmospheric Science and Technology Directorate. The building will contain office space, oceanographic laboratories, staging areas, a small machine shop, electronic and secure laboratories, and computing facilities for research and development in ocean science and remote sensing. Construction is planned to start in November 1997 and be completed by mid-1999.

Vacuum Ultraviolet Space Instrument Test Facility

The Space Science Division facilities include an ultraclean solar instrument test facility in Building A-13 on the main NRL campus. The new facility is designed to satisfy the rigorous contamination requirements of state-of-the-art solar spaceflight instruments. The facility has a 400-square-foot Class 10 clean room and a large Solar Coronagraph Optical Test Chamber (SCOTCH). This completely dry-pumped, 550-cubic-foot vacuum chamber is maintained at synchrotron levels of cleanliness. Solar instrumentation up to 1 m in diameter and 5 m in length may be physically accommodated in the chamber. The instrument's optical performance is probed and calibrated with a variety of visible and XUV sources mounted on the chamber's 11-m beamline. The optical testing and characterization of the Large-Angle Spectrometric Coronagraph (LASCO) instrument for the European Space Agency's Solar Heliospheric Observatory satellite were conducted in this chamber. Coronagraph stray-light characterization was carried out by mounting a set of baffles in the main beamline, illuminating the instrument with a simulated solar beam, and measuring the residual radiation. A stray light background measurement of 10^{-12} was successfully measured in the LASCO C3 channel. Coronagraph calibration was carried out by installing back-illuminated calibrated opals in front of the instrument entrance aperture. Instrument polarization

properties were analyzed by using a variety of polarizers installed in a wheel located between the opal and the instrument. The wheel was remotely controlled from outside the chamber. Instrument Mueller matrices were verified with a 12-in. diameter, two-plate partial polarizer. Calibration and focus of XUV solar instrumentation are accomplished by exposing the instrument to an XUV windowless collimator at the end of the tank. The facility also has a small thermal bake/vacuum test chamber used for vacuum conditioning and thermal testing of spaceflight components and subassemblies. Both the SCOTCH and the small test chamber are instrumented with temperature-controlled quartz-crystal monitors and residual gas analyzers for real-time, quantitative measurements of volatile contamination.

Remote Sensing

To validate numerical and theoretical efforts ongoing within the Remote Sensing Division, extensive hierarchical-coupled experiments are planned within a new, Free-Surface Hydrodynamics Laboratory. This laboratory will be used to study free-surface turbulence interactions, wave-generation phenomena, jet-flow phenomena, vorticity dynamics, and free-surface/surfactant interactions. Of particular importance is the detailed study of surfactant materials, both in shear and surface wave flows. State-of-the-art diagnostic tools are available, such as Langmuir film balance to measure the properties of surface films, hot-wire and laser-Doppler anemometry, and the new quantitative flow techniques of laser speckle, particle tracking, and particle image velocimetry. The laboratory is also equipped with an IR camera with a 20×10^{-3} K resolution. These experimental diagnostic techniques use high-powered lasers, high-tolerance optical lenses, and extensive ultra-high-resolution video-imaging hardware and PC-based computerized systems. Further computational assets consist of powerful graphical computer work stations, the NRL Connection Machine, and other off-site CRAY supercomputer systems.

Marine Geosciences

The Marine Geosciences Division will greatly enhance the capabilities and quality of seafloor sediment fabric analyses through completion of installation and staff training for it's 300 kV transmission electron microscope (TEM) and accompanying environmental cell (EC) in FY 97. The TEM-EC is housed in a specially built facility imparting a null effect on the functioning of the TEM-EC electronics. The new facility will improve transition of developed capabilities and sediment fabric understanding to applied issues of acoustic and shock-wave propagation, mine burial, and mine countermeasures.

REHABILITATION OF SCIENTIFIC FACILITIES

Specialized facilities are being installed or upgraded in several of the research and support divisions.

Flight Support Detachment

NRL's Flight Support Detachment (FSD) has continued to improve both capabilities and diversity among its aircraft platforms. Aircraft 153442 continues to undergo extensive modifications with Lockheed Martin to install a "roto-dome" antenna and full AEW radar system. These modifications will support the Navy's Theater Air Defense programs, while providing a testbed for advanced EW radar research. Additionally, all aircraft are undergoing extensive bomb-bay design improvements that will allow the aircraft to carry more diverse scientific payloads. Aircraft 158227's communications capabilities were significantly upgraded with a state-of-the-art satellite telephone. These upgrades and modifications will ensure that NRL will have the finest airborne research capabilities well into the next century.

Information Technology

The Information Technology Division continues to upgrade its local area network and research into high-performance network testbeds, including ATM/SONET technology. The 256-processor CM-500e massively parallel computer has been upgraded to 400 Gbytes of storage in the Scaled Disk Array and now has an Extended Control Processor tied in with an SCI ring that will include an SCI-ATM gateway in the future. The architectures and performance of the three new scalable massively parallel systems (the SGI/Cray Origin2000, the HP/Convex Exemplar SPP-2000, and the Sun Ultra HPC) will be evaluated and the systems will be upgraded for continued research into heterogeneous parallel processing in connec-

tion with the existing two NRL CM-500e systems and will provide an alternative globally shared memory programming paradigm. An upgrade for the Human-Computer Interaction Laboratory will integrate and enhance its video and audio presentation and recording capabilities.

Materials Science and Technology

Renovation is in progress for Building 3, which is composed of two of the original five buildings at NRL, to contain modern laboratories for studies of thin-film deposition and characterization, superconducting materials, magnetic materials, and other materials science projects. The new space will feature the most modern molecular beam epitaxy and other materials synthesis and processing equipment, an up-to-date fatigue and fracture laboratory, and state-of-the-art diagnostic equipment, including electron microscopes, spectrometers, and electron and X-ray diffraction equipment. The renovated building will also contain office and laboratory space for approximately 70 technical personnel.

Plasma Physics

A state-of-the-art short-pulse (<0.5 ps), high-intensity (>2 TW) Table-Top Terawatt (T^3) laser has been in operation for a variety of physics studies. The T^3 laser will be upgraded to boost its power to >20 TW. This will provide a facility to do fundamental physics experiments in intense laser-plasma interactions and intense laser electron beam interactions.

A low-frequency (300 MHz to 10 GHz), high-power microwave facility that uses a relativistic klystron concept is being upgraded to produce multigigawatt coherent radiation pulses.

A plasma mirror used to steer high-frequency (X-band) radar beams has been developed. This laboratory device represents a prototype of a low-cost, high-performance, shipboard multifunction microwave beam director.

Electronics Science and Technology

The Electronics Science and Technology Division continues to upgrade and expand its capability in nanofabrication science. As a result, renovation is continuing in Building 208 to create the Joint Laboratory for Proximal Probe Nanofabrication. This laboratory will serve as a resource for the characterization of electrical and mechanical properties of nanostructures, for establishing the limits to high-resolution material patterning, and for process development leading to advanced nanodevice fabrication. The following capabilities will initially reside in this new laboratory: controlled ambient scanning probe lithography, high-vacuum scanning tunneling microscopy, in-situ high-resolution etch diagnostics, nanostructure electrical characterization, and atomic-force microscopy.

Highlights of NRL Research in 1997

Microwave Microscopes
Radar Division

Scattering from environmental features such as the ocean surface limits the detection capability of Navy radars. This scattering is believed to be caused by a dynamic mix of small- and large-scale surface features. Scattering measurements with sufficient resolutions to separate the individual contributing elements can be performed, however extremely high-resolution measurements pose technical problems. For the specific case of ocean surface backscatter at X-band radar frequencies, resolutions comparable to 3-cm wavelength and sampling responses quicker than several milliseconds must be achieved. An ultrawideband, ultrahigh-resolution, dual-polarized measurement radar system—the microwave microscope—has been designed, implemented, and used in the field to measure ocean surface scattering at X-band frequencies. This device uses an impulse excited traveling wave tube and unique direct sampling receiver techniques to support ultrawideband instantaneous bandwidths. Ocean surface measurements at radar resolutions as fine as 2 cm are revealing new characteristics of the scattering process. This system has been used at the Atlantic Underwater Test and Evaluation Center to measure the ocean surface backscatter under high wind, rough sea conditions. This experimental radar system is providing backscatter measurements that were previously unattainable.

Multicast Routing for Advanced Distribution Simulation
Information Technology Division

A multicast network capability was developed for the Synthetic Theater of War (STOW) Advanced Concept Technology Demonstration (ACTD) that provides efficient use of bandwidth to meet the highly dynamic connectivity requirements with low latency and high reliability. The multicast router aggregates up to 3000 multicast groups from a local area network to a wide area network using asynchronous transfer mode point-to-multipoint switched virtual circuits. Virtual circuit management maintains a nearly optimum mesh of virtual circuits with quality of service to ensure reliable delivery of the time-critical simulation traffic. This multicast network solution developed for STOW enabled the largest ever trans-Atlantic (US-UK) secure, distributed, entity level training simulation and supports the requirements of Advanced Distributed Simulation and other communication service models that need many-to-many interactions.

Optical Oil Debris Monitor
Optical Sciences Division

Early detection of the type and severity of mechanical faults of metals is vital to prevent catastrophic failure and to enable life-extension and condition-based maintenance. Current means of detection—on-line electric systems of chip detectors—have no early warning capability. Likewise, analysis through atomic emission spectroscopy, X-ray fluorescence, and microscopic analysis of debris particles are either not reliable or are too costly or time-consuming, sometimes involving unacceptably long delays for forward deployed forces. To alleviate this problem, a new, real-time, on-line optical debris monitor has been developed to identify the type, severity, and rate of progression of mechanical faults by measurement of size, shape, and rate of production of debris particles. In one form (LASERNET), the monitor detects failure-related debris, providing early warning of potentially catastrophic conditions and allowing preservation of platforms and crew. In another form (LASERNET FINES), the monitor provides a record of the onset of excess wear conditions, providing information vital for life extension of machinery and condition-based maintenance that can

reduce the need for maintenance personnel as well as cost. By identifying the type and severity of mechanical faults, the new monitors will provide the fault-specific information needed in real time to reduce the false alarm rates that are now being experienced in health and usage monitoring systems currently being deployed.

Eager—Preferential Acquisition Decoy

Tactical Electronic Warfare Division

The Eager decoy is a tethered, electrically powered, rotary wing autonomous platform, which carries an active RF electronic payload to provide an enhanced self-defense capability against radar guided antiship missiles. By positioning the decoy prior to missile detection, reaction time of the ship is reduced to zero, which is a key advantage for high effectiveness under littoral warfare conditions. Effectiveness is further improved because the decoy responds to the first pulse from the incoming threat radar so that the threat never has a clear look at just the ship alone. Providing continuous threat protection also helps to address the problem posed by rules of engagement, which permit no aggressive response until after the enemy has launched an attack. Eager communicates with the ship via optical fibers within its power transmission tether. Control information is passed up to the decoy, and status information is sent down to the ship. RF signals are also sent up and down the tether over fiber-optic lines, allowing the ship-based hardware to be employed for signal analysis and technique generation. Eager has demonstrated the feasibility of using a tethered, electrically powered, rotary wing autonomous vehicle to position, for an extended period of time, an active RF payload as a preferential acquisition decoy near a defending ship. Four flight vehicles containing this capability have been constructed and flown successfully. Eager provides instantaneous reaction and continuous multiple engagement protection against radar-guided antiship missiles. Eager might also be used as a platform for other payloads, such as electronic signal measurements or active jamming.

A Highly Accurate Format for Performing Quantum Crystallographic Calculations

Laboratory for the Structure of Matter

Quantum mechanics is the fundamental theoretical tool of many scientific disciplines. Accurate quantum mechanical models can permit the calculation of, for example, accurate information concerning various energies, electron density distributions, and electrostatic potentials. With the use of a test substance—maleic anhydride—a highly accurate procedure that applies quantum crystallography to problems of interest has been developed. Key features are the correction of the experimental crystallographic data for vibrational motion and for systematic errors, resulting in very close agreement between the experimental data and the quantum mechanical model. Applications of quantum crystallography can enhance the development of unique and more powerful energetic materials. Preliminary calculations have begun on nitro-substituted cubane compounds. Octa-nitrocubane is the current goal of synthetic chemists and the quantum crystallography program because this cubane will probably be the most energetic substance known.

Reduction of Fuel Deposits on Hot Surfaces by Hindered Phenol Diimines

Chemistry Division

The F/A-18 E/F aircraft will be operating at the ragged edge of current jet fuels' resistance to hot surface deposits, generally known as jet fuel thermal instability. Currently, the Navy relies on a nonquantitative pass/fail fuel specification test. The purpose of this research is to ensure that this nonquantitative test remains valid for the newer aircraft engines and to explore additive chemistry as one potential solution to this fuel dependent phenomenon. For 40 years the Navy has used a hindered phenol diimine type of additive to reduce high-temperature fuel deposits in aviation turbine engine components only when aviation fuel was known to be contaminated with copper. During this period, there were few quantitative demonstrations of the supposed benefits to real aircraft systems using copper-contaminated or copper-free fuel. NRL has now studied this type of additive using a long-duration, high-temperature laminar flow system with copper-free aviation fuels. The results, which quantitatively measure surface deposit weights, indicate that

the hindered phenol immine additive provides significant beneficial effects. This is the first demonstration of the additive effectiveness during long-term duration (150 hours) testing using copper-free fuel. To the Navy it provides increased confidence in the use of additives to counteract significant levels of jet fuel thermal instability in newer high heat load propulsion systems.

Fatigue Crack Initiation Mechanism

Materials Science and Technology Division

Material failure processes involve both crack initiation and propagation. If there are no pre-existing flaws, the material goes through damage accumulation, initiation, and then propagation. Aggressive environments such as saltwater may accelerate both crack initiation and propagation and shorten the fatigue life of a structure. Cracks almost always initiate from surface imperfections; initiation sites may include pre-existing flaws, inclusions that are at or near the surface, and slip steps formed by fatigue process-corrosion pits. The mechanisms of corrosion-fatigue crack initiation by pitting of a high-strength aluminum alloy were studied. The 7000 series alloys were chosen because these Al alloys are used extensively on Navy aircraft. For this series, there are A-type (about 25%), C-type (about 75%), and Si-containing (very few) constituent particles, varying in size from 1 to 30 μm. In saltwater, A-type particles are anodic relative to the matrix and dissolve to form pits; C-type particles are cathodic relative to the matrix and the matrix around them dissolves away and forms pits; and the Si-containing particles are neutral and do not play a role in pit formation.

Formation Mechanisms of Ferrous Microstructure

Materials Science and Technology Division

The true three-dimensional shapes of microstructural features play an important role in microstructural evolution. In addition, the influence of precipitate shape on mechanical properties has also been established. Nevertheless, microstructural characterization is usually accomplished by methods that enable only two-dimensional observations. That is, optical and scanning electron microscopy (SEM) are restricted to observations of a single plane of polish while transmission electron microscopy (TEM) is limited to thin foils of material. Even though traditional metallographic techniques can be used for rapidly characterizing many microstructural features, even simple three-dimensional shapes often cannot be deduced by examining random planes of polish, much less the complex morphologies and distributions of grains and precipitates found in many materials. This methodology has provided detailed information about the true three-dimensional morphology, connectivity, and distribution of cementite precipitates and has yielded a more precise characterization and classification of precipitates than was previously possible with two-dimensional microscopy techniques alone. This type of information is critical in understanding and controlling microstructural evolution, and thus mechanical properties, in steels and other metals and provides critical input to current predictive microstructural evolution models.

High T_c Materials for Superconducting Motors

Materials Science and Technology Division

Superconducting motors under development by the Navy require high critical temperature (T_c) superconducting materials that can sustain higher current densities with lower power losses than those presently available. Because the current transport capability of a given wire or tape depends strongly on the microstructure of the high T_c superconductor, superconducting properties and microstructural features must be quantified from the same section of material and then correlated. Superconducting properties have been measured on an initial set of silver BiSrCaCuO (BSCCO) tapes consisting of high T_c superconducting layers based on the 2212 phase coating both sides of a silver foil. An examination of the tape surfaces and longitudinal cross sections revealed platelike 2212 grains as well as nonsuperconducting alkaline earth cuprates, 2201 grains, and pores. Texture measurements from the broad surfaces of the tapes indicated a high degree of c-axis alignment of the 2212 grains, which is linked to high current capacities, but longitudinal sections of the

tapes showed localized variations in the directionality of the grains. A second set of silver-BSCCO tapes produced by a different method had a nominally 2212 phase core encased in silver. Two different types of heat treatments of the latter tapes yielded substantially different critical current densities that were lower than those for the first set of tapes. The results of these mircrostructural analyses will lead to processing parameters that improve the current density and creep resistance of high T_c superconducting tapes that will ultimately be used in Navy motor applications.

Chemical Mechanical Polishing of Copper Interconnects in Magnetoelectronic Circuits

Materials Science and Technology Division

The military has a need for high-density, radiation-hard, nonvolatile memory to replace outdated memory in existing military platforms and to provide higher levels of functionality. Current developments in applying magnetoelectronic circuit elements to fabricate computer memory identified the need to eliminate electrical contact resistance between the copper metallization and the magnetic memory elements. This has been achieved by the development of new chemical mechanical polishing techniques to planarize the copper contacts. These results provide a practical approach to ensure high yield production of wafers incorporating these low-resistance memory elements. The new technique will be applied to the development of memory circuits currently underway at NRL.

Controlled Structure Technology (CST) Route to Significant Improvements in Ceramic Fiber Composites

Materials Science and Technology Division

Previous work on ceramic matrix composites has focused on control of fiber-matrix interface properties. This is a very difficult task in terms of modeling and characterization and one where processes to improve and control critical interface properties add significantly to the cost. In this study, work has focused on control of composite heterogeneity on a scale where analysis and process control are far more feasible and far cheaper and where the resultant material property improvements are as large as those obtained by control of the fiber-matrix interface. Techniques have been developed for control of ceramic fiber/ceramic matrix composite heterogeneity, at the scale of fiber tows, which permit improvements in composite strength and toughness and reductions in processing costs. The effectiveness of these techniques has been verified by numerical modeling and by experiments on ceramic matrix composites. Numerical modeling of fracture in these composites has been used effectively to optimize the heterogeneity and structure for particular application requirements. CST composites are 12% stronger, 50% tougher, and incorporate 15% less expensive fiber reinforcement. They also retain greater structural integrity following fracture than conventional ceramic matrix composites. Significantly, the CST concept is applicable to all continuous fiber ceramic matrix composite systems because it is structure rather than composition dependent.

Fatigue Crack Precursors

Materials Science and Technology Division

A major shortcoming of life prediction technologies for fatigue critical structures and rotating machinery is that the prediction requires a reasonably accurate knowledge of the loading over the life of the component, either estimated from the planned service life or inferred from accelerometer data. Unexpected or undetected loading and external damage can lead to erroneous life predictions. The internal metallurgical damage that leads to fatigue failure progresses through stages of severity. The use of thermal imaging is being explored as a means to observe the progression of fatigue damage in metals. A high-speed thermal camera with specialized software is interfaced with a fatigue test machine to synchronize image acquisition with the phase of the fatigue load cycle. The software generates a thermoelastic image produced by alternate heating and cooling resulting from the cyclic loading. Preliminary thermoelastic images of a test specimen were obtained under several different levels of fatigue loading. Circuitry was constructed to facilitate detection of

plastic deformation. Further development of this technique will also permit production of images resulting from plasticity. The technique for detecting stages of fatigue damage has broad applications for nondestructive inspections and condition-based maintenance of naval and other structures and machinery.

Raman Measurement of the Superconducting Energy Gap in Doped and Cation Substituted High T_c Cuprates

Condensed Matter and Radiation Sciences Division

As the field of high temperature superconductivity has matured, the most important questions to be answered spectroscopically revolve around the size and symmetry of the superconducting energy gap. These properties can be sensitive functions of the density charge carriers within the sample or the doping level. NRL has used the technique of Raman scattering to demonstrate several unusual properties characteristic of the cuprate high critical temperature (T_c) superconductors. By using polarized light for the incident excitation and appropriately selecting the polarization of the scattered photons, it is possible to directly measure the angular dependence of electrons, even in the superconducting state. This property firmly establishes the trend toward an isotropic superconducting energy gap in overdoped samples, while the gap is highly anisotropic at optimal doping. In particular, the cationic substitution of Pb^{2+} for Bi^{3+} in $Bi_2Sr_2CaCu_2O_{8-\delta}$, which leads to hole doping, has been shown to reduce the gap anisotropy. Similarly, a study of the $HgBa_2CuO_{4+\delta}$ superconductor with some Bi substituted at the Hg site has clearly placed the present samples on the overdoped side of the phase diagram. The superconducting energy gap, which should be a crucial indication of the mechanism for the superconductivity, is if fact quite anomalous as a function of the carrier concentration. This provides information critical to ultimately understanding superconductivity in high T_c materials.

Pulsed Laser Deposition of Ferroelectric Thin Films for Active Microwave Electronics

Condensed Matter and Radiation Sciences Division

Pulsed laser deposition is a unique physical vapor deposition technique that has been developed for the growth of high quality thin films of multicomponent materials with complex crystalline structures. Research in this area at NRL has had a great impact on the basic physical and chemical investigation of electronic ceramic thin films as well as their insertion into next generation prototype devices. The goal of the current program is to fabricate a prototype broadband, low-phase noise voltage controlled oscillator (VCO) to be used in a space-based microwave system. The enabling technology is a varactor fabricated from a high quality ferroelectric thin film. In the pulsed laser deposited ferroelectric thin films, the dielectric constant can be reduced by a factor of 4 in an electric field ($\leq$ 200 kV/cm), which currently meets the tuning range for the VCO. Although demonstrated in bulk materials, the electric field effect has yet to be exploited in thin films, because of the unavailability of high quality material. The active dielectric behavior has been demonstrated in thin film prototype microwave devices fabricated from $Sr_xBa_{(1-x)}TiO_3$ thin films deposited by a new physical vapor technique—pulsed laser deposition. The availability of high quality thin films of this ceramic material has led to the development of an entirely new class of tunable microwave electronic devices. These devices offer incremental improvements in existing technologies and revolutionary device concepts. The development of thin film processing conditions that yield low-loss ferroelectric films will allow the implementation of these new device concepts for the first time.

Atomistic Dynamics of Rapid Fracture

Condensed Matter and Radiation Sciences Division

Fracture is a multibillion dollar, national-scale engineering problem. More particularly, materials failure within the U.S. armed forces presents a significant strategic problem that compromises battle readiness and is costly to our defense system. In this work, crack propagation has been studied in single crystal three-dimensional nickel as a function of crack face using atomistic simulation for 20 to 100 million atoms. It was

discovered that crystal orientation with respect to unilateral loading is important: the solid fails by brittle cleavage for a notch with (1 1 0) faces and by ductile plasticity for a notch with (1 1 1) or (100) faces. For brittle fracture, chemical bonds are broken; for ductile failure, plastic deformation occurs via rows of atoms sliding past one another on preferred "slip planes." These results can be explained by a competition between bond-breaking and interplanar slippage governed by the nonlinearity and anisotropy of the crystal elasticity near materials failure. If the speed of the (1 1 0) brittle crack can be made to exceed approximately one third of the Raleigh sound speed, then a brittle-to-ductile dynamic instability occurs. The present series of three-dimensional atomistic simulations makes up for many of the deficiencies of continuum mechanics, is able to explain many experimental observations, provides detailed insight into the fracture process, and is able to predict how cracks in single crystals will behave as a function of orientation. Work continues regarding cracks interacting with defects and voids, on cracks in polycrystalline metal, and on cracks in ceramic (semiconducting) systems.

Applications of Nonlinear Dynamics

Plasma Physics Division

Finding orbits that govern global phenomena is important in many problems of Navy interest; for example, fluid-structure interactions play a vital role in Navy logistics. Location, stabilization, and control of unstable phenomena in high-dimensional experiments are important in improving field performance as well as in generating instabilities, such as sustained mixing in combustion and spreading energy in resonant structures. The basic research problem is to extend and design mathematical methods for analysis and control of nonlinear problems based on time series analysis. The advantage to such an approach is that it allows real-time analysis and nonlinear prediction capabilities for experiments in which models are incomplete or unknown or the dynamics are nonstationary. NRL has developed a rigorous underlying theory of tracking method for dynamical systems experiments, applicable to systems employing pole-placement, stable projection, occasional proportional feedback (OPF), and differential delay control. OPF is widely used in numerous experiments in the control of chaos. A procedure to construct low-dimensional models for spatio-temporal systems was designed, and a bifurcation structure to chaos in reaction-diffusion systems was identified. The Karhunen-Loeve filter was designed and used to control spatio-temporal processes directly from data, a new technique for sustaining chaos in arbitrary dimensions when it disappears was introduced, and the first theoretical explanation of why chaos appears in lasers so often was constructed. This work is significant because it introduces many new concepts of unstable phenomena that can be used to understand observed behavior. Many of these techniques may be applied directly to experimental work in which models are incomplete or unavailable.

Ionospheric and Atmospheric Specification from Global Positioning System (GPS) Remote Sensing

Plasma Physics Division

There is need for global and regional ionospheric and atmospheric specification and forecasting for a variety of military and civilian communications, navigation, and surveillance systems. The disturbed ionosphere can lead to several adverse system effects, for example, GPS tactical position errors and loss of signal lock for precision navigation, interruption of space-based communications, space surveillance errors, loss of tactical communications, and space tracking errors. Also, water vapor concentrations in the lower atmosphere can strongly affect microwave sensing and communications systems. The development of nowcasting and forecasting techniques of global ionospheric and atmospheric weather will be useful for the mitigation of aspects of these system effects. A model and methodology that can accurately calculate features of ionospheric and atmospheric specification, in near real time, using GPS phase delay observations under a range of conditions has been developed. By using GPS phase delay data, the ionospheric electron density profile, initial conditions for ionospheric weather in the form of equatorial spread-F bubbles, and the vertical profile of temperature and water vapor in the lower and middle atmosphere globally in near real time can be specified.

Modeling and Design of High Efficiency Vacuum Power Boosters for Microwave Power Modules (MPMs)

Electronics Science and Technology Division

For many applications of traveling wave tubes (TWTs) in the defense arena, including EW, radar, and communications, TWT amplifiers are required to provide simultaneous amplification of multiple frequencies. In these applications, intermodulation, amplitude, and phase cross modulation take place as a result of the nonlinearities in the amplification process. When the number of carriers is large, this phenomenon becomes even more complex. Moreover, the requirement of further increasing the efficiency, the frequency, and the power level of TWTs makes the attainment of these levels of intermodulation and cross modulation even more difficult. Thus, interest has been refocused on designing TWTs that minimize intermodulation and cross modulation distortion without significant reduction in efficiency. A new model and computer code CHRISTINE have been developed that simulate the operation of TWTs. The advantages of this code are that it can relatively quickly simulate situations in which the amplifier is driven by multiple input frequencies, and it is relatively easy to vary parameters while designing a device. The model includes a multifrequency description of the fields of the RF structure and the space charge. This allows the study of harmonic and intermodulation distortion. The new code was benchmarked with experimental data from several high-efficiency vacuum power boosters developed for C-band microwave power modules and with data from multifrequency TWTs. Simulated performance accurately predicts experimental data. This includes very good agreement with the predicted and measured drive curves for both fundamental and second harmonic frequencies.

Electron Scattering Simulation

Electronics Science and Technology Division

Simulation is increasingly being used as a guide to optimization of micro/nanoelectronics processing. Being able to understand not just simple issues of resolution but also to process latitude, proximity effects, and beam spreading has expanded the applicability of this type of simulation to a number of research challenges. Over the past few years, Monte Carlo-based simulations of electron scattering have been developed as guides for electron beam lithography. Codes have now been developed and verified experimentally that predict three-dimensional profiles of energetic electron beams that have passed through, or backscattered from, structures comprising single or many thin layers. The importance of the relevant physical electron-solid scattering mechanism has been identified by an extensive series of lithographic studies as well as measurements of the spatial profile of electrons scattered as they pass through a series of thin films. These studies have involved a variety of materials that are important in microelectronics processing. These computational tractable Monte Carlo codes have permitted insights into the key physical mechanisms responsible for issues such as resolution in high-energy e-beam lithography and beam blurring by passage through thin films. These simulations are being applied to electron beam nanolithography, proximity effect correction in e-beam direct write and mask making, and the design of a novel position detector for the patterning of membrane masks.

Growth of SiGe Diodes by Molecular Beam Epitaxy

Electronics Science and Technology Division

The incorporation of Ge into Si device technology gives an additional degree of freedom in the device design that increases the functionality of Si devices. By using knowledge already obtained of Si and Ge molecular beam epitaxial growth, NRL was able to grow a hyperabrupt n–p junction inside a SiGe quantum well. These structures have now been fabricated at the University of Michigan into the first SiGe Esaki diodes and device characterization. During the growth of this structure, great care was taken to prevent strain relaxation of the SiGe quantum well and minimal segregation of the dopants, while maintaining high quality epitaxial growth. The Si buffer layer and p+ contact layer were grown at 650°C. Reduced temperature epitaxy at 400°C was used for the SiGe quantum well. In the center of the well, a growth pause was

initiated for the buildup of Sb. After the formation of the p-n junction, the temperature was further reduced to 350°C for the growth of the n+ contact layer. Device characterization showed that at room temperature the peak current was 27 mA and the valley current was 3.4 mA for a peak-to-valley ratio of 7.9. The current density of the Esaki diode was 4×10^4 A/cm^2. The next step is the integration of the Esaki diodes with heterojunction bipolar transistors for ultrafast, monolithic digital integrated circuits, with a special emphasis on multivalued logic.

Nonrubbing Liquid Crystal Alignment Layer

Center for Bio/Molecular Science and Engineering

All current liquid crystal displays (LCDs) initialize a rubbed polyimid layer as the alignment layer to orient liquid crystals. However, there is a need for a nonrubbing alignment layer technology to improve the yield of LCDs and to enable a new generation of LCDs with a large viewing angle. A new technology to align liquid crystals has been developed that combines the self-assembling chemisorption process with photo-induced dimerization and creates an isotropic surface that orients liquid crystal molecules on a variety of surfaces. The mechanism of alignment has been elucidated on the molecular level. A unique feature of this technology is the ability to achieve a homogeneous orientation of the liquid crystal molecules whose "pre-tilt" at the surface can be controlled by the interfacial interaction vis-a-vis the chemical structure of the alignment layer. This new alignment layer technology has the potential to make a major impact on the $22 billion flat-panel display industry. It can also lead to the development of higher resolution/high information displays needed for military applications.

Acoustic Propagation in a Random Shallow Water Waveguide

Acoustics Division

Efficient computation of three-dimensional acoustic fields over large regions of shallow water with varying bottom topography is an urgent unsolved problem. Any acoustic model adopted for use in such an environment will require the interpolation of large amounts of environmental data obtained from a sparse set of measurements. Standard interpolation methods break down in the vicinity of data discontinuities such as thermoclines or pycnoclines. Curvilinear coordinate systems may be constructed using a W.K.B. approximation for a reference eigenfunction such that mode coupling is minimized. Such coordinate systems naturally adapt to the environment even with realistic sound-speed profiles that include discontinuities as well as sloping bottom bathymetry. They provide an adiabatic normal-mode basis for constructing acoustic models in the fully three-dimensional environments of continental shelf regions. They also provide a rational basis for interpolating three-dimensional data such as sound-speed and buoyancy profiles. An acoustic propagation model based on these principles has been successfully tested against several benchmarks. Environmentally adaptive coordinates provide a rational basis for the interpolation of three-dimensional acoustic fields. They have also been successfully used to interpolate the sound-speed fields required by a three-dimensional, uncoupled, normal-mode acoustic propagation model.

Evaluation of Azimuth-dependent Surface Ship Sonar Performance Due to Internal Wave Soliton

Acoustics Division

Tidal forcing of the water column in continental shelf environments induces the creation of highly directional oscillations (internal waves) of the water's density stratification. These oscillations create strong three-dimensional inhomogeneities in the water column that have been observed to affect acoustic propagation from low frequencies through several kHz. Little attention has been paid to acoustic implications of the fact that these internal waves are strongly anisotropic. This work was a pilot study to determine whether the internal waves' anisotropic character is likely to cause anisotropic surface ship active sonar (at acoustic frequencies of several kHz) performance. Acoustic modeling of transmission loss at midfrequencies was

performed for a shallow water environment in which the sound speed profile was perturbed by internal waves. The directional characteristics of the internal wave field were modeled by propagation of the internal wave field along several propagation directions. By using a combination of parabolic equation and normal-mode modeling techniques, it was determined that the anisotropy of the acoustic environment induced by the internal wave field can potentially have significant effects (performance degradation as well as detection opportunities) on sonar performance if the ship is in the vicinity of an internal wave field.

Inverse Scattering via Shape Deformation

Acoustics Division

The problem of determining the shape and material parameters of an acoustic scatterer from the scattered fields has been explored, but insofar as this "obstacle problem" is concerned, attention has been focused almost exclusively on the impenetrable scatterer. In stark contrast to the impenetrable obstacle problem, inversion results for transmission obstacles are meager. A novel approach for determining the shape of an acoustic target by inversion of its scattered field has been developed. This approach allows for the reconstruction of the density and sound speed of penetrable obstacles as well as the shape of penetrable and impenetrable obstacles, based on the scattered fields. Reconstruction is possible even when the scattered field is measured over only a small range of angles. The technique involves expressing the shape as a superposition of deformations from circularity and employing a very efficient inversion algorithm. An "image" of the shape is formed at acoustic frequencies too low for conventional imaging systems. This accomplishment is the first successful demonstration of an inverse approach to identify an obstacle only by inverting a sector of its scattered field. The technique has great promise for the identification of buried, submerged mines where the low frequencies allow penetration into the sediment.

Advanced Sonar Processor

Acoustics Division

Towed array sonar systems are extremely complex electromechanical acoustic intelligence gathering systems that operate in the hazardous near-surface ocean environment. Because of the dynamic nature of the physical environment, the normal status of a towed array sonar system is to function in a degraded state of operation. The challenge for the operational Navy is to have an accurate and rapid assessment of the functionality of the sonar, to present that assessment in such a manner that facilitates a stop or continue decision by the sonar officer, and to have products that will aid in the trouble shooting and repair process by a skilled technician, if the decision is made to stop and repair it. A dual-purpose computer software system, designated WILBR, has been transitioned to the SPAWAR's Strategic Systems Programs Office. WILBR will assess the functionality of the TRIDENT SSBN towed arrays and provide easily and rapidly understood products that aid in trouble shooting and repair. The system will also provide a new breed of signal processing algorithms that access a new and independent source of gain by exploiting the physics of acoustic fluctuations in signals and noise in the undersea environment. Additional gains include enhancements to signal-to-noise ratio, increased spatial and spectral resolution, clutter suppression/elimination, an unalerted automatic detection capability, and the provision of analysis and operational products in less time, thus reducing the time required to make critical decisions.

Multiple-Influence Detection and the Phase Correlation of Acoustic and Nonacoustic Signals in Shallow Water

Acoustics Division

The Multiple-Influence Detection Task has involved research issues dealing with environmental physics and the potential impact of the shallow water ocean environment on multisensor system performance. The objective of the task has been to determine the impact of the shallow water environment on the potential payoff in detection, localization, and classification offered by the incoherent and coherent fusion of acoustic

and nonacoustic signals. Multiple deployable undersea warfare systems are currently being developed for future use in the fleet. System projects begun at NRaD/NCOSSC have been underway for several years and have included the fabrication and testing of test bed multisensor arrays. Sensors considered include acoustic and nonacoustic types. More recently, NAWC has initiated the development of an air-deployed acoustic/nonacoustic buoy. The Multiple-Influence Detection Task provides direct transitional support to these ongoing development programs. The task has now successfully completed its joint participation in the ONR Strataform multisensor experiment that was performed in 62 m of water off the mouth of the Eel River near Eureka, California. The NRL receiving packages included acoustic, seismic, and nonacoustic sensor types that were collocated on the bottom in the test area. Data processing and analysis in FY97 demonstrated the successful phase correlation of acoustic and extremely low-frequency nonacoustic signals created by the simultaneous tows of an acoustic source and a nonacoustic dipole source. The added gain in probability of detection of this coherent fusion over incoherent fusion was demonstrated to be greatest when the signal-to-noise ratios of both the acoustic and nonacoustic signals were in the 3 to 5 dB range (given a fixed probability of false alarm of 0.001).

MODIS Near-IR Water Vapor and Cirrus Cloud Algorithms

Remote Sensing Division

NASA's Moderate Resolution Imaging Spectrometer (MODIS) has implemented narrow channels near the 0.94 μm and 1.38 μm water vapor band centers. Using the 0.94 μm channel plus nearby channels in atmospheric window regions, it is possible to derive column water vapor amounts from MODIS data over land areas and above clouds. However, the sensitivity of the 1.38 μm MODIS channel to detect thin cirrus clouds during the day is expected to be one to two orders of magnitude better than that obtained by current infrared emission techniques. Therefore, a much larger fraction of the satellite data will likely be identified as being provided by cirrus clouds. To make better studies of surface reflectance properties, effects caused by thin cirrus clouds must be removed from satellite images. There exists a need, then, to develop algorithms for retrieving column atmospheric water vapor and for estimating cirrus cloud reflections from MODIS data. Such algorithms for retrieving column atmospheric water vapor amount, cirrus cloud reflectance, and detection of aircraft contrails from MODIS data have been developed by NRL and will soon be delivered to the MODIS Project Office. The water vapor values to be derived from the algorithms will be significantly more reliable than water vapor values obtained by infrared emission techniques. Also, the sensitivity of the cirrus and aircraft contrail detections from MODIS data will be one to two orders of magnitude better than that obtained currently. These values have important applications in meteorology, hydrology, and climate research.

Tides and Currents in The Yellow Sea

Oceanography Division

Recent advances in data assimilation have paved the way for assessments of shallow water currents and tidal heights that are detailed, accurate, economical, and rapid. NRL's approach uses in situ measurements taken inside the domain of interest to force a numerical model in which the known dynamics are embodied. Although various techniques for data assimilation have been known for some years, the conceptual clarity and ease of implementation of the present method make it especially appealing. Data from the Yellow Sea consisting of historical coastal tidal coefficients, acoustic Doppler current profiler (ADCP) and bottom pressure data from three interior sites, and bathymetric data from various sources were combined through a data assimilation technique based on the shallow water equations of motion. A solution to the equations was found that provides a very close fit to all the data. Moreover, NRL found that vertically integrated currents from the three ADCPs are sufficient to describe tidal heights and currents in the area, whereas the several dozen coastal stations are not sufficient to describe well the current field. It has therefore been shown that a few current measurements can determine the littoral current and surface height over an extended area. This finding has important implications for how data are collected and how models are forced. It creates the possibility of environmental monitoring without having to enter into militarily or diplomatically inconvenient waters.

Numerically Modeled and Observed Shelf Wave Response to Wind Forcing in the Yellow and East China Seas

Oceanography Division

One of the fundamental responses of the Yellow and East China Seas to wind forcing is in the form of a Kelvin wave, generated in the northern area and propagating southward along the Chinese coast. Strong northerly winter wind bursts produce southward surface currents that depress the sea surface height in the northern Yellow Sea by as much as 50 cm. The potential energy stored in this sea surface height anomaly is released when the wind forcing ceases. A fundamental dynamical response by the ocean to an impulsive forcing is expected in the form of Kelvin waves. These waves have a peak amplitude at the coast and decay exponentially away from the coast. The wave speed is about 12 m/s in the Yellow and East China Seas. Associated with the waves are along-shore currents. The largest wave amplitudes occur mainly in the winter with peaks near 20 cm. The along-shore currents associated with this wave amplitude are expected to reach 24 cm/s. This response to wind forcing in this region has never been observed, modeled, or even proposed prior to this work. The capabilities to model the environment numerically and observe variations remotely are central to the success of future Navy monitoring and prediction systems. Through this work, the capability to use satellite altimeter data in the littoral region is greatly enhanced.

Spacial Characteristics of Short Wind Waves in the Ocean

Oceanography Division

The basis for relating radar measurements to wind speed is the realization that radar backscatter is caused by surface roughness. In the ocean, the surface roughness is mainly contributed by wind-generated surface waves. The measured radar intensity, however, was found to differ significantly from theoretical calculations using equations derived from scattering processes and measured physical properties of the surface roughness. These calculations consistently indicated that the sea surfaces detected by radar were rougher than those detected by optical instruments that depended on submicrometer wavelength light. This NRL study found that the tilting effect of long waves produces an attenuation of the radar backscattering cross section. The calculated attenuation factor is in excellent agreement with TOPEX/POSEIDON measurements. Two major contributors to the tilting mechanism are the wind-generated waves with wavelengths much longer than the radar wavelength and the ambient waves generated elsewhere and propagated into the measurement region. Using wave number spectra of short capillary-gravity waves measured in the ocean and an estimate of the ambient tilting wave components from the ocean, the calculated attenuation factor is in excellent agreement with TOPEX measurements. With the tilting effect accounted, the agreement of the wind speeds derived from the TOPEX Ku-band altimeter improved by 40% compared to those from collocated ocean buoys.

High-Resolution Airborne Gravimetry

Marine Geosciences Division

Gravity data are required over the oceans as input to strategic and technical guidance systems. For many years, data were collected using conventional surface ships. Attempts have been made to replace or supplement these shipboard measurements by using airborne techniques, however the accuracy resolution of these measurements were insufficient to meet Navy requirements. A high-resolution version of the NRL airborne gravity measurement capability has recently been demonstrated. Improved airborne operational measurement and processing techniques led to a significant reduction in error with a simultaneous increase in the resolution of short wavelength features. An rms difference between the airborne and shipboard gravity measurements of less than 1.5 mGals (10^{-3}cm/s^2) was achieved on numerous test profiles. This indicates that the airborne measurements were nearly as accurate as the shipboard data, but with a factor of 10 increase in data collection speed and large operational cost savings. The level of accuracy/resolution is now deemed sufficient to meet approximately 90% of the Navy's survey requirements. These data will allow the development of predictive capabilities of surfzone mine behavior and will be used by researchers to support similar models derived from wave-flame studies.

Fronts and Atlantic Storm Track Experiment (FASTEX)

Marine Meteorology Division

In many forecast situations, a high percentage of forecast error in operational numerical weather prediction (NWP) models is attributable to deficiencies in the initial conditions, and initial condition uncertainty is central to future improvements in NWP. Techniques for adaptive observation were tested during the Fronts and Atlantic Storm Track Experiment (FASTEX) field phase. The comprehensive data set collected during FASTEX provides a unique opportunity to test targeted observational strategies in real time and to evaluate data impact on 1- to 3-day forecasts of extratropical Atlantic cyclogenesis. Targeting results from assimilation of data obtained during FASTEX demonstrated the skill of adaptive observation methods by assimilating data in target areas and achieving reductions in forecast error with a nonlinear forecast model. An adjoint model is used to define the target areas for special observations. The impact of aircraft dropsonde, GOES-8 winds, and rawindsonde observations were evaluated and compared. Proof of concept includes data impact in target and null areas and discussion of how target structure related to synoptic features. The results of this study suggest that adjoint singular vector and sensitivity information derived in real time can provide useful guidance for adaptive observations in forecasts of extratropical cyclones, even though approximations and assumptions are involved in the adjoint targeting procedures. The assimilation of dropsonde and satellite wind data shows that model analysis error occurs in areas targeted with adjoint-derived singular vectors, and the initial condition error in these sensitive locations can control a significant percentage of total forecast error in extratropical cyclone predictions. The results of targeted observation studies using FASTEX data are directly relevant to decisions concerning the value and mix of observations in forecast situations relevant to Navy operations.

Parallel Processing for Space Surveillance Cataloging Operations

Spacecraft Engineering Department

The Naval Space Command (NSC) maintains a space object catalog. Various other products associated with this catalog are also provided by NSC. The computations necessary to perform tasks related to this catalog have grown with the number of objects in the catalog. Until recently, fast computers could do no more than keep up with the increasing computational load. A need for better accuracy and additional capabilities has been growing, especially for activities such as collision avoidance for the space station. Recently, NRL has demonstrated the feasibility of using a distributed parallel processing system to accomplish computing tasks, including computing the collision distance between objects in space, processing and cataloging unknown objects detected with the space surveillance radars, and maintaining the space object catalog with special perturbations. This parallel processing environment developed by NRL enabled NSC to use personal workstations, which were lightly used for other work, to perform tasks. This effort demonstrated that parallel processing can make efficient use of existing resources to perform computationally intensive tasks, and that, for the right tasks, it is much more cost effective to use multiple, medium-speed computers than to use expensive serial computers. This effort also established that a distributed parallel processing system is sufficiently robust to meet the needs of an operational command like NSC.

"Our People Make the Difference

featuring ..."

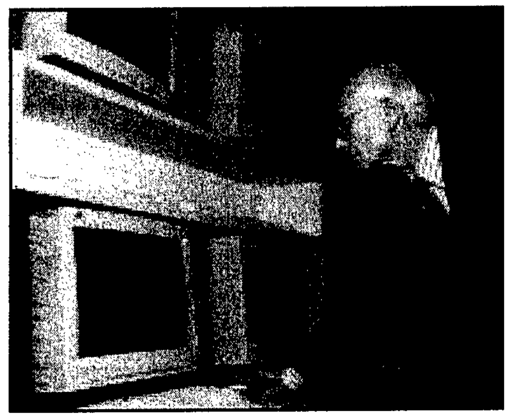

Dr. Guenter E. Brueckner is head of the Solar Physics Branch, Space Science Division. Branch scientists focus on studies of the Sun and its interaction with the Earth. What causes solar flares—the source of violent outbreaks of high energetic particles and large amounts of plasma energy? What causes so-called Coronal Mass Ejections (CMEs), which trigger large geomagnetic storms, and how do CMEs travel through interplanetary space? What causes the 11-year cycle of solar activity? What are the long-term variations in the solar radiative output and how do they govern potential long-term climate changes on the Earth? These studies are carried out exclusively from space, using sounding rockets, satellites, and manned space missions. For the past 2 years, a host of new solar phenomena has been recorded by NRL's Large Angle Spectrometric Coronagraph (LASCO) experiment on the NASA-ESA Solar and Heliospheric Observatory (SOHO) satellite. SOHO has made a major contribution to the understanding of solar phenomena and the forecast of the Earth-space environment. (See also article on page 202 of this publication.)

"I have always been convinced that an advanced defense laboratory such as NRL is the proper place to carry out these studies. It is likely that warfare will expand into space more and more. The understanding of the space environment and its prediction, therefore, is of paramount interest to the military."

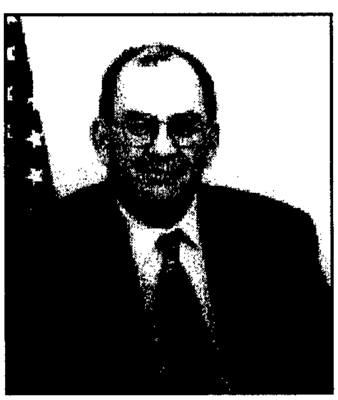

Dr. Philip E. Merilees was appointed as Superintendent of the Marine Meteorology Division of NRL, in Monterey, California, on April 7, 1997. Division scientists conduct research on the atmosphere and its effect on Navy operations. In particular, the laboratory designs and evaluates complex atmospheric analyses and predictions that are used by Fleet Numerical and the Navy Meteorology and Oceanography centers around the world. Dr. Merilees comes to NRL from Toronto, Canada, where he was Director General of Research for the Atmospheric Environment Service.

"I was honored to be selected for the position of Superintendent of the Marine Meteorology Division of NRL, where the scientific and administrative staff are top-notch. I am proud to be associated with a Laboratory that is leading the world in several basic research areas while at the same time developing new weather-based products for the operational Navy. The people in the Division not only have the satisfaction of intellectual achievement but also seeing their work being implemented into practical benefits for the Navy—the best of both worlds."

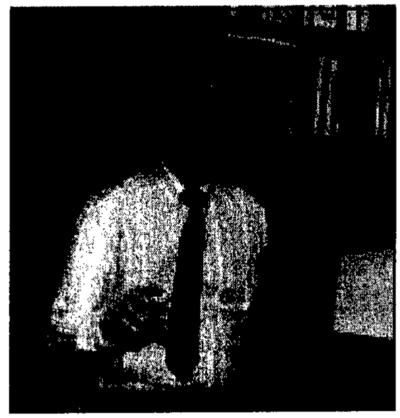

Dr. Gerard V. Trunk is Superintendent of the Radar Division and was selected for this position in 1997 culminating a career of almost 30 years in the Radar Division. The Division conducts basic research into phenomena of importance to radar, investigates new technologies for radar, demonstrates the feasibility of new radar concepts and systems, and performs radar system analyses. The emphasis is on new and advanced radar concepts and technologies that will enhance the Navy's capability to conduct its mission. During his career, Dr. Trunk has worked in the areas of automatic detection and tracking, detection of small targets in sea clutter, single and multiplatform radar integration, radar-electronic support measure-infrared integration, sea clutter analysis, radar cross-section reduction, pulse-Doppler radar, ambiguity resolution, point defense, phased arrays, and radar system design, analysis, and simulation.

"NRL has provided me the opportunity to reach my full potential. I joined NRL in 1967 as a researcher and progressed steadily through the positions of Section Head, Staff Head, Branch Head, Associate Superintendent, and finally to Superintendent of the Radar Division. The strength of NRL is its people, and what makes NRL truly exceptional is its variety of experts in so many diverse disciplines."

CAPT James R. Campbell is the Program Manager for Biotechnology and Environment, in the Chemistry Division. He is also Chairman of the NRL Environmental Quality Coordinating Committee, which facilitates research on all aspects of Navy environmental problems. Funding for NRL environmental projects currently exceeds $22M, and is derived from programs such as the Strategic Environmental Research and Development Program, the Environmental Security Technology Certification Program, the Department of Energy, and others. The Department of the Navy takes environmental stewardship quite seriously, not only because it directly impacts the Navy's ability to perform its mission, but also because of genuine concern for the quality of the land, sea, and air upon which we all depend. The complex nature of many environmental problems requires multidisciplinary solutions, and this is the unique strength that NRL provides. Chemistry, acoustics, and biosensors are but a few areas that bring technology to bear in a collaborative approach to solving Navy environmental problems.

"Environmental considerations are beginning to play a much broader role in decisions regarding acquisitions and fleet operations. Cradle-to-grave responsibility for Navy equipment and platforms influences warfighting policy, and environmental pollution affects the health and well-being of our sailors and marines. As a Navy Medical Service Corps officer, I understand the concerns of the Navy Environmental Health Center and the Bureau of Medicine, as well as fleet operational needs, and I am committed to promoting NRL as the Navy's premier institution for addressing environmental threats."

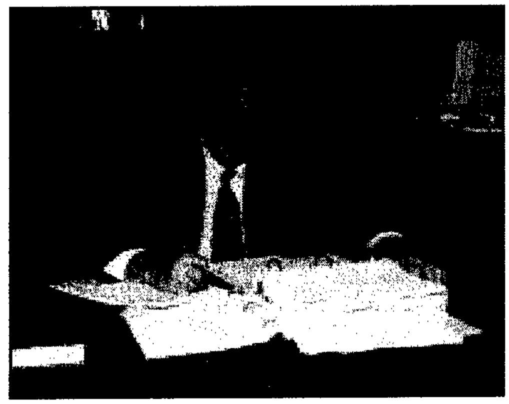

Mr. Robert E. Doak is the Associate Director of Research for Business Operations. He is the advisor to the Commanding Officer and the Director of Research on all business support matters of the Naval Research Laboratory. His Directorate provides executive management, policy development, and program administration covering the full spectrum of business operations. This support is in the areas of legal counsel, manpower management, financial management, supply, public works, and management information systems support.

"As the leader of a major segment of the NRL support team, my principal objective is to provide services to the NRL technical team in the most cost-effective manner. Working at NRL and supporting the NRL research team has been the most rewarding experience in my entire 30-year career with the Department of the Navy. It's truly a privilege to come to work each day and know that you are associated with an organization that has a world-class reputation."

Ms. Louise McDonald was appointed Head of the Office of Program Administration and Policy Development in October 1997. She provides managerial, technical, and administrative support to the Director of Research. Her office is responsible for the administrative program management of the NRL Science and Technology Base Program, Congressional Liaison, the General Laboratory Scientific Interchange Program (GLSIP), Facility Modernization and Management Programs, NRL Directives, and management information systems support to the Director of Research. During her 24 years at NRL, she has been exposed to a broad cross section of the NRL community, such as fluid dynamics research, development of warfare decoys, communications sciences, and satellite design, integration, and launch.

"It has been an exciting time for me. There is a spirit of invention and adventure here at NRL where new ideas grow and challenging projects create first-rate accomplishments. Administrative, management, and support personnel hold key roles in the execution of these programs and contribute to the success of the Laboratory. I hope to demonstrate NRL's can-do spirit by bringing many of the programs coordinated by Code 1006 in full automation and availability to the research codes, eliminate those that are redundant, and improve the remainder along the way."

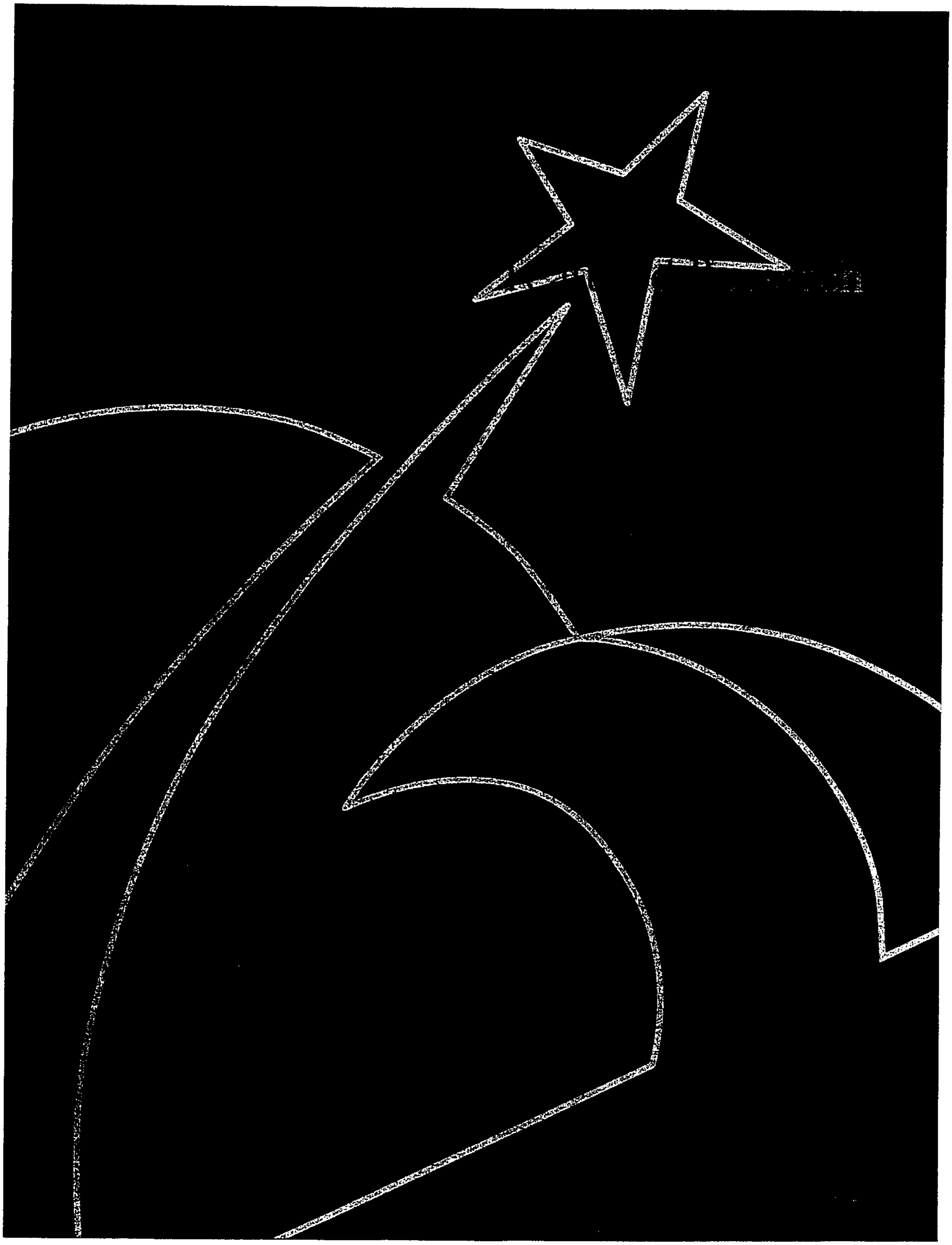

Design and Implementation of the Link 22/NILE Testbed

D.G. Kallgren, J.P. Cheng, K.E. Grant, L.N. Pham, J.S. Schlorff, and S.A. Kapuschansky
Information Technology Division

Link 22 is a tactical data link that exchanges information between naval platforms. The Link 22 design uses a compact loss-tolerant message standard, multiple communications media, time-of-day-based information security, lightweight distributed routing protocols, and adaptive time-division multiple access (TDMA) procedures to overcome the limitations of the current tactical data link (Link 11) it is slated to replace. As a risk-reduction and prototyping exercise, NRL developed key subsystems and integrated a suite of advanced development models and testbed facilities on behalf of the NATO Improved Link Eleven (NILE) Project Management Office to test and validate the Link 22 System design. The testbed was developed using real-time hardware-in-the-loop simulators and commercial off-the-shelf components and implements a basic four-node HF/UHF TDMA network to validate Link 22 component, subsystem, and interface specifications. Key contributions to the Link 22 effort have included validation of the functional design, subsystem interfaces, UHF fixed-frequency waveforms, HF fixed frequency waveforms, and node-to-node synchronization.

INTRODUCTION

The Link 22/NILE Program is an international cooperative development project involving Canada, France, Germany, Italy, Netherlands, United Kingdom, and the United States. Its goal is the development of NATO Standardization Agreements, critical software components, and a reference system for an improved tactical data link (i.e., TADIL or data network) that replaces the Link 11 (TADIL A) [1] first developed in the 1960s. Link 22 will augment the jam-resistant Link 16 TADIL J now being introduced.

The fundamental design and implementation problems for the Link 22/NILE system are typical of those for any computer communication system: Does the functional partition work? Do the interfaces work? Do the protocols work? What key parameter values must be set? Are the specifications coherent and understandable? Also typical of the development of complex modern systems, many of these issues for Link 22 were addressed by detailed simulation of the node architecture and protocol suite and were subsequently evaluated against a variety of test scenarios. The use of user-extensible commercial-off-the-shelf simulation tools tailored for network engineering (i.e., OPNET™) was established early in the design and development phase. The tools allowed a detailed and precise top-down devolution of the system architecture and requirements, including node placement at the network level, processor-to-processor connections within a node, and specification of processor functionality as a finite state machine. A NILE simulation laboratory was established as a joint activity by NRL and the international sponsors to specify and validate the protocol specifications and top-level performance characteristics. The limitations of simulation in validating the correctness of implementation-dependent parameters and the viability of the architectural partition were addressed by establishing a Link 22/NILE testbed as a risk-reduction and system validation tool.

LINK 22 DESIGN FEATURES AND REQUIREMENTS

Link 22 is a secure, medium-speed tactical data link with the multiple network architecture shown in Fig. 1. NILE units in the Supernetwork use an

adaptive variant of time-division multiple access (TDMA) to share each transmission medium (i.e., network), using distributed handoff-assigned multiple access to dynamically reallocate channel capacity as a function of the offered traffic and channel utilization at each NILE unit.

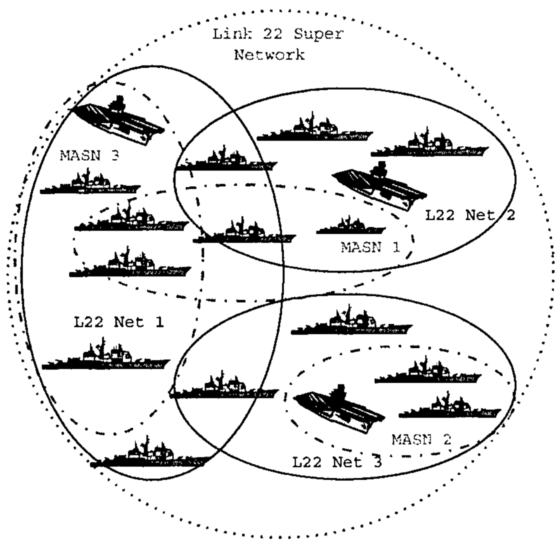

Fig. 1 — Canonical Link 22 multiple-network architecture.

The Link 22 protocol suite for communication transport and network management services is intended for a variety of transmission media. It is currently specified for both HF (2-30 MHz) and UHF (225-400 MHz) fixed-frequency and frequency-agile waveforms. The protocols support point-to-point, broadcast, and group-addressing modes for the creation of Mission Area Subnetworks tailored to operational needs.

A time-division net-cycle structure, shown in Fig. 2, is defined for each transmission medium with assignment slots and interrupt slots defined for scheduled and controlled access to the channel. The adaptive TDMA protocol allows NILE units to cooperatively change slot sizes or to reallocate slot ownership to NILE units with unmet traffic delivery requirements. Other protocols in the Link 22 Supernetwork architecture support relay, routing, and network management services to reliably deliver traffic among dispersed naval forces.

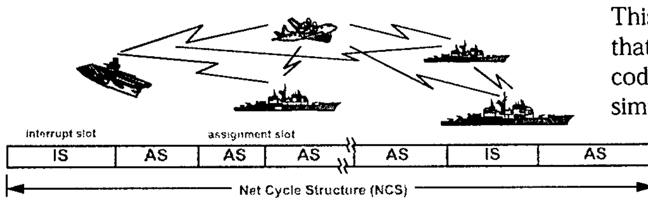

Fig. 2 — Link 22 TDMA Network architecture, one of several nets in the Link 22 Multinetwork architecture.

The NILE-unit architecture is layered, with the functional partitions shown in Fig. 3. The platform's sensor, command, and control system interface to Link 22 is the data link processor (DLP), which manages the message-exchange requirements for tracked objects and command/control dialogs in accordance with the Link 22 Standardization Agreements. Communication transport (CT) and network management (NM) services are implemented in a system network controller (SNC), which implements time-division media-access and link-layer communication security services through its interfaces to the link-level COMSEC (LLC) and the signal processor controllers (SPCs) for each transmission medium.

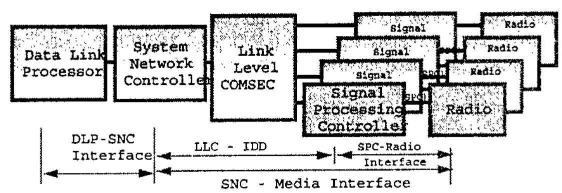

Fig. 3 — Link 22 node architecture.

RAPID PROTOTYPE/HARDWARE IN-THE-LOOP SIMULATION

In augmenting the Link 22 simulation effort with a hardware testbed, we wished to reuse much of the networking-protocol and scenario-generation software written for the development and simulation phase. As a result, two new capabilities were added to the commercial-off-the-shelf simulation environment to enable the Link-22 simulation models to be used to create "prototype" hardware in a real-time testbed [2]. These capabilities extended the tool use to applications unforeseen by the vendor.

The first capability added was the synchronization of simulation time with the host's time clock. This was done—crudely but effectively—in a way that did not change the structure of the simulation code. The second addition was the capability for simulation models to communicate with each other over a local area network in real time while running on separate hosts. The latter capability was added by translating host operating system events, such as the receipt of User Datagram Protocol/Internet Proto-

col network packets over an asynchronous (interrupt driven) socket interface [3], into simulation events and placing them in the event queue for further processing.

TESTBED DESIGN CRITERIA

The NILE testbed demonstrates integrated operation of the hardware and software components of Link 22 prototypes and advanced development models, to determine implementation-dependent performance limits of candidate software and hardware configurations. The testbed was required to demonstrate and to test the following capabilities with sufficient fidelity in its implementation to discover and solve system-level integration problems that would be masked by simulation-studies alone.

- **Transmission Modes** - With other media, Link 22 specifies HF transmission with fixed-frequency single-tone modulation and a 16 kb/s UHF fixed-frequency modulation. The testbed was required to demonstrate these transmission modes among four advanced development model nodes using propagation simulators in a controlled laboratory environment.
- **Node-to-Node Synchronization** - Node-to-node synchronization must be maintained with independent clocks and timing systems at each advanced development model node. Performance validation of advanced development model synchronization was required at several levels:
  - *TDMA Slot Timing*: Advanced development models in the testbed are required to maintain synchronization to the TDMA protocol slot structure;
  - *SPC-to-SPC Modem Synchronization*: Advanced development models in the testbed are required to synchronize their modems to the transmissions of other advanced development model nodes;
  - *LLC-to-LLC Crypto Synchronization*: Advanced development models in the testbed must be capable of communication through synchronized link-level COMSEC cryptos.
- **Interface Prototypes**: The testbed is required to demonstrate prototypes for the three critical interfaces in the NILE system, as follows:
  - *DLP/SNC Interface*: The testbed is required to implement a prototype of the interface between a NILE-compliant SNC and a DLP;
  - *SNC/SPC Interface*: The SNC/SPC interface must validate all functions required to implement and operate the adaptive TDMA protocols specified for NILE and demonstrate them with UHF and HF fixed-frequency media.
  - *Link-Level COMSEC*: This interface shall support all functions required for time-of-day based encryption for traffic sent between advanced development model nodes.

TESTBED SUBSYSTEMS

The top-level testbed design produced to meet these requirements is shown in Fig. 4. The Link 22/NILE testbed implements a four-node supernetwork wi th two fixed-frequency media (HF and UHF). Advanced development models developed for each node in the testbed include the LLC, an HF SPC, and a UHF SPC. The testbed facilities provide a wrap-around stimulation and simulation environment that includes a scenario-generator/stimulator (SG/S), TDMA traffic generator, propagation simulators for HF and UHF fixed-frequency transmission, and test-instrumentation and equipment for data-extraction and reduction. In addition, an SNC-LLC emulator is included for back-to-back testing of SPCs without using the entire testbed.

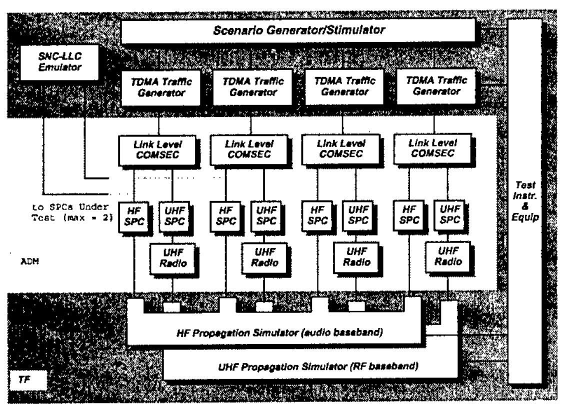

Fig. 4 — NILE testbed block diagram.

SCENARIO GENERATOR/STIMULATOR

The testbed's SG/S software is derived from a partition of the Link 22 simulation code corresponding to four emulated DLPs, one for each node in the testbed. The SG/S simulation software is augmented with the real-time synchronization and external interprocess communication capabilities described previously. The SG/S processor

model for one of the emulated DLPs is shown as the left half of Fig. 5. Following our migration strategy for rapid prototyping, the SG/S resides as a stand-alone real-time executable simulation on a SPARC20, with network interfaces to each of the four testbed processors hosting the TDMA traffic generators.

Poisson or deterministic) for the detection and loss of objects under surveillance within a platform's sensor range. While detected, transmit service requests for track-reporting messages are offered to the communication transport server (i.e., TDMA traffic generators) at a rate determined by the object's type.

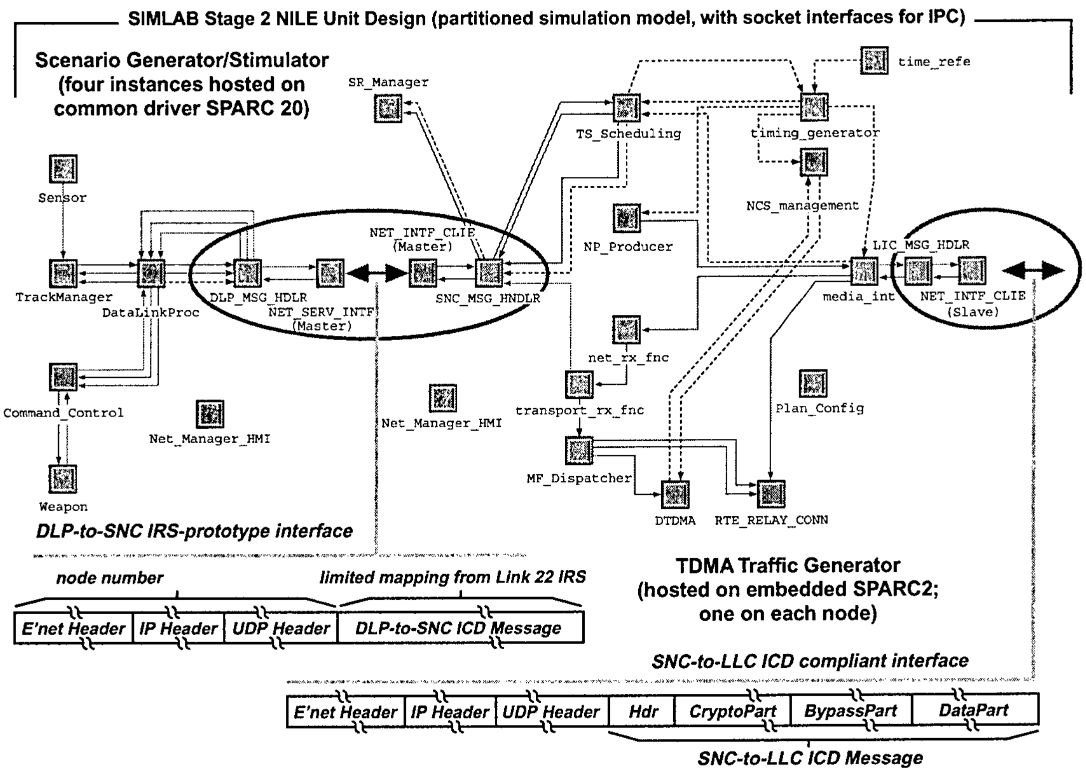

Fig. 5 — SG/S and TDMA traffic generator processor diagrams.

The SG/S is script-driven. Scenario scripts provide time-dependent parameters for the traffic generation models implemented in the SG/S's sensor, track-manager, and DLPs. These models provide realistic shaping of the Link 22 message traffic load without the necessity for exact encoding of the geometry or sensor characteristics in the scenario. Script files can represent a complex, time-dependent scenario in a compact form.

A TADIL's offered surveillance-message traffic is not random. It is the superposition of periodic reports on all of the detected targets within sensor range of the reporting platform. Traditional statistical models of offered network traffic using only Poisson or more general interarrival times for message traffic are not accurate models of the shape and level of a TADIL's offered traffic load.

The SG/S surveillance-message traffic generator uses user-selected statistical models (including

Also to ensure realism, force command and control messages are modeled by the SG/S as a correlated dialog of directive/response messages exchanged by Link 22 platforms. Rudimentary command/control and weapon characteristics are modeled in the respective SG/S processors, which communicate with their peers on other modeled platforms.

The scenario scripts for the SG/S encode the message-reporting requirements for given object classes and the command/control dialogs (i.e., the Standardization Agreement 5522 rules) as well as the time-dependent birth/death rates for objects (i.e., the tactical scenario).

The interface between the SG/S and the TTG complies with Link 22's message-oriented design, with message exchange over a UDP/IP datagram socket. Each of the DLP_MSG_HANDLER processors in the SG/S communicates with an

SNC_MSG_HANDLER in a TTG to submit transmit-service requests and messages for transmission, as well as to receive messages. Message translation between the internal data structures tailored within the simulation tool and their external representations defined by the testbed's prototype interface design is performed by the NET_SERV_INTF processor in the SG/S and by the NET_INTF_CLIE (master) processor in the TTG. The translations performed by these processors and their interface to the host's socket input/output system are the major modifications to the original simulation code.

TDMA TRAFFIC GENERATOR

The TTG software is likewise derived from a partition of the Link 22 simulation code, corresponding to the system network controller. Like the SG/S, it is a standalone real-time executable simulation, but with each of the four instances corresponding to each NILE unit running on a separate SPARC-2CE host processor. Each TDMA traffic generator has a datagram socket interface with its corresponding data-link processor simulator running within the SG/S and another datagram interface with its attached suite of media through the SNC-to-LLC interface.

As the principal goal of the testbed is validation of the interface operation, system timing, and media performance, the TTG does not implement the full Link 22 protocol suite (nor was the suite fully defined when the testbed was built). Rather, the TTG implements a critical subset of the SNC requirements representing its interaction with other Link 22 subsystems: external interface management, basic communication transport services, transmission-service request processing, network packet formation and injection, receive network packet and message processing, and red-side control of the HF and UHF fixed-frequency SPCs for fixed-TDMA networks operation.

Link 22 and the testbed implement a just-on-time transmission service designed to avoid data senescence that complies with the Link 22 requirements and sensor-reporting systems in general. Since message-reporting requirements are not necessarily synchronous with the slot-assignments in a TDMA net cycle structure, transmit-service requests, rather than the actual messages, are queued within the TS_scheduling processor. Based on a (highly) modified algorithm for first-in-first-out with priority scheduling, the messages corresponding to a transmit-receive request are scheduled in priority order for injection in future time timeslots, as determined by the TTG timing generator and the NCS_management processor. Just before a transmit time slot, the NP_producer processor determines which transmit-service requests will be serviced, and requests the DLP (emulated in the SG/S) to generate the corresponding messages and provide them to the TDMA traffic generator for injection by the media_int processor over the SNC-to-LLC interface. The approach ensures that the most recently obtained sensor data for an object will be sent to other Link 22 units and permits track extrapolation to the time of injection in the TDMA net cycle structure, thereby saving the overhead required by an explicit time stamp.

Receive message processing is straightforward. The media_int processor schedules reception attempts by a signal-processor controller through control messages sent over the SNC-to-LLC interface. Messages received by a signal-processor controller are sent to the system-network controller through the link-level COMSEC interface, unpacked by the net_rx_fn and transport_rx_fn processors and sent to the data-link processor over the DLP-to-SNC interface.

Parameters defining a NILE unit's membership in Link 22 networks, slot duration, slot ownership, and other transport-related parameters are specified in a scenario-script file that is a prototype of the Link 22 OPTASKLINK message.

LINK-LEVEL COMMUNICATION SECURITY

The LLC, shown in Fig. 6, serves several critical functions. Using an embeddable INFOSEC product developed for the Navy, the LLC provides Type 1 encryption and decryption (i.e., COMSEC) services for all messages carried by Link 22 networks. It provides trusted bypass of a defined set of control parameters that support SPC scheduling of transmit and receive slots in the adaptive TDMA net cycle structure. Finally, it provides multiplex and demultiplex services so that a system-network controller (or TDMA traffic generator) can interface to and control as many as four SPCs simultaneously.

The LLC interface message formats are based on and extend the functionality of SPC formats specified by France for its nationally developed Link 22-related systems. The final message design consists of a three-part message. The crypto part contains parameters controlling LLC operation and is present only on messages on the LLC's red-side (i.e., SNC-to-LLC) socket interface. The bypass part contains parameters that control SPC operation and slot scheduling and that are also used by

the LLC for synchronization of encrypt and decrypt services, via time-stamps both for the time-of-encryption and the scheduled time of transmission for network packets. The data part of the interface message contains a network packet as plaintext (i.e., unencrypted) data on the red-side interface and ciphertext (i.e., encrypted) data on the black-side interface. The black-side interface is a balanced asynchronous serial interface, with selectable data rates up to 115.2 kb/s to support different SPC designs.

SNC-LLC EMULATOR

The SNC-LLC emulator is a standalone driver for back-to-back testing of signal-processor controllers. Developed for NILE, with the testbed by France's Centre d'Electronique de l' Armement, the SLE is a real-time stand-alone simulation

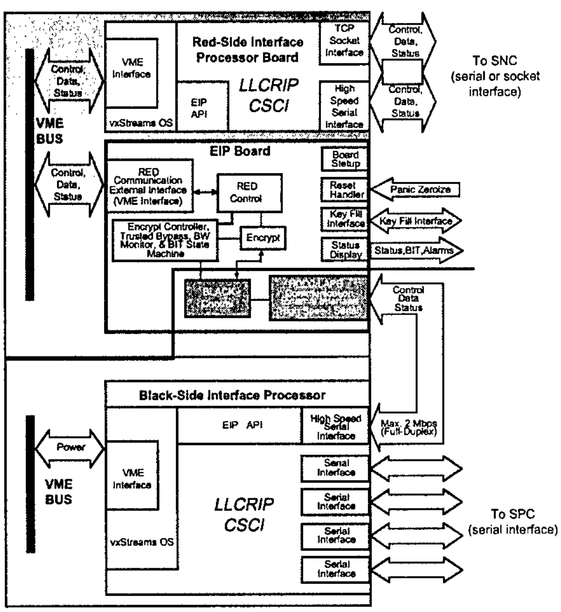

Fig. 6 — LLC architecture.

hosted on any of the SPARC20 processors in the testbed. The SLE uses the host's RS-232 serial interfaces to control a pair of signal-processor controllers in a simple, two-slot TDMA structure, generating test traffic and collecting performance statistics. The SNC-LLC emulator predates the testbed's SG/S and TTG software but is based on the same commercial-off-the-shelf simulation tool with a far simpler traffic-generation and node model than that used in the SIMLAB software ported to the testbed. The SLE uses techniques similar to those in the testbed for real-time synchronization and external interface to off-host hardware.

HF AND UHF SPCS

The HF SPCs in the testbed were implemented as a software-only upgrade to the AN/USQ-125 Link 11 Data Terminal Set used by the U.S. Navy. Using a single 6U Versa-Module Eurocard board with a general-purpose baseband processor and dual digital signal processors, the USQ-125 vendor implemented the serial baseband interface, serial time-of-day interface, and audio baseband interfaces required of HF SPCs. Reed-Solomon Block codes [4] are used in conjunction with adaptively equalized single-tone waveforms, providing significant performance improvements over the Link 11 waveform in a variety of channel conditions.

The prototype UHF SPC shown in Fig. 7 was implemented by NRL using commercial-off-the-shelf general purpose 68040 processors, with custom hardware required only for the digital-to-audio interface to the UHF radio. Software implementing the UHF medium's Reed-Solomon error-correction and detection code [5] was developed through modification of a general-purpose encoder design posted publicly on the INTERNET, converting what was a tutorial example of decoder design into a real-time implementation. The remaining UHF-SPC software was developed in-house. The final design demonstrated the required interface to AN/WSC-3 UHF line-of-sight radios, validating the waveform design and its compatibility with existing radios assets.

HF/UHF PROPAGATION SIMULATOR

The testbed includes a propagation simulator for the HF and the UHF transmission media. Each may be controlled interactively or by timed, script-driven scenarios through a common interface.

The HF propagation simulator provides independent control of the amplitude, Doppler, Doppler-spread, and multipath parameters for each of the 12 transmission links that exist among four nodes in a network, using a Waterson groundwave-plus-skywave model implemented on a DSP card for each of the 12 links [6]. Radio receivers at each node introduce automatic gain control effects for the SPCs. These capabilities allow simulation of arbitrary network connectivity and waveform modification in HF-FF media in the testbed for up to four nodes. The interface to the HF propagation

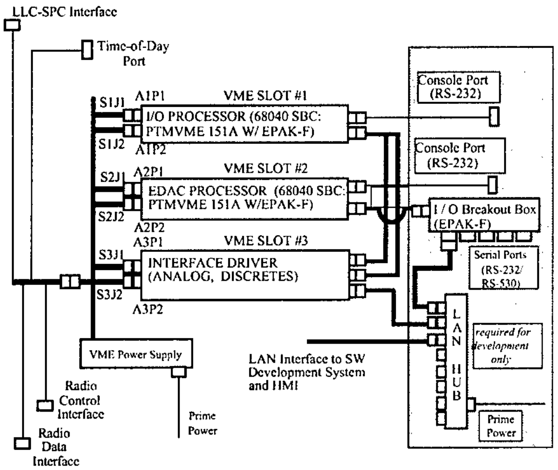

Fig. 7 — Block diagram and interfaces for the in-house UHF-SPC design.

simulator is at audio baseband (3 kHz), allowing direct connection of the HF signal processor controller.

The UHF propagation simulator supports RF input and output from four UHF radios and allows control of signal attenuation and additive noise levels (both Gaussian and burst modes) for all transmission links between nodes. Multipath and fading phenomena are not modeled in hardware in the UHF simulator as they are in the HF simulator. Slow-fading phenomena are modeled with a scenario script through dynamic control of path attenuation and noise level.

TEST INSTRUMENTATION AND EQUIPMENT

The testbed uses both commercial-off-the-shelf and custom test instrumentation and equipment for integration testing of the Link 22 advanced-development models. The test interfaces are those interfaces specified between advanced-development model subsystems, and the advanced-development models provide readily accessible test points (e.g., a buffered or isolated RF or audio port for power measurements).

Data collection is automated using measurement sensors and systems distributed through the testbed reporting to a common relational database (ORACLE™) to facilitate data reduction and extraction

Customized local area network analyzers that recognize the message catalogs for the SG/S-to-TTG interface and the SNC-to-LLC interface were developed based on the "tcpdump" software widely available from INTERNET web sites and some operating systems. Customized serial protocol analyzers for data capture and extraction on the LLC-to-SPC interfaces were derived from the LLC interface code. Custom data extraction and reporting programs for spectrum analyzers, oscilloscopes, and RF power meters were developed using a commercial-off-the-shelf visual engineering tool that obtains measurement data and places custom reports into the testbed database on demand.

NILE DATABASE ANALYSIS TOOL

Analysis of data extracted from the test bed is eased by the NILE database analysis tool, a graphical browser for reviewing data that has been captured and placed in the database. NILE data analysis tool's top-level window mimics the architectural layout of a Link 22 unit and its interfaces, as shown in Fig. 8. Detail windows that present summary data of the messages or signals captured on a given interface may be displayed by activating the corresponding button on the top-level window.

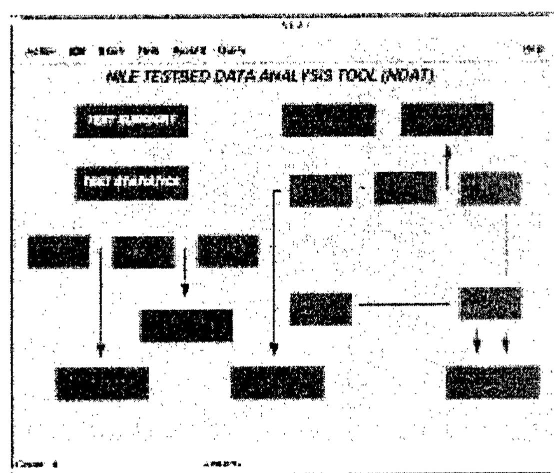

Fig. 8 — Top-level GUI for the NILE database analysis tool.

TIME SYNCHRONIZATION AND DISTRIBUTION

Node-to-node synchronization in the NILE testbed is maintained with independent clocks and timing sources for each node. The key processes that require synchronization are the traffic source (i.e., the SG/S), TDMA controller, and signal processor controllers at each node. The quality and synchronization method for each source differ, and the testbed uses a mixed set of techniques for node

synchronization and time distribution (as shown in Fig. 9); commercial-off-the-shelf and freeware/shareware sources were used to assemble the timing subsystem.

The testbed's common timing sources are satellites in the Global Positioning System (GPS). The hosts for the SG/S and TTG are synchronized using the INTERNET network time protocol, with a commercial off-the-shelf network server with GPS receiver as the common time source. Serial time codes are provided once a second to the HF and UHF SPCs from GPS-synchronized clocks.

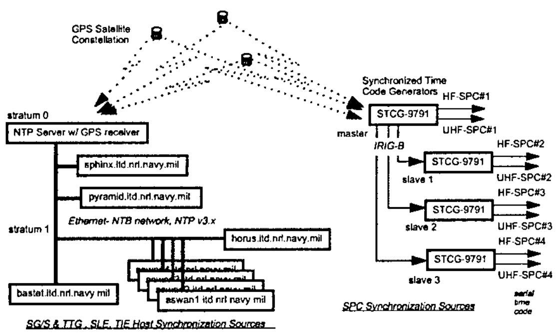

Fig. 9 — Time synchronization and distribution in the Link 22 testbed.

CONTRIBUTIONS TO LINK 22 DEVELOPMENT

The Link 22/NILE simulation laboratory and testbed efforts provided critical performance validation data and proof-of-concept prototypes for key areas of the Link 22 system design. The development and test of viable interfaces between node subsystems validated the functional partitions specified for the Link 22/NILE unit. Performance tests taken with the HF-SPC, SNC-LLC emulator, and HF propagation simulator validated the LLC-SPC interface and waveform performance. Interface tests with the SG/S and TTG have validated the basic performance and requirements for the DLP-to-SNC interface specified for Link 22. Validation and certification of the key design features and embeddable INFOSEC product in the link-level COMSEC was a critical milestone in the development of the Link 22 system.

Successful completion of the Link 22 simulation laboratory and testbed efforts were milestones enabling the NILE program to move on to the next phase of its development, which is final implementation of the SNC computer software component and the NILE reference system, with subsequent delivery to the navies of the seven nations.

[Sponsored by NATO Improved Link 11 Project Management Office]

REFERENCES

1. *Understanding TADIL Planning and Operations: A Guidebook for Operators, Planners, and Managers*, prepared for the Program Executive Officer for Space, Communications, and Sensors, by Logicon Tactical Systems Division, San Diego Calif., Oct. 1996

2. J.S. Schlorff and D.G. Kallgren, "Hardware-in-the-Loop Emulation and Prototyping with OPNET™," conference paper presented at OPNETWORK '97, Washington, D.C., May 1997.

3. W.R. Stevens, *Advanced Programming in the UNIX® Environment* (Addison-Wesley, Reading, Mass., 1992).

4. A.M. Michelson and A.H. Levesque, *Error Control Techniques for Digital Communication* (John Wiley and Sons, New York, 1985), Ch. 6.

5. P.J. Crepeau and J.C. McCanless, "Coding and Synchronization Analysis of the NILE UHF Fixed-Frequency Waveform," NRL/MR/5520--95-7776, Sept. 1995.

6. J.P. Macker, "A Channel Simulation Processor for the Multi-Node Tactical Network Simulator," NRL/MR/5523--93-7184, Jan. 1993. ◆

THE AUTHORS

DONALD G. KALLGREN is the head of the Tactical Networks Section in the Communication Systems Branch of NRL's Information Technology Division. His areas of interest include protocols, simulation, radio communications, prototyping, information security, and signal processing. Mr. Kallgren is a graduate of the University of Maryland College of Engineering, where he received a B.S. degree in electrical engineering and an M.S. degree with specialization in communications and controls. Mr. Kallgren's work at NRL has included research and development related to the Mark XII Interrogate Friend-or-Foe (IFF) system, the Joint Tactical Information Distribution System (JTIDS), communication intercept systems, anti-jam low-probability-of-intercept (AJ/LPI) satellite communications, high-frequency anti-jam (HFAJ) communications, cooperative engagement systems, multimedia integrated communications, system verification and validation, information security techniques, and lightweight distributed network protocols for naval tactical communication.

JOHN P. CHENG is an electrical engineer in the Tactical Networks Section in the Communication Systems Branch of NRL's Information Technology Division. Mr. Cheng received his B.S. degree in electrical engineering from the University of Virginia in 1992. Prior to joining NRL in 1995, Mr. Cheng's work involved information security. Since coming to NRL, Mr. Cheng's work has also included research and development related to protocols, radio and satellite communications, and signal processing using prototyping and computer simulation methods.

KAREN E. GRANT joined the NRL Tactical Electronic Warfare Division's Central Target Simulator (CTS) Facility following graduation from Worcester Polytechnic Institute (WPI) in May 1988, where she received a B.S. degree in applied mathematics. Ms. Grant attended the United States Naval Academy before transferring to WPI where she participated in the NRL Cooperative Education Training Program. Ms. Grant received an M.S. degree in electrical engineering from the University of Maryland in May 1995, while working full time at NRL. She also participated in the NRL Edison Memorial Training Program for two years while pursuing her degree. Ms. Grant designed and developed the automated scenario initialization system for the CTS Facility. She was also the principal investigator for the 6.2 Force Assessment Resources Management (FARM) effort. Ms. Grant transferred to the Information Technology Division's Tactical Networks Section in October 1995, where she designed and developed the data collection system for the NATO Improved Link Eleven (NILE) Testbed. Ms. Grant also developed the NILE Data Analysis Tool (NDAT), which was successfully demonstrated to the NILE Steering Committee and was transitioned as prototype for the NILE Reference System.

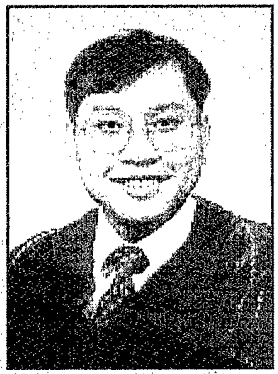

LAM N. PHAM is a member of the Tactical Networks Section in the Communication Systems Branch of NRL's Information Technology Division. Mr. Pham was awarded a B.S. degree in electrical engineering from the University of Maryland in College Park, and an M.S. degree in electrical engineering from the John Hopkins University. His areas of interest include protocols, simulation, radio communications, and information security.

JOHN S. SCHLORFF received a B.S. degree in electrical engineering from the Pennsylvania State University in 1987. He received an M.S. degree in electrical engineering from the University of Maryland at College Park in 1995. His thesis research focused on end-to-end quality of service for self-similar traffic and trafficshaping in Asynchronous Transfer Mode (ATM) networks. Mr. Schlorff joined the Information Technology Division's Tactical Networks Section at NRL in 1988. His areas of interest include networking protocols, mixed-media and multimedia networks, computer simulation, information security, and distributed network applications. While at NRL, Mr. Schlorff was involved in the early stages of the NATO Improved Link-Eleven (NILE) project (Link-22). His work has included computer simulation, mathematical modeling, prototyping, system concept development, specification writing, and information security.

SCOTT A. KAPUSCHANSKY first came to NRL in the summer of 1991 as a Science and Engineering Apprentice Program student working in the Laboratory for Computational Physics and Fluid Dynamics. After graduating from DeMatha Catholic High School in 1992, he joined the Information Technology Division, Tactical Networks Section. He received his B.S. degree from the Rochester Institute of Technology in 1997. Mr. Kapuschansky has worked on hardware test and integration as well as software development for the Link 22 Project. He has also performed automation in test and data collection and reduction.

Demonstration of W-Band Gyroklystron Amplifiers for Radar Applications

M. Blank, B.G. Danly, and B. Levush
Electronics Science and Technology Division

There is current interest within the Department of Defense (DoD) to develop high-power W-band gyroklystron amplifiers for enhanced millimeter-wave radar systems. Potential applications include high-resolution imaging, precision tracking, and cloud physics studies. However, the relatively high atmospheric absorption in the millimeter-wave band necessitates the use of high-power amplifiers for many applications. Vacuum devices based on the gyrotron interaction can yield significantly higher powers than are possible with conventional slow-wave device technology. In this article, the results from high-power W-band gyroklystron and gyrotwystron amplifier experiments are presented. These results represent world record achievements in both peak power and power-bandwidth product from a W-band amplifier and provide the radar system designer with order of magnitude advances in driver performance over currently available sources.

INTRODUCTION

High-power, millimeter-wave (> 30 GHz) amplifiers are needed in present and future DoD radar and electronic warfare applications. High angular resolution and accuracy of a tracking radar are more easily achieved at millimeter-wave frequencies, as compared to conventional microwave radar, with implications for improved ship self-defense concepts using command guidance of defensive missiles or projectiles. For imaging applications, operation at high frequencies provides larger Doppler shifts for a given target rotation; this feature will result in improved inverse synthetic aperture radar performance when applied to noncooperative target recognition. Finally, the theoretically predicted enhanced scattering from small surface irregularities at high frequencies suggests the use of millimeter-wave radar for the detection of low observables.

Vacuum electronic amplifiers traditionally used in millimeter-wave radar systems, such as coupled-cavity traveling wave tubes (TWTs) and extended interaction klystron amplifiers, are capable of producing only limited powers (< 5 kW peak, < 1 kW average) in W-band (75-110 GHz) because of the underlying interaction physics of the devices. In these slow-wave devices, the circuit is used to modify the dispersion of the electromagnetic wave to achieve synchronism between the beam and the wave. Typical transverse circuit dimensions required to effectively slow the phase velocity of the wave are on the order of 10% of the free space wavelength. For W-band, the wavelengths range from 2.7 to 4 mm, and slow-wave transverse circuit sizes are fractions of a millimeter. As a result of this small size, thermal loading due to beam interception severely limits the peak and average power that can be achieved.

GYRO-AMPLIFIERS

In fast-wave devices, such as gyrotrons and free electron masers, the beam dispersion is modified by a constant or periodic magnetic field to obtain synchronism between the beam and wave. Consequently, circuit sizes can be several times the free-space wavelength. Because of the 10-fold increase in circuit dimensions, fast-wave devices are capable of achieving much higher powers at millimeter-wave frequencies than are slow-wave devices.

In a gyrotron, a fast-wave device based on the cyclotron maser instability, an annular beam composed of mildly relativistic electrons traveling in helical paths interacts with the electromagnetic fields of a fast-wave circuit in the presence of a strong magnetic field [1]. As some of the electrons—initially randomly distributed in phase—are acceler-

ated by the electric field, they gain relativistic mass and slip back in phase. Those electrons that are decelerated lose relativistic mass and move forward in phase. This process leads to the formation of a bunch of electrons from which energy is resonantly coupled to the electromagnetic wave with frequency close to the relativistic cyclotron frequency of the electrons, $\omega_c = eB/m\gamma$, where e is the electron charge, B is the applied magnetic field, m is the electron rest mass, and γ is the relativistic mass factor. For high-frequency operation, the required high magnetic fields are generally produced with a superconducting magnet. For example, a gyrotron amplifier, or gyro-amplifier, operating at W-band requires a magnetic field ~3.4 T. The continued advances in the development of high-temperature superconductors and cyrocoolers make it possible to consider the use of a closed-cycle cryocooled superconducting magnet for a gyro-amplifier.

The cyclotron maser interaction has been used to produce high-power millimeter-wave radiation in a number of oscillator and amplifier configurations. Gyrotron oscillators are widely used for electron cyclotron resonance heating of fusion plasmas and for industrial processing of materials. Gyrotron amplifiers are of great interest for high-power millimeter-wave radar and communications. Depending on specific system requirements, gyrotron amplifiers of three different types can be used. In a gyroklystron, the interaction between the spiraling electron beam and the RF field takes place in several resonant cavities separated by drift regions in which the electromagnetic wave cannot propagate. Figure 1 is a schematic of a typical gyroklystron amplifier. The beam is produced at the cathode of the magnetron injection gun and is compressed as it enters the high field region of the superconducting magnet. The resonant cavities are placed in the flat field region of the magnet. The beam interacts with the electromagnetic fields in the cavities. The beam, which is increasingly bunched as it progresses from one cavity to the next, produces higher RF fields in each successive cavity. Finally, the spent beam and amplified wave propagate together out of the high field region. As the magnetic field tapers off, the electron beam expands and is collected on walls of the collector while the EM wave propagates out the vacuum window. Because the bandwidth of a resonant cavity is approximately the inverse of the loaded quality factor Q_l, the gyroklystron is capable of producing very high output powers at moderate bandwidths (typically < 1%).

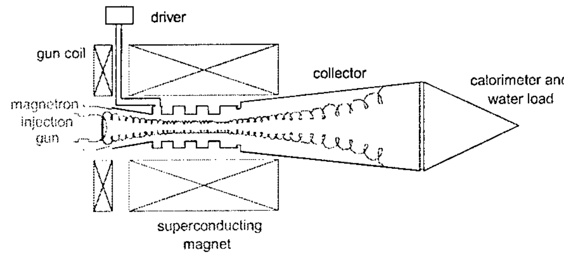

Fig. 1 — Schematic of a typical gyroklystron amplifier.

To achieve greater bandwidth from a gyrotron amplifier, the standing wave output cavity can be replaced by a traveling wave output section. This hybrid device, known as a gyrotwystron, is capable of producing high powers at large bandwidths (typically 1% to 2%). For even greater bandwidths (> 2%), the gyro-traveling-wave tube (gyro-TWT), in which the interaction takes place entirely in a traveling wave circuit, is the appropriate amplifier technology. Bandwidths in excess of 20% (32-39 GHz) have been demonstrated by a Ka-band gyro-TWT [2]. However, the power capability of gyro-TWTs is generally lower than that of gyroklystrons.

Figure 2 shows the demonstrated peak output powers and bandwidths of various W-band high-power vacuum electronic devices of interest for radar applications, including slow-wave and gyrotron amplifiers. Note that gyroklystron amplifiers have achieved peak output powers more than 20 times greater than those achieved by the slow-wave coupled cavity TWT.

In this article, the designs and results of experimental demonstrations are presented for two W-band gyroklystron amplifiers, indicated by the two red circles in Fig. 2. The results from a W-band gyrotwystron amplifier experiment, shown by the blue square, are also discussed. The measured performance of these devices represent world

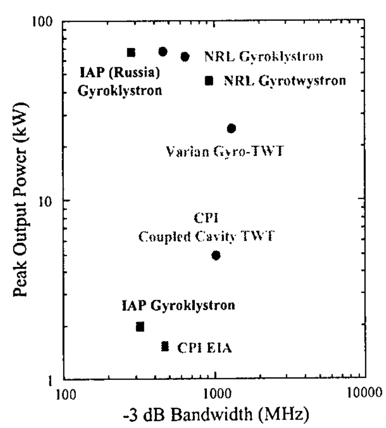

Fig. 2 — Current state-of-the-art power and bandwidth for W-band amplifiers of interest for radar applications.

record achievements in both peak power and power-bandwidth product from a W-band amplifier. The gyro-amplifiers described below provide the radar system designer with order of magnitude advances in driver performance over currently available sources.

W-BAND GYROKLYSTRON DESIGN

A set of theoretical models and numerical design tools were used to design the two gyro-klystron interaction circuits and determine the parameters of each cavity, which are summarized in Table 1. These models are used to predict operating characteristics of the gyroklystron such as gain, efficiency, output power, and stability. The models include the effects of beam velocity spread, magnetic field profiling, and circuit loading due to lossy dielectrics.

As shown in Table 1, the second and third cavities of both circuits are designed with cold resonant frequencies f_0 higher and lower, respectively, than the frequency of the output cavity. The purpose of this stagger tuning is to broaden the bandwidth of the amplifier. The first circuit has a modest amount of stagger tuning, and the output cavity Q_l is 300. This circuit was specifically designed to demonstrate high efficiency and gain. The second circuit was designed for increased bandwidth at the expense of peak output power, efficiency, and gain. This increased bandwidth is achieved through increased stagger tuning and a reduced output cavity Q_l of 166.

Table 1 — Design Parameters for the Two W-band Gyroklystron Amplifier Circuits

	Circuit #1 Design		Circuit #2 Design	
	f_0 (GHz)	Q_l	f_0 (GHz)	Q_l
cavity 1	93.00	125	93.00	125
cavity 2	93.52	175	94.20	175
cavity 3	92.89	175	93.24	175
cavity 4	93.18	300	93.86	166

The field amplitude in each cavity vs frequency for the second, wider band circuit design is shown in Fig. 3. The figure clearly shows how the well-established method of stagger tuning cavities can lead to broadband device performance. The cold resonant frequencies of each cavity are shown with the solid vertical lines. The resonant frequencies of cavities 1 and 3 lie below the resonant frequency of the output cavity—cavity 4—and the resonant frequency of cavity 2 lies above. The field amplitude in cavity 2 is enhanced at the lower frequencies due to the resonance at 93.3 GHz in the previous cavity. Similarly, the field amplitude in cavity 3 is greatly enhanced at frequencies near 93.4 GHz by the interaction in cavity 2. Thus, the stagger tuning leads to an overall broader band performance than would be achieved with all four resonant frequencies the same. Figure 3 also shows how the presence of the beam changes the resonant frequencies of the cavities. For instance, the peak in field amplitude in cavity 1 occurs at 93.2 GHz while the cold resonant frequency was 93.0 GHz. It is important to include the beam loading effects when designing the cavity stagger tuning.

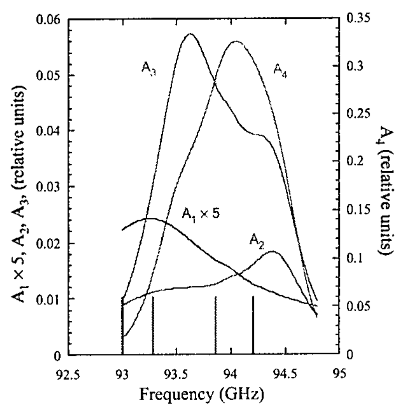

Fig. 3 — Field amplitudes in each cavity of the second circuit as a function of drive frequency for a 55 kV, 4 A electron beam with $\alpha = v_{perp}/v_z = 1.5$ and 9% rms perpendicular velocity spread. The field amplitude in cavity 1 has been multiplied by 5 for visibility.

An important component of any amplifier is the input cavity, which must efficiently couple power from the driver source into the desired mode of the interaction circuit over a broad range of frequencies. For all three circuits described here, the drive power is coupled into the circuit through a coaxial cavity, shown in cross section in Fig. 4. A single cylindrical waveguide excites the TE_{411} mode of the outer cavity. Power is then coupled from the TE_{411} mode in the outer cavity to the TE_{011} mode in the inner cavity through four slots positioned symmetrically around the azimuth of the cavity. The coaxial cavity used for all circuits was analyzed with a finite-element electromagnetic code, the high frequency structure simulator (HFSS), and found to have a resonant frequency of 93 GHz, with $Q_{ext} = 150$ and $Q_{ohmic} = 800$. HFSS simulations also show that approximately 75% of the energy is stored in the TE_{411} mode and 25% is

stored in the TE_{011} inner cavity mode at a drive frequency of 93.35 GHz; this stored energy ratio is nearly constant over the operational frequency range.

To achieve the desired circuit performance, the second and third cavities must have relatively low loaded Q's of 175. For the low duty demonstrations performed in this study, the cavities were ohmically loaded with rings of lossy dielectric. A scattering matrix formulation was used to predict resonant frequencies and Q's of the loaded idler cavities. The output cavity consists of a straight section followed by an iris, which is cutoff to the TE_{011} mode at 93 GHz, and a linear uptaper to the collector radius. The wave is coupled out diffractively, and there is no ceramic loading the output cavity.

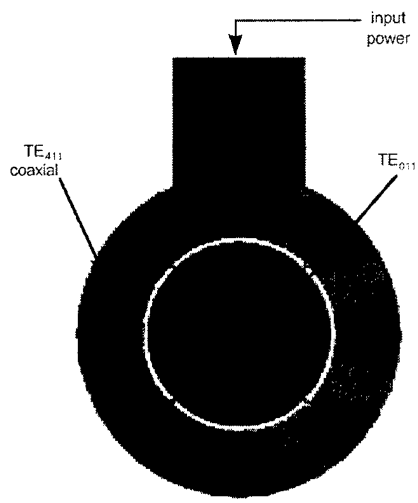

Fig. 4 — HFSS simulation of coaxial drive cavity in cross sectional view showing $|E|^2$.

EXPERIMENTAL DEMONSTRATION

In the experimental test stand used for both gyroklystron circuits and the gyrotwystron circuit, a 4.5 A, 55 kV annular electron beam is produced by a double anode MIG. The magnetic field at the cathode, which is nominally 1.5 kG, can be varied to control the beam velocity ratio, $\alpha = v_{perp}/v_z$. The beam is adiabatically compressed as it enters the region of high magnetic field generated by the superconducting magnet. The four cavities of the gyroklystron circuit are positioned in a region of constant magnetic field. The output cavity tapers up to the collector, which is followed by a quartz vacuum window. A conically shaped, water-backed teflon load is positioned on the atmospheric side of the vacuum window. The temperature rise of the water due to the RF is then measured and calibrated against the temperature rise due to resistive heating. The frequency of the input and output RF signals is measured with a spectrum analyzer. The drive power is supplied by an extended interaction oscillator (EIO), which is mechanically tunable from approximately 92.5 to 95.5 GHz. The EIO provides pulses up to 2 μs in duration; the beam and EIO are typically pulsed at 250 Hz for an RF duty cycle of 0.05%. The drive line between the EIO and input cavity includes two 90° bends in overmoded waveguide and one circular-to-rectangular transition at the input window. Cold test measurements were made to determine the losses in the drive line so that the measured gain could be compared to theoretical predictions. Measurements showed that approximately 4 dB of drive power are lost between the EIO and the drive cavity.

The four cavity circuits were manufactured and cold tests were performed with a vector network analyzer to determine the resonant frequencies and Q's of each cavity. The cavities were excited and sampled through two holes positioned 180° apart in the side wall. The measured cold test values for the two gyroklystron circuits are summarized in Table 2, and the hot test results are described below.

Table 2 — Summary of Cold Test Results for the Two W-band Circuits.

	Circuit #1		Circuit #2	
	f_0 (GHz)	Q_l	f_0 (GHz)	Q_l
cavity 1			-	-
cavity 2	93.59	130	93.74	108
cavity 3	93.05	128	93.14	107
cavity 4	93.24	299	93.49	145

FIRST CIRCUIT DEMONSTRATION

Upon completion of the cold test, the first circuit was installed in the test stand. In order to compare the measured performance of the amplifier to predictions of theory, parameters of the beam, including velocity spread and beam pitch factor $\alpha = v_{perp}/v_z$, are required. In the experiment, the beam α and velocity spread were not measured but were deduced through a combination of theoretical modeling and empirical determination. Studies with the EGUN electron trajectory code indicate that beam α's between 1.3 and 1.8 and perpendicular velocity spreads between 4% and

12% are expected for the nominal operating parameters. In addition, hundreds of measured data points were matched with theoretical predictions assuming a consistent pair of α and perpendicular velocity spread values. The good agreement of theory and experiment over a wide range of operating parameters with a consistent pair of α and velocity spread values suggests that these values are valid.

Figure 5 shows the measured and predicted output power and efficiency as a function of frequency for the amplified TE_{011} mode. A peak saturated output power of 67 kW, corresponding to 28% efficiency, was achieved with a 55 kV, 4.3 A electron beam. The FWHM bandwidth is greater than 460 MHz [3]. Under these operating conditions, the amplifier was unconditionally stable. For the theory curve in Fig. 5, the experimentally determined values of cold resonant frequencies and Q's for the idler and output cavities were used. The HFSS predictions of the drive cavity resonant frequency and Q were assumed. The experimental values of beam voltage, beam current, and magnetic field in the interaction circuit were used. As shown in Fig. 5, the theoretical predictions are in good agreement with experimental data.

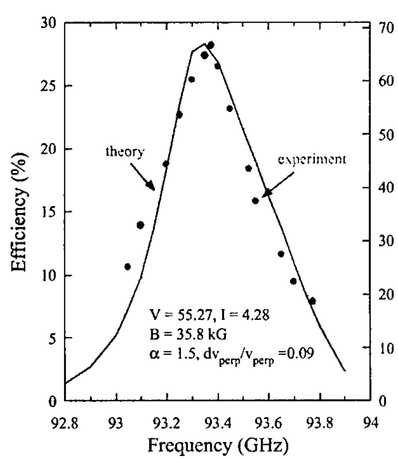

Fig. 5 — Theoretical (blue line) and experimental (red circles) power and efficiency as functions of driver frequency for the first circuit.

Figure 6 shows the measured output power, efficiency, and gain for a slightly reduced beam voltage of 52.6 kV. For the data shown in the figure, the input power is measured at the output of the EIO, and no correction is made for losses in the drive line or energy storage in the TE_{411} cavity. As shown in the figure, the output power reaches saturation at an input power of approximately 87 W. The saturated gain is 29 dB, and the small signal gain is approximately 38 dB. The theoretical prediction of efficiency vs input power is also plotted in Fig. 6. For the theory curve, the input power was multiplied by 10 to take into account that the power coupling into the TE_{011} mode of the drive cavity is 10 dB down from the power at the EIO output. Figure 6 also shows that the agreement between theory and experiment is very good.

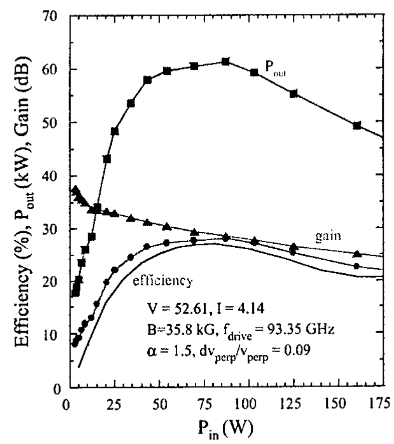

Fig. 6 — Experimental efficiency (red circles), output power (blue squares), and gain (green triangles) vs input power for the first circuit. The theoretical prediction of efficiency is shown by the black solid line.

SECOND AND THIRD CIRCUIT DEMONSTRATIONS

Next, the second wider band circuit was built, cold tested, and installed in the test stand. Figure 7 shows the efficiency and peak output power as a function of drive frequency for the amplified TE_{011} mode in the second circuit. A peak saturated output power of 60 kW, corresponding to 25% efficiency, was achieved with a 58 kV, 4.2 A electron beam. The FWHM bandwidth is 640 MHz. Under these operating conditions, the amplifier was unconditionally stable. For the theory curve in Fig. 7, the experimentally determined values of cold resonant frequencies and Q's for the idler and output cavities were used. As shown in Fig. 8, the theoretical predictions are in good agreement with experimental data.

The results from second circuit tests show how increased stagger tuning and decreased output cavity Q can be used to broaden the bandwidth at the expense of efficiency and peak output power. To further broaden the bandwidth, a third circuit, in which the output cavity of the second circuit was

replaced by a traveling wave section, was experimentally tested. This hybrid gyrotwystron circuit demonstrated 44 kW peak output power, corresponding to 16.5% efficiency with a FWHM bandwidth of 920 MHz (Fig. 8).

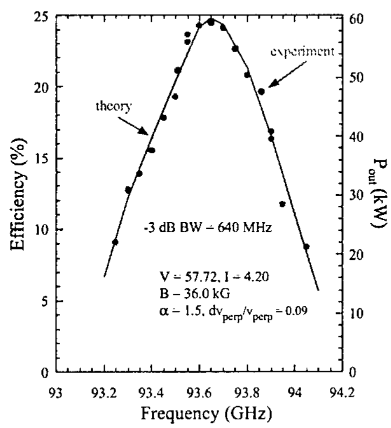

Fig. 7 — Theoretical (blue line) and experimental (red circles) peak output power and efficiency as a function of drive frequency for the second circuit.

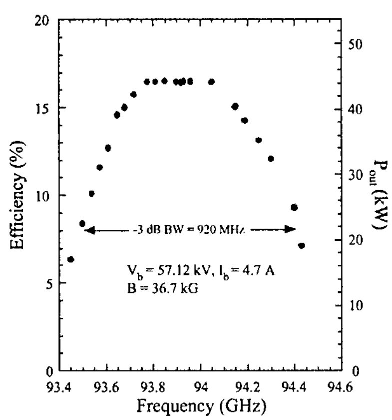

Fig. 8 — Experimental peak output power and efficiency as a function of drive frequency for the gyrotwystron.

The demonstrated performance for the three W-band gyro-amplifiers shows that high output powers can be achieved at broad bandwidths. Individual system needs can be examined to determine the optimal trade-off between peak output power, gain, and bandwidth.

SUMMARY

The experimental results from W-band gyroklystron and gyrotwystron amplifier experiments are presented. Three circuit configurations have been tested. The first circuit, which was specifically designed to have high peak output power, efficiency, and gain, achieved 67 kW peak output power, corresponding to 28% efficiency. The FWHM bandwidth was measured to be 460 MHz, which is significantly larger than the bandwidth demonstrated in previous W-band gyroklystron amplifiers [4]. The second circuit, which was designed to have a broader bandwidth, produced 60 kW peak output power at 25% efficiency with a 640 MHz FWHM bandwidth. A gyrotwystron circuit achieved 44 kW peak output power at 16.5% efficiency with 920 MHz bandwidth. These results represent a record power-bandwidth product at this frequency. The experimental results were compared to theoretical predictions, and excellent agreement was obtained, demonstrating the predictive capabilities of the computational models used in the design of the gyroklystron amplifiers. The experimental results have demonstrated more than an order of magnitude increase over the peak power achievable by conventional coupled-cavity TWT technology. Millimeter-wave radar systems with high-power gyroklystron amplifiers will offer opportunities to the system designer for a host of improvements in radar detection, imaging, and tracking.

A high average power version of the gyroklystron amplifier described here is presently being built in a collaborative effort between NRL, Litton, Communications and Power Industries, and the University of Maryland. This W-band amplifier is designed to achieve 10 kW average output power, 80 kW peak output power, an efficiency of 20%, and a bandwidth of 740 MHz. The device will be delivered to the NRL Radar Division for the Millimeter Wave Radar Project. This amplifier technology is also expected to be applicable to many other Navy and DoD systems in the future.

ACKNOWLEDGMENTS

The authors thank P.E. Latham, D. Pershing, M. Barsanti, F. Robertson, R. Kyser, B. Sobocinski, and M. Ngo for their technical assistance. The authors are grateful to D. Lohrmann for the loan of the EIO driver and to J. Hirshfield for many fruitful discussions. The computational work was supported in part by a grant of High Performance Computing (HPC) time from the DoD HPC Center Naval Oceanographic Office, Stennis Space Center, Mississippi.

[Sponsored by ONR]

REFERENCES

1. A.V. Gaponov-Grekhov and V.L. Granatstein, eds., *Applications of High-Power Microwaves* (Artech House, Norwood, Mass., 1994).

2. G.S. Park, J.J. Choi, S.Y. Park, C.M. Armstrong, A.K. Ganguly, R.H. Kyser, and R.K. Parker, "Gain Broadening of Two-Stage Gyrotron Traveling Wave Tube Amplifier," *Phys. Rev. Lett.* **74**, 2399-2402 (1995).

3. M. Blank, B.G. Danly, B. Levush, P.E. Latham, and D.E. Pershing, "Experimental Demonstration of a W-band Gyroklystron Amplifier," *Phys. Rev. Lett.* **79**, 4485-4489 (1997).

4. I.I. Antakov, E.V. Zasypkin, and E.V. Sokolov, "Design and Performance of a 94-GHz High Power Multicavity Gyroklystron Amplifier," Conference Digest of the 18th International Conference on Infrared and Millimeter Waves, *Proc. SPIE* **2104**, 466-467 (1993). ◆

THE AUTHORS

MONICA BLANK received a B.S. degree in electrical engineering in 1988 from the Catholic University of America, Washington, D.C., and M.S. (1991) and Ph.D. (1994) degrees, also in electrical engineering, from the Massachusetts Institute of Technology, Cambridge. Her dissertation work involved theoretical and experimental studies of quasi-optical mode converters for high-power gyrotron oscillators. In 1994, she joined the Vacuum Electronics Branch of the Naval Research Laboratory as an electronics engineer, where she is responsible for the design and demonstration of high-power millimeter-wave vacuum electronic devices.

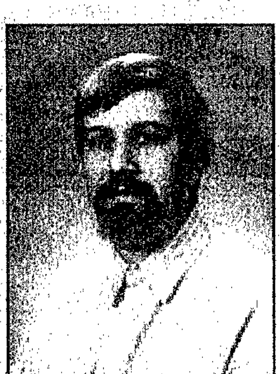

BRUCE DANLY received a B.A. degree in physics from Haverford College in 1978 and a Ph.D. degree in physics from the Massachusetts Institute of Technology in 1983. From 1983 to 1995 Dr. Danly was a member of the research staff at MIT Plasma Fusion Center, first as research scientist from 1983 to 1992, and then as principal scientist from 1992 to 1995. While at MIT, Dr. Danly participated in research on gyrotrons, free-electron lasers, relativistic klystrons, and other high-power RF source technologies for use in plasma heating and high-gradient RF linear accelerators. In 1995, Dr. Danly joined the Naval Research Laboratory as head of the High Power Devices Section, Vacuum Electronics Branch, in the Electronics Science and Technology Division. The high power devices section carries out experimental research and development on new concepts for high power microwave, millimeter-wave, and infrared sources based on both slowwave and fastwave interaction mechanisms. Technologies under investigation include gyrotron amplifiers (gyroklystrons, gyrotwystrons, gyro-TWTs), free-electron lasers, TWTs, and klystrons. Dr. Danly is a member of the American Physical Society Divisions of Physics of Beams and Plasma Physics and the IEEE.

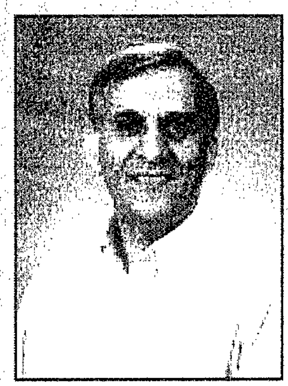

BARUCH LEVUSH received his M.Sc. degree in physics from Latvian University in Riga and his Ph.D. degree, also in physics, from Tel-Aviv University. In 1985, Dr. Levush joined the University of Maryland, where his research has focused on the physics of coherent radiation sources and the design of high-power microwave sources, such as gyrotrons, traveling wave tubes, BWO's and free-electron lasers. In 1995, Dr. Levush joined NRL as head of the Theory and Design Section of the Vacuum Electronics Branch in the Radar Division. Dr. Levush is actively involved in developing theoretical models and computational tools for analyzing the operation of existing microwave vacuum devices and in inventing new concepts for high-power, high-frequency coherent radiation sources. Dr. Levush is a member of the American Physical Society and Senior Member of the Institute of Electrical and Electronics Engineers.

The 1997 El Niño in the NRL Layered Ocean Model

E.J. Metzger, H.E. Hurlburt, J.C. Kindle, R.C. Rhodes, G.A. Jacobs, and J.F. Shriver
Oceanography Division

O.M. Smedstad
Planning Systems, Inc.

Beginning in the spring and continuing through the summer and fall of 1997, there was an overall weakening of the tropical easterly trade winds interspersed with sporadic westerly wind bursts. These atmospheric events are precursors to the oceanic El Niño response, i.e., a rise in equatorial sea surface height and sea surface temperature off the coast of South America. A 1/4° global wind forced version of the NRL Layered Ocean Model (NLOM) clearly depicts the evolution of the 1997 El Niño and compares qualitatively well with satellite altimeter data. The oceanic El Niño response is not confined to the tropics. Poleward propagating Kelvin waves carry the signal far from the equator, and the subsequent trans-Pacific propagating Rossby waves can interact with major oceanic fronts and currents years afterward. The Navy is currently running a 1/4° global ocean nowcast/forecast system, which includes NLOM with assimilation of real-time altimetry from TOPEX/POSEIDON and ERS-2, and in which El Niño and other oceanic phenomena can be monitored on a daily basis.

INTRODUCTION

The 1997 El Niño has become the most publicized and best observed El Niño in history. For the most part, U.S. media attention has focused on the global atmospheric effects of this phenomenon, and questions have been asked about the economic impacts that might be felt. Should Californians be prepared for excessive wintertime rains and potential mudslides? Will Atlantic hurricane activity be greatly reduced? Will extended drought conditions in Australia lead to vast wildfires? These are certainly important questions, but similar questions can be posed from an oceanographic point of view. Is the ocean response to El Niño a purely equatorial phenomenon? Does it produce coastal effects far from the tropics? Does it affect the position and strength of major oceanic fronts and currents years afterwards? Does the Navy have the ability to monitor El Niño in real time and to predict future effects? The NRL Layered Ocean Model (NLOM) [1,2] is used to answer these oceanographic questions.

The El Niño signal is an important oceanographic signal to model because, after the seasonal cycle, it is the second largest ocean-atmosphere variation encountered on time scales less than centuries. Typically, El Niño occurs every 2 to 7 years, but its appearance is irregular. The 1990s have been unusual in that warm anomalies have persisted much of the time in the equatorial Pacific. The 1997 El Niño differs from many of its predecessors because it began earlier in the year and with surprising strength. As measured by the Southern Oscillation Index (SOI)—the sea-level pressure difference between Darwin, Australia, and Tahiti—the 1997 El Niño had higher index values from March through June than the 1982/83 El Niño "of the century." Thus many predictions were made that it would become the largest ever observed. From July through September 1997, the SOI values decreased, but in October 1997, there was evidence of renewed strengthening.

OCEANIC RESPONSE TO ATMOSPHERIC EL NIÑO

The El Niño phenomenon results from a complex interaction of the ocean and atmosphere. However, as discussed below, given the atmospheric forcing, the oceanic evolution of El Niño is predominantly a deterministic response to wind forcing. Thus the ocean model should depict the 1997 El Niño if driven solely with reasonably accurate atmospheric forcing. This means that a realistic El Niño in the ocean model adds credibility to both the ocean model and the atmospheric forcing product. Satellite altimeter data can also be assimilated into the ocean model to further enhance the accuracy of the model's depiction of the El Niño event.

Typically, the easterly trade winds blow continually across the tropics, piling up water in the western equatorial Pacific and creating high sea level and a large pool of warm surface water in the region. At the equator, the sea surface height (SSH) difference across the basin is about 0.5 m and the sea surface temperature (SST) difference is about 8° C. The eastern equatorial Pacific waters are cooler due to upwelling of cold, nutrient-rich subsurface waters that support a diverse marine ecosystem and local fishing economy. During non-El Niño years, the western equatorial Pacific experiences heavy rainfall while the east is relatively dry.

During El Niño events, the trade winds relax in the western and central Pacific and even reverse direction for periods of a few weeks to a month [3]. These reversals, called westerly wind bursts (WWBs), initiate Kelvin wave pulses (a class of shallow water waves found along the equator and coastlines) that travel eastward along the equator, raising the SSH and SST and deepening the thermocline (an almost ubiquitous feature of the ocean where temperature decreases rapidly with depth) [4,5]. This reverses the upwelling in the eastern Pacific and cuts off the supply of nutrient-rich waters. The food chain becomes disrupted all the way up through the fisheries and bird populations. Thus El Niño takes its name from South American fisherman who recognized the unusually warm Pacific waters near the beginning of the year. Literally it means "The Boy" or, specifically, the Christ child, when capitalized—a name that arose because the warm water generally occurred around Christmas. Deep atmospheric convection and thunderstorm activity accompany the shift from cooler to warmer waters in the eastern Pacific. The western Pacific region tends to experience drought conditions during El Niños, and there is an associated change in the sea-level pressure difference between east and west, i.e., the Southern Oscillation. Thus, meteorologists often refer to these phenomena as El Niño/Southern Oscillation (ENSO) events.

THE 1997 EL NIÑO IN NLOM

The 1997 El Niño is clearly depicted in a 1/4° global, 6-layer thermodynamic version of NLOM that includes realistic bottom topography. The model domain extends from 72°S to 65°N, but the figures used here focus on the equatorial Pacific between 30°S-30°N. This model is marginally eddy-resolving, but versions with much higher horizontal resolution are under development at NRL. These are needed to accurately depict meandering ocean current pathways, sharp oceanic fronts, and the eddy field [6]. The model uses the 1990–1997 12-hourly surface wind stress forcing from the Fleet Numerical Meteorology and Oceanography Center's (FNMOC) Navy Operational Global Atmospheric Prediction System (NOGAPS) developed at NRL-Monterey. No assimilation of oceanic data is used in this version of NLOM, although results from a data assimilative version are shown later. Figure 1 compares SSH anomalies (with respect to a long-term mean) from NLOM and TOPEX/POSEIDON (T/P) satellite altimeter data for 13 May 1997. Positive anomalies are yellow-orange-red, while negative anomalies are shades of blue. Although both deterministic and nondeterministic oceanic responses to the atmo-

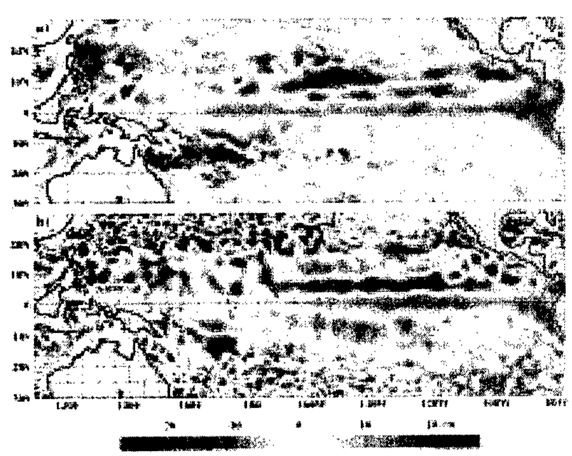

Fig. 1 — Sea surface height anomaly for 13 May 1997 from (a) a 1/4° global, 6-layer thermodynamic version of NLOM and from (b) T/P altimetry. All NLOM anomalies are with respect to its 1990–96 mean and the T/P analysis with respect to its 1993–96 mean. The contour interval is 2.5 cm. Yellow-orange-red indicate positive anomalies, i.e., higher SSH than the average, and shades of blue indicate negative anomalies.

spheric forcing are found everywhere, the oceanic El Niño signal is largely a deterministic response to the prescribed atmospheric forcing, and it has a signature of high SSH anomalies in the eastern equatorial Pacific, as indicated by both the model and the satellite altimetry. Bands of alternating low and high SSH anomalies are also seen north of the equator in the eastern half of the basin, associated with changes in strength and latitude of the North Equatorial Countercurrent and the northern tropical gyre. Typically these are areas where the SSH variability is largely controlled by the atmospheric forcing [7]. Clearly there are differences between the model and altimetry in other parts of the basin, and these are generally areas where SSH variability is predominantly nondeterministic, e.g., due to meso-scale flow instabilities.

WWBs AND THE ONSET OF THE 1997 EL NIÑO

As described above, the onset of El Niño conditions in the eastern tropical Pacific Ocean generally begins with the arrival of equatorial Kelvin wave pulses excited in the western and central Pacific by WWBs. The effects of an intense WWB in December-January of 1996/97 were compensated by anomalously strong easterly trade winds in the central and eastern Pacific. Hence, the WWBs responsible for the onset of the 1997 El Niño began in March 1997 (Fig. 2(a)). During a 4-month period, three WWBs in March, April, and May-June extended westerly winds into the central Pacific, generating three Kelvin wave pulses that reached the eastern boundary in late-April, late-May, and July (Fig. 2(b)), a model result that is in essential agreement with the real-time observations from the Tropical Atmosphere Ocean array [8]. Following a lull in July, two periods of WWBs in August-September and October generated two additional Kelvin wave pulses, the first of which reached the eastern boundary in October. At this writing (November 1997), the Kelvin wave resulting from the October WWB is en route and is expected to arrive at the eastern boundary in approximately mid-December 1997.

OCEANIC EVOLUTION OF THE 1997 EL NIÑO IN NLOM

The evolution of the 1997 El Niño in NLOM is further examined through a sequence of SSH anomaly fields. Figure 3(a) shows the non-El Niño pattern early in the year (17 March 1997). High positive anomalies are found in the western equatorial Pacific, and relatively weak anomalies exist in the eastern half of the basin. The El Niño begins in April when a large Kelvin wave pulse propagates eastward along the equator. On 16 April 1997 (Fig. (3b)), the pulse is marked by the reds centered between approximately 110° and 135°W. By 13 May 1997 (Fig. 1(a)), the Kelvin wave pulse has reached the coast of South America where it generates coastally trapped Kelvin waves that propagate poleward (marked by ribbons of orange-red next to the Central and South American coasts). The SSH build-up caused by these coastally trapped Kelvin waves propagates westward away from the coast as Rossby waves; their speed is latitudinally dependent and decreases away from the equator. Figure 3(c) (27 May 1997) shows that the leading edge of the coastally trapped Kelvin waves have reached the Gulf of California, and the westward-propagating Rossby waves are the dark orange bands, which join near 0°, 105°W and flare poleward toward the east. Weaker equatorial Kelvin wave pulses follow the initial April pulse into July,

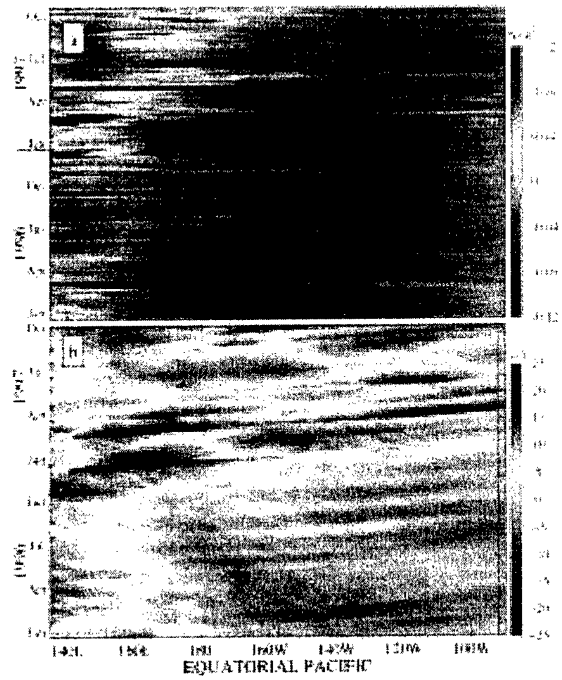

Fig. 2 — Longitude vs time across the entire equatorial Pacific Ocean at the equator for (a) zonal wind stress component (N/m²) from the FNMOC NOGAPS atmospheric model and (b) NLOM SSH anomalies (cm). Yellow to red values denote westerly winds in (a) and positive SSH anomalies in (b); blue indicates easterly and negative values, respectively. Kelvin wave propagation resulting from westerly wind bursts in (b) is seen as a band of yellow-red color slanting upward from left to right, representing a phase speed of approximately 2.5 m/s. The vertical line in (b) near 92°W is model land (the Galopagos Islands).

followed by a lull, but in September-October additional strong Kelvin wave pulses are generated. Figure 3(d) (24 October 1997) shows a large Kelvin wave pulse (centered at approximately 140°-160°W) that is propagating eastward across the Pacific. The ocean model is updated using new wind forcing in near real time and has been integrated to the end of October 1997 at this writing.

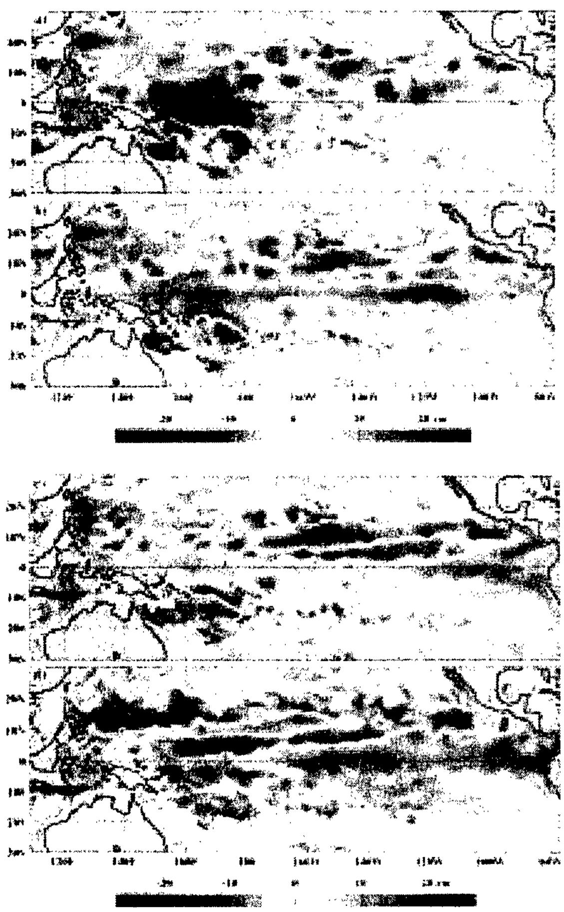

Fig. 3 — NLOM SSH anomaly for (a) 17 March 1997, (b) 16 April 1997, (c) 27 May 1997, and (d) 24 October 1997.

COASTAL EFFECTS OF EL NIÑO

While the SSH signal generated by El Niño is large in the equatorial latitudes, this phenomenon is not confined to the tropics in either the atmosphere or the ocean. As seen in Fig. 3, the coastally trapped, poleward propagating Kelvin waves carry the oceanic signal away from the equator. The waves can propagate to mid- and polar latitudes, and the Kelvin wave signal can be seen as far away as the northwest corner of the Pacific Ocean. This can be demonstrated by comparing NLOM-generated coastal sea level with observational tide gauge data obtained from the Integrated Global Ocean Services System (IGOSS) Sea Level Program at the University of Hawaii. Here, a 1/16° global hydrodynamic model with realistic bottom topography is used. This is the highest horizontal resolution global ocean model run to date and was computed as part of a FY97 DoD High Performance Computing (HPC) Grand Challenge project. The model was forced over the 1979-1993 time frame by 6-hourly European Centre for Medium-range Weather Forecasts (ECMWF) 1000-mb reanalysis winds and extended through 1996 by archived operational ECMWF 1000-mb winds. Because a static atmospheric model and data assimilation formulation were used, the reanalysis winds are devoid of errors or biases generated from operational changes in the model/assimilation system and thus provide a more consistent set of atmospheric forcing through time. Additionally, the longer time series of winds allows us to look at El Niño events before the 1990s.

Figure 4 shows sea level vs time for three stations: Santa Cruz (Ecuador, in the Galopagos Islands on the equator), Prince Rupert (Canada), and Petropovlovsk (Russia, on the Kamchatka Peninsula in the northwest part of the Pacific). The demeaned data have been filtered with a 12-month running mean to highlight interannual variability. At Santa Cruz (Fig. 4 (a)), three prominent El Niño peaks are seen (1982/83, 1986/87, and 1991/92). The global model reproduces the correct phase (correlation coefficient, $r = 0.97$), but the overall amplitude is slightly weaker than observed. The Kelvin waves propagate counterclockwise around the North Pacific. Thus, moving up the North American coast, the same three El Niño–induced sea level peaks can be seen a few months later at Prince Rupert (Fig 4(b)). The overall amplitude of both the observed and model sea level is weaker than that at Santa Cruz, but the El Niño signal still contributes greatly to the interannual variability at this station. Finally, at Petropovlovsk (Fig. 4(c)), the El Niño signature, while further attenuated, remains evident in both sea level curves. Thus the coastally trapped Kelvin wave signal is seen in the interannual sea level variability far from the tropical latitudes where it was generated.

INTERIOR BASIN EFFECTS OF EL NIÑO

Additional to coastal effects, versions of NLOM have been used in conjunction with satellite

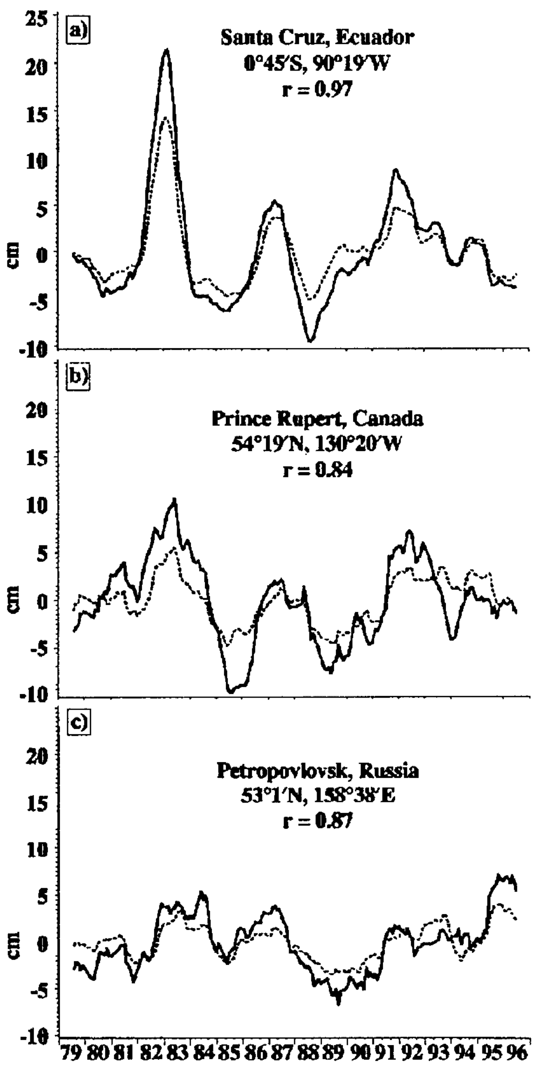

Fig. 4 — Sea level (in cm) vs time from observational IGOSS data (solid) and NLOM (dashed) for (a) Santa Cruz, (b) Prince Rupert, and (c) Petropovlovsk. A 12-month running mean filter has been applied to the time series to highlight interannual variability. The correlation coefficients (r) are 0.97, 0.84, and 0.87, respectively.

altimetry and SST data to discover decadal-scale, trans-Pacific effects of El Niño [9]. Observational satellite data pointed to a rerouting of a portion of the Kuroshio Extension (the Pacific Ocean's counterpart to the Gulf Stream in the Atlantic) to a more northern pathway in the early 1990s. A decadal NLOM simulation was used to link this with the 1982/83 El Niño.

The scenario developed as follows. The 1982/83 El Niño began as outlined above: relaxation of the equatorial trade winds, westerly wind bursts, generation of equatorial Kelvin waves that reached the west coast of South America spawning poleward, coastally trapped Kelvin waves, and their subsequent westward propagation as Rossby waves [10]. The Rossby waves were not expected to travel an appreciable distance into the basin as coherent structures because it was assumed they would be dissipated by mesoscale oceanic eddies. However, both model and observations indicated that the Rossby waves remained intact well over a decade later. The trans-Pacifics propagating Rossby waves then interacted with the Kuroshio Extension, shifting the latitude of the associated front and rerouting a portion of the flow north of its normal latitude. This led to significant increases in SST in the northern latitudes of the North Pacific that were similar in amplitude and spatial extent to those seen in the tropics during major El Niño events. These changes may have influenced weather patterns over the North American continent during the past decade and demonstrate that the oceanic effects of El Niño events can be extremely long-lived.

DATA ASSIMILATIVE VERSION OF NLOM

The wind-forced 1/4° global version of NLOM described above is part of the first generation in a progression of planned ocean nowcast/forecast systems to be delivered for naval operations. This model assimilates satellite altimeter data [11] and is currently running in real time at FNMOC with assimilation of real-time altimetry from T/P, ERS-2 (and eventually the Navy's new Geosat Follow-On mission) obtained from the Altimetry Data Fusion Center at the Naval Oceanographic Office. Future versions will be eddy-resolving (1/8° or higher, with embedded higher resolution basin-scale models), which will allow depiction of meandering currents and oceanic fronts and eddies [6]. The systems will also include assimilation of infrared frontal analyses from multichannel sea surface temperature data.

As demonstrated above, the wind-forced version of NLOM is capable of simulating the oceanic El Niño response when given accurate atmospheric forcing. In fact, this is a first-order requirement for any ocean model assimilating altimeter data. The model and the assimilation must work in tandem to produce an improved representation of reality. Assimilation of data into a numerical ocean model is not an effective way to compensate for inaccurate ocean model dynamics. Rather, the assimilation will be more useful in adding the capability to track nondeterministic variability and for correcting errors brought into the system by atmospheric forcing.

Figure 5(a) shows the SSH anomaly from the data assimilative version of NLOM for 24 October 1997, which can be compared to Fig. 3(d), from the wind-forced version. Figure 5(b) shows the corresponding T/P SSH anomaly data used in the assimilation. The assimilation is clearly effective. The T/P data indicate another large Kelvin wave pulse (centered between 120°-165°W) propagating eastward along the equatorial waveguide. This signal has been enhanced in the assimilative version of NLOM, and increases in SSH anomalies are also seen near the South American coast.

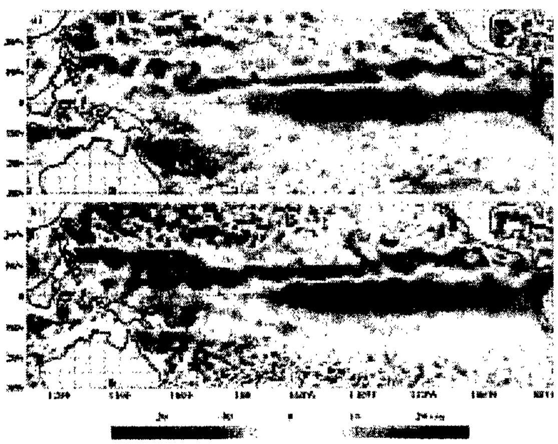

Fig. 5 — SSH anomaly for 24 October 1997 from (a) a version of NLOM that includes assimilation of (b) T/P altimetry.

The assimilation should have its most significant impact in regions where the SSH variability is nondeterministic due to mesoscale flow instabilities. A striking example is seen in the Gulf of Mexico where a large eddy shed from the Loop Current is seen in the T/P altimetry and the assimilative version of NLOM (Fig. 5, positive (red) anomaly in the central Gulf) but not in the nonassimilative version (Fig. 3(d)). In the Pacific region covered by Fig. 5, nondeterministic variability is prominent from approximately 10°-20°S in the central and eastern Pacific and in the region west of the Hawaiian Islands to the western boundary [7]. Again, the assimilative model compares more favorably with the assimilated T/P altimetry.

CONCLUSIONS

As described above, the oceanic response to the prescribed relaxation of the equatorial trade winds and westerly wind bursts during El Niño is primarily deterministic. Since it is such a large-scale event, even marginally eddy-resolving ocean models can reproduce it given accurate atmospheric forcing. However, the oceanic effects of El Niño are not limited to the equatorial latitudes. Its signal can be followed poleward along the west coasts of South and North America and beyond. Additionally, previous research has shown that planetary waves generated by El Niño events can remain coherent on decadal time scales and can affect ocean currents well into the interior of the basin.

The Navy is currently building a real-time ocean nowcast/forecast system in which El Niño and other oceanic phenomena can be monitored on a daily basis. A first-generation system, which was forced only by atmospheric wind data, has already been upgraded to include assimilation of satellite altimetry. Increases in computer power now present the opportunity for global and basin-scale models that are fully eddy-resolving and that will allow predictions of oceanic fronts and eddies and of major current systems like the Gulf Stream in the Atlantic and the Kuroshio in the Pacific. These ocean models will play a valuable role in the assimilation and synthesis of global satellite surface data. This new capability for accurate ocean nowcasting and forecasting will lead to Navy advances in application areas such as the following: antisubmarine warfare and surveillance; tactical planning; optimum ship track routing; search and rescue; high-resolution boundary conditions that are essential for even higher-resolution coastal models; inputs to ice, atmospheric and biophysical models and shipboard environmental products; environmental simulation and synthetic environments; observing system simulations; ocean research; pollution and tracer tracking; and inputs to water quality assessment.

ACKNOWLEDGMENTS

Numerical simulations were performed on Cray T3Es at the Army Corps of Engineers Waterways Experiment Station (CEWES), Vicksburg, Mississippi, and the Naval Oceanographic Office, Stennis Space Center, Mississippi. Both are part of the Department of Defense High Performance Computing (HPC) Modernization Program. This includes an FY97 DoD Challenge HPC grant on the CEWES Cray T3E for the first 1/16° global ocean model.

We thank Dr. Alan Wallcraft for his work on ocean model development for NLOM, including development of the first scalable, portable ocean model using a tiled data parallel programming style. As a result, the model runs efficiently and interchangeably on almost all DoD HPC systems. We also thank Dr. Charlie Barron and Mr. Kirk Whitmer for their work analyzing the near-real-time T/P altimeter data supplied by the Altimeter Data Fusion

Center (ADFC) at the Naval Oceanographic Office (NAVO), Stennis Space Center, MS. The real-time altimeter data capability was developed jointly by the NAVO/AFDC, the NASA Jet Propulsion Laboratory, the NOAA Laboratory for Satellite Altimetry, and Delft University.

[Sponsored by ONR and SPAWAR]

REFERENCES

1. H.E. Hurlburt and J.D. Thompson, "A Numerical Study of Loop Current Intrusions and Eddy-Shedding," *J. Phys. Oceanogr.* **10**, 1611-1651 (1980).

2. A.J. Wallcraft, "The Navy Layered Ocean Model Users Guide," NOARL Rep. 35, Naval Oceanographic and Atmospheric Research Laboratory, Stennis Space Center, Miss., Dec. 1991.

3. D.S. Luther, D.E. Harrison, and R.A. Knox, "Zonal Winds in the Central Equatorial Pacific and El Niño," *Sci.* **222**, 327-330 (1983).

4. M.H. McPhaden, P. Freitag, S.P. Hayes, B.C. Taft, Z. Chen, and K. Wyrtki, "The Response of the Equatorial Pacific Ocean to a Westerly Wind Burst in May 1986," *J. Geophys. Res.* **93**, 10589-10603 (1988).

5. J.C. Kindle and P.A. Phoebus, "The Ocean Response to Operational Westerly Wind Bursts During the 1991-1992 El Niño," *J. Geophys. Res.* **100**, 4893-4920 (1995).

6. H.E. Hurlburt, A.J. Wallcraft, W.J. Schmitz, Jr., P.J. Hogan, and E.J. Metzger, "Dynamics of the Kuroshio/Oyashio Current System Using Eddy-resolving Models of the North Pacific Ocean," *J. Geophys. Res.* **101**, 941-976 (1996).

7. E.J. Metzger, R.C. Rhodes, D.S. Ko, and H.E. Hurlburt, "Validation Test Report for OCEANS 1.0," NRL/FR/7323--97-9673, submitted 1997.

8. M.J. McPhaden, "The Tropical Atmosphere Ocean (TAO) Array Is Completed," *Bull. Amer. Meteor. Soc.* **76**, 739-741 (1995).

9. G.A. Jacobs, H.E. Hurlburt, J.C. Kindle, E.J. Metzger, J.L. Mitchell, W.J. Teague, and A.J. Wallcraft, "Decadal-scale Trans-Pacific Propagation and Warming Effects of an El Niño Anomaly," *Nature* **370**, 360-363 (1994).

10. R. Lukas, S.P. Hayes, and K. Wyrtki, "Equatorial Sea Level Response During the 1982-83 El Niño," *J. Geophys. Res.*, **89**, 10425-10430 (1984).

11. M.R. Carnes, D.N. Fox, R.C. Rhodes, and O.M. Smedstad, "Data Assimilation in a North Pacific Ocean Monitoring and Prediction System," in *Modern Approaches to Data Assimilation in Ocean Modeling*, P. Malanotte-Rizzoli, ed. (Elsevier Science Publishing Company, New York, 1996), Vol. 61, pp. 319-345.

THE AUTHORS

E. JOSEPH METZGER received a B.A. degree in physical geography from the Ohio State University in 1982 and an M.S. degree in meteorology from the University of Wisconsin-Madison in 1984. Before coming to NRL-SSC (then NORDA) in 1986, he worked with automated weather station data from both coastal and moored buoy sites maintained by the National Data Buoy Center. At NRL, he has worked as part of the Large-Scale Modeling group on both global and basin-scale ocean models. Recent research includes a journal article on the coupled dynamics of the Pacific Ocean and the South China Sea, and future work will focus on the Kuroshio penetration and eddy-shedding into this semienclosed sea. Mr. Metzger has also been actively involved in transitioning the research version of the NRL Layered Ocean model to NRL's Data Assimilation and Rapid Transition group. He is a member of the American Geophysical Union.

HARLEY E. HURLBURT received a B.S. degree in physics from Union College, Schenectady, N.Y., in 1965 and M.S. and Ph.D. degrees in meteorology from Florida State University, Tallahassee, in 1971 and 1974. Prior to graduate school, he served as a Weather Officer in the U.S. Air Force (1965–69). He was a postdoctoral fellow in the Advanced Studies Program at the National Center for Atmospheric Research in Boulder, Colorado, during 1974/75. Since then, he has done ocean modeling for the U.S. Navy, first as a contractor at JAYCOR for NRL in Washington, D.C., and for NRL-SSC (then NORDA) since 1977. He received a Meritorious Civilian Service Award in 1991. In addition, he is an Adjunct Faculty Member at Florida State University and the University of Southern Mississippi. His primary research interests are ocean modeling and prediction, especially the investigation of ocean dynamics using eddy-resolving global and basin-scale ocean models. His research has led to more than 80 publications, and he is listed in *Who's Who in America*.

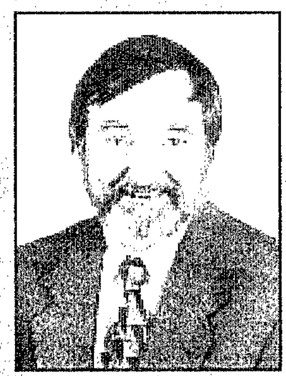

JOHN C. KINDLE received a B.S. degree in physics from the University of Dayton in 1969, an M.S. degree in physical oceanography from New York University in 1971, and a Ph.D. degree in physical oceanography from the Florida State University in 1979. After postgraduate work in the Computer Sciences Department at Yale University, he joined NRL-SSC (then NORDA) in 1981. His research interests include numerical modeling, tropical dynamics, coastal upwelling regimes, coupled biological-physical processes, the development of real-time ocean prediction models, and the evaluation of surface flux fields derived from atmospheric models.

ROBERT C. RHODES received a B.S. degree in atmospheric science from The State University of New York at Albany in 1982 and an M.S. degree in meteorology from Texas A&M University in 1984. He is now head of the Ocean Monitoring and Prediction System Section in the Ocean Dynamics and Prediction Branch at NRL. He joined the Oceanography Division at NRL-SSC (then NORDA) in 1985 where he conducted research studying global circulation using the NRL Layered Ocean Model (NLOM). In 1988, he began working with Harvard University on validation of a first-generation Gulf Stream forecast system that was transitioned to the Naval Oceanographic Office (NAVO). Mr. Rhodes accepted a position at NAVO in 1989, where he helped transition an upgrade to the Gulf Stream system and developed a thermal analysis system for the Mediterranean Sea based on the OTIS 3.0 system from FNMOC. Mr. Rhodes returned to NRL in 1991 and has worked on the development of ocean nowcast/forecast systems from the global to the tactical scales. He worked as leader of the Data Assimilation and Rapid Transition group, which developed a system for the North Pacific Basin that led to a book chapter which won an Alan Berman Publication award in 1996. Currently, Mr. Rhodes is concentrating on the transition of 1/4° global version of NLOM to FNMOC which includes altimetry data assimilation. He is a member of the American Geophysical Union.

GREGG A. JACOBS received his B.S. degree at the University of Colorado in Boulder in aerospace engineering in 1986. After receiving an M.S. degree in physical oceanography at Oregon State University, Corvallis, in 1988, he applied the Navy's Geosat altimeter satellite data set to observing Rossby waves in the Pacific Ocean. He received his Ph.D. degree in 1991 from the University of Colorado, Boulder, in aerospace engineering. After a 2-year postdoctoral position with NRL starting in 1991, Dr. Jacobs continued his work with NRL as a full-time employee.Continuing to understand ocean dynamics and develop methods for monitoring ocean processes through remote sensing, Dr. Jacobs is presently working to expand capabilities into the littoral zone through combining numerical models with a range of measurement systems.

JAY F. SHRIVER received a B.S. degree in meteorology and mathematics from the State University of New York College at Brockport in 1987 and M.S. and Ph.D. degrees in meteorology from the Florida State University in 1989 and 1993, respectively. He was a National Society for Engineering Education postdoctoral fellow at NRL from 1993–95. Since 1995 he has been an oceanographer in the Ocean Dynamics and Prediction Branch at NRL. He has published in the areas of El Niño, decadal variability, and global and basin-scale ocean circulation. His current research interests include the global thermohaline circulation, low latitude western boundary currents, and nonlinear ocean dynamics.

OLE MARTIN SMEDSTAD received a B.A. degree in applied mathematics in 1981 and an M.S. degree in physical oceanography in 1983 from the University of Oslo, Norway. He received a Ph.D. degree in geophysical fluid dynamics from the Florida State University in 1989. Since 1989, Dr. Smedstad has been employed as a contractor for NRL at the Stennis Space Center and is presently employed by Planning Systems, Inc. He has published more than 20 papers in the area of open boundary conditions in numerical models, ice modeling, and data assimilation in ocean models. His experience with data assimilation methods ranges from simple techniques such as optimal interpolation/nudging to advanced methods such as variational (adjoint) assimilation techniques.

Exploring an Active, Methane-hydrate-infested Mud Volcano on the Ocean Floor

P. R. Vogt
Marine Geosciences Division

Although methane gas is rare in the Earth's oxidizing atmosphere, large amounts (ca. 10,000 Gt carbon) are entombed in icelike hydrates in subseafloor sediments below the continental margins. The distribution, physical properties, and stability of these hydrates and the free gas/dissolved-methane containing porewaters below the hydrate-cemented layer (which is typically several hundred meters thick) are of more than academic interest. Methane is a clean-burning fuel and a potent greenhouse gas; as hydrate or free gas, it dramatically alters sediment acoustic properties. Hydrates can clog gas pipelines and, if dissociating, destabilize man-made seafloor structures and trigger massive submarine landslides. Although most of the hydrate-cemented sediments can be studied only in boreholes or by seismoacoustic waves transmitted and received in the ocean, methane gas seeps or mud volcanoes locally bring concentrated gas and fluids up to the seafloor and into the water column. At such active vents, methane hydrate can be found exposed or within a meter of the seafloor. Although fizzing away under normal atmospheric pressures and temperatures, hydrate is widely stable under the high pressures and low temperatures at the ocean bottom and up to 1000 m below. A 1989 NRL-led cruise to the Norwegian Sea used an 11 kHz sidescan sonar to image a 1-km-diameter circular feature which, upon closer investigation in subsequent cruises in 1995 and 1996, materialized as an active, warm mud volcano with an "icing" of seafloor hydrates and white bacteria mats. The round, cookie-shaped feature wafts anomalously warm water rich in dissolved methane into the overlying ocean. Small tubeworms with methane-consuming bacteria in their intestines populate this chemosynthetic oasis, which is also home to numerous bottom fish (eelpout) and almost 20 new species of tiny, benthic organisms. Besides CH_4, H_2S and NH_4 are also present as chemosynthetic energy sources. The mud volcano is an unexcelled natural laboratory in which to investigate the processes involved in the formation, transport, and consumption/dissociation of methane and methane hydrate in the marine environment. C,O,H, and S isotope abundances were found to be valuable measures for these processes.

INTRODUCTION: IMAGE AND DISCOVERY

There may be "nothing new under the sun," but in the sunless depths of the ocean floor, there is always something new. I describe the Haakon Mosby mud volcano, first imaged as a sidescan sonar object by NRL in 1989 [1] and later revealed as a hydrate-covered, methane-spewing sediment volcano after an NRL-led U.S./Norwegian expedition in 1995 and a 1996 U.S./Russian/Norwegian expedition examined it [2] (Figs. 1-5). Sediment volcanism is like regular volcanism except that watery and/or gassy mud is erupted instead of hot, molten rock. Sediment (or mud) volcanoes are usually much smaller than regular volcanoes but are similarly driven by gravity; low-density materials at depth squeeze their way through higher density materials to the surface.

The fact that this 1-km-diameter feature was not discovered until 1989 illustrates the glacial pace of high-resolution seafloor imaging (comparable in resolution to NRL's 1994 *Clementine* satellite video imaging of the Moon). An exhaustive, largely NRL-authored synthesis volume, *The Nordic Seas* [3], contained no mention of this mud volcano nor other features unknown when the

volume was published in 1986. Even today, *Clementine*-scale (100 m) spatial resolution imagery such as was collected over the dry lunar "seas" (marea) is available from less than 10% of the Nordic Seas and the rest of the world's oceans. Higher-resolution (1-10 m; Fig. 2(c)) images cover less than 1% of the ocean floor [4]. The discovery of the mud volcano was as much serendipity as science since no one predicted its existence.

The Haakon Mosby mud volcano is located in the North Atlantic, northwest of Norway (Figs. 1,2(a)), in water depths of about 1,250 m. The acoustic imaging that detected the volcano was performed on a U.S.-Norwegian, NRL-led expedition using the Hawaii Institute of Geophysics SeaMARC II 11 kHz sidescan sonar and swath-bathymetric system towed behind the University of Bergen's (Norway) vessel F/S *Haakon Mosby*. (The mud volcano and the research vessel are named for the famous Norwegian oceanographer, Prof. Haakon Mosby.)

Unless priorities change, a complete North Atlantic-wide acoustic image of 100-m resolution still lies decades in the future. By comparison, *Clementine* imaged the North-Atlantic-area Moon in just 8 weeks! Imaging all the world's ocean floors, equal in area to two Mars-sized planets plus two Moons, would require several hundred ship-years of effort [4] and perhaps should be done with unmanned, remote-controlled robot vehicles.

Naval applications of an "acoustic *Clementine*" mission include characterization of seafloor geotechnical properties (especially the propensity for failure), and active-sonar clutter, background for lost-asset searches, and, at shallower depths, navigation hazards.

Ocean floor scientists bemoan those laws of physics which, through scattering and absorption, make it impossible to image any but the shallowest seabottoms using electromagnetic waves, as has now been done for various terrestrial planets and moons. But the deep ocean floors can at least be made "visible," from the sea surface, to soundwaves of frequencies up to 15-20 kHz. Such waves travel 200,000 times slower than light, as the ship that emits and receives them wallows above the ocean floor at mere meters per second, vs kilometers per second for many planetary orbiters. Ocean-floor geoscientists can only envy their extraterrestrial colleagues, but there are compensations for students of the ocean floor. After the Haakon Mosby mud volcano was imaged as a backscatter feature (Fig. 2(b)), later expeditions could be sent to examine it up close with deep tow sidescan sonar (Fig. 2(c)), photography (Fig.3), and sampling (Fig. 5). Such ground-truthing expeditions are orders of magnitude cheaper than comparable extraterrestrial probes. Also, no extraterrestrial body has been found that rivals Earth, even the seafloor, in the presence and diversity of life and the complexity of physical/chemical/biological processes at work. Earth is the most relevant and, to many, the most interesting planet, whose seas are the medium of the U.S. Navy.

A systematic world-wide seafloor-imaging mission is increasingly overdue. Indeed, seafloor studies may help us design certain interplanetary missions. Chemosynthesis-based (CH_4 or H_2S oxidizing) ecosystems such as those found on the Haakon Mosby mud volcano (Fig.2(e)) may be the most likely analogs to other life in the solar system, possibly on the ice- and maybe ocean-covered Jovian moon, Europa. A long-term acoustic *Clementine*-like mission to map the ocean floors could possibly discover all the Haakon Mosby mud volcanoes and a myriad of similar and smaller sized features, many not even imagined today. Granted, to image is not necessarily to understand, but an acoustic *Clementine* mission would provide the scientific road map, navigating future researchers

Fig. 1 — Sites where gas, water, and/or mud is venting at the seafloor in the Atlantic region. H, hot water vents along the Mid-Atlantic Ridge; MV, mud volcanoes; P, pockmarks; D, mud diapirs. MOR, axis of the Mid-Oceanic Ridge, where new oceanic crust is being formed as plates diverge; COB, boundary between oceanic and continental crust. The Haakon Mosby mud volcano is within the box labelled "NRL study area."

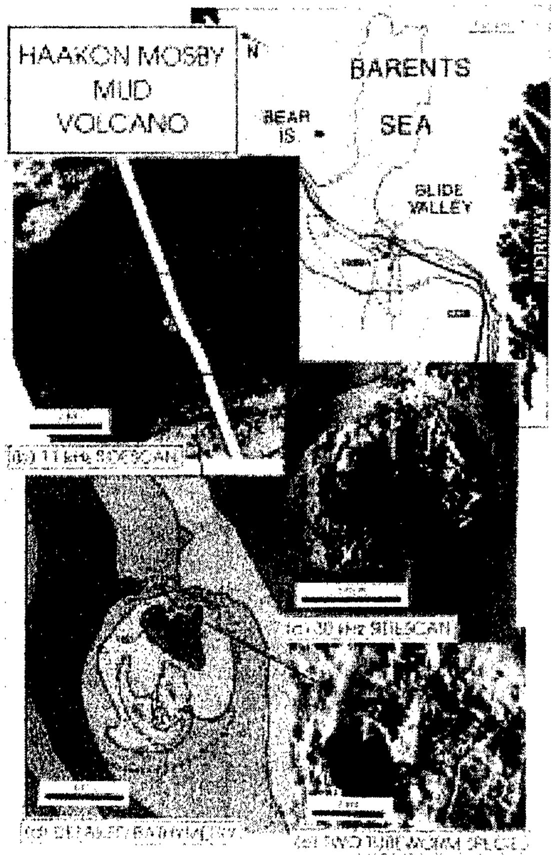

Fig. 2 — Haakon Mosby Mud volcano: (a), regional setting, with water depths in meters; (b) SeaMARC II 11 kHz sidescan sonar image of mud volcano, with warm colors denoting stronger acoustic backscatter; (c) deep-tow (40 m above seafloor) 30 kHz sidescan sonar image; (d) detailed bathymetry, with contours at 5-m depth intervals, and dots showing 1995 sample sites; (e) photograph of box core surface, showing Vermicelli-spaghetti-like tubeworms.

to whatever invites detailed imaging, sampling, seafloor/subseafloor experimentation, and, in the end, successful process modeling.

METHANE

If the Haakon Mosby mud volcano is about anything, it is about methane (CH_4). But to put the findings in perspective, a bit of background information is required. Before evolution invented photosynthesis as a way to liberate gaseous oxygen, methane (CH_4) was probably common in the Earth's ancient reducing atmosphere, roughly before 2 billion years ago. Although still abundant in the "gas giant" outer planets, methane has seemingly been banished from our oxygenated planet. Or has it? True, methane forms only two parts per million of our open atmosphere, and, as NRL researchers corroborated in the early 1970s, the oceans, in which methane is not very soluble, are highly undersaturated with this gas. But sample the air above a termite mound, a household sewer gas vent, or a wastewater treatment plant and you will find methane produced by bacterial degradation of organic matter. Methane pockets are highly explosive in our oxidizing atmosphere, as coal-mine disasters remind us.

Poking a stick into the bottom of a river or a freshwater pond will also release bubbles of CH_4 (also called "swamp gas"), while in brackish and salt waters, you may have to poke several meters because methane rising from deeper in the sediment column is oxidized by sulfate $(SO_4)^{-2}$ ions seeping into bottom sediments from ocean waters above. Due to the high acoustic impedance (density times sound speed) contrast between methane bubbles and surrounding water and sediment, even a few volume % bubbles scatter sound so effectively that the resulting acoustic wipeouts can hide buried mines and geologic structures across a wide range of frequencies.

Besides this biogenic methane, ocean floor sediments can also host thermogenic methane, for example, in the northern Gulf of Mexico, where organic matter has been buried (and heated and

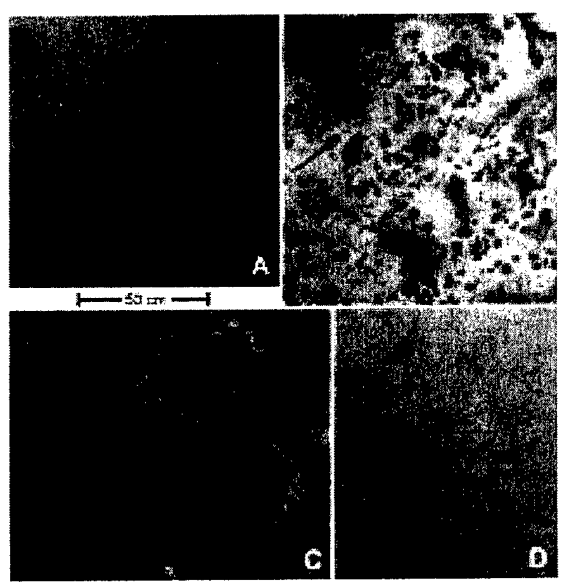

Fig. 3 — Seafloor photographs on the Haakon Mosby Mud Volcano: (a) furrowed seafloor with eelpout (Lycoides frigidus, a bottom-dwelling fish found in high latitudes) in volcano's center; (b) extensive but thin white areas (*Beggiatoa* bacterial mats and/or methane hydrate) and eelpout; (c) tubeworm patches, white to light-gray hydrates (or bacteria), gas ebullition pits (small holes), eelpout, and a skate; (d) nodules believed to be $CaCO_3$ precipitated at the seafloor.

pressurized) so deeply that methane and higher hydrocarbons are being "cooked" out of the deep mud. The origin of methane found at any particular site can be discovered by looking at its isotopic character (both C and H) and by its association with heavier hydrocarbons (such as ethane, propane, and butane). Thermogenic methane is associated with relatively more abundant heavy hydrocarbons and relatively more of the heavier isotope C^{13} (relative to C^{12}). Gas hydrate and dissolved methane squeezed from Haakon Mosby mud volcano sediments were found to be (isotopically speaking) in the borderline area between thermogenic and biogenic methane. However, hydrocarbons heavier than methane together constitute less than 1% of the gas. Our Russian colleagues learned that the methane at the volcano is partly produced directly by microbial action and partly by modest "cooking," probably not deeper than 1 or 2 km below the sea floor. Thus, our mud volcano is not like those under the Gulf of Mexico.

This agrees with another difference. In the Gulf, gas seeps and mud volcanoes are associated with the upward movement of deeply buried and gravitationally unstable salt. The Haakon Mosby mud volcano erupts from a 6-km-thick sediment pile without any salt layers at depth. We know this from oil industry seismic exploration.

Tubeworms growing like unkept lawns (Figs. 2(e), 3(c)) offer another example of how isotope ratios clarify biogeochemical processes on the mud volcano. Do the tubeworms live off planktonic debris that snows down from the upper ocean layers above? Or do the worms feed off the methane rising from below via symbiosis with special chemosynthetic bacteria in their intestines? The former case predicts tissue carbon distinctly heavier than the latter. We sent frozen sediment, including tubeworms, to colleagues at the University of North Carolina (UNC), who picked out and homogenized a number of the small worms. The UNC's mass spectrometer had the answer. The worms are living off the methane, not off photosynthesis. (NRL's Condensed Matter and Radiation Sciences Division has since assembled a trace-element accelerator mass spectrometer (TEAMS) to perform such radioisotope measurements.) Moscow colleagues participating in the 1996 cruise later measured the rates of bacterial methane oxidation inside tubeworm tissues—up to 2 mg of carbon per milligram protein per hour.

Bacteria and the two species of tubeworms living on the Haakon Mosby mud volcano are not the only creatures populating this small seafloor oasis that do not use photosynthesis but methane-based chemosynthesis as the base of their food chain. Taxonomists found almost 20 new species of meiofauna (sand-grain-sized animals from various families) in one sediment sample, while photographs revealed a bottom-fish density hundreds of times higher than expected on a normal seafloor. The fish, yet to be sampled and studied, seem to be dominated by a species of eelpout, measuring the length of a pen (Fig. 2). We suspect that the fish congregate opportunistically on the mud volcano, much as seagulls do at the local dump. However, we have clearly just scratched the surface in understanding this sunless ecosystem.

METHANE HYDRATE

Had the Haakon Mosby mud volcano been located, say, in the Chesapeake Bay, our chemists would have dealt with methane either in solution or as free gas—together with biochemistry and mineralogy, challenges enough! However, the mud volcano's water depth (1,250 m) and seafloor temperature (-0.5° C) place the seafloor and near subbottom squarely in the methane hydrate stability field. Methane hydrate is a type of gas hydrate that comprises methane molecules trapped inside the cagelike spaces formed in a lattice structure of water molecules [5]. The resulting icelike structure is stable at water depths below about 500 m under typical ocean temperatures and, at the higher pressures of the deep ocean (4,000 m), may be stable up to 20° C. Depending on local heat flow, such temperatures are reached only at depths of 500 m or more below the seafloor. As a result of organic matter burial under the vast submerged continental margins, enough methane has been generated to form a vast carbon reservoir of the order 10,000 Gt C [5] in the form of methane hydrates. This vast reservoir and the free methane gas locally trapped below the layer of hydrate-cemented sediment could become a major fossil fuel source. Hydrate dissociation may trigger submarine landslides and, since methane is a powerful greenhouse gas, become part of the climate change equation. Hydrates can clog deep-sea pipelines and, where dissociating, destabilize man-made seafloor structures such as drilling platforms.

Navy mid- to low-frequency acoustic propagation and reverberation models require knowledge of subbottom hydrates and free gas, both differing greatly from normal water-logged sediment in their acoustic properties.

Most of the vast hydrate reservoir can be reached only by deep drilling or explored by seismoacoustic prospecting. However, in a few

places, hydrate exists at or near the seafloor. One such place is the Haakon Mosby mud volcano. Although the feature was known to be located within the hydrate stability field, hydrate had not been expected because no evidence for it (no bottom simulating reflectors) was seen in surrounding seismic reflection lines. However, a 2-m-long sediment core raised from the mud volcano on the 1995 cruise contained small, booklike white crystals, typically 1 × 3 × 10 mm in size in the core catcher. The crystals fizzed and bubbled away. We had discovered methane hydrate!

Returning in 1996, we raised numerous cores containing up to 25% hydrate, some with hydrate at all levels in the 3-m-long cores (Fig. 5). The hydrates formed isolated crystals or radish-sized crystal aggregates. Hydrate abundance started from zero outside the mud volcano and increased toward the center. The sizes and abundance of the hydrates qualitatively explain the very high acoustic backscatter observed in the central part of the mud volcano (dark area, Fig. 2(c)). (However, in a small zone in the very center, hydrate was completely lacking.) The hydrate chunks were fished out of the bubbling mud and placed in containers so that the evolved gas could be analyzed later. We did not carry equipment onboard for recovering the hydrate at its ambient seafloor pressure and temperature.

Seafloor photography (Figs. 3(b,c)) revealed numerous patches of white material, locally covering 75% of the seabottom (Fig. 5). Is this material methane hydrate, exposed on the sea-floor? Or is it mats of the giant sulfur bacterium, *Beggiatoa*? We cannot be sure until we examine this white material and sample it by submersible. Seafloor hydrate poses interesting problems. Although stable, it is surrounded by methane-undersaturated seawater. How long can the hydrate exist there? How fast does the methane diffuse out of its "cages?"

A VERY WARM "COLD SEEP"

Localized gas, fluid, and/or mud vents are referred to by scientists as "cold seeps" to distinguish them from the "hot vents" (Fig. 1) where recirculated sea waters, heated in contact with hot rock at depth, blast out of the seafloor at temperatures up to 400° C. Hot vents generally occur scattered along the axis of the mid-oceanic ridge, where tectonic plates are pulling away from each other.

Should we call the Haakon Mosby mud volcano a "cold seep?" We think not. Our first thermal station (1995 cruise) was a pipe with thermistors on outriggers that measured a subbottom gradient of 0.314° C per meter on the north rim of the feature. While this may seem modest, it was (until then) the highest thermal gradient measured in the oceans away from active plate boundaries or other real volcanic sites. The normal subseafloor increase in temperature in that region is about 0.05° to 0.075° C per meter near the ocean floor.

Returning in 1996 on the Russian vessel, N/S *Professor Logachev*, we targeted the center of the mud volcano. Here the gradients were too high for the calibration range of our thermistors. However, by simply sticking thermometers into on-board sediment cores before they had equilibrated, we were able to show that gradients in the thermal eye in the center of the mud volcano exceeded 5° C and may reach 10° C per meter (Fig. 4). With such thermal gradients, the hydrate stability field could be only meters thick—so thin one could penetrate it with standard coring techniques. We had exceeded by an order of magnitude our own thermal gradient record of the previous summer! We had also achieved another first, by detecting a temperature anomaly in the water above the seafloor. The

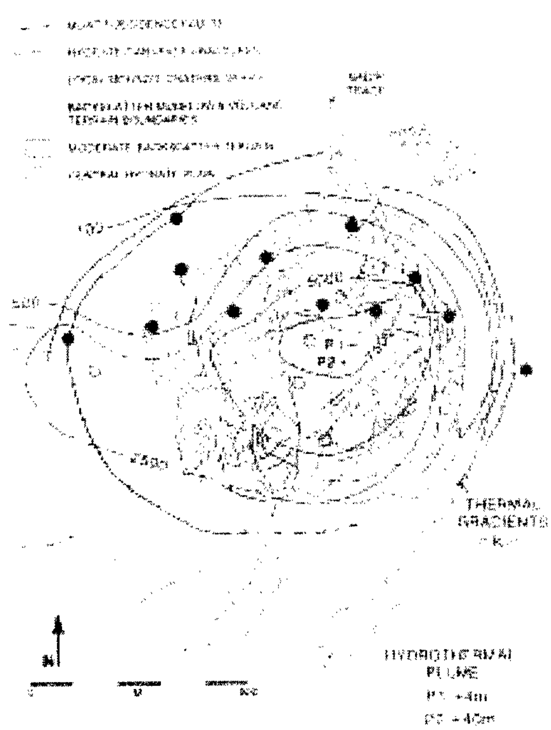

Fig. 4 — Subseafloor thermal gradient, in millidegrees per meter, in colors, superposed on interpretation of sidescan sonar image (Fig. 2(c)). Note that strong-backscatter central part of mud volcano generally is the warmest and also tends to have the most hydrate in the sediment cores (Fig. 5). Solid circles show thermoprobe data, and open circles are measurements on sediment cores.

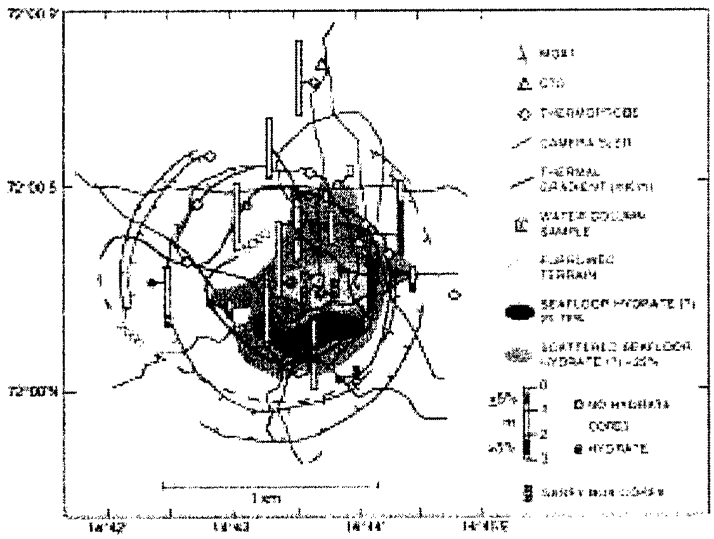

Fig. 5 — Seafloor provinces (from sidescan and photos) in relation to sediment cores, with % range of methane hydrate indicated along the length of the cores.

anomaly, although only +0.04° C, was well above the background at the measurement height (40 m above the center of the volcano), and demonstrated venting of warm water. This result agrees with the dissolved methane we found at water samples raised from 70 m and 90 m above the mud volcano's center. The concentrations of this gas (more than 24×10^{-3} ml/l H_2O at 70 m) far exceed levels typical for the open oceans.

What can account for the warmth at this "cold" seep? We do not yet have all the answers. However, seismic and other data rule out molten igneous rock (magma) within the 6-km-thick sediment column (Fig. 6). Warm fluids could be rising from far down in the oceanic crust. However, our methane carbon isotopes do not support "cooking" of organic matter at high temperatures. Helium isotope measurements from future samplings could prove or disprove a truly deep origin. Most likely, the mud volcano is driven by dewatering or methane-generating processes in the upper 3 km of the sediment pile. These upper sediments are known to have been deposited during the repeated glaciations of the last 2.5 million years, when Barents Sea ice sheets and the icebergs calved from them repeatedly dumped large amounts of sediment in this area. When marine sediments are rapidly deposited, compaction and dewatering are incomplete. Once pressurized under masses of younger mud, the low-density, watery mud or just pore water seeks to escape upward. From the normal regional geothermal gradient, water or mud rising from a 2-km depth within the glacial sediments would be 100° C hot if the rise speed is fast enough (say, meters a year or more) to overwhelm thermal equilibration with the cooler surrounding muds. At a 2-km depth and 100° C, organic matter would begin to "crack," thus explaining the borderline thermogenic carbon isotope character of the methane we sampled. The apparent continuity of seismic reflectors more than 2-3 km below the mud volcano (Fig. 6) is also consistent with a relatively shallow source depth. However, a narrow column of mud or fluid rising from greater depth could have escaped seismic detection.

We know that somewhere at depth, significant amounts of methane are being produced; otherwise we would have neither hydrates nor chemosynthesis nor porewaters rich in dissolved methane. Since glacial sediments tend to be poor in organic carbon, we suspect that interglacial sediments, perhaps deposited during times when the deep Greenland Sea became deficient in oxygen, are the likely sources of the carbon converted to methane. Although free methane gas need not exist at any depth, we see strong acoustic reflectors below the mud volcano (Fig. 6), and these may be caused by gas bubbles; also we photographed seafloor pits (Fig. 3(c)) that may be due to gas ebullition. However, we lack unambiguous photographic or acoustic evidence for free gas. As the methane-containing porewaters rise from below the hydrate stability zone, methane solubility falls with decreasing pressure. Solubility rises with decreasing temperature, but rapid upflow will keep the materials from cooling significantly. Therefore, in the lower part of the mud volcano's structure, methane becomes less and less soluble as the mud rises, and may at some point exsolve gas bubbles. This might explain some of the anomalous disturbed seismic reflections we see below the volcano

in Fig. 6. Once the rising materials enter the hydrate stability zone, three-phase equilibrium conditions pertain, and remarkably, gas solubility now decreases (very rapidly) with decreasing temperature. Thus, as the near-0° C temperatures at the seafloor are sensed within meters or tens of meters below the mud volcano, gas hydrate will precipitate directly from dissolved methane. Free gas is not needed. However, methane gas may be bubbling through the hydrate-infused mud from below. If the water molecules in the hydrate stability zone have all been "spoken for," free gas may reach the seafloor, reacting with the plentiful water there to form the seafloor hydrate we may have photographed in Fig. 3(b,c).

QUESTIONS POINT WAY TO FUTURE RESEARCH

Beginning with an acoustic backscatter image, NRL scientists and collaborators from various U.S., Norwegian, and Russian institutions have begun to understand a complex system called the Haakon Mosby mud volcano. This understanding has been achieved by a multidisciplinary team, drawing on sciences such as seismoacoustics, oceanography, biogeochemistry, isotope chemistry, physical chemistry,

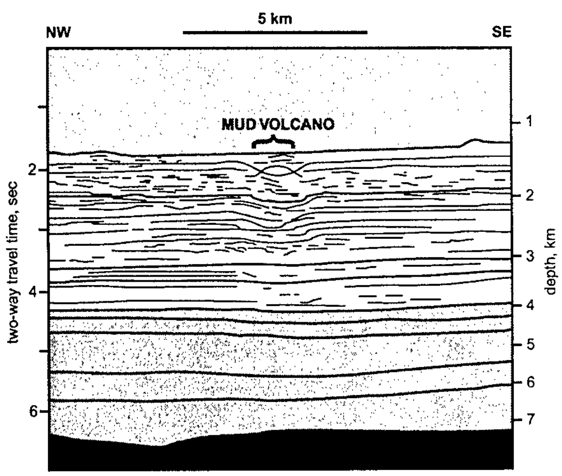

Fig. 6 — Multichannel seismic profile across the mud volcano, showing possible gas or hydrate horizons (strong local reflectors). Upper glacial sediments are yellow, and older, preglacial sediments are brown. Volcanic oceanic crust is black. Note that seismic reflecting horizons (lines) apparently continuous deep below the mud volcano seem "pulled down," perhaps an indication of gassy sediment, through which sound is known to travel more slowly, increasing the round-trip echo time from the research ship. Seismic reflectors appear disturbed only up to 2-3 km below the mud volcano, but a thin column of rising mud or fluid at greater depth might have escaped seismic detection.

sedimentology, geothermometry, and marine biology. As in other investigations of this sort, our learning begs more relevant questions. Some of the most obvious questions have not been answered. For example, is the "white stuff" we photographed methane hydrate or is it bacterial mats? We found hydrate in many cores, but what is the actual spatial distribution of the hydrate? Are the chunks we recovered pieces of broken conduits or broken layers or isolated nodules? Can we quantify and model the carbon and other chemical cycles and ecosystem functioning on the mud volcano surface? Why are there apparently no clam beds, which are common on other known methane seeps? Can we use the high-resolution NRL deep-towed acoustics geophysical system (DTAGS) to image the upper 500 m below the volcano's surface? What are the shape and fluxes of the hydrothermal and dissolved methane plumes we detected in the ocean above? Can we use these plumes as natural tracers to model deep water dynamics? From the deep-tow sidescan sonar image, we see that the mud volcano has belched out numerous mud flows, but over what time scale does this activity take place? How do dissolved methane and water flux vary over time? When, if ever, does the feature emit clouds or plumes of free methane bubbles? Given the mud volcano's location in a landslide valley (Fig. 1(a)), did the landslide's sudden depressurization coax the mud volcano into being, or did a preslide mud volcano cause the landslide? Can we model the formation of "steady-state" hydrate in contact with methane-undersaturated seawater? Can a deep-towed, dissolved-methane sensor system be developed to map out the plume in the water column? What does it take to turn on a mud volcano, and how/when does it expire?

And finally, how can we make use of our knowledge? Once we know the shapes and distribution of hydrate lumps vs depth, can we use acoustic models to reproduce the strong backscatter we observed in Fig. 2(c)? Is the distribution and character of hydrate in the mud volcano a useful representation of what we may expect at depth within the normal, nonventing hydrate stability zone? After high-resolution (100-m or better) imaging over more of the ocean floors, how many other mud volcanoes/gas seeps are sprinkled across the ocean floors? Could such vents some day be used as "gas stations" to refuel unmanned underwater vehicles? These questions give our team a metaphoric "road map" for future research. However, the best *literal* road map, rich in naval and other applications, would be an "acoustic

Clementine" backscatter image of all the world's ocean floors at 100-m spatial resolution or better. A matchless "resolution" to initiate the new millenium!

ACKNOWLEDGMENTS

This research was supported by the Office of Naval Research, Program Element 61153-N.

We thank the universities of Bergen and Oslo in Norway, VNIIOkeangeologiya in St. Petersburg, and the Shirshov, Microbiological, Vernadsky Institutes in Moscow, and the U.S. National Science Foundation for supporting this investigation. Professor Kathy Crane of Hunter College and NRL, Dr. Fred Bowles and Ms. Joan Gardner of NRL, Professor Eirik Sundvor of Bergen, Drs. Georgii Cherkashev, Gabriel Ginsburg, and Alexey Milkov of St. Petersburg, and Drs. Alla Lein and Nikolai Pimenov from Moscow are the scientists whose contributions helped make this article possible. I thank Dr. B. Hjelstuen for the original version of Fig. 6. From NRL, I thank Dr. David Nagel for sharing his ideas of using such vents as future seafloor "gas stations," Dr. Rick Coffin for review, Mr. H. Fleming and Dr. H. Eppert for leadership and encouragement, and Dr. E. Hartwig for platform support funds. Ms. I. Jewett provided help with the illustrations. Special thanks to Dr. T. Coffey who contributed funds for the 1996 cruise on the N/S *Professor Logachev*.

REFERENCES

1. K. Crane and A. Solheim, "Seafloor Atlas of the Northern Norwegian-Greenland Sea," Meddelelser No. 137, Norwegian Polar Institute, Oslo, 1995.

2. P.R. Vogt, G. Cherkashev, G. Ginsburg, G. Ivanov, A. Milkov, K. Crane, A. Lein, E. Sundvor, N. Pimenov, and A. Egorov, "Haakon Mosby Mud Volcano Provides Unusual Example of Venting," *EOS*, Trans. Am. Geophy. U., **78**, 549, 556-557 (1997).

3. B.G. Hurdle, Ed., *The Nordic Seas* (Springer, New York, 1986), p. 777.

4. P.R. Vogt and B.E. Tucholke, "Imaging the Ocean Floor: History and State of the Art," P.R.Vogt and B.E. Tucholke, eds., *The Geology of North America, Vol. M, The Western North Atlantic Region* (The Geological Society of America, Boulder, Colorado, 1986) pp. 19-44.

5. M.D. Max, R.E. Pellenbarg, and B.G. Hurdle, "Methane Hydrate, A Special Clathrate: Its Attributes and Potential," NRL Memorandum Report 6101, Feb. 1997.

THE AUTHOR

PETER R. VOGT received a B.S. degree With Honor in geophysics from the California Institute of Technology in 1961. After spending a year at the University of Innsbruck, Austria, on a Fulbright scholarship studying glaciology, he entered graduate school at the University of Wisconsin, where he received an M.A. degree (1965) and a Ph.D. degree (1967) in oceanography. Dr. Vogt began as a marine geophysicist at the Naval Oceanographic Office in 1967 and came to NRL in that capacity in 1976. His research in the 1970s and 80s focussed on oceanic magnetic anomalies, plate tectonics, seamounts, and the nature of mantle hotspots thought to be responsible for such features as Iceland and the Hawaiian island/seamount chain. Since 1989 he has focussed his research more on sidescan-sonar characterization of the seafloor and on the sediment dynamics responsible for many of the features discovered in the sonar imagery. Dr. Vogt has authored or coauthored more than 100 articles in the peer-reviewed literature. He is an associate editor and Fellow of the Geological Society of America and member of the American Geophysical Union. He has received two NRL Alan Berman Research Publication Awards.

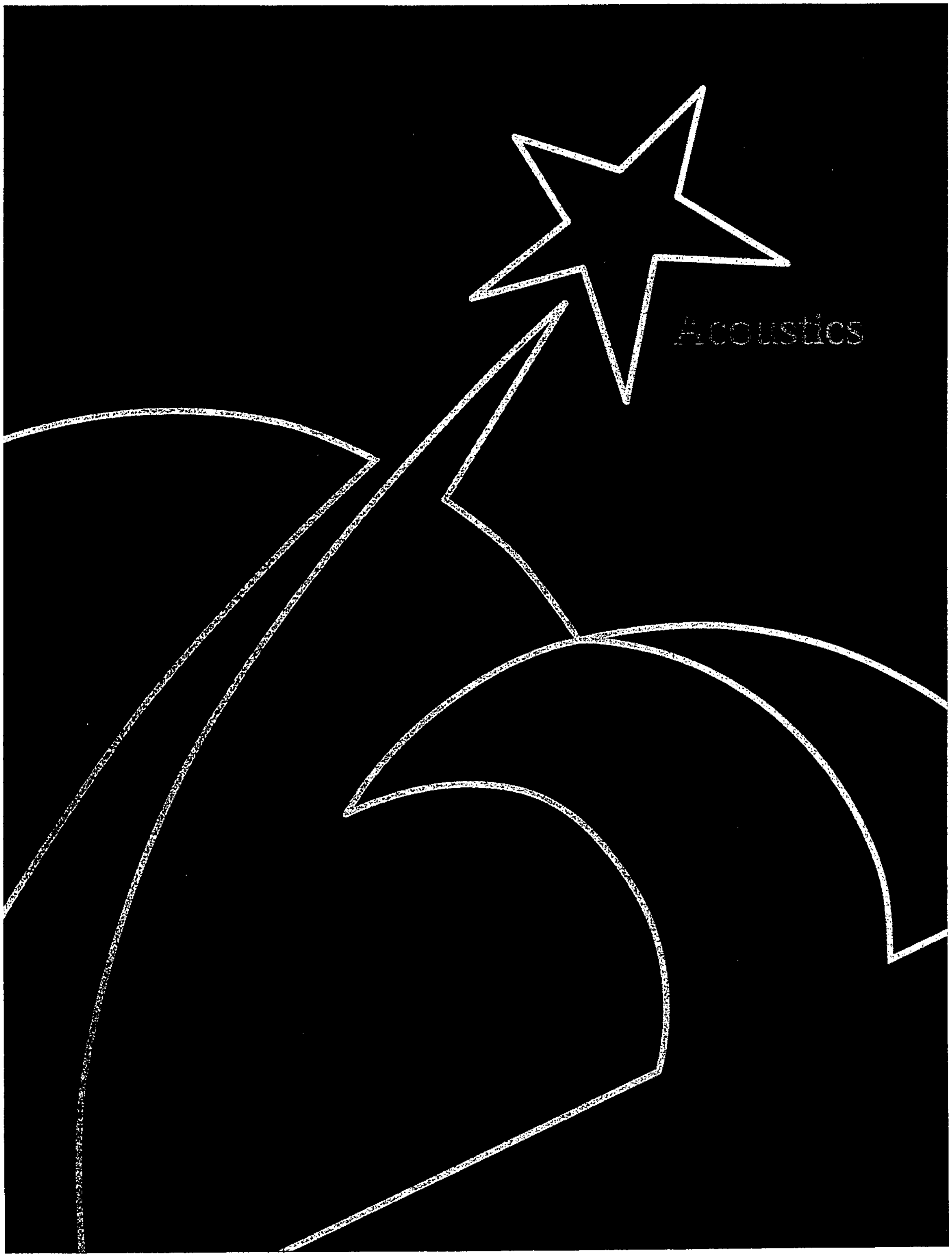
Acoustics

Structural Acoustic Techniques to Identify Underwater Mines

J.A. Bucaro and B.H. Houston
Acoustics Division

T.J. Yoder
SFA, Inc.

Introduction: The Naval Research Laboratory is using its world-renowned structural acoustics facilities (originally developed for scaled submarine programs) to study acoustic scattering from proud and buried underwater mines. The objective is to discover what information is contained in the broadband properties of the scattered signal that might be exploited for target identification purposes. Current acoustic mine-hunting systems form acoustic images that replicate the rough geometric shape of the target. To obtain sufficient resolution, these systems must operate at frequencies that are too high for anything but time-consuming, close-in looks at the target. Even then, they often confuse mines with minelike targets such as oil drums.

In contrast, structural acoustic clues such as mine casing resonances, elastic wave propagation, and internal structure scattering are available at lower frequencies, allowing for much longer ranges of operation as well as the construction of unique "fingerprints" by which to identify the target as a mine. Additionally, at lower frequencies the ocean sediment is more readily penetrated by acoustic waves, creating the possibility for buried mine detection.

Structural Acoustics: The structural acoustic approach to target identification differs fundamentally from the various acoustic imaging techniques currently used in mine-hunting operations. Traditional acoustic imaging, such as optical imaging, uses a two-step process to form an image for identifying a target as a mine: (1) the incident energy is diffracted by the target in a manner determined by the detailed target shape and associated reflectivity; and (2) the diffracted energy is focused by a lens or an array to form the final image. Image resolution—the ability to resolve the object's spatial detail—is proportional to the product of the illuminating frequency and the size of the lens or array. Traditional mine-imaging systems use high frequencies (with wavelengths much shorter than the desired spatial resolution) and focusing elements as large as is practical in order to "see" the geometrical detail. The necessity of using high frequencies (which are highly attenuated) and large focusing elements (whose length grows linearly with range) limits high-resolution imaging systems to very short ranges.

In contrast, the structural acoustic approach uses low frequencies (with long wavelengths) to excite an internal response from the target. This idea is best understood from the following example. Consider two soda cans, one full and one empty. It is easy to tell the full can from the empty one by simply tapping the cans and listening to the responses. A normal image is, however, useless since it is impossible to tell the difference by looking at them. Likewise, the unique internal structure of a mine produces an acoustic fingerprint that can be used to distinguish it from a myriad of false targets such as oil drums, rocks, and pier pilings, all of which produce acoustic images similar to the mine. While close-in, high-resolution images can often be used to separate these targets, it is impossible to differentiate them via acoustic imaging at moderate ranges, say tens of meters. Figure 1 is considered to be a state-of-the-art computer-enhanced acoustic image of two different minelike targets at a range of approximately 50 meters. It is clear from this figure that acoustic images of a mine and, for example, an oil drum would be indistinguishable at this range. This ambiguity causes mine clearing operations to be halted for time-consuming and potentially risky close-in looks at every object whether false target or live mine.

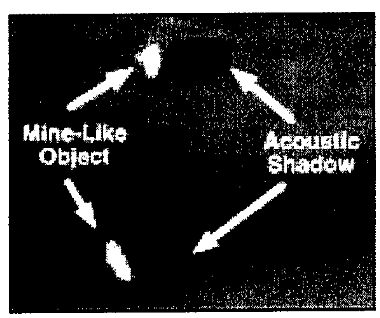

Fig. 1 — Enhanced acoustic image of minelike targets located at a range of approximately 50 m.

The structural acoustic approach includes potential advantages beyond merely lowering the false alarm rate at moderate ranges. Because the structural acoustic approach uses low frequencies, the transmitted and scattered sound is not highly attenuated. This opens the possibility of long-range

identification and detection at hundreds or even thousands of meters. Still another advantage is the ability to detect and identify completely buried mines. This becomes possible because low-frequency acoustic waves more readily penetrate the sediment, exposing the buried mine. As an added bonus, some of the structural acoustic fingerprints become enhanced when a mine is buried. Contrasted to this, high frequency waves used in acoustic imaging are so highly attenuated by the sediment that they are almost useless for detecting, let alone imaging, buried mines.

Mine Identification via Structural Acoustics: Mine identification via structural acoustic clues requires separation of echoes based on the internal response of the target. By using sophisticated computer processes that automatically identify targets, this identification can be as effective as the auditory process used to distinguish full soda cans from empty ones. We present one simple example of a structural acoustic identification algorithm that differentiates a water-filled oil drum sitting on a sandy bottom from a group of minelike targets with complicated internal structures that are either on or half-buried in the sand.

High-fidelity experimental data containing various source/target/receiver configurations were collected in the Porous Media Facility at NRL's Physical Acoustics Branch's Laboratory for Structural Acoustics. Figure 2 displays a typical acoustic fingerprint constructed with data from an oil drum and a minelike target. The acoustic fingerprints display the acoustic color or frequency content as a function of arrival time for an echo. The fingerprint from the minelike target has a large low-frequency highlight caused by the complicated internal structure of the target. This highlight is absent from the oil drum fingerprint because the internal structure is different. The existence of the internal structure highlight is used in a simple algorithm to automatically differentiate between the minelike targets and the oil drum. Specifically, the ratio of the acoustic color at two frequencies is plotted as a function of target angle for a group of minelike targets and the oil drum in Fig. 2. The simple threshold value displayed in the figure clearly separates these two groups of targets and demonstrates structural acoustic identification of minelike targets in the presence of what is considered to be a difficult false target.

Conclusions: The payoff from a structural acoustic approach to mine countermeasures is associated with the long-range identification potential against both proud and buried mines. The new ability to detect and identify buried mines can reduce serious risk to the Fleet. In addition, long-range identification would greatly increase the speed of mine clearing operations and reduce risk to assets by eliminating close-range operations currently used to identify a target.

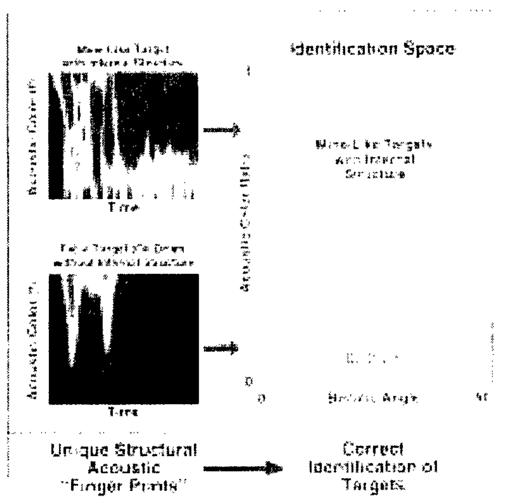

Fig. 2 — The structural acoustic "fingerprints" are time-frequency realizations of target echoes. Visual inspection of the acoustic fingerprints clearly shows differences between a complicated minelike target with internal structure and an oil drum. A simple identification algorithm compares the acoustic color of the echoes and produces a clear separation of the oil drum from five different minelike targets for multiple bistatic scattering angles.

Acknowledgment: The authors thank the Naval Surface Warfare Center Coastal System Station, Dahlgren Division, Panama City, FL, for the image data in Fig. 1.
[Sponsored by ONR]

Bioacoustic Absorption Spectroscopy

O.I. Diachok
Acoustics Division

Overview: The loss of acoustic energy (i.e., transmission loss) at tactical sonar frequencies (0.5 to 5.0 kHz) as it propagates in shallow water is controlled primarily by the oceanic sound speed profile, the reflectivity of the ocean bottom, and absorptivity caused by pelagic fish (i.e., those that are generally restricted to the continental shelf regions) with swim bladders, such as sardines and anchovies. Isolation of these effects requires long-term measurements with a fixed broadband source and a fixed receiver. The broadband source permits measurement of the frequency and magnitude of absorption lines associated with swim bladder resonance, which change when they descend and form schools at sunrise and when they ascend and disperse at sunset. Fixing the source and receiver eliminates temporal change in the loss of acoustic energy from bottom reflectivity and minimizes temporal change in the loss of acoustic energy from spatial variability in sound speed structure associated with mesoscale fronts and eddies. While detailed to NATO's Saclant Undersea Research Centre in 1995, I conducted Modal Lion, a multidisciplinary experiment designed to isolate absorptivity due to fish from other effects on long-range (12-km) propagation at a relatively shallow (83-m) site in the Gulf of Lion. The resultant measurements demonstrated that the frequencies and magnitudes of absorption lines, which were attributed to adult 16.5-cm-long and 7-month-old 7.0-cm-long sardines, vary with changes in the average depth and spacing between sardines, which occur at sunrise and sunset. Fish choose neighbors of similar size with which to form schools. In this experiment, absorption lines attributed to dispersed 16.5- and 7.0-cm-long sardines, and the 16.5-cm-long sardines in schools were evident. The magnitudes of absorption losses were 18 dB at 1.3 kHz at night when about half of the sardines are dispersed near the surface, 15 dB at 1.7 kHz during the day when virtually all sardines are in tightly formed schools near the bottom, and 35 dB at 2.7 kHz at dawn when sardines are dispersed near the bottom, before school formation.

Experimental Results: The experiment was conducted with a fixed parametric source that was deployed from the NATO research vessel (RV) *Alliance*, which was four-point moored. Signals were received on a bottom-moored vertical line array and telemetered to the ship from a range of 12 km. The vertical array consisted of hydrophones that spanned most of the water column. A thermistor string near the vertical array and conductivity and temperature vs depth (CTD) measurements made at the ship provided mean sound speed profiles for sound propagation models, and information on sound speed variability due to internal waves. Measurements were made by transmitting 2-s-long continuous wave signals at 0.6, 0.7, 0.8, 0.9, 1.0, 1.2, 1.4, 1.6, 1.8, 2.0, 2.2, 2.4, 2.7, 3.0, 3.4, 3.8, 4.2, 4.6 and 5.0 kHz every 15 s (as in a hearing test). Each sequence of transmissions (from 0.6 to 5 kHz) lasted 5 min. This sequence of signals was transmitted continuously for 7 h. Each 7-h measurement period was centered around sunrise and sunset. Figure 3 is an example of the resultant transmission loss data recorded on near-surface and near-bottom hydrophones. The near-surface hydrophones were sensitive to absorbing layers at all depths, whereas the near-bottom hydrophones were only sensitive to absorbing layers below the thermocline. Figure 4 shows the corresponding echo sounder record.

Model: The resultant measurements were modeled with a numerical sound propagation model that incorporates absorption layers in the water column. Matching data with theory permitted estimation of the average absorption coefficient and the depth and thickness of absorption layers. The layer depth and thickness estimates from sound propagation measurements were in good agreement with echo sounder data. The measured resonance frequencies of dispersed fish at night were in good agreement with theoretical computations, based on swim bladder dimensions derived from near-coincident samples of 16.5-cm-long sardines, and historical measurements of 7.0-cm-long sardines, as illustrated in Fig. 5. This figure also shows that the resonance frequency of schools was significantly smaller than that of dispersed fish. The observed frequency shift is analogous to

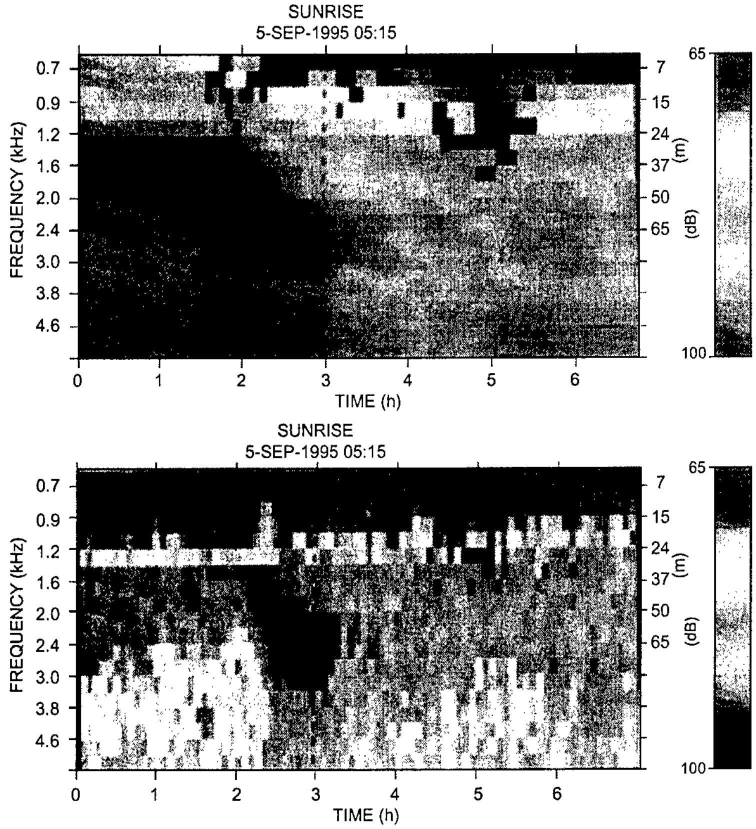

Fig. 3 — Transmission loss vs time and frequency on near-surface (top) and near-bottom (bottom) hydrophones near sunrise. Low signal-to-noise ratio (SNR) (< 2 dB) pixels are black. High absorption at night on near-surface hydrophones at ~1.4 kHz is attributed to dispersed sardines; high absorption near sunrise, starting at ~1.4 kHz and ending at ~2.7 kHz on near-surface and near-bottom hydrophones is attributed to descending, dispersed sardines. Scale on right: theoretical depths of dispersed sardines. High absorption during night at ~1.5 kHz and during day at ~1.7 kHz on near-bottom hydrophones is attributed to sardine schools. During daytime, the low SNR at $f < 2$ kHz is caused by noise from fishing vessels.

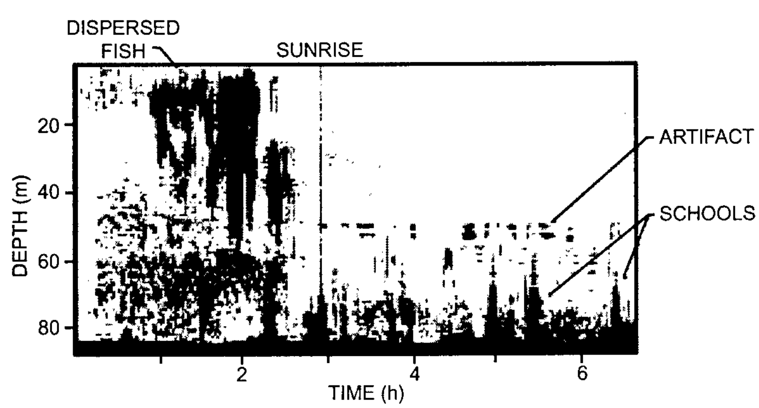

Fig. 4 — Echo-sounder record of the temporal evolution of the depth dependence of fish (sardines), and their transition from (1) dispersed and school modes at night to (2) primarily school mode during daytime. An artifact, which is due to reflections from the RV *Alliance*'s mooring chain, is evident at ~50 m.

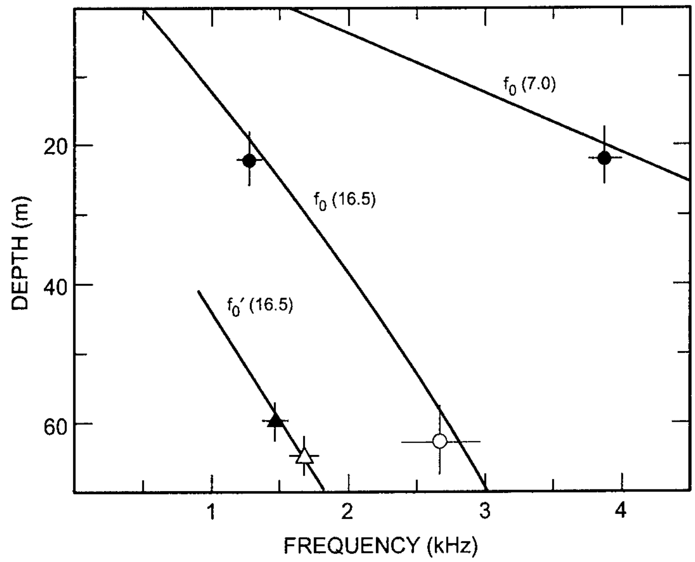

Fig. 5— Measured resonance frequencies of dispersed sardines at night (●) and dawn (○); schools of sardines during night (▲) and day (Δ) as a function of depth; and theoretical calculations of f_0 of 7.0- and 16.5-cm-long dispersed sardines, and f_0' of 16.5-cm-long sardines in schools.

previously observed frequency shifts associated with coupled oscillations (in particular, the first normal mode) of "bubble clouds," in which the spacing is small compared to the acoustic wavelength, and is consistent with a theoretical computation of its magnitude.

Significance: There are two applications of this research: tactical sonar performance prediction and biomass estimation. These results indicate that the detection range of naval tactical sonars may be significantly reduced when operating in shallow-water environments where large numbers of pelagic fish are present. Strategically important areas where the concentrations of pelagic fish (primarily sardines and anchovies) may be sufficiently high to affect sonar performance include the Mediterranean Sea, the Black Sea, and the shallow seas off China, Korea, the west coast of the United States, and the west coast of Europe. Since the spectral width of the resonance frequency lines is relatively narrow, combatants with sonars that operate at different frequencies could find themselves in situations where one sonar (operating, for example, at 5 kHz) may have a very long detection range (e.g., > 10 km), whereas the other (operating, e.g., at 4 kHz) may have a very short detection range (< 1 km) in the same environment. This research also suggests a new approach to estimation of the biomass (number densities) of pelagic fish, based on absorptivity measurements made with widely spaced broadband sources and receivers.

[Sponsored by NATO and ONR]

References

1. O. Diachok and C. Ferla, "Measurement and Simulation of the Effects of Absorptivity Due to Fish on Transmission Loss in Shallow Water," in *Proceedings of Oceans 96*, pp. 524-529, IEEE Press, 1996.

2. O. Diachok, "Fish Absorption Spectroscopy," in *Proceedings of the Third European Conference on Underwater Acoustics*, J. Papadakis, ed. (E.C. Press, Luxembourg, 1996).

3. O. Diachok, "Effects of Absorptivity Due to Fish on Transmission Loss in Shallow Water," submitted to the *Journal of the Acoustical Society of America*. ◆

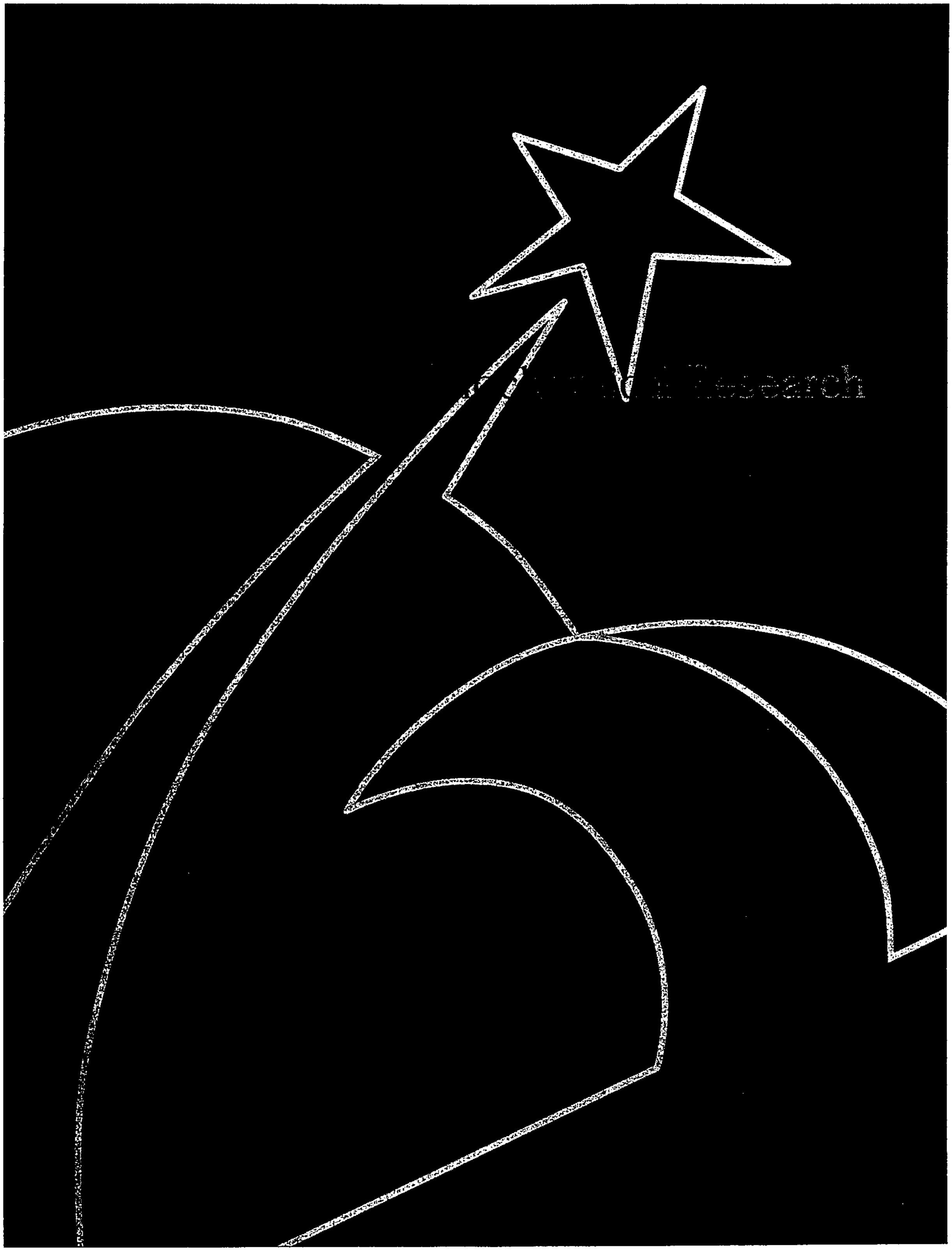

Designing Drugs for the Future

J.R. Deschamps, C. George, and J.L. Flippen-Anderson
Laboratory for the Structure of Matter

Background: Opiates, drugs that are isolated or derived from opium, such as morphine and heroin, are potent analgesics but possess a number of "undesirable" side effects that seriously limit their use. Morphine, first isolated in 1803, replaced opium, a crude extract made from the poppy plant (*Papaver somniferum*) that was addictive and toxic. Only after morphine became a mainstay of clinical medicine did it become apparent that it shared opium's "undesirable" properties. Heroin, derived from morphine, was used with the hope of avoiding morphine's addictive properties, but soon it was also found to be addictive.

The human body produces its own pain killers, opioid peptides. The endogenous opioid peptide enkephalin (Tyr-Gly-Gly-Phe-Leu(Met)) was isolated and identified in 1975. Enkephalin does not exhibit the undesirable side effects of the opiates, but it is also a much less potent analgesic. Despite its lower potency, this discovery spurred renewed interest in the search for nonaddictive opiate drugs.

Relationship Between Structure and Activity: Both the opiates and the opioids are ligands that act by binding to receptors in the central nervous system. Some structural elements of these compounds are necessary for receptor binding while others have no apparent effect on their biologic activity. The new wave of opiate research identified at least three main opioid receptors: μ, δ, and κ [1]. Opiates do not bind to all of these receptors equally. Morphine, an agonist (a compound that binds to a receptor and elicits the normal physiological response), is selective for the μ-receptor. Activation of this receptor is thought to be responsible for the "reinforcing characteristics" of opiates [2]. These "reinforcing characteristics" are related to the addictive properties of this drug.

Enkephalins, on the other hand, have a higher affinity for the δ-receptor, although they are not very site specific, since they have binding affinity for both the μ and δ receptors. Figure 1 depicts the three conformations of enkephalin revealed by structural studies [3]. These conformations are fully extended, single-bend (proposed as the bioactive conformation at the δ-receptor), and double-bend (which may represent the conformation required for binding at the μ-receptor).

The conformational flexibility of enkephalin coupled with its low selectivity prompted the synthesis of constrained analogues. Since the "single-bend" conformation was thought to be the biologically active form, the object of the constraints was to lock the peptide into this conformation. The most successful constraints applied have been cyclization or incorporation of a highly constrained residue (Fig. 2). The use of these constraints has resulted in peptides with increased potency and selectivity.

Subtle changes in the peptide structure can result in large changes in the biologic activity. One of the most dramatic examples of this is TIPP (Fig. 2, bottom) and D-TIPP (Fig. 3, bottom (dark gray)). By changing only the absolute configuration of the second residue in TIPP from L-Tic to D-Tic, the biologic activity changes from a potent highly selective δ-receptor antagonist (a compound that inhibits the action of an agonist) to a μ-selective agonist.

By studying the activity of a large number of opioid-related compounds and comparing the structures of these compounds, scientists have identified certain functional groups essential for opioid activity. These functional groups, referred to as pharmacophores, consist of two aromatic rings, one of which has a hydroxyl group, and an amine nitrogen [4]. The relationship between the groups required for activity at either the δ or μ opioid receptor is illustrated in Fig. 3. In the top half, the aromatic rings of a δ-selective peptide (JOM-13) and potent nonpeptide ligand (SNC80) were "matched." This results in close proximity of the oxygen (red) and nitrogen (cyan) atoms in these two compounds. Similarly, two μ-selective compounds, heroin and D-TIPP, may be compared. The two molecules are similar in shape, and the biologically important oxygen atoms are in close proximity as shown at the bottom of Fig. 3.

Although the exact requirements for δ-selectivity or μ-selectivity are not known, new generations of opioids are more potent and selective than their predecessors. By gaining an understanding of the requirements for receptor binding at the molecular level, it should be possible to "design" away the undesirable side effects of opiate drugs while at the same time maintain, or even increase, their potency. The goal of structural studies conducted at NRL is ultimately to deduce the requirements for receptor binding, which is the first step in designing the next generation of drugs.

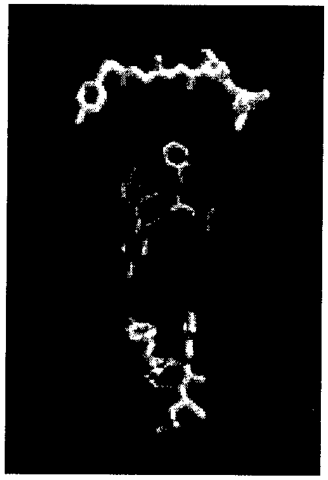

Fig. 1 — Conformations of the endogenous opioid peptide, enkephalin, observed by X-ray diffraction analysis (top to bottom): fully extended, single-bend, and double-bend.

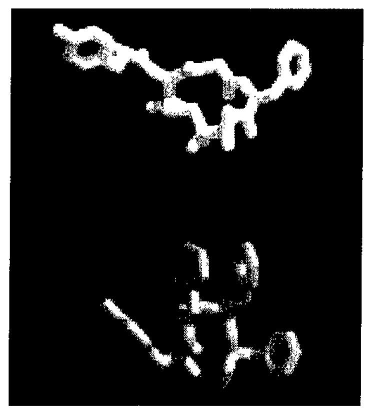

Fig. 2 — Conformations of the constrained opioid peptides DPDPE (Tyr-*cyclo*-[D-Pen-Gly-Phe-D-Pen]) and TIPP (Tyr-Tic-Phe-Phe). DPDPE (top) is a potent δ-selective agonist, which is constrained by cyclization through the side-chains of its two D-penicillamine residues. TIPP (bottom) is a potent δ-selective antagonist, which is constrained by incorporation of a Tic (tetrahydroisoquinoline-3-carboxylic acid) residue in position two.

Fig. 3 — Superimposition of peptide (white) and nonpeptide (grey) opioids. Alignment of JOM-13 (Tyr-*cyclo*-[D-Cys-Phe-D-Pen]) and SNC80, two δ-selective agonists (top) and D-TIPP (Tyr-D-Tic-Phe-Phe) and heroin, two μ-selective agonists (bottom). Other atoms important to binding are highlighted in red (oxygen atoms) or cyan (nitrogen).

[Sponsored by ONR and the National Institute on Drug Analysis]

References

1. P.W. Schiller, in *Progress in Medicinal Chemistry, Vol. 28*, G.P. Ellis and G.B. West eds. (Elsevier Science Publishers, Amsterdam, 1991), pp. 301-340.

2. G.F. Koob, "Neural Mechanisms of Drug Reinforcement" in *The Neurobiology of Drug and Alcohol Addiction*, P.W. Kalivas and H.H. Samson, eds., *Annals of the American Academy of Sciences, Vol. 654* (New York Academy of Sciences, New York, 1992), pp. 171-191.

3. J.R. Deschamps, C. George, and J.L. Flippen-Anderson, "Structural Studies of Opiod Peptides: A Review of Recent Progress of X-ray Diffraction Studies," *Biopolymers (Peptide Science)* **40**, 121-139 (1996).

4. G.D Smith and J.F. Griffin, "Conformation of [Leu[5]] Enkephalin from X-ray Diffraction: Features Important for Recognition of Opiate Receptor," *Science* **199**, 1214-1216 (1978).

◆

Duplex Foul-Release Silicone Coatings

Chemistry Division, NRL; GE (Corporate Research and Development), Schenectady, N.Y.; Naval Surface Warfare Center (Carderock Division), West Bethesda, Md.; Florida Institute of Technology, Melbourne, Fla.; State University of New York, Buffalo, N.Y.; and Bridger Scientific, Inc., Sandwich, Mass.

Introduction: Historically, marine antifouling paints have used compounds that are toxic to marine organisms to combat fouling. In recent years, the environmental impact of these toxic coatings has come under increased scrutiny. Concerns about copper toxicity effects at the high leach levels required for their effectiveness have led to a major effort to discover nontoxic coating alternatives. Foul-release coatings do not use copper or any other metal toxicant to provide effective biofouling control; rather their unique surface chemistry creates a surface to which fouling cannot easily adhere. Because they use a physical rather than a chemical means to reduce fouling, these silicone coatings have been ruled exempt from reporting under the Federal Insecticide, Fungicide, Rodenticide Act (FIFRA) (Public Law 95-396).

NRL has developed and patented an advanced foul-release coating (the duplex silicone coating system) to address the durability issues associated with silicone elastomeric coatings [1, 2]. Figure 4 shows the NRL-GE duplex foul-release coating system profile. Designed for ship hulls (aluminum or steel), the duplex system consists of two layers of epoxy: anticorrosive (AC) epoxy, an epoxy amide mist coat (EPON 828/Versamid 140 in butylalcohol) to ensure bonding of the Silgan J501 to the AC coating, and an elastomeric silicone topcoat (GE 1154, which is RTV11 + 20% SF1154 silicone oil or GE Exsil 2200). Although a number of tough elastomeric materials could fulfill duplex bond coat requirements, Silgan J501, produced by Wacker Chemie, Ltd., is the only commercial material that has been identified for bonding the foul-release silicone topcoat to the anticorrosive system for ship hulls or to the epoxy paint on concrete walls in power plant water intakes. The duplex coating system provides excellent bonding of all coating layers, enhanced durability because of the unique bond coat, and foul-release with the silicone elastomeric topcoat.

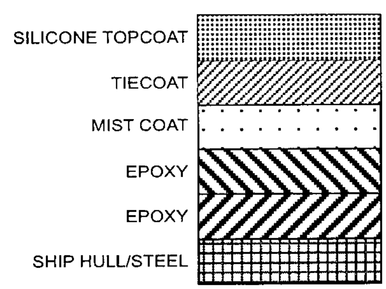

Fig. 4 — Duplex foul-release coating system profile.

Field Demonstrations/Validations: A joint effort funded by the Environmental Security Technology Certification Program (ESTCP) and managed by NRL looked at (a) durability of the coatings determined by scratch tests at the Naval Surface Warfare Center (NSWC), Carderock Division, Bethesda, Maryland, and NRL; (b) retention of fouling resistance after periodic brush

abrasion and wear to determine durability at the State University of New York-Buffalo; (c) barnacle and oyster adhesion measurements to evaluate the fouling resistance of these coatings in the field done by the Florida Institute of Technology, Melbourne [3]; and (d) demonstration/validation projects done by the consortium members. These demonstrations began in March 1995 and include

- aluminum-hull boats (five 41-ft and 55-ft U.S. Coast Guard utility training boats (UTBs); two 31-ft Navy range boats; one 100-ft Navy transporter; 104-ft prototype SLICE); and
- concrete tunnel walls, steel deflecting veins, steel trash racks, and steel traveling screens in power plant cooling water service intakes (Consumers Power in Bay City, Michigan, with a zebra mussel fouling problem; New England Power in Brayton Point, Massachusetts, with a barnacle fouling problem; Ontario Hydro's Nanicoke Station with a zebra mussel and quagga mussel fouling problem).

Boat hulls were assessed for coating condition (physical integrity and mechanical damage), fouling (percent cover, type, and distribution on the hull), fouling adhesion (by ASTM D 5619), and cleanability (water-jet testing). Figure 5(a) shows the April 1997 inspection of the GE 1154 duplex system on USCG UTB 41393 (coated in June 1995 at Yorktown, Virginia). Figure 5(b) shows Navy range boat 1 coated with GE Exsil 2200 after 1 year in the water at Patuxent River, Maryland, and at NSWC Dahlgren Division, Dahlgren, Virginia. The duplex system is easily cleaned (200-psi water hose).

The Consumers Power Plant in Bay City, Michigan, can experience significant performance and availability problems related to fouling by zebra mussels. In March 1995, the duplex silicone coating system was applied to 1,100 ft^2 of the circulating water system tunnels in Unit #1. In 1997, the tunnel was inspected. Figure 6(a) shows the duplex system with Exsil 2200 on the left

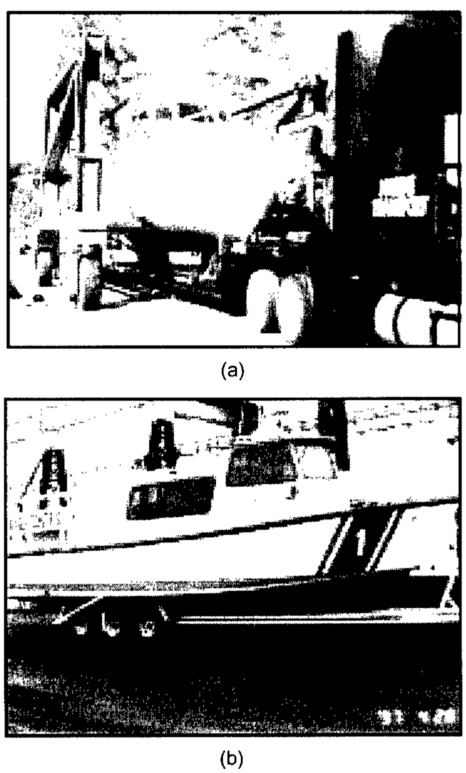

Fig. 5 — (a) Duplex coating system with GE 1154 silicone topcoat on USCG UTB 41393 (2-year inspection; boat as pulled from water) and (b) Navy range boat coated with GE Exsil 2200 after 1 year in the water at Patuxent River, Maryland, and at NSWCDD.

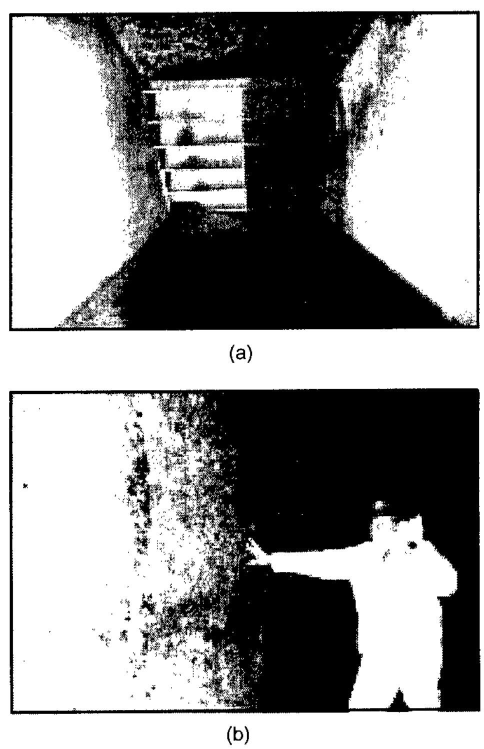

Fig. 6 — (a) Consumers Power Plant Unit #1 intake (Exsil 2200-coated concrete on left-hand side and on half of steel deflecting veins; RTV11-coated concrete on right-hand side of tunnel) and (b) Exsil 2200-coated concrete (left-hand side) vs uncoated concrete (right-hand side) with heavy build-up of zebra mussels.

concrete wall of the intake tunnel and on the left half of the steel deflecting veins. The right half of the steel deflecting veins is not coated and has a zebra mussel/quagga mussel build-up. The duplex system with RTV11 topcoat is on the right concrete wall of the intake tunnel. Just by draining the water from the tunnel, one can see that the zebra mussel settlement falls off the duplex silicone coating system, while the uncoated concrete and steel surfaces are 100% covered with 4 to 6 in. of zebra mussels (Figs. 6(a) and (b)).

[Sponsored by ESTCP]

References

1. J.R. Griffith, "Nontoxic Antifouling Systems," U.S. Patent 5,449,553, (issued September 12, 1995).

2. J.R. Griffith, "Nontoxic Antifouling Systems," U.S. Patent 5,593,732, (issued January 14, 1997).

3. G.W. Swain, M.P. Schutlz, J. Griffith, and S. Snyder, "The Relationship Between Barnacle and Pseudo-Barnacle Adhesion Measurements: A Method to Predict the Foul Release Properties of Silicones?," Paper 10 (9 pages) in the Proceedings of the U.S. Pacific Rim Workshop "Emerging Nonmetallic Materials for the Marine Environment," March 18-20, 1997, Honolulu, Hawaii. ◆

The State of Halon Replacement Research

R.S. Sheinson, A. Maranghides, J.W. Fleming, and B.A. Williams
Navy Technology Center for Safety and Survivability

Halon 1301 is a very effective fire suppression agent that has been used extensively in the military and commercial sectors for more than two decades. More than 2,200 shipboard Halon 1301 fire-suppression systems currently exist. However, production of stratospheric ozone-depleting halon has been banned by the Montreal Protocol and U.S. Clean Air Act amendments since December 31, 1993. The Navy has decided to eliminate Halon 1301 in new construction and minimize existing usage. Most halon replacements acceptable for civilian applications are not acceptable for weapons platforms primarily because of space and weight restrictions.

Program Significance: Under the Navy hydrofluorocarbon (CFC)/halon replacement and elimination effort, NRL has the lead responsibility to provide guidance for shipboard fire protection to maintain mission capability without ozone-depleting substances (ODSs). Our task is to identify and evaluate potential backfit capabilities and provide fire protection in new construction ships without halon.

Approach: Agents are first screened by using a laboratory cup burner (small liquid pool fire), which provides data to formulate empirical predictive models of an agent's suppression potential. Supporting follow-up efforts involve laboratory flames investigated with laser diagnostic techniques, computer flame modeling to investigate chemical mechanisms and agent/flame interactions, and small, intermediate, and heavily instrumented full-scale realistic total flooding fire extinguishment system tests.

Laboratory Studies: The cup burner is used for gaseous and vaporized agents. Cup burner studies have included CFCs, hydrofluorocarbons, perfluorocarbons, model compounds, and blends as well as extinction in synthetic air (O_2/N_2) atmospheres. These studies pointed out that 1,1,1,2,3,3,3-heptafluoropropane would be an acceptable fire suppressant but only for new construction because of weight and space penalties. A more effective agent must be found. Detailed systematic studies of potential agents are required to identify better solutions. To search for new agents in an educated, systematic manner, details on the fire suppression mechanism of potential agents is required. Real fires exhibit flames with a range of strain, the rate of change of the air velocity as it approaches the flame. We have examined the extinction strain rate vs agent concentration for several potential agents including nongaseous compounds. Figure 7 shows results for the hexa- and heptafluoropropane isomers for a propane/air diffusion flame. These isomer studies show that for diffusion flames, the structure of the agent is more significant to suppression than the agent composition [1]. We are also providing data on the flame temperature and flame radical species relevant to the suppression of HFC agents as well as investigating the effectiveness of particle and liquid aerosols to determine the controlling suppression parameters for condensed phase fire suppressants.

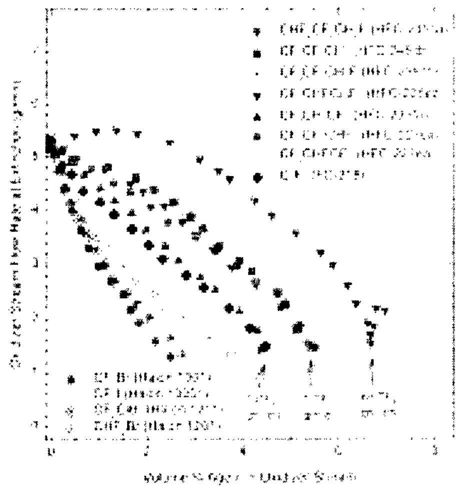

Fig. 7 — Propane-air counterflow flame extinction—results for several halon and hydrofluoropropane suppressant agents. The falloff of the extinction strain rate as the agent concentration increases is a measure of the agent's effectiveness. Effectiveness depends on number of CF_3 groups, not on number of fluorine atoms.

Intermediate and Full-Scale Halon Replacement Testing: Intermediate and full-scale halon replacement testing characterizes agent fire suppression and reignition performance. Fire suppression times, reignition potential, and to a lesser extent, by-product formation must be determined as a function of fuel type, fire size, preburn particulars, agent design concentration, and agent discharge time.

Full-scale tests are designed to emulate realistic shipboard fire scenarios [2]. The tests are performed aboard the *ex-USS Shadwell*, NRL's fire research and test ship or at NRL's Chesapeake Bay Detachment (Fig. 8). Understanding suppression from the laboratory level assists in interpretating these complex large-scale tests. The dynamics of fire suppression are key to optimum system development. A thorough evaluation of the fire threat, the fire suppression system performance criteria, and the discharge system performance allows a recommendation on the agent of choice, design concentration, and discharge system particulars.

NRL-recommended systems have been incorporated by the Naval Sea Systems Command (NAVSEA) into the LPD-17, the Navy's newest ship class. Current research is providing guidance for future platforms (CVN-76, DD-21, as well as CV(X)). The NRL/NAVSEA interactions are directly transitioned into Navy shipboard systems

(a) (b)

Fig. 8 — (a) The Flammable Liquid Storeroom Halon Replacement Facility at NRL's Chesapeake Bay Detachment and (b) testing at the facility.

and construction specifications. Additionally, the U.S. Army has also incorporated NRL systems in its watercraft. Close interactions with U.S. Coast Guard and the National Fire Protection Association have created additional transition pathways within both defense and civilian sectors worldwide. Our research program has been awarded three EPA Stratospheric Ozone Protection Awards in 1995, 1996, and 1997 and recognition by the Secretary of Defense.

Summary: Research in the NRL Halon Replacement Program continues to provide better understanding of and solutions to fire extinguishment issues relevant to Navy applications. These investigations provide experimental information about flame extinguishment and "real world" performance. The ultimate goal of the program is a predictive capability and higher level of understanding to address the Navy's short- and long-range fire protection needs.

[Sponsored by NAVSEA]

References

1. B.A. Williams, J.W. Fleming, and R.S. Sheinson, "Extinction Studies of Polyfluoropropanes and Halons in Methane/Air and Propane/Air Counterflow Diffusion Flames," NRL/MR/6185--97-7961, 27 June 1997.

2. R.S. Sheinson, A. Maranghides, B.H. Black, and M.J. Peatross, "The Effects of a Water Spray Cooling System During Real Scale Halon 1301 Replacement Testing on Post Fire Suppression Compartment Reclamation," NRL/MR/6180--97-7938, 14 April, 1997. ◆

Environmental Remediation Research

R.A. August, Jr.
Condensed Matter and Radiation Sciences Division

Introduction: All branches of the Armed Forces are conducting environmental restoration programs under the auspices of each service's investigation and remediation program (IRP). These IRPs must follow the protocols and statutory amendments of the Comprehensive Environmental Response, Compensation, and Liability Act (CERCLA), which provides a regulatory framework under which to complete environmental restoration activities at all military facilities. Unfortunately, compliance at individual sites can often mean multiyear programs costing many millions of dollars. Even then, cleanup can be restricted to little more than moving the hazardous material to an approved storage facility. This is especially true when the contaminant is mixed waste, a combination of chemical and radionuclear hazards.

NRL's Radiation Detection Section initiated a pilot program at Kirtland AFB, New Mexico, to study new methods of environmental characterization and restoration of sites contaminated with mixed wastes. The initial FY97 program studied four sites contaminated with radioactive thorium. Geophysical, nuclear, and chemical analyses were performed during the initial phase. The program is structured as two parallel research thrusts: characterization methods and remediation alternatives.

Characterization Methods: The typical mixed waste site characterization process involves bringing a team on site for geophysical characterization, then a second team for soil sampling. When the second team has finished its work, the samples are sent off site to an independent laboratory for chemical and radionuclear analysis, in strict accordance with all shipping and safety regulations for both chemical and radionuclear hazards. Only after actual characterization and sampling activities are completed, can the relevant data be brought together and synthesized to draw conclusions about the site as a whole. Typically, the data raise as many questions as they answer, requiring further study and beginning the entire process again. The process can, in fact, go through several iterations before the site can be declared sufficiently characterized; it can take many years and be prohibitively expensive.

NRL's program streamlines this process by conducting all phases of the process on-site. This eliminates public health concerns about transportation of hazardous waste, provides a more efficient and effective way to take and process samples, and provides on-site expertise to guide sampling and analysis, thereby ensuring a complete characterization in one deployment.

NRL contracted and worked with Search Technologies, Inc., to perform the geophysical survey using their portable Magnetometer Sensor Array with integrated differential global positioning system (DGPS). This system uses surface towed ordnance locator system (STOLS) technology

originally developed by NRL's Chemistry Division to detect and image buried ferrous items with a relative point-to-point precision of 10 to 20 cm. Figure 9 shows a sample survey from the corner of one site. Distinct buried objects show in red. These survey results were available to NRL on-site to guide selection of soil sampling sites.

Numerous soil samples were taken via hand corer and analyzed in an on-site laboratory for radionuclear contaminants using high-resolution gamma-ray spectroscopy in a device consisting of a portable lead shield and a mechanically cooled Ge detector and electronics. NRL personnel collaborated with Professors Mark Harper and Martin Nelson of the Naval Academy, and Commander Stephen Gann of the Science & Technology 108 Naval Reserve Unit in the on-site laboratory. The only radionuclear contaminant found in the soil samples was thorium, which ranged from background levels to over a thousand picoCuries per gram of soil.

Because the levels of chemical contaminants were known to be low in the samples taken during the initial program phase, the chemical component of the on-site laboratory was not deployed initially; it, however, will be in full operation during the current fiscal year. Instead, limited numbers of samples were sent off-site and analyzed to ensure no significant contamination by metals, semi-volatile organic compounds, and total petroleum hydrocarbons, according to EPA standards. JWK International Corporation provided the chemical expertise for this analysis and will provide expertise for setting next year's chemical component of the on-site laboratory.

Remediation Alternatives: The initial study focused on looking for correlations between

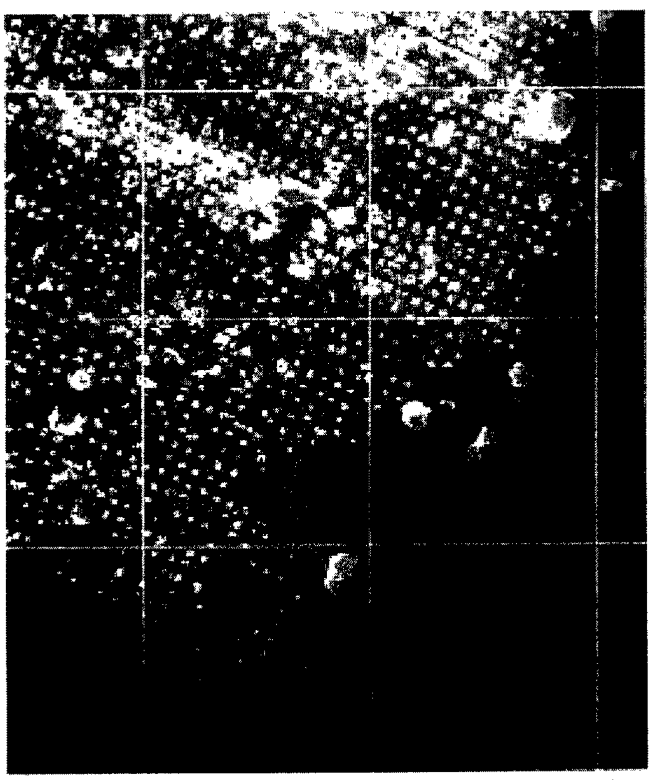

Fig. 9 — A sample geophysical survey from the corner of one site. A chain link fence at the site perimeter shows as a diffuse purple region with red highlights. Distinct buried objects within the site show in red. This site is covered by a grid of small metal marker flags that show in red and yellow on the figure.

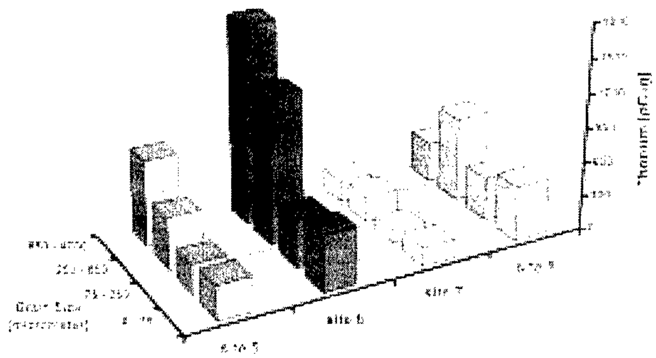

Fig. 10 — Thorium content in picoCuries per gram of soil (pCi/g) is shown for each of the grain size bins for the four most contaminated areas (labeled as sites 5 through 8).

Fig. 11 — Thorium actually measured in each grain size bin compared with the distribution expected if there were no correlation between thorium content and grain size. The result is expressed as a percentage of the expected amount.

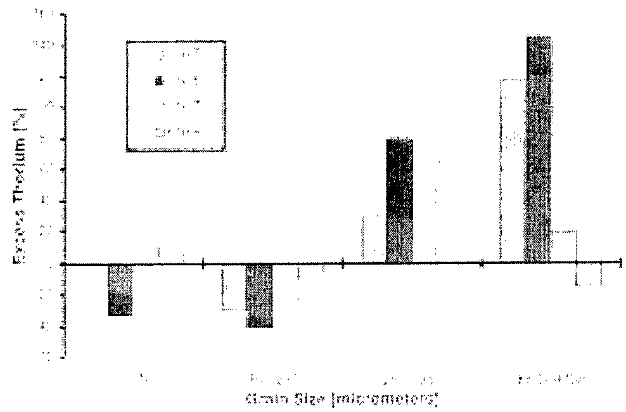

radiation content and soil grain size with the intent of exploiting any effect for remediation. Soil samples from the four most thorium-contaminated areas were physically separated by a mechanical sieve shaker into grain size bins of 0-75, 75-250, 250-850, 850-4700, and >4700 μm. The >4700 μm bin consisted of essentially uncontaminated pebbles and was not included in the analysis.

The raw data shown in Fig. 10 reveal a tendency for the thorium to accumulate in the larger grain sizes. However, the data in this figure show thorium content per gram of soil and do not account for how the mass of each soil sample is distributed in the various size bins. To take the mass distribution into account, Fig. 11 compares the thorium actually found in a grain size bin with what would be expected for a sample showing no correlation between thorium content and grain size. This figure clearly demonstrates a correlation with larger grain sizes. This is a surprising result from a purely physical standpoint, since the smaller grains have a higher surface area to volume ratio, and would, therefore, be expected to better accumulate the thorium. Since the larger grain sizes contain the bulk of the organic material, we suspect a biological process may be accumulating the thorium.

Conclusions: The volume, quality, and completeness of the data already accumulated in the characterization phase of this project, along with the short time period required for collection, clearly demonstrate the cost and time savings realizable with a site-deployed laboratory. We expect the addition of full chemical analysis capabilities in the current year to fully prove this principle.

The demonstrated correlation of thorium content with grain size suggests exploiting this effect to reduce the volumes of soil that require removal to an off-site hazardous waste dump. The possibility of a biological component to this accumulation process will be further studied in the current year, with the intent of identifying a mechanism for enhancing the effect.

[Sponsored by the Environmental Research Branch, Kirtland AFB] ◆

Stamping Antibody Micro-Arrays

D.C. Turner, B.D. Martin, and B.P. Gaber
Center for Bio/Molecular Science and Engineering

Advances in warfare agent sensing and medical diagnostics are essential for maintaining the health and strength of our military in the 21st century. Miniaturized, portable sensors with the capability of observing multiple agents simultaneously are among DoD's most important technological goals for the next decade. The fabrication of chemical or biological arrays on a single chip, coupled with an appropriate sensing scheme, is an approach that holds great promise for reaching these technological goals. Unfortunately, while many effective sensing schemes are in place today, very few biological array fabrication schemes are available that can place more than a few different reagents on a single chip without severe cross-contamination or defects among the reagents (see, for example, a photolithographic approach in Ref. 1). In addition, none of these methods are particularly rapid or cost effective. In light of these facts, it is desirable to produce a new patterning methodology with the following features: (1) simultaneous parallel patterning of all reagents for high-throughput chip manufacture, (2) rapid pattern deposition with control of feature sizes larger than 1 μm, and (3) protein deposition without loss of functionality. Ideally, this process would be carried out with a simple, low-cost setup with a long cycle time (as measured in number of chips produced between failure), thereby allowing the production of a low-cost disposable chip that could be used in a variety of configurations.

Concept: Over the past year we have developed a biomolecule patterning method that we believe satisfies the constraints listed above. Our method is based on the direct delivery of macromolecules to a surface from a micromolded hydrogel "stamper." (A hydrogel is a lightly cross-linked hydrophilic polymer network that takes up many times its weight in water. Common examples include gelatin, disposable contact lenses, and jellyfish. When the hydrogel is formed in a container, it takes the shape of the container.) The hydrogel is preformed in a mold, swollen in a solution containing the desired macromolecule, and then brought into contact with a capture surface to directly deliver the molecule to the surface. The shape of the contact area defines the shape of the resultant spot on the surface. Figure 12 is an outline of the process. This concept is similar to the microcontact printing (μCP) method developed by Whitesides and coworkers [2]. However, the hydrogel stamper itself acts a reservoir for the macromolecule and directly delivers it to the surface rather than delivering a self-assembled monolayer (SAM) film to the surface. Direct delivery of the macromolecule is a substantial advantage over selective adhesion of the macromolecule to a μCP-patterned SAM film, nonspecific adsorption of the macromolecule cannot occur outside of the stamped region, and, therefore, no cross-contamination with previous or subsequent patterned reagents is possible. Also, since the macromolecule is delivered directly to the surface, an array of hydrogel stamps loaded with different macromolecules can be used to produce multi-reagent arrays in parallel with a single stamping process. Finally, since the hydrogel acts as a large reagent reservoir, the stamp can be reused many times without being re-inked.

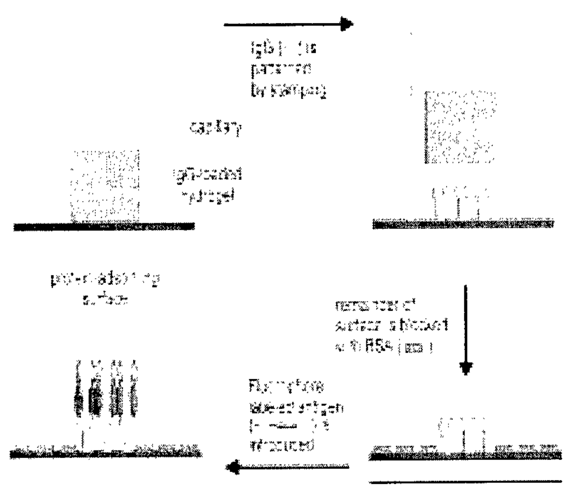

Fig. 12 — General scheme for antibody "stamping" followed by exposure to labeled antigen. IgG orientation is idealized.

Protein Array: To demonstrate the hydrogel stamper, we fabricated a patterned array of three different antibodies: rabbit anti-mouse (A), rabbit anti-goat (B), and goat anti-human (C). The arrays were prepared by using three individual capillary hydrogel stampers loaded with antibodies A, B, and C, respectively, using the procedure shown in Fig. 12. Between two and four spots of each

antibody were delivered to the surface, resulting in the pattern shown in Fig. 13. Typical spot sizes are 80 μm, and each spot was delivered to the surface with a contact time of about 1 s. Upon completion of patterning, the surface was washed and blocked with bovine serum albumin for passivation of unpatterned regions. Patterns were visualized by using immunofluorescence microscopy. The surface was exposed sequentially to fluorescently labeled antigens to antibodies A, B, and C and was viewed with fluorescence microscopy at each step. As a result, the spots develop sequentially when the appropriate fluorescent antigen enters the chamber (Fig. 13). Each set of spots has a characteristic shape that derives from the 3-D shape of the hydrogel stamper "nib." These images tell us two things: the antibodies have been delivered to the surface with spatial control and they retain biological activity when bound to the surface. This is an important point since many patterning processes denature proteins during delivery to a surface.

A complete characterization of the stamped antibody spots was carried out using fluorescence microscopy, radiolabeling, and atomic force microscopy. Radiolabeling indicated that the surface density of antibodies delivered from the stamper was roughly half of the density observed when directly depositing the antibodies from solution (1-h contact time). This difference probably results from the large difference in contact time with the surface between the two methods and may be rectified by increasing the stamper contact time. Interestingly though, fluorescence intensity indicates that the stamped regions are at least 75% of the brightness of the solution-deposited regions. This indicates that the stamped antibodies are more active on the surface. Typical fluorescent signal-to-background ratio for the stamped antibodies was greater than 30:1, and the signal-to-noise ratio was greater than 6:1. Atomic force microscopy indicated that the stamper delivered a uniform film of antibody consistent with submonolayer surface density.

Future Directions: The next step toward producing large antibody arrays is to deposit all the proteins in the array in parallel rather than in the sequential approach that we have used to date. A microarray of capillaries individually loaded with hydrogel and protein solutions could be used for parallel array fabrication (Fig. 14). In such an array, each hydrogel acts as an individual nib, and each capillary acts as a large reagent reservoir. The stamper array, therefore, could be used to mass produce substrates in parallel with a very short cycle time—making it possible to produce dispos-

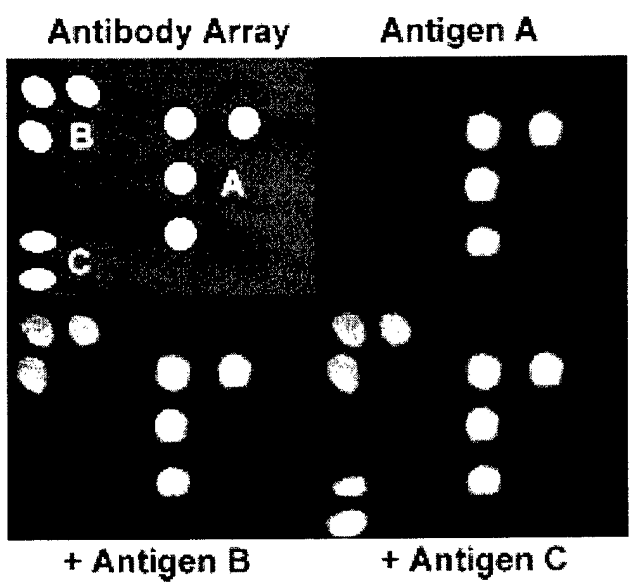

Fig. 13 — Sequential visualization of three different antigens bound to stamped IgGs. (A) stamped RAG IgG/FITC-goat IgG; (B) stamped RAM IgG/FITC-mouse IgG; (C) stamped GAH IgG/FITC-human IgG. The "ghost" patterns in A (left-hand side) arise from nonspecific adsorption/cross-reaction of RAM and GAH towards FITC-goat IgG. Scale bar = 100 μm.

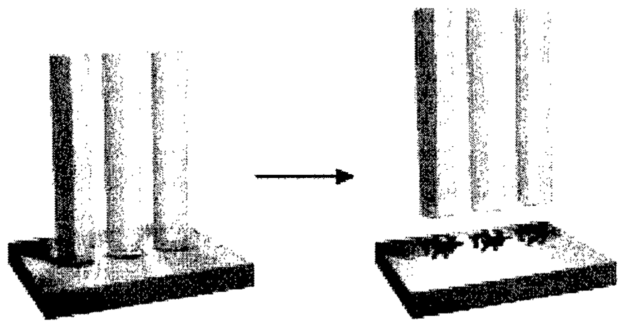

Fig. 14 — Triple capillary hydrogel microstamp. Hydrogel is formed in each microcapillary and each capillary is then loaded with a different molecular species. The gel is extruded from the end of the capillary when the gel swells during loading. The array is then placed into contact with the receiving surface and removed to apply the molecular pattern.

able "biochips" with large (> 10) arrays of biological molecules for low-cost multiplexed, sensing, and diagnostic applications.

[Sponsored by DARPA and ONR]

References

1. M. Chee, R. Yang, E. Hubbell, A. Berno, X.C. Huang, D. Stern, J. Winkler, D.L. Lockhardt, M.S. Morris, and S.P.A. Fodor, "Accessing Genetic Information with High-Density DNA Arrays," *Science* **224**, 610-614, 1994.

2. A. Kumar, H. Biebuyck, and G. Whitesides, "Patterning Self-Assembled Monolayers: Applications in Materials Science," *Langmuir* **10**, 1498-1511, 1994. ◆

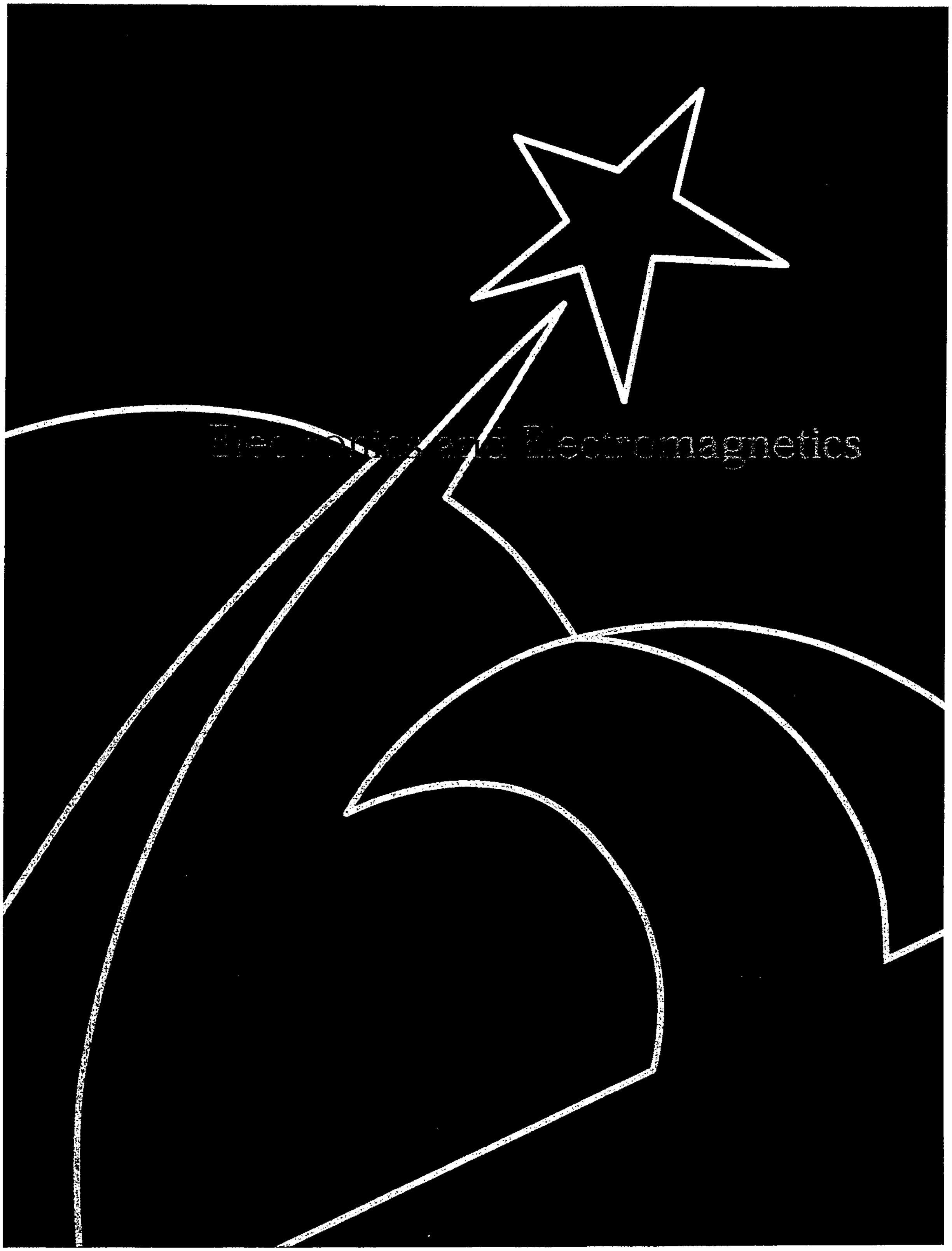

Electronics and Electromagnetics

Microwave Properties of Ferroelectric Thin-Film Varactors

S.W. Kirchoefer and J.M. Pond
Electronics Science and Technology Division

J.S. Horwitz
Condensed Matter and Radiation Sciences Division

Introduction: Ferroelectric materials have unique electronic properties, which hold great promise for significant utility in applications of interest to the Navy. Recent advances in deposition techniques for thin ceramic films have opened the door to a wide variety of new possibilities for ferroelectric materials in frequency-agile electronic applications. Ferroelectrics is a class of materials that exhibits an electric-field dependent relative dielectric constant. When incorporated into electronics devices, this allows manipulation of the microwave properties of the material with a dc bias voltage. The most basic application for these materials is in the production of interdigitated capacitors used as varactors in high-frequency circuits. Ferroelectric thin films of $Sr_{0.5}Ba_{0.5}TiO_3$ deposited on MgO, $LaAlO_3$, and $SrTiO_3$ substrates have been fabricated into interdigitated capacitors [1]. Microwave reflection measurements have been used to characterize these devices in the frequency range from 50 MHz to 20 GHz. These devices have tuning ranges and high-frequency losses that are comparable to semiconductor varactors.

Fabrication and Characterization Procedures: The ferroelectric thin films used in this study were deposited by pulsed-laser deposition. This technique deposits a thin film on a substrate, which is attached to a heated stage and positioned in proximity to a target of source material. The target is composed of a sintered pellet of $SrTiO_3$ and $BaTiO_3$ in the correct ratio to result in a deposited film of the desired stoichiometry. A pulsed eximer laser is used to ablate material from the target, and this material is deposited on the substrate at a rate of approximately 0.2 nm per laser pulse. Typically, films of about 0.5-μm total thickness are deposited.

These films are fabricated into interdigitated capacitors using standard photolithographic techniques. In order to keep high-frequency metal film losses to a minimum, a 1.5-μm silver film followed by a 0.05-μm gold film is employed for the capacitor metallization. The device processing uses metal liftoff patterning so as to minimally damage the thin ferroelectric layer. This process involves the initial deposition and patterning of photoresist, then the depositing of the metal film through windows in the resist. The metal film is removed from the undesired areas by dissolving the underlying photoresist and floating the unwanted overlying metal off the sample in these regions. The mask used to delineate the electrode pattern contains devices with a variety of dimensions suitable for microwave characterization. A typical device has two contact pads, each with dimensions of 200 × 100 μm. The active area of the device is contained between the contact pads and consists of six pairs of 80-μm-long, 10-μm-wide fingers separated by 5-μm-wide gaps.

Microwave characterization of these devices is accomplished by measuring the one-port scattering parameters. An HP 8510 vector network analyzer is used in conjunction with a Picoprobe probe station to measure the microwave reflection S_{11} from the device. Data are collected at room temperature in the frequency range from 50 MHz to 20 GHz. Dc bias is supplied to the capacitors by means of an external biasing circuit, which is connected to the probes through the internal bias tees of the network analyzer. Bias voltages are typically in the range of -40 to +40 volts, as determined by the limitations of the biasing circuitry. Figure 1 shows a typical device under test.

Microwave Performance: Figure 2 shows typical microwave reflection data plotted on a Smith chart, which shows the data normalized to the 50-ohm characteristic impedance of the circuit.

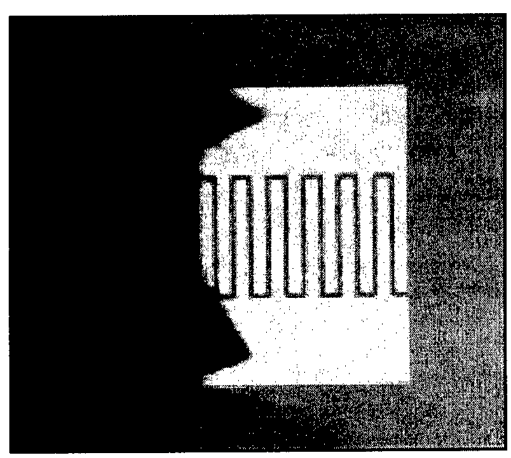

Fig. 1 — A 200 by 300 μm ferroelectric interdigitated capacitor under the microwave probe.

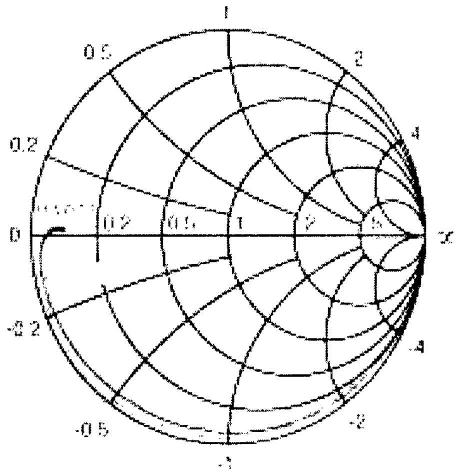

Fig. 2 — Polar plot of the microwave reflection data from 50 MHz to 20 GHz plotted on a Smith chart for dc biases of 0 volts and 40 volts.

The low-frequency data begin near the open circuit point, and continuously sweep around the unit circle toward the short circuit point as the frequency increases. At the high-frequency end, the data depart significantly from this simple capacitive behavior because of electrical size effects. This is a natural consequence of the high dielectric constant of this material, which reduces the radiation wavelength in the layer to such a degree that the device no longer appears as a lumped-element capacitor. Figure 3 shows the capacitance, device quality factor Q, and relative dielectric constant as a function of bias voltage for this device. The capacitance and Q are calculated by modeling the device as a simple circuit composed of an ideal capacitor in parallel with a resistor. The dielectric constant is calculated using the model of Gevorgian [2]. These data demonstrate a capacitive tuning range of 4:1 at 10 GHz.

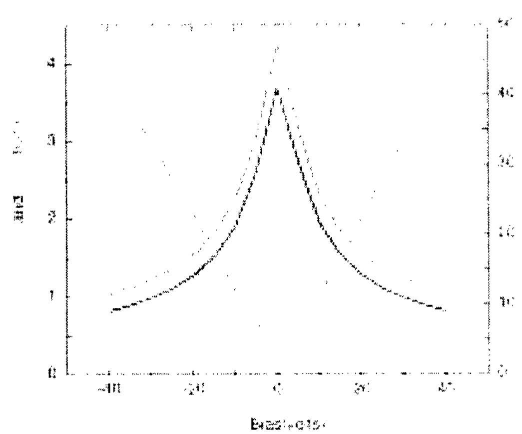

Fig. 3 — Plot of capacitance, relative dielectric constant (ε_r), and device quality factor as a function of dc bias for the device of Fig. 2.

Summary: This research demonstrates the promising potential for advanced ferroelectric thin films as varactors in microwave applications. We expect improvements in film quality as the deposition technique is further refined. This should result in improved varactors with use in a wide variety of frequency-agile microwave circuits.

[Sponsored by ONR and SPAWAR]

References

1. J.S. Horwitz, D.B. Chrisey, J.M. Pond, R.C.Y. Auyeung, C.M. Cotell, K.S. Grabowski, P.C. Dorsey, and M.S. Kluskens, "$Sr_xBa_{1-x}TiO_3$ Thin Films for Active Microwave Device Applications," *Integr. Ferroelectr.* **8**, 53 (1995).

2. S.S. Gevorgian, T. Martinsson, P.L.J. Linnér, and E.L. Kollberg, "CAD Models for Multilayered Substrate Interdigital Capacitors," *IEEE Trans. Microwave Theory Tech.* **44**, 896 (1996).

◆

Reconnaissance Sensor Development

M.R. Kruer and D. Linne von Berg
Optical Sciences Division

The Navy is developing improved capabilities for reconnaissance and intelligence gathering and dissemination. The primary Navy capability for manned reconnaissance and battle damage assessment has been film cameras in the Tactical Airborne Reconnaissance Pod System (TARPS) on F-14 aircraft. TARPS uses a short-range camera directed forward or downward in the front bay, a medium-range camera directed side oblique in the second bay, and a wide field-of-regard infrared scanner operated in a whisk broom fashion in the third bay. The film system is limited because of the time delays and chemical handling for wet film processing. Prototype and future reconnaissance cameras will record electronic images in spectral bands that allow day/night operation and that can be disseminated in a more real-time manner. To replace the existing TARPS film reconnaissance capability, the Navy is exploring TARPS CD (com-

pletely digital) for the F-14 aircraft and Super Hornet Advanced Reconnaissance Pod (SHARP) for the F-18 aircraft. In order to improve survivability against anti-air missile threats, the SHARP system will use long-range (about forty miles) cameras but will also include medium-to-low cameras for operating under weather. NRL is working with the Defense Airborne Reconnaissance Office (DARO) to develop framing cameras using large area staring arrays with on-chip forward motion compensation and with NAVAIR to develop prototype pod systems. Other reconnaissance efforts such as the Advanced Tactical Airborne Reconnaissance System (ATARS) for the Marine F-18 aircraft are developing electronic pushbroom cameras using scanning charge coupled device (CCD) arrays.

Framing Camera Development: Framing cameras using very large area focal plane arrays are fabricated under competitively awarded contracts and tested in Navy aircraft. Figure 4 shows the 25 megapixel silicon CCD manufactured by Recon Optical Inc. (ROI). Current contracts with ROI and Lockheed Martin are developing 100 megapixel equivalent CCD cameras. Current efforts are also developing cameras operating in the midwave infrared for thermal imaging and night operation that use four megapixel staring arrays with forward motion compensation. Cameras operating at multiple wavelengths are also being explored. The cameras are flown in Navy aircraft using equipment shown in Fig. 5.

Flight Imagery: Figure 6 shows imagery of the Norfolk area obtained during the August 1997 flight test of the CA-261 step-stare framing camera. The camera was configured to provide multiple cross-flight steps in addition to the 56% in-flight frame overlap needed for stereo image interpretation. The imagery generated from this flight test included reduced resolution thumbnail frames (shown on the left) as well as the full resolution 5k × 5k images (full resolution extract of the target area shown on the right).

Data Compression: Typical tactical operation of these digital airborne framing sensors requires that imagery data be transmitted over

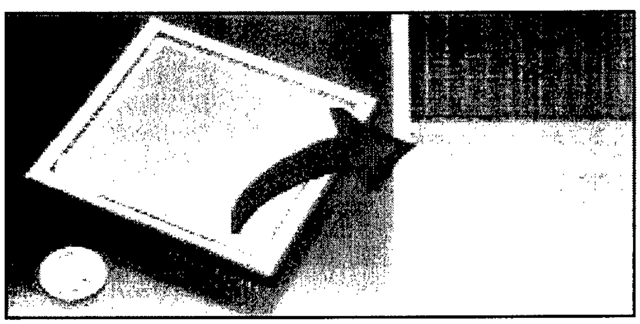

Fig. 4 — ROI 25 megapixel CCD with forward motion compensation.

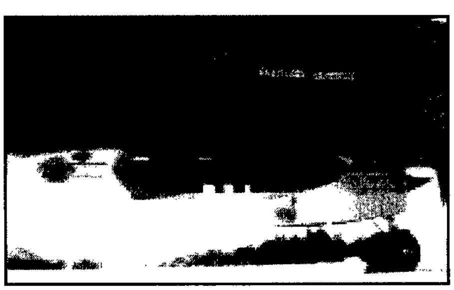

(a)

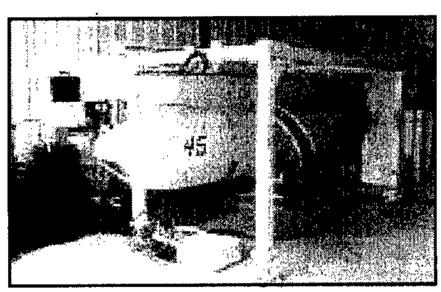

(b)

Fig. 5 — NRL test platforms: (a) NRL P-3 587 with bomb-bay equipment pallet having optical windows allowing cameras to record wingtip-to-wingtip imagery and (b) TARPS pod at NRL's Flight Support Detachment, Patuxent River, Maryland, awaiting mounting of electronic framing cameras.

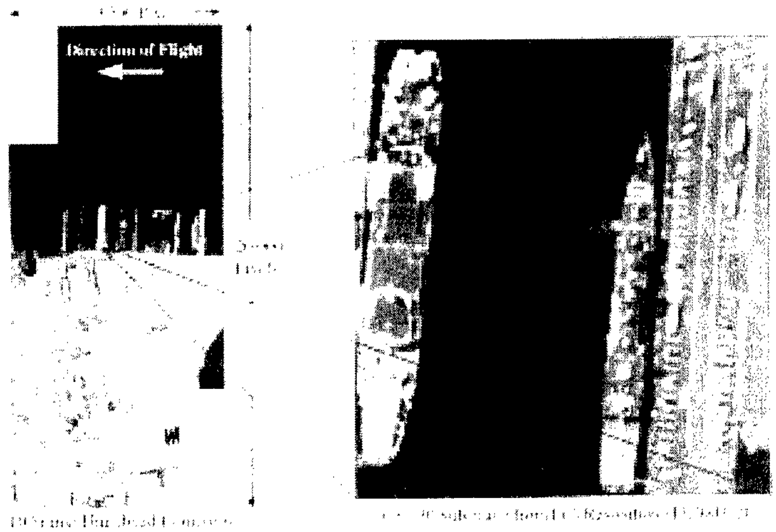

(a) (b)

Fig. 6 — Imagery from CA-261 step-stare P-3 flight-test (Aug. 97) over Norfolk showing broad area coverage (a) and detail from full resolution (b).

buses, between platforms, and/or stored for onboard or nonreal-time ground processing. The volume of data generated by even monochromatic sensors exceeds the available bandwidths in both real-time transmission and storage devices. This bandwidth limitation becomes more restrictive with multispectral cameras systems, which can have tens to thousands of spectral bands. Because of this bandwidth limitation, NRL developed a compression program to address the needs of tactical airborne reconnaissance in the development of a new international compression standard for still imagery, JPEG 2000. This new wavelet-based standard will provide improved image quality at higher compression ratios over the existing discrete cosine transform-based JPEG standard, as seen in Fig. 7. Some of the additional desired features of JPEG 2000 include a unified algorithm for lossless

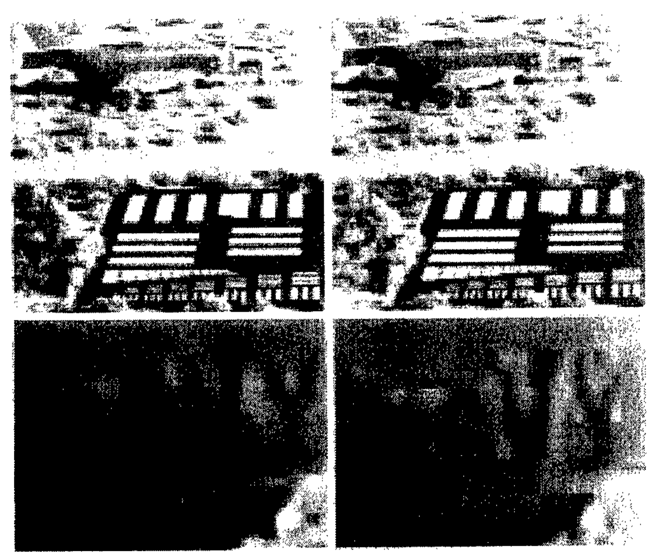

Fig. 7 — JPEG 2000 compression (wavelet-based) will provide improved image quality at higher compression ratios over standard JPEG (discrete cosine transform-based).

and lossy compression; compression of numerous imagery types (such as binary, computer graphics, and gray-tone (visible, SAR, medical); compression of imagery sizes > 64k × 64k with up to 16 bits/pixel; region of interest coding; fixed rate/fixed size operation modes; and progressive transmission. NRL has become the primary Navy representative to the ANSI and ISO Still-Imagery Compression Standards Committees and is coordinating efforts with the National Imagery Mapping Agency to ensure that the needs of tactical airborne reconnaissance will be met by the developing standard and that future recce systems will be compliant with the National Imagery Transmission Format Standard for secondary imagery dissemination.

Summary: Advanced reconnaissance cameras and data processing techniques being developed at NRL will improve the Navy's ability to provide timely and detailed reconnaissance and battle damage information and dissemination. This technology is being considered for the Navy TARPS CD and SHARP programs, which look to an initial operational capability in 2003.

[Sponsored by DARO and NAVAIR] ◆

Nuclear Nanospectroscopy of Semiconductor Quantum Dots

D.G. Gammon, E.S. Snow, and T.A. Kennedy
Electronics Science and Technology Division

Semiconductor quantum dots (QDs) are structures so small that their confined electrons must be described in terms of fully localized, quantum mechanical wave functions with energy spectra that are completely quantized. In other words, their internal electronic energy can take on only certain discrete values much like the electron in a hydrogen atom. In fact, QDs are often described as solid state atoms. Currently, materials scientists are designing new optical and electronic properties, and many groups are studying optical quality QDs with the hope of using them for lasers and memories with superior properties. Ultimately, however, it may be possible to arrange QDs into useful artificial molecules, cells, and crystals. If control of the structure and the function of QDs and related nanostructured electronic materials could be brought into maturity, the resulting nanostructured materials systems would have enormous potential for future technologies. One could envision entirely new computing paradigms based on quantum logic or neural networks, or perhaps even more likely, it would become possible to explore technologies not yet articulated or even imagined.

Currently, however, QDs are still in an embryonic stage. Recently, it has been possible to fabricate QDs with excellent optical quality. However, variation in parameters such as size and shape lead to fluctuations in confinement energies from dot to dot. These energy fluctuations are reflected in the optical spectra as inhomogeneous broadenings that blur the spectra and seriously limit scientific investigation into the fundamental physics of QDs. In response to this challenge, we are developing techniques that allow us to probe the spectra of individual QDs with ultrahigh spatial and spectral resolution. A QD is excited, and the resulting photoluminescence is detected through a very small aperture in a metal mask that has been developed directly on the QD sample. The apertures are lifted off with e-beam lithography at NRL's Nanoprocessing Facility with diameters ranging from 25 mm down to 200 nm. In this way, individual QDs can be studied by a large variety of optical spectroscopic techniques [1].

Spectroscopy of Electronic Excitations: In the specific GaAs QD system that we have studied, the QDs have sizes on the order of 10 nm and energies in the near infrared with confinement-induced splittings of several meV. Figure 8 shows the spectrum of an individual QD including the excited states. In previous ensemble measurements, these lines were completely lost in the inhomogeneous broadening, and it was impossible to measure the excited state spectrum. Now the atomiclike spectrum of the single QD is clearly seen with the very sharp and discrete bound states that merge into an energy continuum at higher energies. Furthermore, we measure with great clarity the energy splittings, intensities, linewidths, polarization properties, and even completely unexpected phenomena such as fine structure splittings corresponding to the lifting of an electronic spin degeneracy (Fig. 8, left inset) [2].

Spectroscopy of Nuclear Excitations: It is the electronic excitations of QDs that determine their optical and electronic response characteristics and that will ultimately serve useful functions for the engineer. Moreover, it is the electronic excitations that are observed directly with the very high sensitivity and selectivity of optical spectroscopy. However, the electrons are only part of the picture. To obtain a complete understanding of the physics

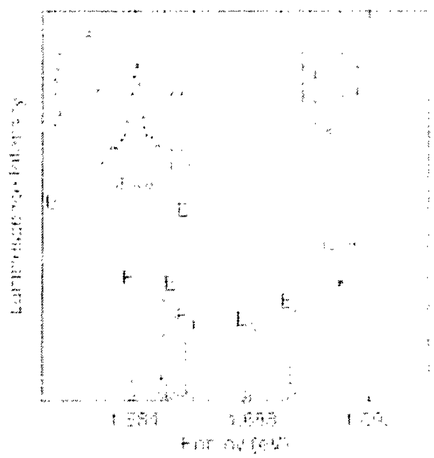

Fig. 8 — Electronic spectrum of a single GaAs QD measured through luminescence spectroscopy. The right inset schematically shows the measured optical transitions between the crystal ground state and the confined QD states. The left inset shows the fine structure splitting of the spin states associated with the first excited state E_1.

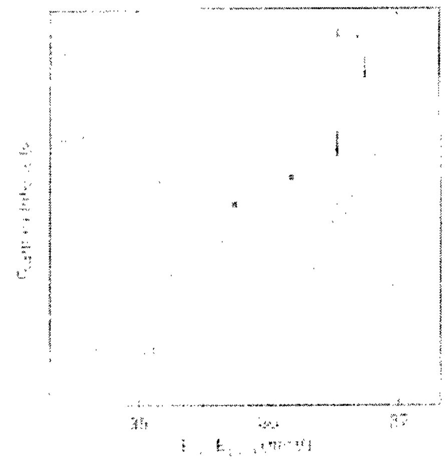

Fig. 9 — Optical phonon spectra of a single QD and an ensemble of QDs measured through Raman spectroscopy. The inset shows the corresponding luminescence spectra of the electronic states.

of QDs, we also need to measure the low-energy excitations of the underlying nuclei—the lattice vibrations and the nuclear spin polarization. The lattice vibrations are often studied spectroscopically by Raman scattering, and the nuclear spin is typically probed through nuclear magnetic resonance (NMR). Unfortunately, conventional Raman and NMR spectroscopies are relatively insensitive and lack the selectivity necessary to probe individual QDs. However, the nuclear excitations do make themselves felt by the electrons, and it is possible to measure resulting energy shifts and changes in intensity of the electronic spectral lines in the optical spectra of individual QDs. By measuring these nuclear signatures, it is possible to obtain spectra of both the phonons (Fig. 9) and the nuclear spins (Fig. 10) associated with the particular QD that we are optically probing [3]. These QDs typically have about 10^4 nuclei, which is five orders of magnitude fewer than researchers have measured previously in semiconductors. Moreover, we potentially now have probes that are sensitive to chemical composition at a spatial resolution of 10 nm and a completely new and relatively complete perspective on the physics of QDs. Such ultrahigh-resolution probes are necessary as we attempt to understand and control material at the nanometer scale.

The research results described here were obtained through collaboration with S.W. Brown, D.S. Katzer, D. Park, and B.V. Shanabrook.

[Sponsored by ONR]

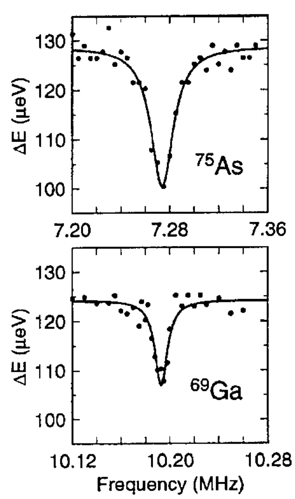

Fig. 10 — Nuclear magnetic resonance spectra of the ^{75}As and ^{69}Ga within a single QD. These spectra were obtained in a static magnetic field of 1 T by measuring the magnitude of the hyperfine shifts as a function of the frequency of a transverse RF field.

References

1. D. Gammon, E.S. Snow, B.V. Shanabrook, D.S. Katzer, and D. Park, *Science* **273**, 87 (1996).

2. D. Gammon, E.S. Snow, B.V. Shanabrook, D.S. Katzer, and D. Park, *Phys. Rev. Lett.* **67**, 2391 (1996).

3. D. Gammon, S.W. Brown, E.S. Snow, T.A. Kennedy, D.S. Katzer, and D. Park, *Science* **277**, 85 (1997). ◆

Ferromagnet-Semiconductor Nonvolatile Gates

M. Johnson and M.M. Miller
Materials Science and Technology Division

B.R. Bennett, M.J. Yang, and B.V. Shanabrook
Electronics Science and Technology Division

The field of digital microelectronics has consistently enjoyed incremental progress since its beginning, resulting in remarkable improvements in packing density and operating speed. This approach, however, is unable to confront fundamental problems of architecture. In particular, the paradigm for computer memory systems is intrinsically redundant. A high-speed, low-density dynamic random access memory (DRAM) is available for processing needs but is volatile—memory is lost when power is removed. Consequently, a high-density system with slow access times, such as a magnetic disk drive, is provided for nonvolatile storage. We have developed a novel magnetoelectronic device [1], which offers a new paradigm for memory systems—a single integrated nonvolatile random access memory (NRAM) that combines the speed of DRAM with the density and nonvolatility of magnetic storage. This kind of memory, which is also radiation hard, is appropriate for any Navy application requiring high density and low power consumption. The same attributes will lend the technology to a transition to broader applications.

Device Concept: The operation of the device is based on a simple concept, presented schematically in Fig. 11. A thin ferromagnetic film F is fabricated above a semiconductor Hall cross, electrically isolated from the carrier layer. One edge of F, the "active edge," is positioned over a central region of the cross. When F is composed of a transition metal ferromagnet, its magnetization M is constrained to the film plane and it can be made with an easy axis along the $\hat{x}$ axis so that M is bistable with orientations $\pm\vec{M}$ along $\hat{x}$. Figure 11(a) shows that, when M is saturated along $-\hat{x}$, a large magnetic fringe field B is generated by the "active edge," and this local field has a large component perpendicular to the plane of the carriers and pointing down, $-B_z$. The component $-B_z$ is spatially inhomogeneous but nonetheless is sufficiently large to apply a Lorentz force on the carriers in the semiconductor. When biased with a current I from left to right, a "negative" Hall deflection is generated on the carriers and a negative voltage is developed between terminals $S1$ and $S2$.

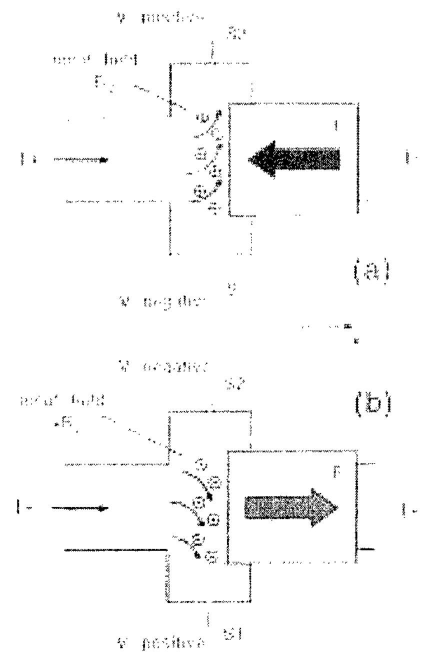

Fig. 11 — Device concept: (a) When the magnetization is $-M\hat{x}$, the field at the Hall cross is $-B_z$ and the output voltage $V_{S1,S2}$ is negative. (b) When the magnetization is $+M\hat{x}$, the field is $+B_z$ and the output voltage is positive.

Figure 11(b) shows that, when the magnetization orientation is reversed so that M is saturated along $+\hat{x}$, the magnetic fringe field near the "active edge" changes sign, the perpendicular component $+B_z$ changes sign, and a "positive" Hall deflection is generated. Thus, reversing the magnetization of F reverses the local field at the "active edge" and reverses the polarity of the output voltage at terminals $S1$ and $S2$. The result is a magnetoelectronic device with a very simple bilayer geometry and intrinsically bipolar output. By adding a small series resistance, the output levels can be shifted to zero (LOW) and HIGH. Combining the nonvolatility of the F element with the binary capability of the output characteristic, the device can be called a "nonvolatile gate."

Prototype Devices: Prototype device sets were fabricated using a high-mobility indium arsenide single quantum well for the semiconducting Hall cross. Dimensions of the device were the order of 1 μm. Figure 12 presents typical data from a device where F was a thin cobalt film with thickness $d_f \approx 150$ nm. By using a small lithographic asymmetry, the output levels correspond-

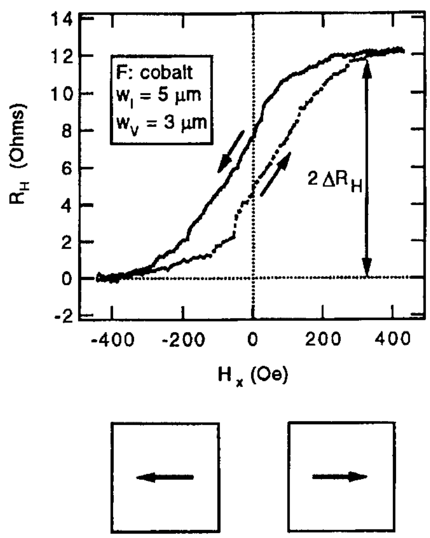

Fig. 12 — Typical data, R_H vs H_x at 295 K. Device HA1-B-I. Dotted line–sweeping field up; solid line–sweeping field down. The bottom diagrams represent magnetization states of F film for negative and positive values of H_x.

ing to saturation magnetization are LOW (approximately zero) and HIGH. The output amplitude is $2\Delta R_H = 12.1\ \Omega$, and the amplitude increases as the device dimensions shrink—the spatial profile of the fringe fields generated at the active edge of F is characterized by a submicron-length scale so that carriers in smaller structures experience a larger Lorentz force. Devices with 2-μm-wide arms have output levels of 0 and 20 Ω.

The cobalt film has substantial remanence so that two, well separated bistable output states, $R_H = 5\ \Omega$ and $R_H = 8\ \Omega$, exist in the nonpowered and nonvolatile state, $H_x = 0$. Ideally, the $R_H(H_x)$ traces would form a square hysteresis loop with the remanent magnetization equal to the saturation magnetization. In this case, the two bistable states would be those with magnetization saturated along $+\hat{x}$ and $-\hat{x}$ (refer to the diagrams at the bottom of Fig. 12), and the nonvolatile output states would have greater separation. Fabrication of F elements with square hysteresis loops requires the use of a suitable magnetic anisotropy, such as a shape anisotropy, and independent experiments on rectangular F elements show that square hysteresis loops can be achieved.

Conclusion: The Ferromagnet-Semiconductor Nonvolatile Gate is a novel magnetoelectronic device that has shown excellent characteristics. Demonstrated output levels of 0 and 100 mV are comparable with DRAM output, implying a relatively straightforward integration with RAM architecture. Optical measurements [2] have measured the switching speed of F elements to be about 1 ns, faster than DRAM write times. Beyond these favorable comparisons with DRAM, the device is radiation hard, its readout is nondestructive, and its memory is nonvolatile. Furthermore, the device is characterized by inverse scalability—output levels increase as dimensions shrink. Individual prototypes have been fabricated with submicron dimensions and have been successfully tested. This simple device structure may provide the basis for a paradigm shift in computer memory systems.

[Sponsored by ONR]

References

1. M. Johnson, B.R. Bennett, M.J. Yang, M.M. Miller, and B.V. Shanabrook, "Hybrid Hall Effect Device," *Appl. Phys. Lett.* **71**, 974-976 (1997).

2. W.K. Hiebert, A. Stankiewicz, and M.R. Freeman, "Direct Observation of Magnetic Relaxation in a Small Permalloy Disk by Time-Resolved Scanning Kerr Microscopy," *Phys. Rev. Lett.* **79**, 1134 (1997).

◆

Improved Models of Radar Backscattering and Radiowave Propagation Over Rough Ocean Surface

J.G. McGraw and K.D. Brown
Tactical Electronic Warfare Division

F.J. Ryan
Ocean and Atmospheric Sciences Division NCCOSC

Introduction: It is well known that backscatter from the surface of the sea limits the performance of radar surveillance systems. For shipboard radars and some airborne radars, detection of low-altitude targets, such as stealthy, sea-skimming antiship cruise missiles (ASCMs) and submarine periscopes at near grazing incidence can be complicated by large sea clutter returns. Sea clutter characterization, either empirically or theoretically, continues to be an active research area. Also, with the operational Navy deployed in littoral environments, where atmospheric ducting is common, sea

clutter coupled with propagation effects within the atmospheric boundary just above the sea surface presents an even greater challenge to the researcher.

Recently, the Navy electronic warfare (EW) community has increased its interest in sea clutter characterization and has begun appraising the state of knowledge in the field of radar sea clutter. Trends in the proliferation of advanced technology of ASCMs and emphasis on ship self-defense in littoral environments have prompted this renewed interest. Detection of low cross-section ships, such as the proposed DD-21, by sea-skimming missile threats typically involves very low grazing angles where sea clutter may dominate. This requirement to deal in a low grazing angle regime in littoral environments demands models that take into account the "spiky" nature of the sea and propagation within a nonstandard atmosphere.

Several high-fidelity physical models exist, which are based on the parabolic-wave equation (PE) that captures forward propagation in complicated atmospheric conditions, varying in both range and altitude; however, backscatter propagation is neglected in these models. A composite surface model for radar backscatter from a rough ocean surface has been constructed within a high-fidelity, range-dependent, PE-based propagation model called variable terrain radiowave parabolic equation (VTRPE). The primary scattering mechanism is assumed to be Bragg scattering for which normalized radar backscattering is proportional to the spectral density of the resonant Bragg water waves. The effects of tilt and modulation of the Bragg resonant waves by longer gravity waves are implicitly included in the PE calculation. A rough sea-surface gravity wave model based upon fetch, wind speed, wind direction, sea temperature, and surfactants (such as oil slicks) has been implemented.

Recently, the VTRPE model has been added to the Tactical Electronic Warfare Division Effectiveness of Electronic Warfare Systems (ENEWS) Program's inventory of models and simulations to aid in the evaluation of Navy EW performance in a variety of realistic tactical and environmental conditions. Initially, the model was used in an effort to generate a tactical memorandum (TACMEMO) for airborne radar operation in the Persian Gulf region. However, the model is expected to provide a more widespread applicability to the Navy EW performance evaluation.

VTRPE: The VTRPE model is a physics-based electromagnetic propagation code developed by the Naval Command Control and Ocean Surveillance Center RDT&E Division. The code is range-dependent and is suitable for prediction of signal strength in complex sea, land, or littoral environments for frequencies of 1 MHz to 100 GHz. The model physics incorporates refractive and ducting propagation paths as well as terrain scattering and diffraction. It is equally applicable to both radar (two-way propagation) and ESM (one-way propagation) applications. The model is based on the split-step Fourier PE algorithm and incorporates sophisticated internal error controls to automatically select appropriate range and altitude mesh grids. The model accounts for forward propagation and backscatter from rough dielectric surfaces as well as atmospheric refractive effects.

Figure 13 shows VTRPE output for a standard atmosphere and depicts the propagation factor (dB relative to free space) vs target altitude and range. The example is for an X-band airborne radar looking down from 245-m altitude. The characteristic lobing structure of the Lloyd's mirror is evident.

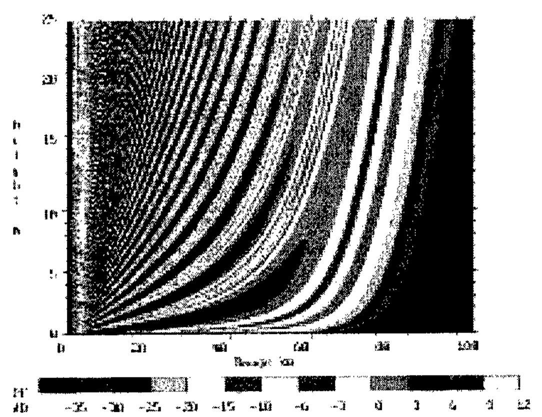

Fig. 13 — Propagation factor for a standard atmosphere.

Figure 14 represents the same sensor, except that the atmospheric refractivity profile is based on measured data collected during a SHAREM exercise in the Persian Gulf and contains a 250-m surface-based duct. The figure shows a large signal enhancement visible at 40 km, a significant "hole" between 50 and 90 km, and the beginning of a surface "skip" zone at 100 km. Clearly, the presence of the atmospheric duct has significantly changed the coverage diagram relative to the standard atmosphere case.

Rough Sea Surface Propagation: RF propagation over a rough sea is fundamentally

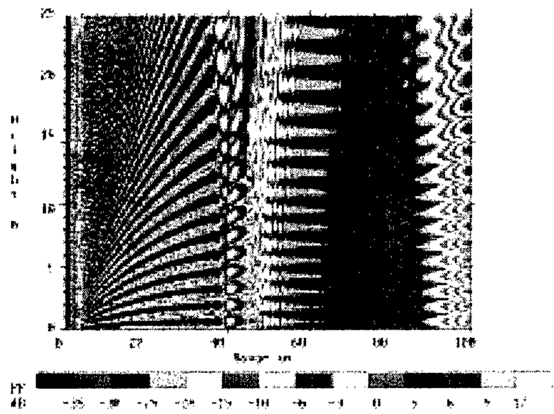

Fig. 14 — Propagation factor under ducting conditions.

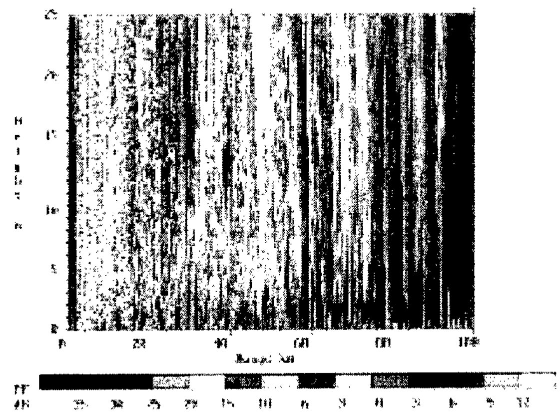

Fig. 15 — Propagation factor for rough ocean surface under ducting conditions.

different from a calm sea. The rough sea surface causes incident RF energy to be backscattered to the radar where it interferes with the target echo—surface clutter. (There is no surface clutter return from a smooth surface.) At low grazing angles, the surface clutter return is dominated by large amplitude, short duration "sea-spikes." For targets on or near the surface, the sea clutter often obscures or shadows the target echo thereby leading to a reduction in radar mean detection range. The amount of sea clutter is related in a complex fashion to surface wave conditions (wave height) and to the relative orientation of the radar antenna beam and wind direction, being lower when the radar is pointed perpendicular to the wind. In addition to producing surface clutter, the rough ocean surface modifies the forward scatter surface multipath leading to a vertical rotation in the lobing pattern and a filling-in of the interference nulls.

To simulate the effect of the rough sea surface, the VTRPE code employs a multiple forward scatter, single backscatter PE algorithm using a composite sea surface derived from a two-dimensional (2-D) spectral wave model Φ. In this model, the PE field is forward scattered from a nonflat ocean, while the backscattered signal is computed as Bragg scattering via distorted-wave Born approximation. The tilted ocean surface is formed by low pass filtering, where Φ for $k > k_B$, where $k_B = 2k_0\cos\theta$ is the Bragg wavenumber, and then constructing a realization of the resulting surface. This is illustrated in Fig. 15, again using the measured SHAREM data, only now showing the effects of a rough sea surface corresponding to a 20-knot wind speed.

2-D Wave Spectrum: At X-band, the Bragg wavelength is ~ 2 cm, which corresponds to surface capillary waves. The VTRPE code simulates a rough ocean surface by using an empirical 2-D surface wave spectrum Φ that covers the whole spectral domain from swell to capillary waves. For a random ocean surface, Φ is the spatial Fourier transform of the surface correlation function and is a function of wind speed, wind direction, and water surface tension. The spectrum is based upon the Donelan-Pierson directional wavenumber model for low wavenumbers coupled with a high wavenumber capillary wave model, and has the form $\Phi(k,\varphi) = k^4 F(k)D(k,\varphi - \varphi_0)$. The form factor F peaks at $k = k_p$ (which is wind speed dependent), falls rapidly to zero for $k < k_p$, and has a high wavenumber cutoff for $k >> k_p$ related to surface tension. The directional spreading function D controls the azimuthal anisotropy of Φ, having a peak in the direction of the wind $\varphi = \varphi_0$. This form for Φ differs from the traditional isotropic Pierson-Moskowitz spectrum in the high wavenumber capillary cutoff in F and the directional form factor D.

ENEWS Support: Radar Detection Analysis: In support of the preparation of a TACMEMO, ENEWS was tasked to recommend optimal platform altitude and associated antenna tilt for an aircraft equipped with a periscope-detecting radar sensor operating under various atmospheric and oceanographic conditions. The recommendations were based on the results obtained from VTRPE. Plots were produced showing target visibility for a given altitude as a function of antenna tilt, for a variety of sea states at a fixed altitude, and then for various combinations of altitudes and sea states. Finally, the models were run using actual atmospheric data and sea-state data recorded at a specific location and time.

Figure 16 shows the effect that wind speed has on detection performance when looking upwind. It is readily apparent that 15 knots of wind has a significant impact on performance. More typical wind speeds of 20 to 25 knots cause significant target fades. Severe fades are typically due to the wave washing over the periscope, reducing the signal to zero, rather than to a severe rise in clutter return. Reliable detection is reduced to ranges closer than 15 nmi, and even in this region, potential missed detections are probable.

Figure 17 shows the case of looking crosswind in sea-state 5 (25 knots of wind). The detection performance is improved because of the reduction of multipath effects.

Future Work: The current VTRPE sea clutter model includes (a) the effects of shadowing of the waves when the surface is viewed at low grazing angles, (b) the specular reflection from plane facets when viewed at near normal incidence, and (c) the effects caused by the presence of ducts. Backscattering in the model is based upon the Bragg backscattering resonance condition and does not include effects of foam, spray, and spilling waves—the suspected causes of sea spikes. Recently, data have been obtained from laboratory wind-wave tank experiments used to determine hydrodynamic sources of sea spike and its structure. These wave groupings will be input to VTRPE as a variable sea surface to investigate this sea-spike phenomena.

The current VTRPE sea clutter model is based upon scattering from a single realization of the ocean surface averaged along the radar look direction. This surface realization is derived from a directional 2-D gravity wave spectrum convolved with white Gaussian noise. However, this approach results in a "frozen" surface realization, with

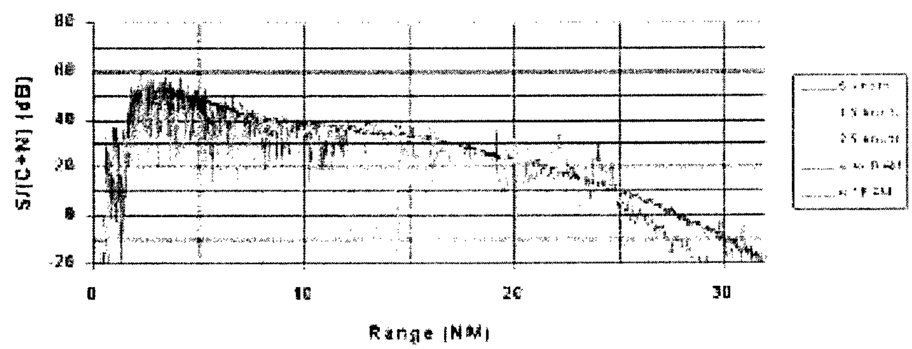

Fig. 16 — Visibility factor vs sea state.

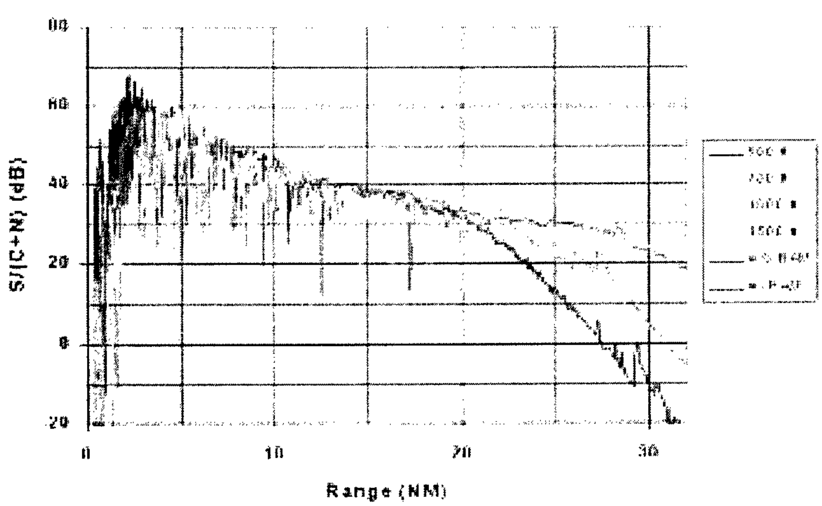

Fig. 17 — Visibility factor vs A/C altitude for sea-state 5.

surface relief independent of cross range or azimuth. The ocean surface model in VTRPE will be extended to include a realistic time-varying surface.

Finally, current ENEWS ASCM simulations perform multipath calculations between the missile threat and ship platform by using an average surface roughness factor, which imposes the following limitations: it overestimates the loss incurred due to multipath for high sea states, and the noncoherent scattering is not directly tied to the geometry of the missile flying over a realistic varying sea surface. Future ENEWS ASCM simulations will integrate the VTRPE forward scattering propagation algorithms.

[Sponsored by NAVAIR, ENEWS Program, and NCCOSC] ◆

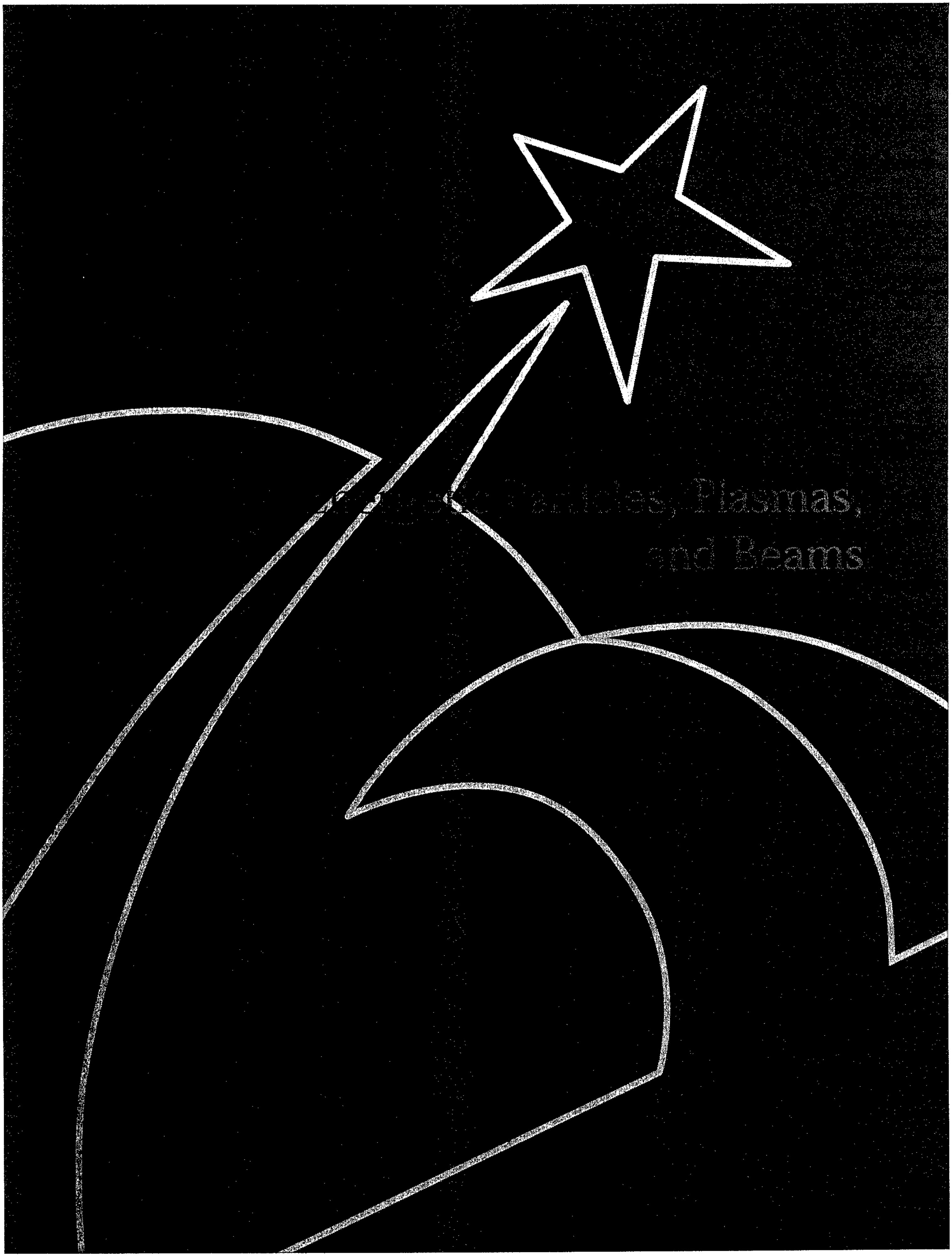

[illegible] Particles, Plasmas, and Beams

Near-Field Scattering Physics Research

D.J. Taylor, P. Loshcialpo, and S.L. Browning
Signature Technology Office

M.G. Parent and W.P. Pala
Radar Division

Introduction: Radar scattering is an area of intense interest both at NRL and elsewhere because of its great practical application in military targeting, detection, and tracking systems. Currently employed radar cross-section (RCS) methodologies focus on far-field solutions because radar threats and systems are designed to operate with targets in the far field. To generalize, most RCS research is based on far-field measurements, which are made in a monostatic mode; the results are then displayed in an amplitude-frequency or amplitude-time domain. However, these approaches provide limited information about the underlying physical mechanisms contributing to the scattered energy.

An advanced measurement/analysis approach perfected by the acoustics community at NRL assessed the near-field and wavevector dependent bistatic scattered acoustic fields to provide a rich source of information on acoustic scattering phenomenology in frequency wavevector ωk space [1]. We have successfully demonstrated the translation of the earlier NRL acoustic ωk approach into the realm of electromagnetics (EM) by applying the ωk algorithms to bistatic scattered EM fields in the near-field reactive region generated by high-fidelity computer simulations using numerical solutions to Maxwell's equations [2].

Near-Field Analysis: The EM equivalent of the acoustic work produced an ωk analysis of EM fields with only minor variations due to the vector nature of the EM fields. The utility of ωk space analysis is that it explicitly separates the near-field energy into radiating and nonradiating components, which we call supersonic and subsonic modes. The subsonic modes have unique signatures in ωk space that provide insight into the physics of the interaction of the incident wave with the scattering body.

A simple application of EM ωk analysis is shown in Figs. 1 and 2. Figure 1 shows the traditional far-field bistatic cross section of a 30-cm-long, 8-cm-diameter metal cylinder. The cylinder was simulated with both a smooth surface and a corrugated surface to demonstrate the different surface wave properties of these two configurations. The corrugations produce Bragg modes, which, depending on the frequency, are either propagating or evanescent. For example, one of these Bragg modes is responsible for the two additional lobes that appear near 75 and 280° in the bistatic amplitude at 5 GHz.

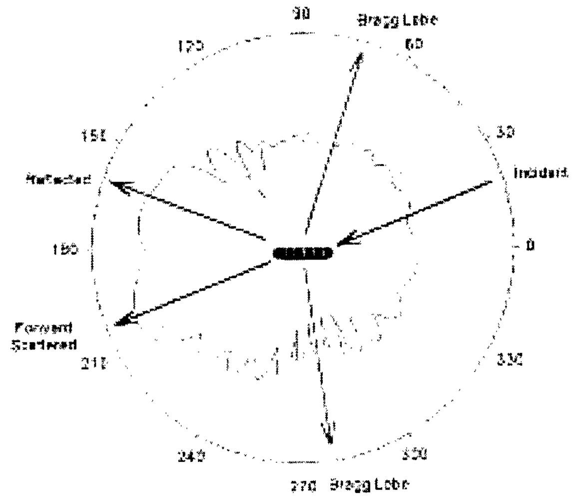

Fig. 1 — Simulated bistatic RCS of a metal cylinder 30-cm long, 8-cm diameter at 5 GHz; smooth surface, black; corrugated surface, red. The major lobes at 160 and 200° are reflected and forward scattered energy. The grooves in the cylinder create additional lobes in the far-field pattern near 70 and 280° not present in the pattern for the smooth cylinder. The incident wave is polarized with the electric vector in the plane (HH), and the incident angle is 20°.

Figure 2 shows that, in ωk space, the mode responsible for these additional lobes appears as a single straight line. The amplitudes in ωk space fall into two distinct regions—a central V-shaped region, which contains the propagating mode energy, and all amplitudes outside this area, which are evanescent. The brightest line sloped up to the right represents the strong reflected and forward scattered waves from the body and has a slope equal to $df/dk_z = c_0/(2\pi\cos\theta_{inc})$. The series of lower intensity lines that run parallel to this bright line represent axial Bragg modes induced by the periodic corrugations. The Bragg modes are separated in k space by $\Delta k_z = 2\pi n/d = 126\ m^{-1}$, where d is the spacing of the grooves in the surface and n is the Bragg mode index. The $n = -1$ mode is evanescent for frequencies below 3.1 GHz, but at 5 GHz it is well within the propagating region. This mode, at 5 GHz, has a small negative k_z value, which indicates that it is moving in an opposite direction from the incident wave and at

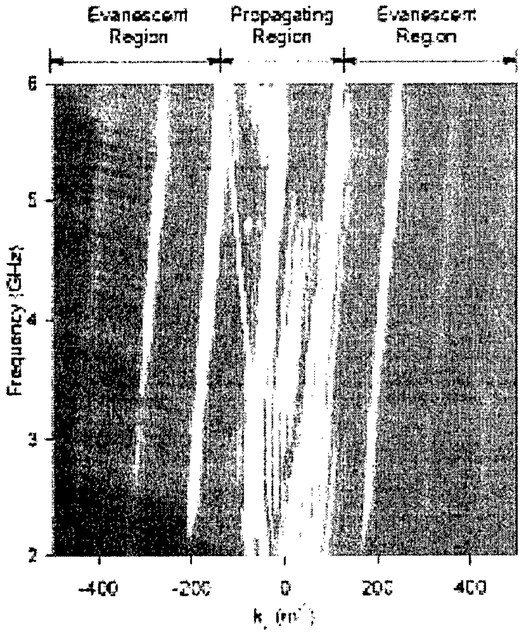

Fig. 2 — Amplitudes in ωk space for azimuthal mode $m = 0$ of the corrugated cylinder described in Fig. 1; white lines have been added to delineate propagating/evanescent regions. Strong forward and reflected energy appears as a bright line at propagating/evanescent region boundary. The remaining lines are Bragg modes, which are largely evanescent; at 5 GHz, one of the modes lies in the propagating region and is the source of the additional structure in the far-field cross section seen in Fig. 1.

an angle nearly perpendicular to the z axis; this is exactly where we observe the two lobes in the bistatic RCS spectrum shown in Fig. 1. At frequencies below 3.1 GHz, these features disappear from the RCS spectrum because the underlying Bragg mode becomes evanescent.

The utility of the ωk analysis tool in electromagnetics is clear; in the example shown, the far-field bistatic RCS was able to provide only a partial picture of dynamics of the scattering from the corrugated cylinder. On the other hand, the frequency wavevector approach was able to provide a concise image of the dynamics of the Bragg mode driven scattering. Future work in this area includes constructing a small-scale facility to measure microwave near fields for subsequent ωk analysis and theoretical research into the application of ωk methods to arbitrarily shaped objects.

[Sponsored by ONR]

References

1. E.G. Williams, "Supersonic Acoustic Intensity," *J. Acoust. Soc. Am.* **97**, 121-127 (1995).
2. D. Taylor, P. Loschialpo, E. Williams, and W. Pala, "Dispersion Analysis of Surface Waves in the Near Field," Proceedings, *Progress in Electromagnetics Research Society*, Cambridge, Massachusetts, July 7-11, 1997, p. 146. ◆

New Multiband Infrared Detector Array for Advanced IR Seekers

E.F. Williams
Tactical Electronic Warfare Division

Introduction: The Tactical Electronic Warfare Division is developing an advanced multiband infrared (IR) detector array and signal processing technology, which is used in an IR seeker simulator. The seeker simulator will be used to evaluate the effectiveness of the fleet's IR countermeasures for the year 2000 and beyond. The detector array used in this seeker simulator must have the capability to scan a 30° area on the sea surface at the horizon and a few degrees below the horizon with high spatial resolution (1 mrad or less) and include as many subbands of the IR as possible. The subbands of the IR selected for this task are those appropriate for use by an IR guided antiship missile. Figure 3 shows the detector housed in a dewar with the control electronics. To reduce the cost of the seeker design, the new detector, replacing an older technology detector dating from the mid 1980s, was designed to fit in an existing telescope and gimbal assembly. This article discusses problems caused by this 1980s design and the technical challenges that had to be overcome to develop the new detector arrays.

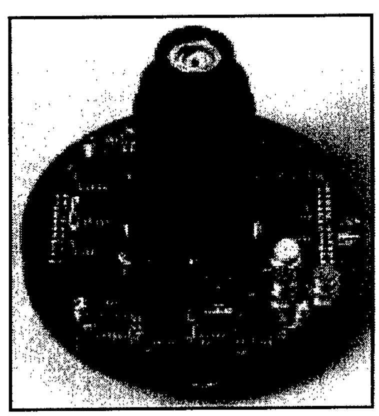

Fig. 3 — New detector dewar and post-amplifier package.

Technical Challenges: The first design issue was improvement of the vertical spatial resolution of the array. The old design covered the required 1.5° vertical field of view with eight detectors of variable height. Figure 4 shows a layout of the old and new detector arrays. The inner four detectors have a vertical field of view of 1.5 mrad, the next detector going out from the center in both directions is 3 mrad, and the detectors on the top and bottom of the array are 6 mrad high. Summing these detector heights would total 24 mrad, or approximately 1.5°, with high spatial resolution in the middle of the array and low resolution at the ends of the array. Imaging two bands of the IR with this scheme required 16 detectors and 16 wires coming out of the detector preamplifier and flexed by the gimbal used to scan the array over the 30° azimuth field of view. The compromised resolution of this system (for all but the i fier detectors) was set by the detector technology of the time in that 16 detectors was the limit of the number that could be handled in the dewar. The new design required 32 elements each of 1 mrad height to give the high spatial resolution required. For a two-band detector, this design would have required 64 wires from the gimbal, causing a very high torque on the gimbal motors. This consideration drove a design decision to move the offset, gain, and analog-to-digital conversion to circuits out of the detector dewar package (circuit boards on back side of Fig. 3). Redesigning the detector package and electronic readout and control in this way meant that only a high-speed serial digital line was coming off the gimbal, reducing the torque load on the gimbal motors.

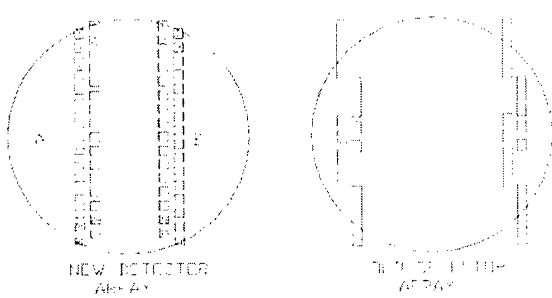

(a) (b)

Fig. 4 — Layout of (a) new detector array and (b) old detector array.

The next technical challenge involved moving the two vertical bands of detectors closer to the center of the field of view of the telescope. Because the blur circle of the telescope increased in direct proportion to the distance from the center of the primary mirror, the blurring of the image was reduced by moving the detectors closer to the center of the telescope; moreover, having the arrays closer together reduced the overscan required by the system. The spacing between the two arrays was mainly driven by how close the filter could be accurately mounted above them to minimize crosstalk between the channels. By controlling the location of these filters, a major reduction in array spacing was achieved. Two different filters also had to be cut, and the filter had to be placed over the two bands with a knife blade between the bands to prevent stray light from passing from one band to the other.

The processing of the data, including mux control, uniformity correction, offset and gain control, and pixel address correction from the staggered arrays, is accomplished by a microprocessor and programmable logic device (PLD) located on circuit boards mounted behind the detector on the gimbal and a VME microprocessor located in the system computer. Moving the analog-to-digital converter closer to the array improved the noise level by about 18 dB, resulting in a significant increase in sensitivity. The uniformity correction and gain for 32 elements per band instead of 8 elements per band is dramatically better. The VME computer, interpreting the data from the detector arrays, corrects the offset and gain based on the contrast and brightness in the image. Both the spatial offset between detectors within the band and the spatial offset between the bands had to be corrected by the signal processing algorithm in the VME computer.

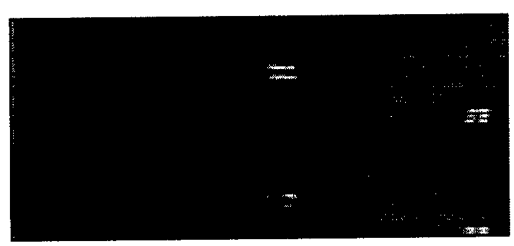

(a)

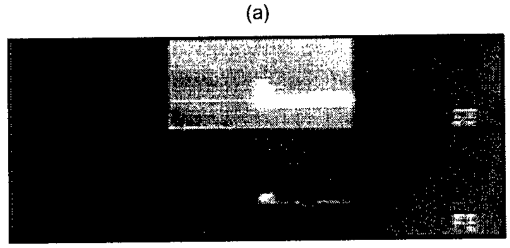

(b)

Fig. 5 — Image from (a) old detector and (b) new detector.

Conclusions: Figure 5 shows the improvement in the image quality from the old dual-band, 16-element detector (top) to the new dual-band, 64-element detector (bottom). All of this hardware was configured to fit in a small existing gimbal and had to function in an aircraft environment.

Acknowledgments: The authors thank Cincinnati Electronics for help with the design of the detector array and the manufacturing of the array and R.G. Hanson & Associates for the design of a new cryostat for the detector array.

[Sponsored by NAVAIR] ◆

Low-Cost Stack Modification for Enhanced Ship Survivability

D.S. Fraedrich and G.E. Friedman
Tactical Electronic Warfare Division

A. Landsberg and W.C. Sandberg
Laboratory for Computational Physics and Fluid Dynamics

Introduction: Stealth is becoming an integral part of future weapons platforms. The U.S. Air Force took the lead in this area, designing such aircraft as the F-117, the B-2, and more recently the F-22. Operation Desert Storm showed that stealth not only provides an advantage in a war, but it fundamentally changes the way in which the war is fought. More recently, radar signature reduction technology has been applied to naval ships, such as the U.S. Arleigh Burke-class destroyer, the Israeli *SA'AR 5*, and the French *Lafayette*.

The U.S. Navy is embarking on a new ship construction program, the SC-21, which is scheduled to be commissioned in 2008 (for more information, see http://sc21.crane.navy.mil on the World Wide Web). The Navy has recently funded several studies to determine the most cost-effective level of stealth technology to incorporate into the ship in both radar and infrared (IR) bands [1]. This investigation concluded that incorporation of significant levels of stealth technology is a cost-effective way of improving the ship's electronic warfare capability. This important result, as well as a significant body of previous work in IR signature control, suggested what IR signature reduction measures could be incorporated retroactively into existing ships.

Infrared Ship Signature Basics: The IR signature of a modern well-designed ship (which has blocked internal heat sources from reaching the ship's outer surface) comes from two main sources—the hot stack (where the ship's turbines exhaust) and the remainder of the ship (the hull and superstructure). The hull and superstructure signature is mostly due to solar heating. Signature reduction efforts on this second component were discussed in the *1997 NRL Review* [2].

The stack signature is also chiefly due to two sources—the gaseous emission from the hot turbine exhaust or plume (mainly emitting carbon dioxide at 4.3 μm) and the broadband emission from the metal uptake, which has been heated to elevated temperatures by the hot plume. In recent years, the United States and several other navies have designed stack suppression devices that focus on reducing both the plume temperature and the temperature of the hot metal uptake.

Need for Stack Suppression: The current stack suppression technique used on modern U.S. ships is called the boundary layer induction stack suppression (BLISS) system. Past IR measurements of this system by NRL indicate that, while the system is effective at reducing stack signature, it does not meet the requirements defined by the recent studies. A number of technologies are available that could provide improved suppression for existing ships, but generally these backfit approaches are cost prohibitive. NRL confronted the challenge of specifying an effective low-cost design that could be easily retrofitted to existing ships.

Modification of Current Design: A joint effort between the Tactical Electronic Warfare Division (TEWD) and the Laboratory for Computational Physics and Fluid Dynamics (LCP&FD) has resulted in an effective, low-cost stack modification that lowers IR signature and improves IR decoy effectiveness. In this simple design change, the top of the BLISS uptake is truncated to minimize the area of exposed hot metal visible, as opposed to reducing the metal's temperature (Fig. 6). Historically, NAVSEA stack design rules encourage making the stack height high to minimize any exhaust "blow down" onto the deck that might get drawn into inlet vents, affect personnel on deck, or impair helicopter operations. Until recent concerns over IR ship signature levels, there was no reason to try to minimize the area of this hot metal.

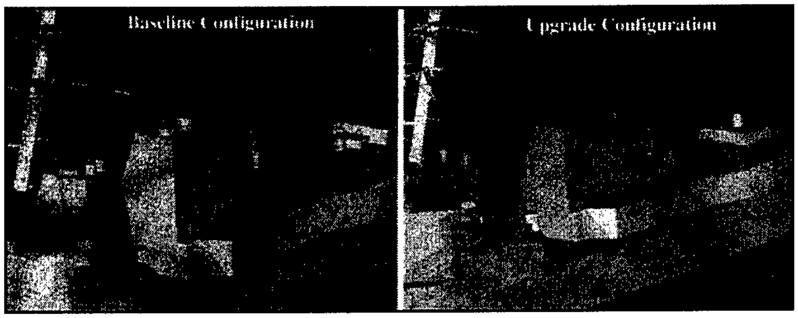

Fig. 6 — Comparison of the existing and new stack designs. In the new design, notice the slightly raised stack housing and the removal of the BLISS caps.

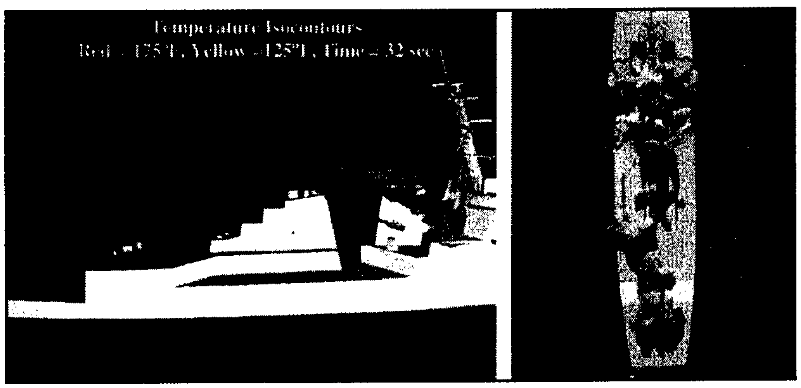

Fig. 7 — Example output of the FAST3D model, showing typical temperature contours for the baseline configuration.

Analyses by TEWD have predicted significant signature reduction and improved decoy effectiveness if such a modification were implemented on an Arleigh Burke-class destroyer. The LCP&FD performed detailed "air wake" studies to predict the impact of this modification on ambient temperature and stack gas concentration at key locations on the deck and at critical intake vent locations. These computational fluid dynamics simulation studies, using the FAST3D code developed within the LCP&FD, predict negligible impact of the stack modification at the aforementioned critical locations. Figure 7 shows an example of computed temperature contours.

Because this design change is a shortening of the existing uptake (plus a simple heightening of the stack housing), the cost and engineering to modify the design and drawings are minimal. Such a design will also have the unintended benefit of reducing topside weight and obviates the need for high-maintenance, radar absorbing material in this area. This modification is expected to be implemented on DDG-89 as well as subsequent ships in the class.

Summary: Cooperative research at NRL between TEWD and LCP&FD, each bringing its own unique expertise to the problem, has resulted in a practical, low-cost, effective way to drastically reduce a major source of IR signature on an important class of U.S. surface combatant. This approach will reduce topside weight and simplify the radar signature design as well.

[Sponsored by NAVSEA]

References

1. C.H. Goddard, D.G. Kirkpatrick, P.G. Rainey, and J.E. Hall, "How Much Stealth?" *Nav. Eng. J.*, 105, May 1996.

2. R.F. Brady, J.D. Adkins, and D.S. Fraedrich, "Low-Solar Absorbance Paint," *1997 NRL Review*, p. 80.

X-ray Backscatter Inspection of Sonar Domes

C.F. Poranski,[1] E.C. Greenawald,[2]
L.J. Levenberry,[2] and Y.S. Ham[3]
[1]*Chemistry Division*
[2]*GeoCenters, Inc.*
[3]*ONR Postdoctoral Fellow*

Oliver Hazard Perry (FFG-7) class frigates are equipped with rubber domes that provide an acoustic window and a hydrodynamic fairing for the ship's sonar. The 7-m-long domes are similar in construction to large tires, as shown in Fig. 8. Periodically, when a ship is in dry dock, the sonar dome must be removed and x-rayed to detect broken steel cords that could allow it to rupture. The Navy plans to lower ship maintenance costs in the future by increasing the interval between dry docking and by doing more maintenance tasks pierside; however, less frequent inspections would increase the risk of dome failures at sea. In response to this dilemma, NRL has developed and fielded a pierside sonar dome inspection system based on a new technology known as X-ray backscatter tomography (XBT).

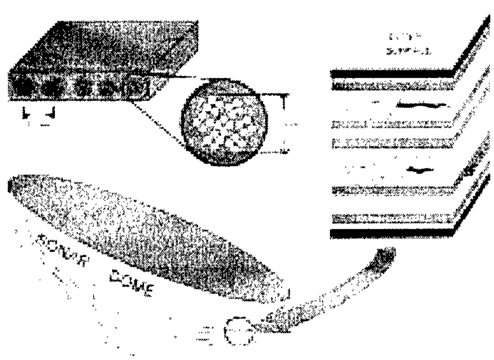

Fig. 8 — A complex lay-up of longitudinal and radial plies, the AN/SQS-56 sonar rubber dome is subject to failure at known high-stress regions. The insets show the steel cord configuration, ply structure, and typical failure sites.

Backscatter Imaging: Of the processes that can take place when X rays interact with matter, Compton scattering predominates in the range of energies commonly used in industrial radiography. In this interaction between an X-ray photon and an electron, the photon is propagated in a new direction with a reduced energy. This scattering occurs in all directions, including back toward the source. Since electron density varies with a material's physical density, a map of the sampled backscattered X-ray intensity from an object can be interpreted as an image representing an object's structure. Unlike conventional radiography, backscatter imaging does not require access to both sides of the object. However, the method is seldom used because attenuation within the object limits inspection depth and can cause artifacts that interfere with image interpretation. Backscatter imaging applications have thus been confined to detecting flaws near the surface of low-density materials.

System Development: In a feasibility study, we used two prototype research devices and a newly available commercial instrument to acquire backscatter data from sonar dome material samples. The commercial system, made by Philips, produced the best results. Its X-ray beam and complex system of slit apertures and multiple detectors scans 22, 5 × 10-cm tomographs simultaneously. Like a medical CAT scan, each tomograph represents a "slice" through the object. The scanner's compact modular design also simplified our plans for remote underwater use. After installing the Philips system at NRL's Chesapeake Bay Detachment, we obtained four sonar domes with internal damage of varying severity. During trial scans, we optimized the detector aperture geometry, X-ray parameters, and dome scanning sequences. We also discovered that a load applied to the dome's wall by partially filling it with water separated the broken cord ends and improved their detection. (We later achieved the same effect on ships with the sonar dome pressurization system.) Attenuation of the scatter signal by the dome's layers of steel cords resulted in poor images, but we were able to improve them by employing image processing methods. Software was also developed to display and analyze the copious data produced by each inspection.

To make the system transportable, we installed the various subsystems in an electronics van designed to serve as a control room in the field. We then took advantage of three opportunities to inspect sonar domes on dry-docked frigates. In each case, the scanner was positioned to inspect a series of rectangular areas covering the high risk regions. Severe damage was detected on all three domes, which were subsequently removed and x-rayed to confirm the results. Figure 9 is a composite of XBT images showing damage to a longitudinal ply of the USS *Nicholas* (FFG-47) sonar dome.

Having demonstrated inspections without dome removal, we next tackled the underwater

implementation. Our submersible system design consisted of a hull attachment fixture, a hydraulic manipulator, an enclosure with a thin aluminum X-ray window to contain the scanner, and a 20-m umbilical to the control room on the pier. To inspect a dome, divers first attach the fixture to the ship's keel. The X-ray window is then moved through a series of positions on the dome surface by the remotely controlled manipulator, with feedback from position sensors and underwater video. An XBT scan is conducted at each position.

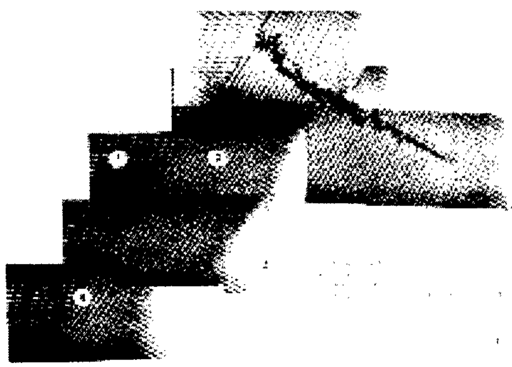

Fig. 9 — This composite of tomographs shows a broken longitudinal ply in the USS *Nicholas* (FFG-47) sonar dome. Construction features, such as ply edges and intersections, also appear in the images and help identify the damage location.

Pierside Trials: A series of trials were begun with an inspection of the USS *Samuel B. Roberts* (FFG-58) at Norfolk Naval Station (Fig. 10). During this shakedown deployment, we identified the need for several adjustments and modifications. Three subsequent trials at the Mayport Naval Station, Florida, resulted in additional improvements and conclusively demonstrated the new inspection

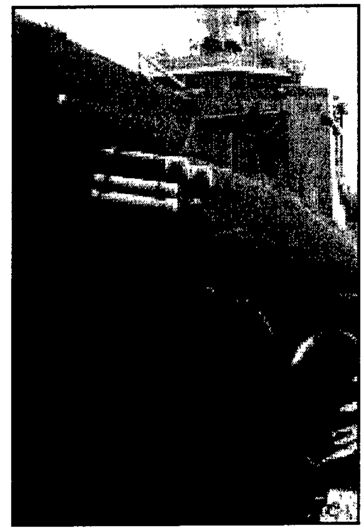

Fig. 10 — The submersible XBT system is retrieved by a crane after inspecting the USS *Samuel B. Roberts* (FFG-58) sonar dome at Norfolk Naval Station. The X-ray scanner and its umbilical are seen below the hull attachment fixture. The large orange pontoons are flooded to control descent.

capability. As an indication of the sensitivity of XBT, tomographs of the USS *Boone* (FFG-28) dome revealed a single broken cord.

Conclusion: The NRL pierside sonar dome inspection system has been demonstrated to be effective. The Naval Sea Systems Command has notified fleet commanders of this new capability and recommended its incorporation into maintenance plans. We can expect a more effective sonar dome inspection program, with better management of failure risks, cost savings, and improved readiness.

[Sponsored by NAVSEA and NRL] ◆

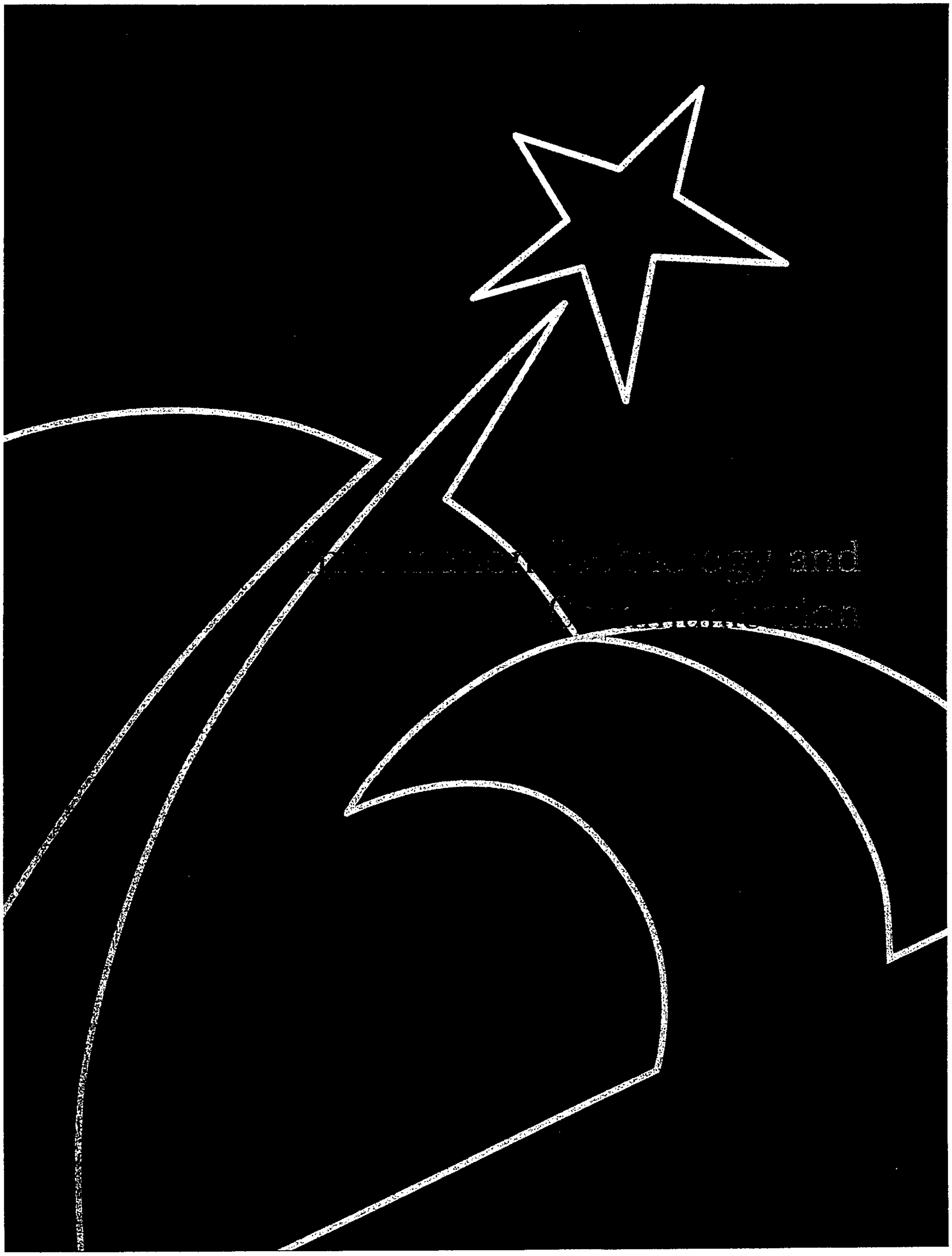
Information Technology and
Communication

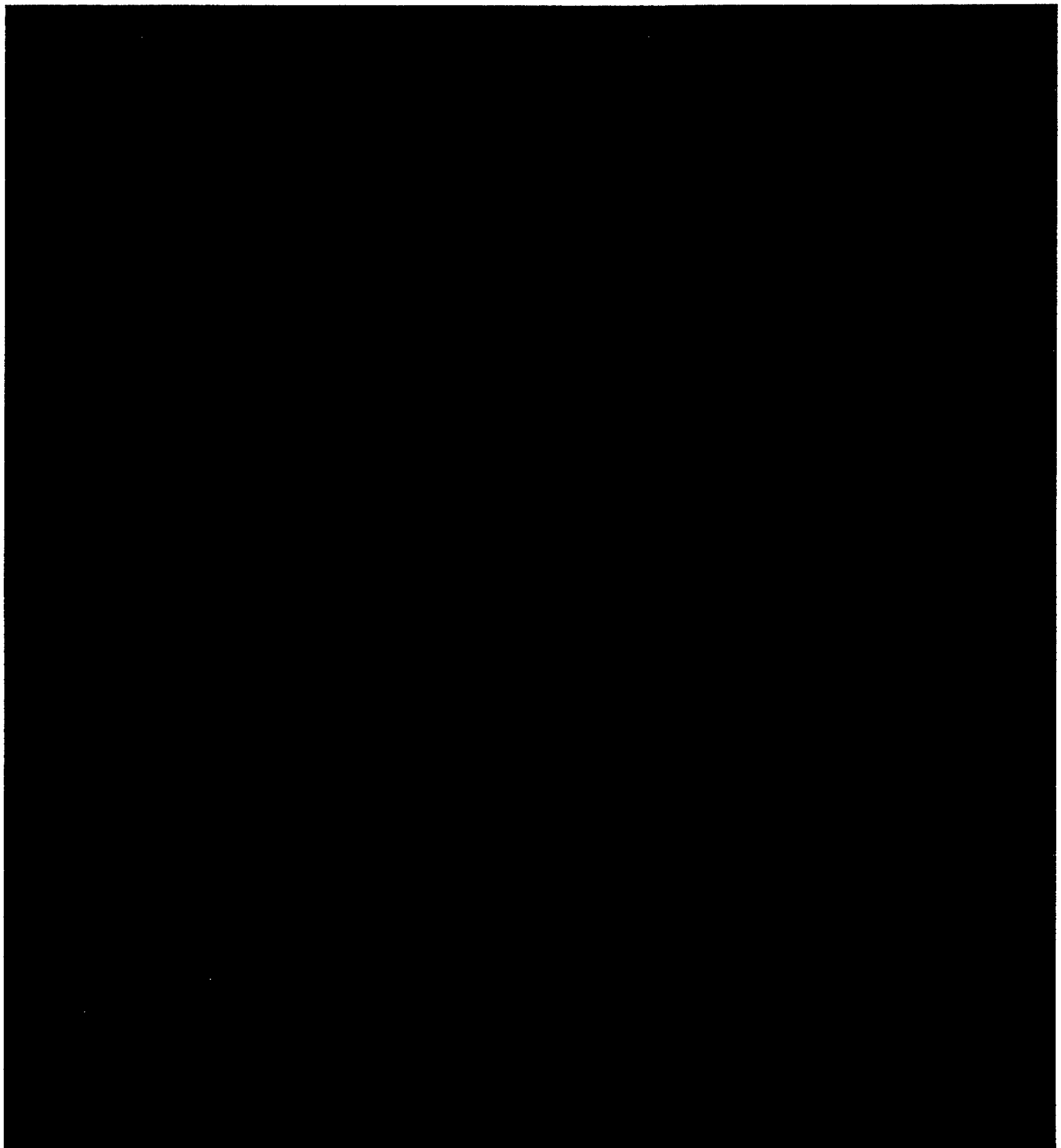

Identification of Distant Ship Smokestack Insignia

B. Kamgar-Parsi,[1] T.C. Zenner,[2] B. Kamgar-Parsi,[1]
J.C. Sciortino,[3] and A. Khan[4]
[1]*Information Technology Division*
[2]*U.S. Naval Academy*
[3]*Tactical Electronic Warfare Division*
[4]*Kaman Sciences Corporation*

Monitoring surface ship traffic is a problem of considerable interest to organizations such as the U.S. Navy, international regulatory agencies, and insurance companies. This problem is being pursued by various Navy organizations in a number of ways, such as radar signature identification, smokestack insignia recognition, and superstructure shape identification. A joint effort by NRL's Information Technology and Tactical Electronic Warfare Divisions has resulted in considerable progress in solving the challenging problem of smokestack insignia identification. The problem requires finding the best match to the encountered insignia in the database of registered shipping line insignias and deciding whether the match is correct. The database of registered insignias, despite its huge size (several thousand items), is incomplete. The problem is further complicated if the extracted insignia (from an image background) is degraded by such factors as its distance or the existence of discrepancies among individual insignias representing the same shipping line. A distant target is typically subject to blurring, noise, and other distortions, so that when it is matched to database items it may turn out to be less similar to its own ideal model than another database item. In this article, we describe the approaches we have developed for processing and indexing the insignias as well as dealing with distant insignias to reduce the likelihood of misidentifications. We note that searching through a large database of almost similar items is an extremely tedious task for a human operator and requires at least some level of automation. The techniques developed here are suitable for building a fully automated system as well as a decision aid to facilitate and enhance the performance of the operator. Figure 1 is a typical image of ships, and Fig. 2 shows a small sample of the database of registered insignias.

Indexing the Database: Searching a database for an item of interest requires indexing, or organizing, the database. Indexing massive databases of visual patterns is an active area of research, which has many applications such as retrieving information from still image or video archives, searching registered trademarks, and identifying fingerprints. Common techniques for indexing visual databases have not yet emerged and appear to be strongly application specific. Unlike the impression given by Fig. 2, smokestacks come in a variety of shapes, including rectangular, trapezoidal, cylindrical, tall, and short. Insignias painted on smokestacks tend to assume the shapes of those smokestacks, and the geometrical proportions of the painted insignia may be significantly different from the registered insignia. For example, consider the insignia in Fig. 2, bottom row, first left, which consists of a black horizontal segment at the top, a blue segment with a circle/star pattern in the middle, and a black segment at the bottom. In a painted insignia, the relative widths of these horizontal segments are typically different from the ideal database insignia; also the circle diameter may be larger or smaller relative to the width of the blue segment. Thus, in an insignia extracted from a real image, neither the boundaries nor the geometric proportions are reliable. These factors result in the failure of conventional pattern matching techniques to align (with an affine transformation) and compare an extracted insignia with database insignias.

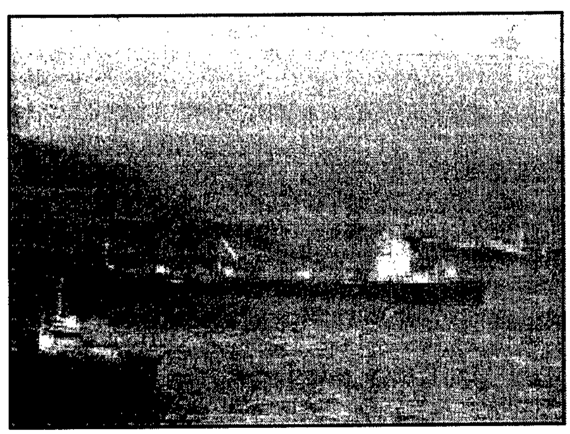

Fig. 1 — Merchant ships with smokestack insignias showing.

After considering and testing several alternatives, we have converged on a representation resembling a qualitative, semantic description of the insignias. This representation avoids the difficulties associated with conventional techniques. Inspection of the insignia database shows that two frequently occurring features are horizontal lines and segments. Therefore, we represent the insig-

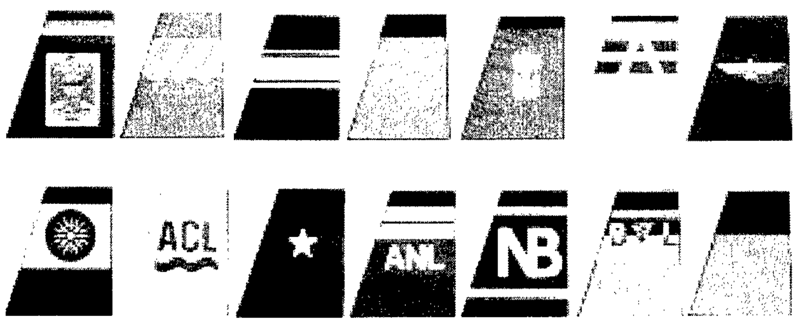

Fig. 2 — A sample of registered shipping line insignias from the database.

nias in terms of the number of horizontal segments, their colors, and the presence or absence of patterns. For example, the insignias in Fig. 2 are described as follows. Bottom row, first left has three horizontal segments (top to bottom): black, blue with pattern, black; bottom row, second left has one horizontal segment: white with pattern. We have developed algorithms that process the database insignias and generate such representations. Horizontal lines are detected from the Hough transform of the gradient image, and the existence of pattern in a horizontal segment is inferred from the color variance of the segment. There are a number of color spaces one can work in to process color images. We have found it most convenient to use the normalized red, green, blue (RGB) space, which is noncircular and insensitive to illumination intensity. Segment colors are represented by the numeric value of the mean normalized RGB and their variances.

To find the best match to an insignia extracted from an image, the processing algorithm is applied to it to generate its representation in terms of the number of horizontal segments. The search algorithm then searches among the database items with the same number of horizontal segments, comparing the corresponding segment colors. The algorithm currently compares colors, even when a segment contains a pattern. Higher levels of sophistication in pattern matching can be incorporated if the image resolution supports it.

Distant insignias: A major source of difficulty in solving this problem reliably is that often the ship is at such a great distance from the camera that the extracted insignia may appear less similar to its own ideal model than another database item. This kind of difficulty is present in many image-recognition applications. Figure 3 shows a recent example from optical character recognition.

To deal with this difficulty, we have developed an approach where the database is enriched to include appropriately degraded versions of the ideal items in the original database. The effectiveness of enriching a database of real images with synthetic distorted images has been demonstrated in a pattern-recognition application in a joint effort by NRL and Michigan State University [1]. One of the image-degradation processes we have particularly experimented with is blurring. The database is enlarged by progressively blurring each ideal insignia and processing it to obtain its representation. When the representation changes, we insert the blurred item in the database. For example, consider the insignia in Fig. 2, top row, third left, which has seven horizontal segments. When we blur it slightly, it still has seven segments, but as we continue to blur it, it eventually appears to have five segments of black, pink, white, pink, and black. This blurred version is then included in the database. When a real blurred instance of this insignia is encountered, its representation matches

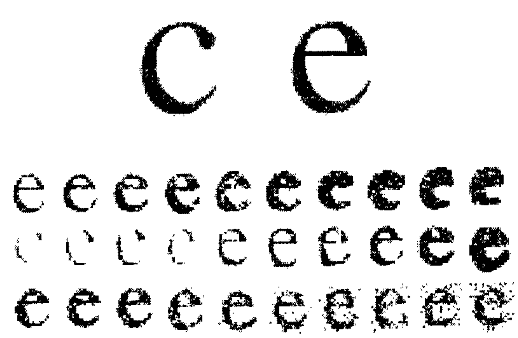

Fig. 3 — An example of degraded versions of a given pattern, which can become more similar to a different pattern. Ideal "c" and "e" and degraded versions of "e" due to blurring (top row), thresholding (middle row), and noise (bottom row). From Ho and Baird, *IEEE Trans. Pattern Analysis and Machine Intelligence* **19**, 1067-1079 (1997).

the blurred version of the ideal insignia. In this manner, the likelihood of misidentification of blurred insignia extracted from images is considerably reduced.

Future Work: The algorithm we have developed processes an extracted insignia and finds and displays best matching database items. Tests on a limited database of about 200 items show promising results. A number of improvements remain to be implemented to develop a usable system as a decision aid for an operator, and even greater challenges remain to make it fully automated. In our tests thus far, insignia extraction from images is done manually; algorithms need to be developed to automate this task. These algorithms will be rather straightforward if the system is used as a decision aid, where the operator places the cursor on the insignia or selects a window around the smokestack to initialize the insignia extraction algorithm.

The insignia representation used here is based on segmenting insignias into horizontal regions. The segmentation algorithm is somewhat tolerant of the orientation angle, depending on how coarse we select the angular bins in the Hough transform. Nevertheless, for a more reliable system, the extracted insignia should be corrected for pose. The pose angle can either be provided by the operator or inferred from the ship orientation, for example, the waterline.

Image analysis algorithms typically involve a number of prespecified thresholds. Currently, our segmentation algorithm also involves a threshold. However, we are developing an algorithm that uses multiple thresholds and generates multiple representations of the same database item. The gains in reliability are expected to outweigh the increased processing and memory requirements.

It is well known that multispectral images are affected by atmospheric conditions. For example, haze scatters blue light more strongly than red; thus, on a hazy day the insignia colors appear more reddish. A preprocessing step for correcting such color distortions may improve the reliability of insignia identification.

Acknowledgments: We thank Tin Kam Ho and Henry Baird of Bell Laboratories for Fig. 3. Todd Zenner, Ens., U.S. Navy, was a midshipman at the U.S. Naval Academy. He is now attending graduate school at the University of Texas at Austin.

[Sponsored by ONR and ONI]

Reference

1. B. Kamgar-Parsi, B. Kamgar-Parsi, and A.K. Jain, "Generation of Exemplars Projecting Near the Classification Boundary for Visual Patterns," Proc. IJCNN 1998, to appear. ◆

Time-Frequency Processing for Radar Imaging

V.C. Chen
Radar Division

Radar range-Doppler (or cross-range) images are usually reconstructed by using the Fourier transform. To use the Fourier transform properly, the scatterers of the target being imaged must remain in their range cells and their Doppler frequency shifts must be constant. If the scatterers drift out of their range cells or their Doppler frequency shifts are time-varying due to rotational motion, the Doppler spectrum obtained from the Fourier transform will be smeared and the radar image will be blurred. In this case, to achieve a focused Fourier radar image, some sophisticated motion compensation algorithms must be used.

The restrictions of the Fourier transform can be circumvented if a time-frequency processing is used to replace the Fourier transform. Because of the time-varying behavior of the Doppler frequency shift, an efficient method to solve the problem of the smeared Fourier frequency spectrum, and hence the blurred image, is to apply a time-frequency transform to the Doppler processing. As is known, the Fourier transform indicates only what frequency components are contained in the signal; it does not tell how frequencies change with time. By replacing the Fourier transform with a high-resolution, time-frequency transform, the image blurring caused by the time-varying Doppler frequency shifts can be mitigated without applying sophisticated motion compensation algorithms.

Time-Frequency Processing: Time-frequency transforms include linear transforms, such as the short-time Fourier transform (STFT), and bilinear transforms, such as the Wigner-Ville distribution (WVD). The STFT is the simplest one, but its resolution is limited by the uncertainty principle. Although the WVD has the highest resolution, if the signal contains more than one component, it will generate cross-term interference that occurs at spurious locations in the time-

frequency plane. To reduce the cross-term interference, the filtered WVD can be used to preserve the useful properties of the time-frequency transform with slightly reduced time-frequency resolution and largely reduced cross-term interference. The WVD with a linear low-pass filter is characterized as a Cohen's class, such as Choi-Williams distribution (CWD), and the distribution with a nonlinear low-pass filter is the time-frequency distribution series (TFDS). Figure 4 shows the performance of these time-frequency transforms for a composite signal consisting of two chirp signals. The STFT has no cross-term interference, but it does have lower time-frequency resolution. The WVD has the highest time-frequency resolution, but it has serious cross-term interference. Depending on the order of the distribution, the TFDS has slightly lower time-frequency resolution than the WVD and even lower cross-term interference than the CWD. Because high time-frequency resolution and low cross-term interference are desired for our time-frequency processing, we chose the TFDS for these two characteristics as well as its easier implementation.

Radar Imaging of Moving Target: Figure 5 illustrates the radar imaging system based on the time-frequency processing. The only difference between the proposed time-frequency radar imaging system and the conventional radar imaging system is that the Fourier transform is replaced by the time-frequency transform followed by time sampling. The Fourier-based imaging approach generates only one image frame from a radar data sample. However, the time-frequency based imaging approach takes the time-frequency transform for each time history series and generates a time-Doppler distribution. By combining these time-Doppler distributions at range cells, a time-range-Doppler cube can be formed. Every element of the cube represents a full range-Doppler image at a particular time instant. Therefore, a two-dimensional (2-D) range-Doppler Fourier image frame becomes a 3-D time-range-Doppler image cube. By sampling in time, a time sequence of 2-D range-Doppler images can be viewed. Each individual time-sampled frame from the cube provides not only a clear image with superior resolution but also time-varying properties from one time to another.

The following examples demonstrate the time-frequency approach to radar imaging of a maneuvering target. The radar is operating at 9,000 MHz and transmits a stepped-frequency waveform. In each burst, a total of 64 stepped frequencies are used, and each frequency step is 7.5 MHz. The pulse repetition frequency (PRF) is 18,000 pulses/s. The translation motion of the target can be compensated by using standard motion compensation algorithms; however, because of the target's maneuvering, even after the motion compensation, the uncompensated phase error is still large. Therefore, the reconstructed image by using the Fourier transform is still blurred as shown in Fig. 6. By replacing the Fourier processing with the time-frequency processing, the single Fourier image frame becomes a sequence of time-varying image frames. Each of them represents a full radar range-Doppler image at a particular time instant. Figure 6 shows five frames extracted from the sequence of 16 time-varying image frames. We can

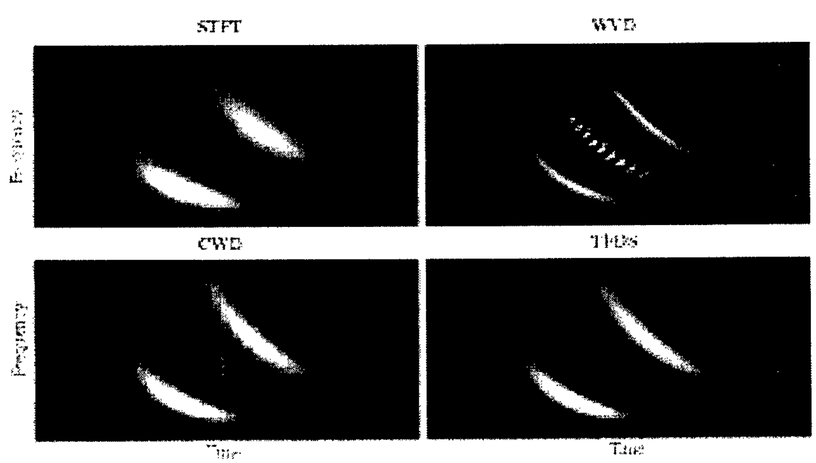

Fig. 4 — The comparison of the STFT, the WVD, the CWD, and the TFDS.

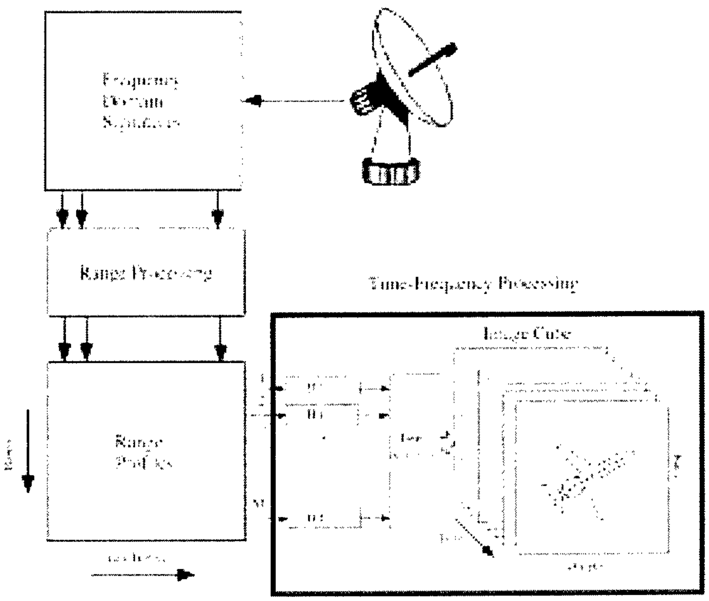

Fig. 5 — The radar imaging system based on the time-frequency processing.

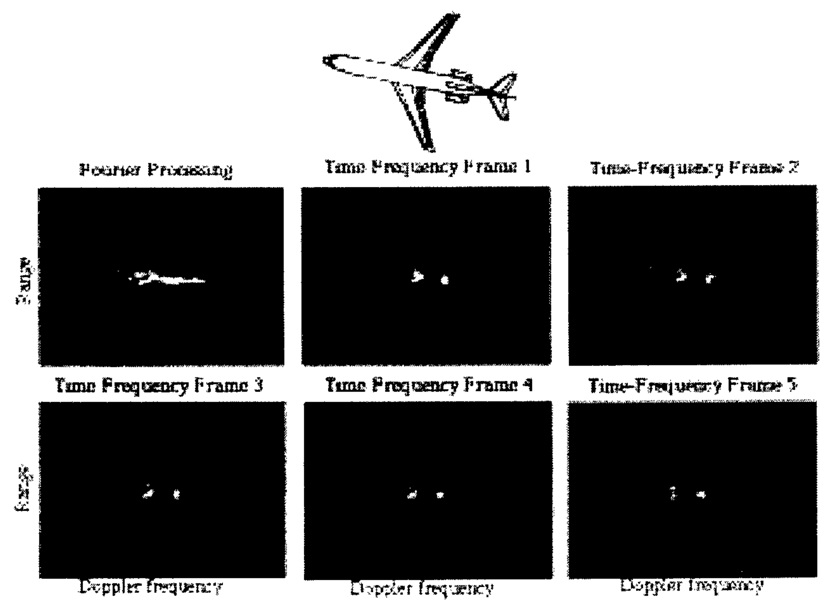

Fig. 6 — The radar image by using the Fourier processing and five image frames by using the time-frequency processing.

easily see that by using the time-frequency processing, the smeared Fourier image is resolved into a sequence of time-varying images with superior resolution.

Summary: We have demonstrated the advantage of using the time-frequency processing for radar imaging of maneuvering targets. The results clearly show that the time-frequency transform can be used to replace the Fourier transform as a means of radar image formation. The time-frequency processing can be used for radar imaging of multiple targets as well as ground moving targets.

[Sponsored by ONR] ◆

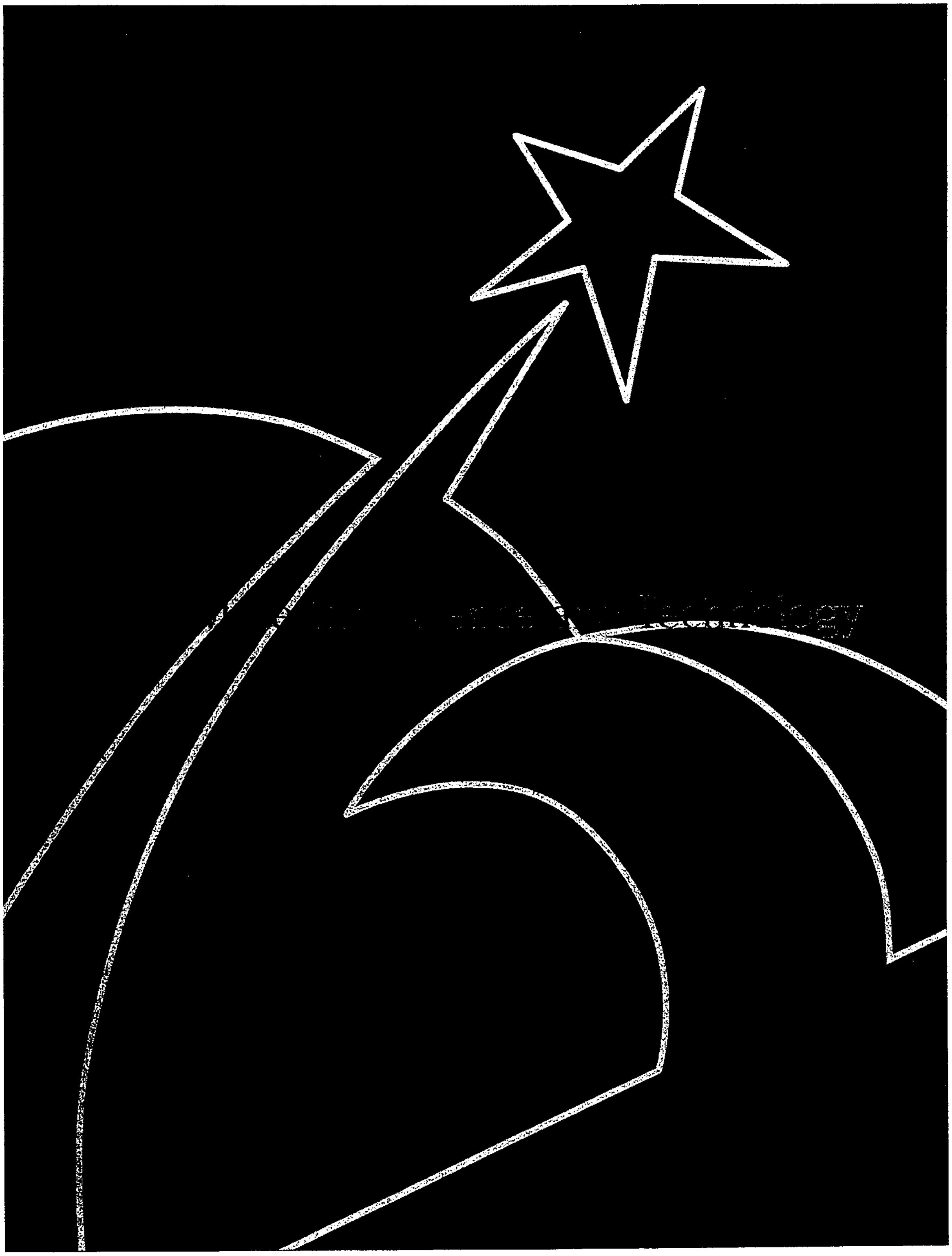

Phase Transformation-Induced Grain Refinement in Rapidly Solidified UHCS

K.P. Cooper, J.D. Ayers, and H.N. Jones III
Materials Science and Technology Division

The current trend in materials processing is to develop methods to manufacture products of near net shape. This is an approach that offers a promise for achieving U.S. Navy manufacturing requirements of affordability and high performance. High strength metal components with complex geometries and long life can be produced, thereby reducing procurement and maintenance costs.

The Objective: One method of near net shape processing is to produce metal powder with a desired microstructure and to consolidate the aggregate into the final geometry. Alloys that exhibit superplasticity are ideal candidates for this method of processing. One class of alloys in which superplasticity has been demonstrated is ultrahigh carbon steels (UHCS) [1]. These steels contain 1.5 to 2.5 wt. % C. They are brittle in cast structures because of the presence of continuous intergranular cementite and are thus not suitable as structural material. However, when thermomechanically processed to produce a fine-grained ferrite+cementite microstructure, they exhibit superior room-temperature strength and ductility and excellent high-temperature formability via superplastic deformation [2]. In previous work on consolidation of UHCS powders [3], coarse initial microstructures prevented direct superplastic forming, resulting in slow, uneconomical densification rates and requiring additional mechanical working. For rapid consolidation of UHCS, the ferrite and cementite grain size must not exceed 1-2 μm, a size that makes it easier for the grains to slide past one another and rotate with respect to one another to achieve superplastic deformation behavior.

The Approach: Our studies attempt to overcome some of the limitations mentioned above by using the higher cooling rates possible with the melt spinning process. The goal is to produce fully austenitic solidification microstructures having a grain size of a few μm and, through thermal treatment at modest temperatures, to form ferrite+cementite mixtures having the desired size, without the need for mechanical deformation. Our UHCS alloy contains 2 wt. % each of C, Al, and Cr; the latter two raise the eutectoid transformation temperature (A_1) and provide a wider temperature range for the decomposition of austenite. Cr also prevents graphitization, which is detrimental to the process. Cementite is precipitated from a rapidly solidified supersaturated solid solution so that it can be made finer than is possible with thermomechanical processing of bulk alloys. The experimental procedure involves making melt spun ribbons with the highest possible quench rate. The ribbons, which are about 2-μm wide and 20-μm thick, can easily be comminuted into particulate form. As shown in Fig. 1, the cyclic heat treatment involves three stages. In HT1, the as-cast ribbon is heated to a temperature below A_1 for 1 h; in HT2, the HT1-treated sample is heated to a temperature above A_1 for 4 min and water quenched; in HT3, the HT2-treated sample is heated to a temperature below A_1 for 1 h. After each processing step, the phases present in the microstructure and their size and shape are determined.

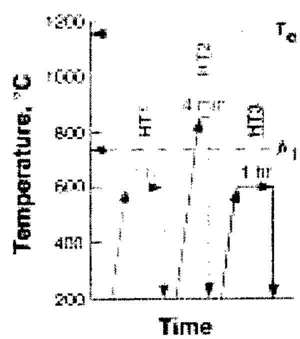

Fig. 1 — Cyclic heat treatment schedule. T_e and A_1 are the respective eutectic and eutectoid transformation temperatures for the binary Fe-C phase diagram and are provided for reference.

The Results: The as-cast microstructure is a nearly equi-mixture of austenite+martensite, as shown by the X-ray diffraction trace in Fig. 2. Scanning and transmission electron microscopy show that the columnar austenite cells and martensite plates are 0.5-1.0-μm wide but several μm long, with the cell boundaries decorated by a continuous film of cementite. After HT1, the microstructure consists of a mixture of ferrite and partially elongated cementite, making it unsuitable

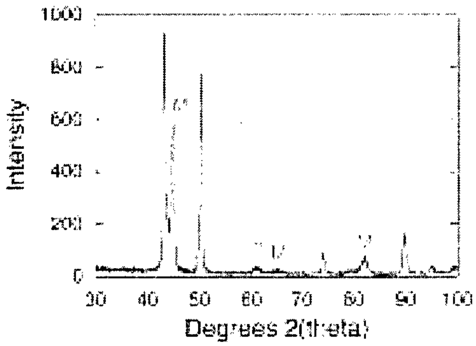

Fig. 2 — X-ray diffraction trace of as-cast melt spun ribbon showing presence of nearly equal volume fractions of austenite (γ) and martensite (M).

for superplastic forming; after HT2, the microstructure consists of a dispersion of fully spheroidized cementite within a fine-scale martensitic matrix; after HT3, the microstructure consists of spheroidal cementite surrounded by fine-grained ferrite, as shown in Fig. 3. The largest ferrite grain is only 0.25 μm across and 1 μm long and the mean cementite size is 0.2 μm. Quantitative

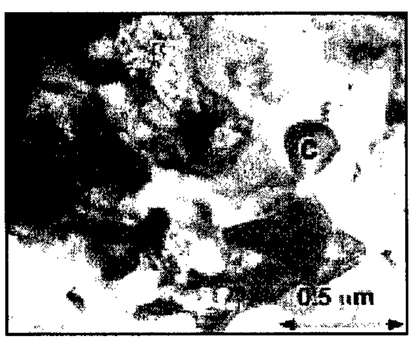

Fig. 3 — Transmission electron micrograph of HT3 sample showing 1 μm and less ferrite (α) grains and sub-μm cementite (C) particles.

analysis shows that the cementite size after HT3 increases only slightly from that after HT2. The HT3-treated sample is very ductile, as shown by the extensively dimpled fracture surface in Fig. 4.

The Mechanism: Both Cr and Al are ferrite stabilizers, but the C content is sufficiently high to cause the formation of metastable austenite as the initial solidification product. Cr helps induce formation of the thin pro-eutectoid cementite film along the prior-austenite cell boundaries. The metastable austenite partially transforms to martensite as the ribbon cools to room temperature. A

Fig. 4 — Scanning electron micrograph of tensile fracture surface of HT3 sample showing highly dimpled structure characteristic of a ductile fracture.

possible grain refinement mechanism is given in Fig. 5. During HT1, tempering of the as-cast martensite (M) occurs, producing ferrite (α) grains with dimensions comparable to the martensite plates. Eutectoid transformation of the retained austenite (Ret γ) also occurs, resulting in many smaller ferrite grains, and the pro-eutectoid cementite (Fe_3C) coarsens and becomes discontinuous (shown in gray). Dispersed within the ferrite grains are fine cementite precipitates (shown in dark blue). HT2 is an austenitization treatment, and the austenite is fine-grained as a result of profuse nucleation at the finely dispersed cementite precipitate sites. The cementite produced by the decomposition of the austenite spheroidizes and coarsens during HT2. During the rapid water quench, most of the austenite grains transform to martensite with dimensions no greater than the austenite. HT3 tempers the fine-grained martensite into fine-grained ferrite and

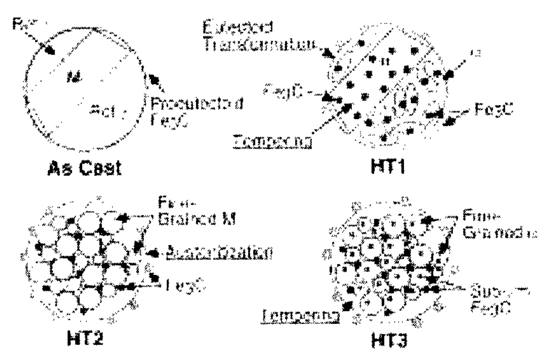

Fig. 5 — Phase transformation-induced grain refinement mechanism in rapidly solidified UHCS.

finely distributed cementite (shown in red). Although HT3 is done at a relatively high temperature of 600°C and for 1 h, coarsening of the cementite phase is modest and the presence of the cementite particles prevents coarsening of the ferrite grains.

Conclusions: Rapid solidification and solid-state phase transformation processing of UHCS results in ultrafine (0.2 μm), spheroidized cementite surrounded by fine-grained (1-μm maximum dimension) ferrite matrix. This fine-scale microstructure is achieved without deformation processing and solely with cycling heat treatment performed at modest temperatures. The thermal stability and ductility of this material makes it a good candidate for net-shape forming via superplastic consolidation. The sub-μm size cementite produced by this approach should prevent grain growth and provide only modest impediment to plastic flow at the consolidation temperature.

[Sponsored by ONR]

References

1. D.R. Lesuer, C.K. Syn, A. Goldberg, J. Wadsworth, and O.D. Sherby, "The Case for Ultrahigh-Carbon Steels as Structural Materials," *JOM* **45**(8), 40-46 (1993).

2. O.D. Sherby, B. Walser, C.M. Young, and E.M. Cady, "Superplastic Ultrahigh-Carbon Steels," *Scripta Met.* **9**(5), 569-574 (1975).

3. O.C. Ruano, L.E. Eiselstein, and O.D. Sherby, "Superplasticity in Rapidly Solidified White Cast Irons," *Metall. Trans. A*, **13A**(10), 1785-1792 (1982). ◆

Intermittence of the Photoluminescence of Single Quantum Dots

M. Rosen
Condensed Matter and Radiation Sciences Division

A.L. Efros
SFA, Inc.

Quantum dots (QDs) are nanometer-size semiconductor crystals embedded in a dielectric matrix that has a band gap much larger than that of the QD. Electron-hole (e-h) pairs excited in these dots by laser radiation are confined there by the QD-matrix interface barrier. As a result, QDs have sharp, discrete, size-dependent spectra, making them extremely efficient sources of tunable luminescence over the whole visible spectrum. Their efficiency comes from the concentration of absorption oscillator strengths at the discrete levels. They are tunable because the level energies are size-dependent. Electro-optical device applications include low threshold lasers in the blue-green to near-infrared, efficient tunable light-emitting diodes, radiation sensors and dosimeters, and optical electromodulators on micro-electromechanical systems (MEMS).

Photoluminescence Intermittency of Single Quantum Dots: The energies of the electron and hole levels are sensitively dependent on the radius a of the dot—they vary as $\sim 1/a^2$. However, even the best QD samples contain a distribution of dots having various sizes and shapes, and important size-dependent effects may be covered up when studying the optical response of these samples. Indeed, using recently developed techniques to study the luminescence of a single QD, a joint Massachusetts Institute of Technology-Lucent Technologies group uncovered surprising, and troubling, new phenomena in the luminescence of a single CdSe QD. These phenomena had been obscured in studies of sample ensembles [1]. In particular, they observed that the luminescence exhibited a random sequence of "on" and "off" periods. It "blinked!" Figure 6 shows their data. They used a sampling interval of 20 ms, which is large compared to typical times for optical processes in QDs. Their "bare" dots are capped with a surface layer of large organic molecules. When

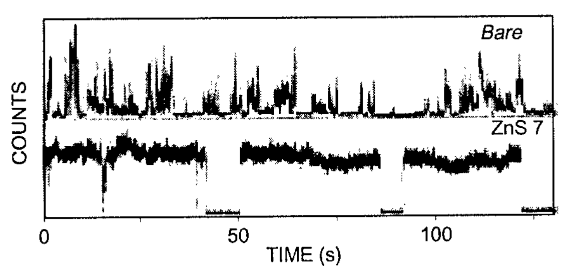

Fig. 6 — Observed luminescence intensity vs time of a "bare" CdSe nanocrystal compared with that of one overcoated with a shell of ~7 monolayers of ZnS, and using a sampling interval of 20 ms.

they overcoated the CdSe with ~7 monolayers of ZnS intervening between it and the organic capping groups, the lengths of the "on" times were considerably lengthened. The question is—what is causing the random quenching of the luminescence?

Auger Quenching of QD Photoluminescence: The intermittence can be understood in terms of nonradiative Auger recombination in ionized QDs. In Auger processes, an e-h pair recombines and gives the recombination energy not to a photon, but to another electron or hole. The probability of this process is greatly enhanced in QDs because the coulomb interaction in these small systems is much greater than that with light, and also because the third "Auger particle" can pick up considerable momentum from the abrupt crystal surface. We have shown that the Auger rate is extremely sensitive to the dot size—the lifetime for an Auger transition $\sim 1/a^{\nu}$, with $\nu = 5 - 7$.

Figure 7 shows schematically how Auger transitions act to quench the luminescence. In a neutral QD, with only one e-h pair, the radiative recombination lifetime is ~1 ns. However, if the dot is charged, then a nonradiative Auger transition occurs at a rate at least an order of magnitude faster. There are two ways to ionize a QD. One is to absorb a second photon, thereby creating a second e-h pair, before the first recombines. Auger autoionization then occurs if the conduction or valence band offset $\Delta E_{C,V}$ is less than the energy gap. The Auger particle escapes the QD and is trapped at a defect site in the matrix. The time τ for it to return to the dot depends on the depth of the trap and the temperature. A nanocrystal can also be ionized via thermal autoionization. All further e-h pairs created in the ionized dot recombine nonradiatively. Thus, "off" periods occur when the dot is ionized and Auger recombination quenches all luminescence. The duration of the "on" periods depends on the intensity of the laser light, i.e., on the probability of multiple photon absorption. All the processes indicated in Fig. 7 compete with each other in an irradiated QD, with probabilities inversely proportional to the lifetimes indicated there. Figure 8 shows the results of a Monte Carlo simulation of the luminescence, using parameters appropriate for CdSe nanocrystals at an excitation energy of 2.5 eV [2]. We used a radiative lifetime of 4 ns, a return time of 0.8 s, an intensity near 0.08 kW/cm^2 so as to observe long periods of brightness and a sampling interval of 10 ms. The intermittency is clearly reproduced. Increasing the intensity by a factor of 3 results in shorter "on" periods with random intensities; lowering the intensity by 3 reduces the number of "off" periods seen. The use of a smaller value of τ_A to simulate both a decreased band offset and the effect of a "more abrupt" CdSe interface clearly demonstrates an increased frequency of "off" periods. This points to how the intermittency can be minimized.

[Sponsored by ONR]

References

1. M. Nirmal, B.O. Dabbousi, M.G. Bawendi, J.J. Macklin, J.K. Trautman, T.D. Harris, and L.E. Brus, "Fluorescence Intermittency in Single Cadmium Selenide Nanocrystals," *Nature* **383**, 802 (1996).

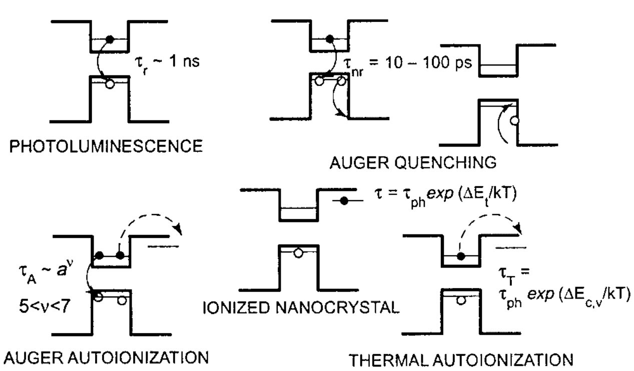

Fig. 7 — Schematic model of the Auger quenching of the luminescence in an ionized quantum dot; τ_r is the radiative lifetime of a single e-h pair in a quantum dot, τ_{nr} is the nonradiative Auger lifetime in a charged dot, τ_A is the Auger ionization lifetime in a dot with two e-h pairs, τ is the return time for an Auger electron trapped at a defect site in the matrix, and τ_T is the thermal ionization lifetime in a quantum dot at temperature *T*.

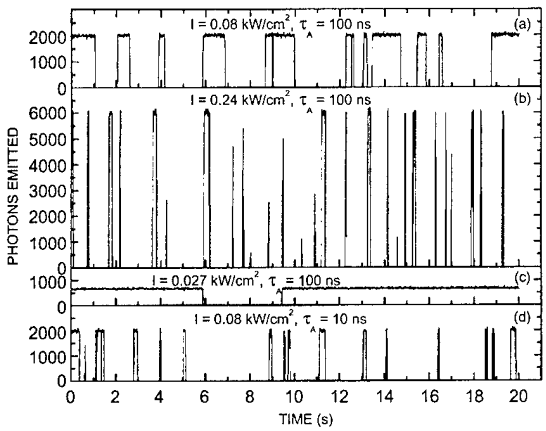

Fig. 8 — The number of luminescence photons in 10-ms sampling intervals as a function of time in a Monte Carlo simulation of the luminescence intermittency of a single CdSe quantum dot.

2. A.L. Efros and M. Rosen, "Random Telegraph Signal in the Photoluminescence of a Single Quantum Dot," *Phys. Rev. Lett.* **78**, 1110 (1997).

◆

Nonlinear Instabilities and Energy Manipulation in Coupled Structures

I.B. Schwartz,[1] I. Triandaf,[1] I. Georgiou,[2]
E. Emaci,[3] and A. Vakakis[3]
[1]*Plasma Physics Division*
[2]*Science Applications International Corporation*
[3]*University of Illinois at Urbana-Champaign*

Introduction: Many systems of current and future interest to the Navy consist of two or more structures that are coupled together. Examples include embedded flexible smart materials, panels and composite hulls of ships, and resonant wings in aircraft. Almost all of these structures are acted on by complicated external forces, which may cause damaging resonant vibrations to occur. It is important both to understand the onset of vibrations and to create active measures to remove them. One new way of manipulating energy being done at NRL is with the use of chaotic dynamics.

Although numerous areas in science are now known to exhibit the nonlinear phenomena of chaos, many science and engineering areas would benefit from the inducement of chaos (see Ref. 1 for examples). In mechanics, chaos could be induced to prevent resonant locking where one can excite chaotic motion of many modes spreading the energy over a wide frequency range. In this paper, we review some of the dramatic new nonlinear instabilities that arise in protoptypes of resonant structures, as well as some of the new tools developed at NRL to remove them. Specifically, we illustrate a method in which energy content initially centered about a resonant frequency can be actively broadened across many frequencies [1]. This technique is quite general and is illustrated in a magneto-elastic material experiment performed at the Naval Surface Warfare Center [1]. In another mechanical system, we show that, for a linear beam coupled to a pendulum, chaos onset excites many modes in a resonant system [2].

Nonlinear Broadband Frequency Expansion: In general dynamical problems, when systems of interest are driven externally, they may be forced at frequencies in which the resulting motion resonates at the same frequency, or a multiple frequency, of the drive. For periodic motion, if one imparts small random changes, or kicks, to the system, the resulting transient dynamics is generally local and linear. However, if the system is nonlinear, it is possible to excite global nonlinear transients by using designed small perturbations.

A particularly useful case occurs when the transients exhibit chaotic behavior. Chaotic behavior has the property that it contains an infinite number of unstable orbits of all periods. Therefore, exciting chaotic transients would spread the frequency content from a narrow resonant band to a broadband range. Figure 9 is an example of broadband frequency spreading for a model of a driven weakly damped conservative system [1]. The frequency of the drive is at unity, and a stable period 2 subharmonic orbit (Fig. 9(a)) has the largest power.

Frequencies that appear in the low power are those of a chaotic transient. After a certain transient time, these frequencies disappear, and the resulting attractor leaves a dominant frequency. In this case, it is a frequency at 1/2 the value of the drive frequency. Figure 9(b) shows the results of perturbing the system every forcing period with a small prescribed parametric kick. (Reference 1 provides details.) The resulting dynamics is such that chaotic behavior, which was previously transient, is now sustained for as long as desired. The power of the resonant peak is now greatly reduced, and the frequencies are spread over a broadband. Therefore, by using small parametric perturbations,

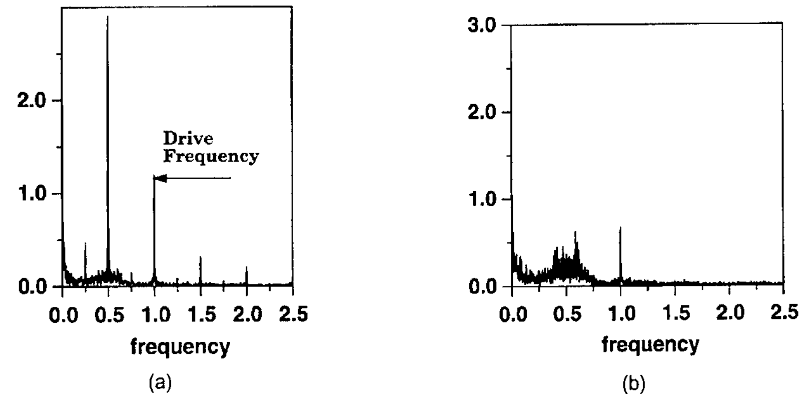

Fig. 9 — (a) The power spectrum of a time series generated from a driven weakly damped conservative system. Chaotic transients are included. The only attractor is a period 2 subharmonic, which appears as a large peak at 1/2 the frequency of the drive. (b) Same as in (a), but now small parametric perturbations are designed to sustain the chaotic transients so that the dynamics is spread broadband.

we have taken an unstable chaotic set and converted it in some sense to an attractor.

The technique may also be applied to real experiments in the absence of a model. A flexible structure experiment exemplifying sustained chaos is that of a driven magneto-elastic ribbon clamped at its lower end [1]. The ribbon is positioned vertically, and an applied magnetic field is approximately parallel to the ribbon. The magnetic field fluctuates in time, changing the Young's modulus, and the position from the vertical of the ribbon is measured at a single spatial point. Rather than examining the power spectrum, we examine the dynamics directly by sampling the position every drive period of the fluctuating magnetic field, which we call an iterate. After transients die down, in the absence of perturbations, the ribbon locks onto a period 1 orbit, which is represented by a line in Fig. 10(a). (A periodic orbit of the drive period corresponds to a fixed iterate of period 1.) We now apply our technique [1] to sustain chaotic transients in the ribbon, and the result is depicted in Fig. 10(b). Notice the chaotic transient time in Fig. 10(a) is extended by more than an order of magnitude in Fig. 10(b). Therefore, as in Fig. 9(b), the power is spread into many frequencies, and the power in the resonant attractor is reduced. One interesting observation is that there is virtually no way of distinguishing the extended chaotic transient, which is an unstable dynamical object, from a chaotic attractor.

Instant Chaos Onset Excites Multiple Modes: In general, if one has a linear structure, due to the superposition of modes, there is no real method of removing energy out of resonant modes with dynamic perturbations. One method around this obstacle is to consider a coupled linear structure to a nonlinear oscillator. A technique such as hanging a simple nonlinear pendulum at the end of a rod is sufficient to couple the rod modes. Because the modes in the linear structure are now coupled through the pendulum, the effects of the dynamics of the linear structure near resonance can be examined.

Specifically, we consider a model of a linear beam, fixed at one end, coupled to a pendulum. The structure is then driven at the fixed end of the beam. Because the beam is not a perfect rigid body, the beam has high-frequency motion that, in general, is fast compared to the slow motion of pendulum. (See Ref. 2 for model details, and Ref. 3 for the dynamics of coupled modes in a plate.) Of course, if the beam is infinitely stiff, the problem reduces to that of the forced, damped pendulum. If the structure is a slightly flexible beam, the pendulum dynamics would be expected to be slightly perturbed from the ideal infinitely stiff case. However, if the structure itself is dynamic, the overall picture may be changed dramatically. When operating at or near resonance, the dynamics changes dramatically in that some critical amplitude of the driving force exists that causes an

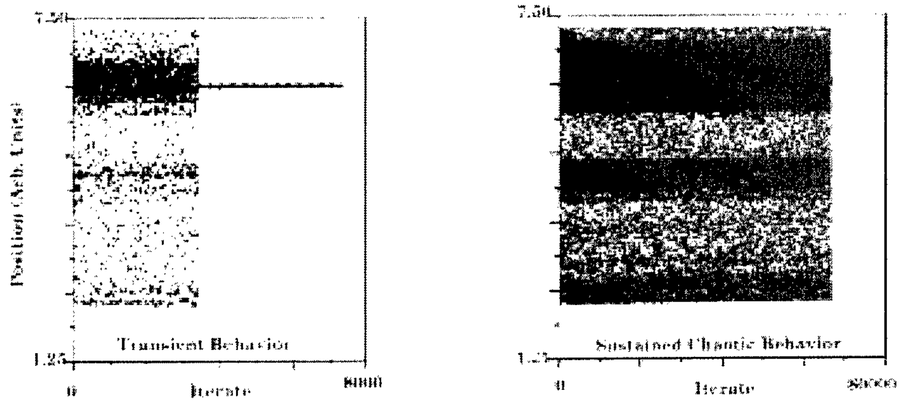

(a) (b)

Fig. 10 — (a) The results of a magneto-elastic ribbon experiment with a periodically driven magnetic field. The position at a single point is shown at every period of the fluctuating magnetic field. The only attractor is a period 1 attractor, represented by a straight line. The transient behavior observed is chaotic. (b) The sustained chaos algorithm applied to the magneto-elastic ribbon shows that the chaotic transient is sustained for more than an order of magnitude, hence spreading the energy broadband.

abrupt change from periodic behavior to high dimensional chaotic behavior.

To illustrate this phenomenon, we tune the parameters of our beam-pendulum model so that the ratio of the frequency of the pendulum to the beam is 1:2. This tuning puts the coupled structure in a resonant situation when the frequency of the drive is equal to the frequency of pendulum. We then simulate the dynamics for a wide range of drive amplitudes that govern the force of the driving at the fixed end of the beam. The frequency of the drive is held fixed.

To analyze the structural dynamics of the linear beam, we compute the dimension of the phase space by performing a Karhunen-Loeve decomposition of the coupled structure for each value of forcing amplitude. This technique gives the best fit of active independent modes in a phase space setting. The results of the simulation are presented in Fig. 11(a). We begin on a low dimensional periodic attractor in which the pendulum and beam act like two oscillators of different frequencies. In this case, the phase dimension is 4, with the beam exhibiting only one coherent mode. As we increase the forcing amplitude, we see that at a critical value of about 1.3, the dynamics jumps to a chaotic behavior in which the dynamics has a much higher dimension. This is due to more independent coherent structures of the beam being activated. If we now decrease the forcing amplitude, we notice a region of bistability where two attractors, both high and low dimensional, coexist. This is due to hysteresis of the dynamics as a function of the forcing amplitude, which is clearly a nonlinear phenomenon.

An experiment of a linear beam coupled to a nonlinear pendulum was performed in collaboration with the University of Illinois to test the existence of the high dimensional chaotic behavior. The result is depicted in Fig. 11(b), where the chaotic behavior illustrates the acceleration of the beam as a function of space (beam length) and time. Notice the excitation of high order modes, along with the first order mode.

Summary: We have given two examples of manipulating the energy content in structural dynamics. In the first, small-amplitude parametric controls were used to sustain chaotic transients. The technique can be applied to situations where the model is unknown or incomplete, as in the case of magneto-elastic ribbons. In the second, a linear beam was coupled to a nonlinear pendulum to couple the modes of the linear structure. Chaos was then used to spread the energy content in both cases. For many vibration and structural dynamics problems in the Navy, these techniques show promise in avoiding damage due to resonant dynamics. In particular, modes that were previously inaccessible from a control point of view can now be targeted to explicitly direct the energy toward higher frequencies or low frequencies, depending

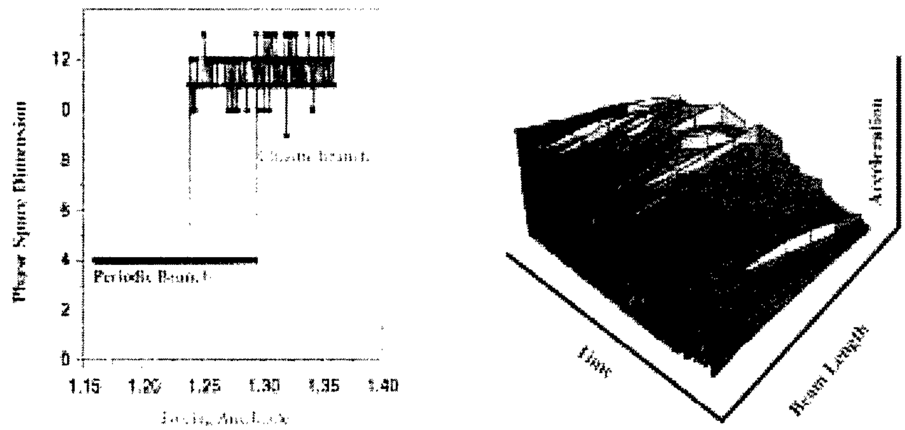

(a) (b)

Fig. 11 — (a) The results of a model of a driven structure consisting of a linear beam coupled to a nonlinear pendulum tuned to resonance. Shown is the phase space dimension as a function of forcing amplitude of the periodic drive. The dynamic behavior is low-dimensional periodic behavior for small amplitudes, and high-dimensional chaotic behavior for large amplitudes. Notice the region of hysteresis; this clearly demonstrates that although the beam is linear, the system behaves nonlinearly when considered as a whole. (b) An experiment of a resonant linear beam coupled to a pendulum shows that when the beam is chaotic, many modes are excited.

on which is more desirable. These nonlinear dynamical problems are currently being worked on in prototypical structures.

[Sponsored by ONR]

References

1. I.B. Schwartz and I. Triandaf, "Sustaining Chaos by Using Basin Boundary Saddles," *Phys. Rev. Lett.*, **77**, 4740-4743 (1996).

2. I.T. Georgiou and I.B. Schwartz, "A Proper Orthogonal Decomposition Approach to Coupled Structural-Mechanical Dynamical Systems," in Symposium on Nonlinear Dynamics and Controls, DE-Vol. 91, pp. 7-12, 96 ASME IECE, Atlanta, Ga., Nov. 17-22, 1996.

3. I.T. Georgiou and I.B. Schwartz, "Slaving the In-plane Motions of a Nonlinear Plate to Its Flexural Motion: An Invariant Manifold Approach," *J. Appl. Mech.* **64**, 175-182 (1997).

◆

Ion-Beam-Assisted Deposition of Thin Films with Nonlinear Optical Properties

C.M. Cotell, S. Schiestel, and C.A. Carosella
Condensed Matter and Radiation Sciences Division

S. Flom
Optical Sciences Division

Metal nanocluster composites are of interest for properties ranging from their intense absorption at a single wavelength for use as stained glass to their picosecond nonlinear response times with effective third-order susceptibilities that make them suitable for use in high-speed optical switches and optical communications. NRL scientists have used ion-beam-assisted deposition (IBAD) to produce thin film nanocomposite structures with high densities of uniformly small clusters [1,2]. Materials of this kind show promise for integration into the next generation of optoelectronic devices.

Experimental Procedures: The thin films were deposited by IBAD in a multihearth chamber by co-evaporation of an active metal and a noble metal under bombardment with O_2^+ ions. Typical evaporation rates were 0.1-0.15 nm s^{-1} for the active metal and 0.02-0.2 nm s^{-1} for the noble metal. Ion bombardment conditions were 75-500 eV and 40-200 μAcm^{-2}. The films were approximately 200 nm thick. Post-deposition oxidizing anneals were conducted in flowing O_2 at 600°C for times between 10 and 120 min.

Nanocluster sizes and distributions were determined from TEM photomicrographs of planview or transverse-sectional samples on Si substrates. The sizes were compared to those predicted by Mie scattering and absorption theory, based on the linear absorption characteristics as measured by VIS/UV spectroscopy. Sample preparation for TEM was by conventional means. In the case of planview samples, the substrate was etched away from the backside leaving electron-transparent film. Transverse section samples were thinned to electron transparency by ion-milling on a liquid nitrogen-cooled stage.

The NLO properties of the nanoclusters were probed experimentally using degenerate four wave mixing (DFWM) and nonlinear transmission (NLT). The output of the laser system had a pulse width of less than 1.2 ps FWHM, with pulse energies up to 1 mJ. The spot size at the sample was 2.4 mm.

Results: Figure 12(a) shows a bright field TEM image from a film of Au clusters in Nb_2O_5, deposited at room temperature with an O_2^+ ion beam at 150 eV and 200 μAcm^{-2} and evaporation rates for Au and Nb of 0.04 and 0.12 nms^{-1}, respectively. The sample was annealed at 600°C in flowing O_2 for 10 minutes after deposition. Figure 12(a) shows particles with an average circular cross section of ~5 nm. Transverse section TEM samples also show a circular shape to the particles in cross section, demonstrating that the particles are spherical. Figure 12(b) shows the linear absorption curve for this sample. A fit to these data using Mie scattering and absorption theory (solid blue curve) shows good agreement with the particle size measured by TEM.

Table 1 shows the nonlinear optical constants for the film in Fig. 12. The value for third-order nonlinear susceptibility is among the highest ever reported: $|\chi^{(3)}_{xxxx}| = 7.3 \times 10^{-8}$. The value of $|\chi^{(3)}_{xxxx}|/\alpha$, the figure of merit for application of

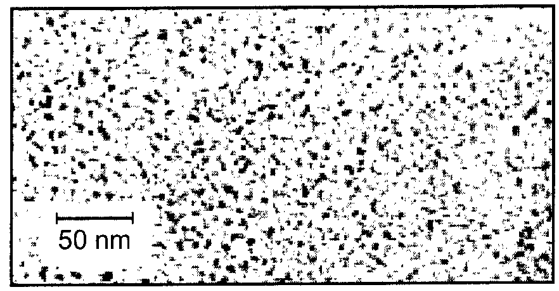

Fig. 12(a) — Transmission electron micrograph of a Au/Nb_2O_5 composite film deposited by IBAD at room temperature. The evaporation rates for Au and Nb were 0.04 and 1.2 nm s^{-1}, respectively, and the O_2^+ ion beam was operated at 150 eV and 200 μAcm^{-2}. After deposition, the film was annealed for 10 min in O_2 at 600 °C. The average Au particle size was ~5 nm.

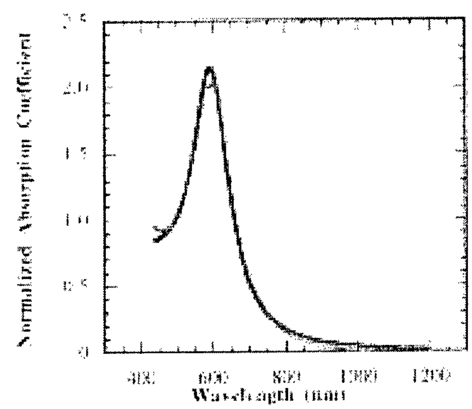

Fig. 12(b) — Optical absorption coefficient as a function of wavelength for the film in Fig. 12(a). The hollow circle data points show the spectroscopic data. The solid blue curve is a fit to the data using Mie theory for absorption and scattering assuming a Au particle size of 5.9 nm and a Au volume fraction of 0.078.

these materials, is less impressive, however, due to the strong linear absorption α of the materials.

IBAD improves the sharpness of the linear optical absorption, as shown in Fig. 13, which compares linear absorption curves for samples of identical volume fractions of Au clusters in SiO_2 deposited in two ways. The blue data points show the optical absorption of a sample that was prepared by co-evaporating Au and SiO_2. The red data points show the optical absorption of a sample prepared by IBAD by co-evaporating Au and Si in the presence of an O_2^+ ion beam at 150 eV. In the case of the IBAD sample, the sharpness

Table 1 — Nonlinear Optical Properties of the Au/Nb2O5 Nanocluster Composite

Au Particle Size (nm)	Au Volume Fraction	$\lvert \chi^{(3)}_{xxxx} \rvert$ (esu)	$\lvert \chi^{(3)}_{xyyx} \rvert$ (esu)	$\lvert \chi^{(3)}_{xxxx} \rvert / \alpha$	$\lvert \chi^{(3)}_{xyyx} \rvert / \lvert \chi^{(3)}_{xxxx} \rvert$
5.9	0.078	7.3×10^{-8}	6.6×10^{-10}	3.3×10^{-13}	0.009

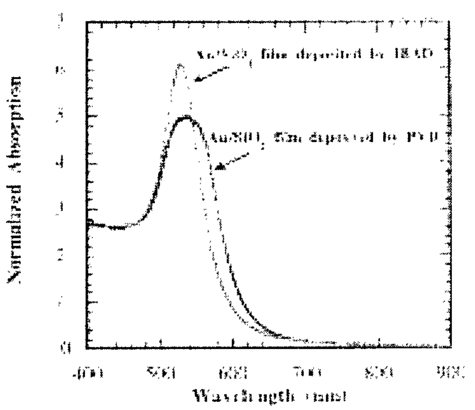

Fig. 13 — Optical absorption coefficient as a function of wavelength for two films of the same volume fraction of Au nanoclusters in SiO_2. The red data points are from a film deposited by IBAD by co-evaporating Au and Si in the presence of an O_2^+ ion beam. The blue data points are from a film deposited by physical vapor deposition (PVD) by co-evaporating Au and SiO_2.

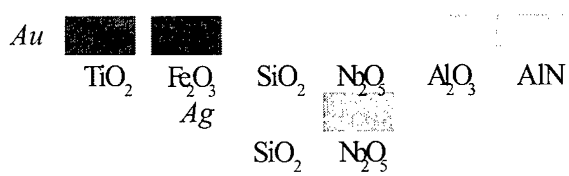

Fig. 14 — Samples of various metal nanocluster films deposited by IBAD on glass substrates.

of the optical absorption very likely is due to the uniformity of the size and shape of the clusters in the IBAD film relative to that of the evaporated film.

IBAD is a flexible technique that allows for the deposition of a range of composite compositions. Figure 14 shows samples of Au and Ag nanoclusters in various different dielectric matrices. The different colors of the samples demonstrate that by judicious choice of matrix and cluster elements, the wavelength of absorption can be adjusted over a wide range. Moreover, by varying the concentration of the cluster species, the intensity of the absorption is adjustable. The concentration can be changed by varying either the relative evaporation rates or the ion beam energy. By means of these adjustments, it should be possible to improve the value of $\lvert \chi^{(3)}_{xxxx} \rvert / \alpha$, the figure of merit for application of these materials.

Conclusions: IBAD has been shown to be an effective means to deposit thin films of nanocomposites. Metal nanocluster composites deposited by IBAD have among the highest values of third-order nonlinear susceptibility ever reported. Moreover, IBAD films show more uniform size and shape distributions of clusters than evaporated films with the same volume fraction of clusters.

In addition to metal nancluster composite compositions, NRL has begun investigating semiconductor nanocomposites using IBAD deposition methods. These films have shown exciting photoluminescence properties. The potential of IBAD for thin film deposition of a wide variety of two phase nanocomposites is just beginning to be realized.

[Sponsored by ONR and DFG]

References

1. C.M. Cotell, S. Schiestel, C.A. Carosella, S. Flom, G.K. Hubler, and D.L. Knies, "Ion-Beam-Assisted Deposition of Au Nanocluster/Nb_2O_5 Thin Films with Nonlinear Optical Properties," *Nuc. Instr. Methods, B*, **127/128**, 557-561 (1997).

2. S. Schiestel, C.M. Cotell, C.A. Carosella, K.S. Grabowski, and G.K. Hubler, "Ion Beam Assisted Deposition of Metal Nanoclusters in Silica Thin Films," *Nuc. Instr. Methods, B*, **127/128**, 566-569 (1997). ◆

A Study of Passive Films Using X-ray Photoelectron and X-ray Absorption Spectroscopy

P.M. Natishan and E. McCafferty
Materials Science and Technology Division

W.E. O'Grady and D.E. Ramaker
Chemistry Division

Introduction: The corrosion resistance of aluminum, as well as many other metals and alloys, is provided by a passive-oxide film that protects the surface from degradation by the environment. However, in environments that contain aggressive anions such as chloride, passive films are degraded locally, causing film breakdown and corrosion. While chloride has long been acknowledged both from engineering and theoretical perspectives to play a major role in this breakdown process, only a limited number of studies have been done to describe its role. This is, in part, due to the difficulty in making the appropriate surface analytical measurements. In this work, advanced surface analytical techniques are being used to shed light on the question of how chloride causes the breakdown of passive-oxide films leading to pitting corrosion.

Chloride incorporation into the oxide film on aluminum leading to breakdown of the passive film was examined as a function of the electrode potential below the pitting potential. The pitting potential is a characteristic potential below which pitting corrosion does not occur. The presence of chloride was determined using X-ray photoelectron spectroscopy (XPS) and X-ray absorption spectroscopy (XAS).

Results and Discussion: *XPS Analysis:* Figure 15 shows a series of XPS $2p_{3/2}$ - $2p_{1/2}$ spectra for chloride obtained from aluminum samples polarized for one hour in deaerated 0.1M NaCl at selected potentials below the pitting potential. The $2p_{3/2}$ - $2p_{1/2}$ doublet is the most prominent XPS spectrum for chloride. Each doublet pair, $2p_{3/2}$- $2p_{1/2}$, represents chloride in a distinct chemical environment. Figure 15(a) shows a chloride spectrum for aluminum that was immersed in a chloride solution under open circuit conditions (i.e., with no applied potential). Deconvolution of the spectrum shows the presence of two peaks, labeled 1 and 2, corresponding to a single $2p_{3/2}$ - $2p_{1/2}$ doublet. Figures 15(b), 15(c), and 15(d) show chloride spectra for samples polarized, with respect to the saturated calomel electrode (sce), at -0.800 V, -0.750 V, and -0.700 V, respectively. These spectra are best fit with the two sets of doublets shown in the figures. The first doublet, peaks 1 and 2, has binding energies that correspond to those of the doublet observed for the open circuit condition. Peaks 3 and 4 correspond to a second $2p_{3/2}$ - $2p_{1/2}$ doublet that has higher binding-energy values than the first doublet. The two sets of doublets indicate that chloride is present in two different chemical environments. The spectra change as the potential is increased (i.e., made more positive), with the second, higher binding-energy doublet becoming more prominent.

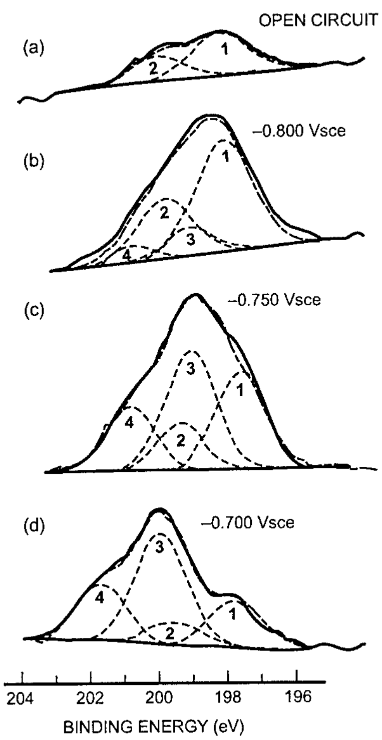

Fig. 15 — XPS $2p_{3/2}$ - $2p_{1/2}$ spectra of chloride on aluminum at: (a) open circuit, (b) -0.800 Vsce, (c) -0.750 Vsce, and (d) -0.700 Vsce.

Figure 16 shows XPS chloride spectra for a sample polarized at -0.750 V before and after sputtering etching the surface. Figure 16(a) was obtained before sputtering and shows the presence of two sets of chloride doublets. Figure 16(b) shows the XPS spectrum obtained after sputtering etching approximately 10Å of the oxide film. In this spectrum, the lower binding-energy doublet, peaks

1 and 2, is no longer present. This result indicates that the lower binding-energy specie is related to chloride on the surface and the higher binding-energy specie is associated with chloride incorporated in the oxide film.

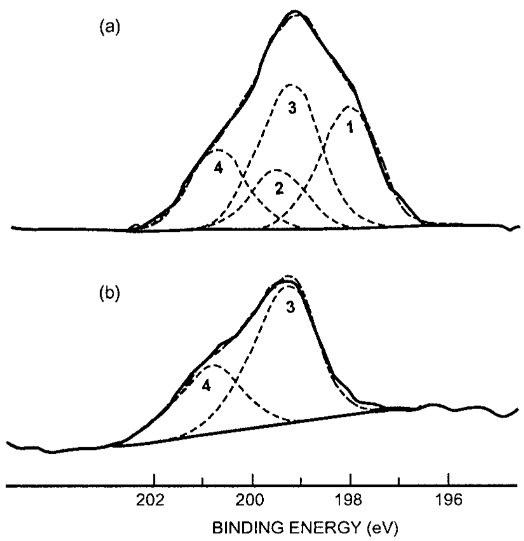

Fig. 16 — XPS $2p_{3/2}$ - $2p_{1/2}$ spectra of chloride on aluminum for a sample polarized at -0.750 Vsce (a) before and (b) after sputtering with argon.

X-ray Absorption Spectroscopy: Figures 17(a) and 17(b) show Cl K-edge X-ray absorption near edge structure (XANES) spectra for NaCl and an aluminum sample polarized at -0.750 V for 1 hour in deaerated 0.1M NaCl, respectively, after removing a linear background in the usual manner. The spectrum shown in Fig. 17(b) shows the presence of chloride on and/or in the oxide film. The X-ray edge for chlorine (i.e., chloride) occurs at nearly the same energy (2823 eV) for both the NaCl standard and the aluminum sample, indicating that the chloride in the oxide has a Cl^- character. Also, the XANES is very similar for both the NaCl standard and for chloride on aluminum. Preliminary theoretical curved-wave multiple scattering cluster calculations show that the XAS spectral line shape for chloride in NaCl is similar to that for chloride in an aluminum oxide lattice, provided that the oxide lattice is expanded to accommodate the chloride ion. Figure 18 shows a spectrum for the sample polarized at -0.750 V after the data have been smoothed by the Savitzky-Golay technique. Deconvolution of this spectrum also shows the presence of chloride in two different chemical environments, i.e., a surface and a bulk component. A major advantage of XAS, which will be utilized in future work, is that it offers a means to examine chloride uptake by surfaces in situ.

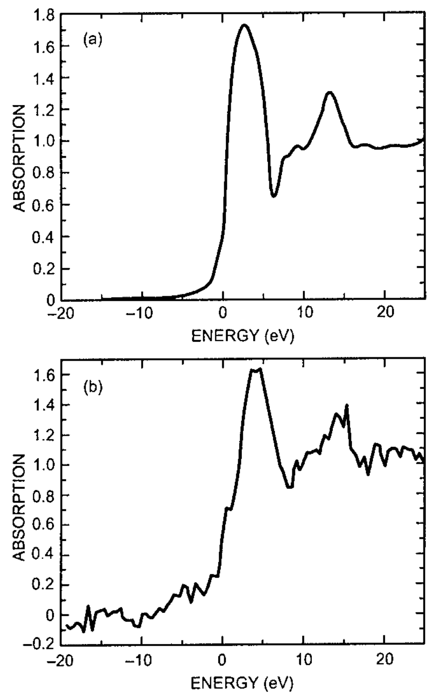

Fig. 17 — X-ray absorption spectra: (a) NaCl and (b) aluminum polarized at -0.750 Vsce for 1 hour in 0.1M NaCl solution.

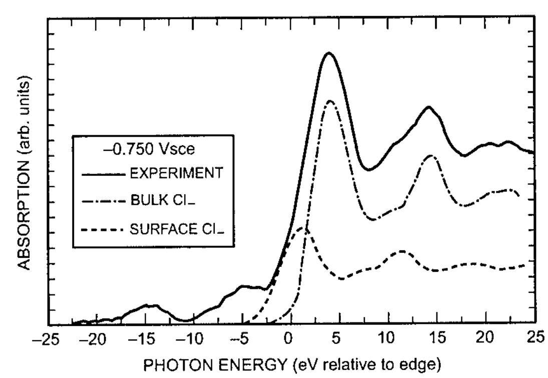

Fig. 18 — X-ray absorption spectra of chloride on aluminum polarized at -0.750 Vsce.

Summary: Chloride was detected in the passive film on aluminum at potentials below the pitting potential using X-ray photoelectron spectroscopy and X-ray absorption spectroscopy. The important point of this work is that chloride was identified in two different chemical environments, i.e., a surface and a bulk component, using two independent techniques.

[Sponsored by ONR]

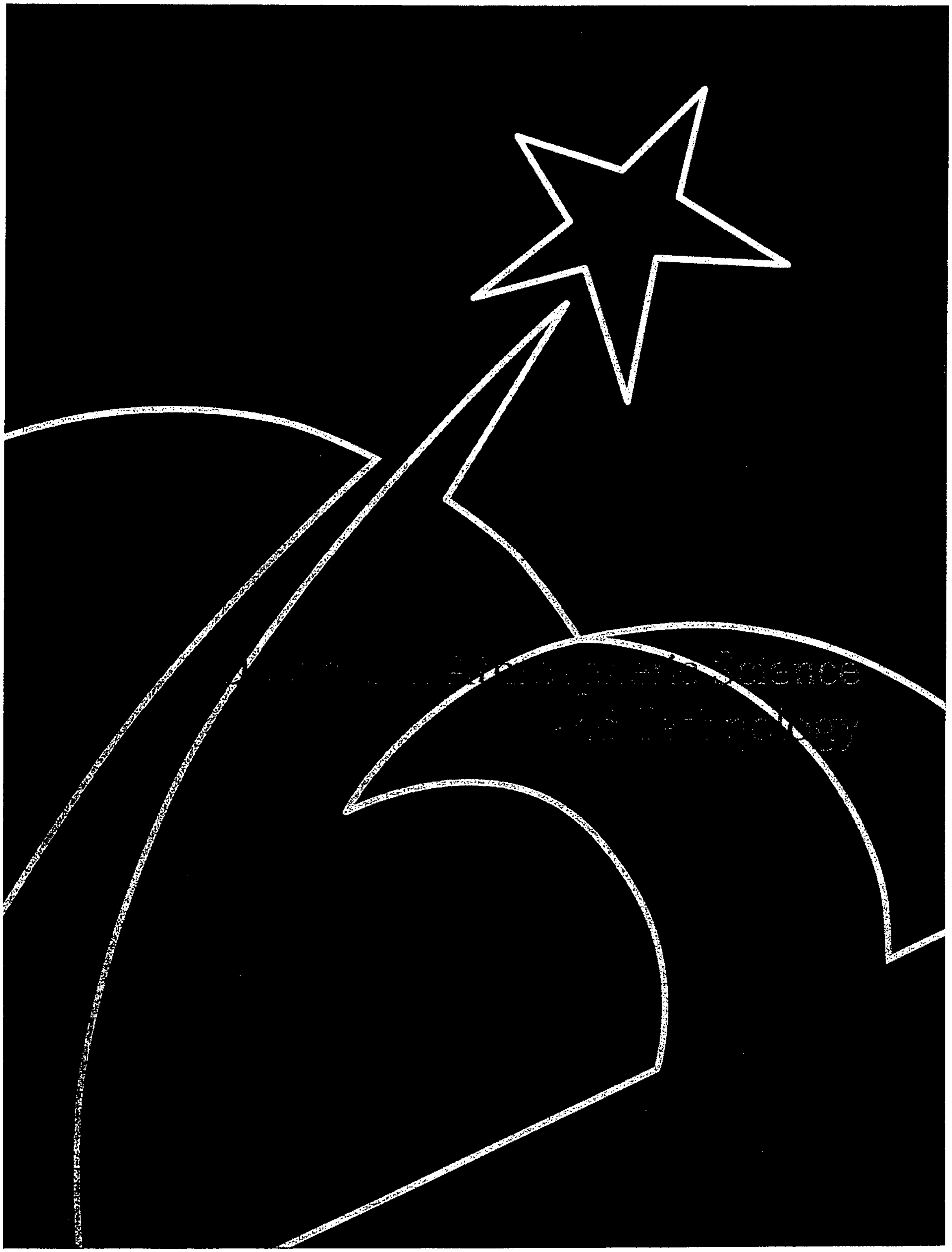
Science

Probing Space Plasmas Using the New HAARP Ionospheric Heater

P. Rodriguez and M. Keskinen
Plasma Physics Division

E.J. Kennedy
Information Technology Division

Introduction: Naturally occurring irregularities of electron density in the space plasmas around the Earth cause disruptions of high-frequency (HF) radio-wave communications and can introduce errors in navigation and positioning systems such as the Global Positioning System (GPS). The new HF Active Auroral Research Program (HAARP) transmitter, being constructed near Gakona, Alaska, is a joint Air Force/Navy research facility to allow powerful HF radio waves to be launched into the ionosphere and magnetosphere of the Earth. Space plasmas at high latitudes are known to contain electron density irregularities with a wide range of spatial scale sizes caused by geomagnetic storms and various other phenomena such as the auroral electrojet [1]. HAARP will allow scientists to conduct experiments to study electron density irregularities and methods of modifying their effects on radio-wave communications. Current plans call for many types of experiments such as "heating" ionospheric electrons, inducing low-frequency radio-wave emission from the auroral electrojet (for submarine communications), and stimulating optical emissions from atmospheric molecules. HAARP transmits at frequencies from 2.8 to 10.0 MHz and will eventually be able to radiate up to 3.2 GW of power. In addition, the beam of radio waves can be quickly pointed to various directions within a 30° cone about the overhead direction. A description of the HAARP facility is on the Internet at http://www.haarp.alaska.edu. In our first experiments using HAARP, we have transmitted radio waves directly through the ionosphere and magnetosphere and into the distant solar wind to investigate the spectrum of electron density irregularities of space plasmas. The HAARP-transmitted radio waves were received and measured by the National Aeronautics and Space Administration (NASA) WIND spacecraft by a special spacecraft radio receiver that is normally used to study solar radio emissions.

WIND-HAARP Experiment Plan: The WIND-HAARP experiment was first conducted on November 16, 1996, when WIND was between 115,000 and 128,000 km (18 to 20 Earth radii) from Earth. Figure 1 shows a schematic of the orbit trajectory of WIND about Earth during the HAARP transmissions. Radio waves transmitted from HAARP refract and scatter away from the direct line of sight because of changes in the electron density in the ionosphere and magnetosphere. If "cloud-like" spatial structures of electron density occur, the radio waves are scattered in multiple directions. The wave amplitudes measured at WIND will then exhibit fluctuations caused by radio waves arriving from different directions. This phenomenon, called scintillation, is similar to fluctuations in the light from stars caused by atmospheric turbulence.

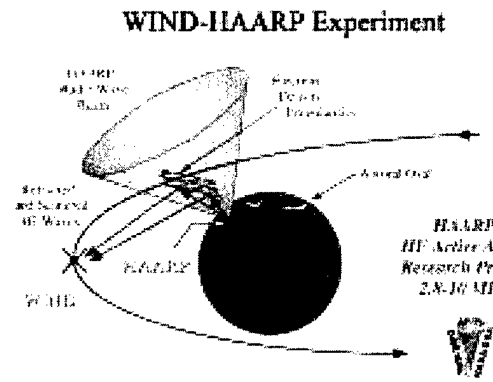

Fig. 1 — Schematic illustrating HAARP transmission to the WIND spacecraft. The radio waves refract and scatter from electron density irregularities in the space plasmas about the Earth.

Radio waves at a frequency of 7.575 MHz were transmitted from HAARP for 1 hour, between universal times (UT) 14:30 and 15:30. Then HAARP switched to a frequency of 9.075 MHz and transmitted for another hour, between UT 15:30 and 16:30. The transmissions were done using an engineering test array formed by 16 crossed-dipole antennas and 32 transmitters, providing a total power of 300 kW. To have a recognizable signature in the WIND measurements, we programmed HAARP to turn the power ON and OFF at 30-s intervals in the first and last 5 min of each hour. At all other times, we used continuous wave (CW) transmission at constant power level.

WIND-HAARP Radio Wave Measurements: Figure 2 shows the radio-wave amplitudes received at WIND during the first 10 min of each

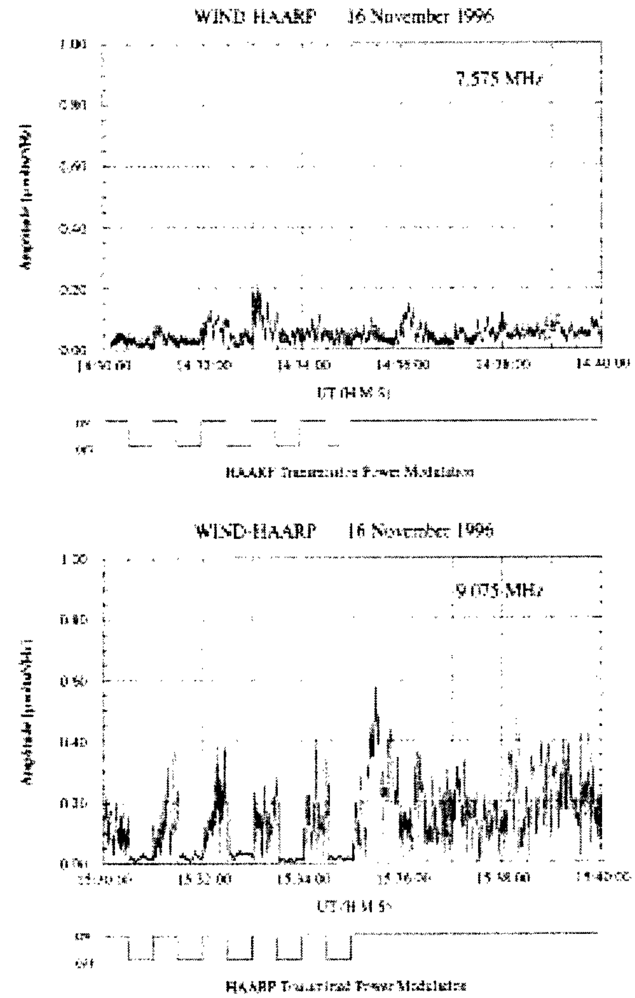

Fig. 2 — Radio wave amplitudes measured at WIND for HAARP transmissions at 7.575 and 9.075 MHz on November 16, 1996. The power profile of HAARP transmissions is shown below each measurement.

hour. Below each plot is a profile of HAARP-transmitted power, showing the 30-s ON-OFF modulation in the first 5 min followed by CW transmission. The ON-OFF modulation is clearly evident in the WIND measurements at 9.075 MHz (lower panel); while at 7.575 MHz (upper panel) the ON-OFF modulation is also present, although less obvious. Thus, we have confirmation that WIND has received the HAARP transmissions. Clearly, the radio waves received at WIND have large-amplitude fluctuations, indicating that the radio waves interact with space plasma density irregularities along the propagation path. The OFF periods of the transmissions provide a measure of the noise background and show that the received radio waves are a few times and a magnitude larger than the noise background. Therefore, the amplitude fluctuations are not caused by noise but are true signal fluctuations.

One way of describing the HAARP radio wave interactions observed with WIND is in terms of the spectrum of fluctuations. Figure 3 shows the spectra of intensity fluctuations of 7.575 and 9.075 MHz radio waves recorded at WIND for 1-min intervals, during the CW transmission periods. The spectra are least-squares fitted by the dashed straight lines. The scintillation index S4 is a parameter used to characterize the radio-wave fluctuations. Values of S4 greater than 0.5 correspond to strong scintillation. Both HAARP-trans-

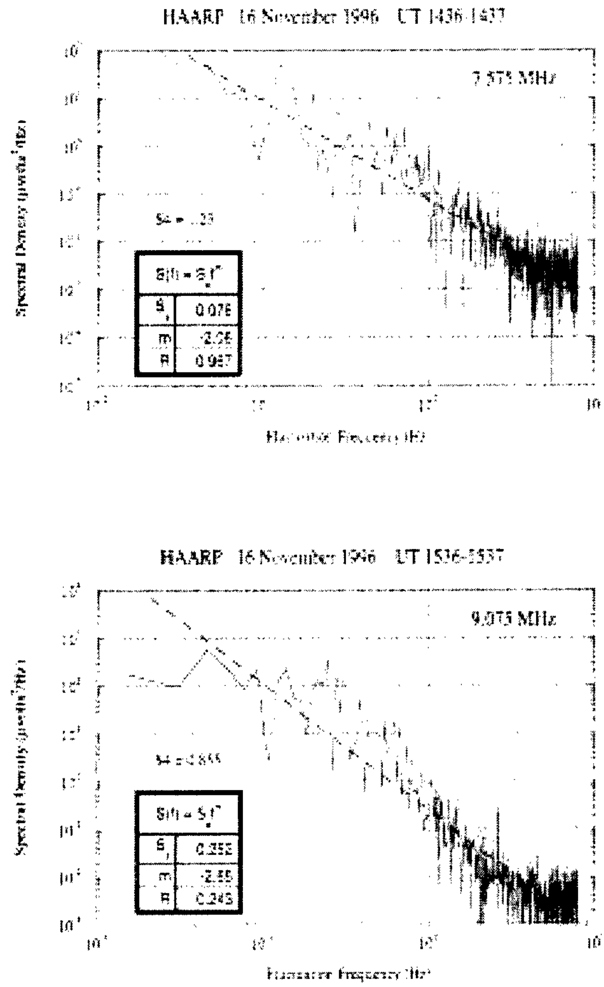

Fig. 3 — Spectra of radio-wave fluctuations at 7.575 and 9.075 MHz. The spectra are least-squares fitted by straight lines and characterized by the scintillation index S4.

mitted frequencies correspond to strong scintillation along the propagation path from HAARP to WIND.

Summation: The WIND-HAARP experiment shows that the HAARP facility will provide an important new approach to the study of space plasmas. Because the transmitted radio waves interact strongly with the space plasmas, the structure and sizes of naturally occurring density irregularities can be studied. In addition, as greater transmission powers become available at HAARP, the radio waves will be used to "heat" the plasma to induce density irregularities that can be studied for new effects on radio-wave propagation. A report on the WIND-HAARP experiment by Rodriguez et al. [2] has been submitted for publication.

Acknowledgments: We thank the Office of Naval Research (ONR) and the Air Force Research Laboratory (AFRL) for the opportunity to use the HAARP research facility. We also thank NASA and the European Space Agency (ESA) for supporting the operations of the WIND spacecraft.

[Sponsored by ONR, AFRL, NASA, and ESA]

References

1. M.J. Keskinen and S.L. Ossakow, "Theories of High-latitude Ionospheric Irregularities," *Radio Sci.* **18**, 1077 (1983).

2. P. Rodriguez, E.J. Kennedy, M.J. Keskinen, C.L. Siefring, S. Basu, M. McCarrick, J. Preston, M. Engebretson, M.L. Kaiser, M.D. Desch, K. Goetz, J.-L. Bougeret, and R. Manning, "The WIND-HAARP Experiment: Initial Results of High Power Radiowave Interactions with Space Plasmas," *Geophys. Res. Lett.* **25**(3), 257 (1998). ◆

Airborne Measurements of Salinity Distributions in Coastal Waters

J.L. Miller
Ocean Sciences Division

Introduction: The scanning low-frequency microwave radiometer (SLFMR), a prototype airborne surface salinity mapper, has been successfully deployed over several littoral regions. This system measures microwave energy radiated from the surface of the sea that corresponds to the concentration of salt in the water. The system can be mounted on a small, light aircraft that can easily map salinity and temperature over an area of 1000 sq km in an hour.

Measurements of sea surface temperature (SST) from aircraft and satellites have been available for decades but, until the advent of this "salinity mapper," there was no way to accurately measure coastal salinity distributions, except by time-consuming in-water sampling. This new data source will for the first time permit rapid, large-area measurements of coastal ocean features that are caused by the discharges from estuaries, bays, and rivers. These features, such as strong littoral currents and plumes of fresh water that issue from bays, are major influences on coastal waters. The salinity mapper will make it possible to analyze and predict them.

The First Image of Sea Surface Salinity: The salinity mapper has recently been used by a team of scientists from government and industry to generate the first remotely sensed image (Fig. 4) of sea surface salinity (SSS). This image of SSS near the mouth of Chesapeake Bay, Virginia, was obtained during the Naval Research Laboratory's (NRL) Chesapeake Outflow Plume Experiment (COPE), elements of which were conducted in collaboration with the National Oceanic and Atmospheric Administration (NOAA). It shows the low salinity plume exiting the Chesapeake Bay and turning southward along the coast. Such images of SSS were used to guide ship-based in situ operations in near real time and to enhance analyses of moored in situ data.

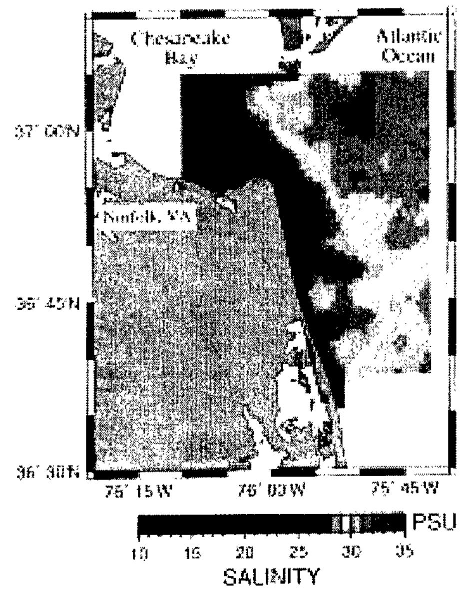

Fig. 4 — The first image of sea surface salinity (SSS) ever produced. The low salinity waters (greens) are exiting the Chesapeake Bay and turning southward to form a coastal buoyancy jet, while higher salinities (reds) lie offshore.

Salinity and the Littoral Zone: Salinity is a key factor governing biological, chemical, and physical processes throughout the ocean. It is especially important on continental shelves where river runoff creates large salinity variations that control the establishment and evolution of coastal buoyancy jets that can have currents of two knots or more. These, in turn, redistribute biological and chemical substances along and across the shelf as well as vertically within the water column. Salinity distributions, thereby, strongly influence biogeochemical processes in the littoral zone.

Unfortunately, measurement of salinity with traditional in situ instruments is laborious and expensive, requiring substantial human and ship resources even for modest surveys of limited areas. The high-frequency (HF) variations caused by tides and other phenomena usually thwart efforts to obtain truly synoptic maps of salinity, even if interest is limited to only surface features. Thus, the new airborne salinity mapper provides a means

of substantially advancing our understanding of coastal oceanographic phenomena and, because it can be flown on small inexpensive aircraft, it can do so in a cost-effective manner.

The Instrument: Designed and built by Quadrant Engineering, Inc., for NOAA, the salinity mapper measures the fundamental parameters (radiometric brightness temperature at 1.4 GHz and sea surface temperature) needed to retrieve SSS estimates via the Klein and Swift [2] algorithm (Fig. 5). The instrument scans a swath resolved by six electronically steered beams. A technical description of the instrument and results from several test flights are described in Goodberlet et al. [1]. For a given noise level in brightness temperature, the quality of the salinity retrieval increases as SSS and SST increase, as indicated by the spreading of the curves in Fig. 5. For a nominal beam dwell time of 0.5 s, the brightness temperature noise is 0.39 K or 0.8 practical salinity units (psu) at moderate SST and SSS. By increasing dwell time and/or spatial averaging, noise levels of 0.1 psu are possible.

Summary: The oceanographic community now has at its disposal a unique technology that has the potential to revolutionize littoral oceanography in the same manner that satellite-based infrared imaging of SST revolutionized basin-scale oceanography—an airborne microwave radiometer mapping system that can measure SSS. Specifically, we now have the capability to image SSS with noise levels of a few tenths psu. SSS images of regions up to 2500 km^2 can be produced in

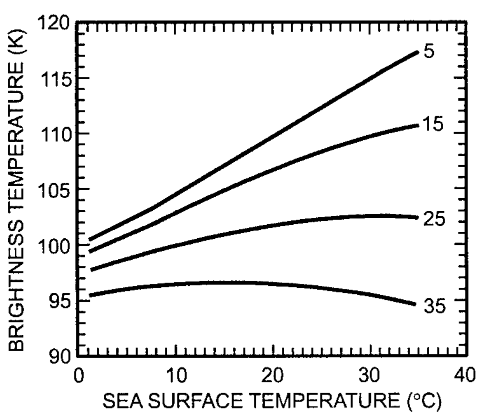

Fig. 5 — Salinity is primarily a function of microwave brightness temperature and sea surface temperature (SST). This family of salinity curves is based on the empirically determined Klein and Swift [2] relationship.

about 3 hours, thereby, avoiding significant aliasing by tides and other short-period processes. These capabilities fulfill the observational requirements of estuarine and inner-shelf studies. This and future generations of the airborne salinity mapper, already planned under NRL's Captial Procurement Program, promise to produce data essential for understanding the dynamics of littoral regions.

[Sponsored by NRL]

References

1. M. Goodberlet, C. Swift, K. Kiley, J. Miller, and J. Zaitzeff, "Microwave Remote Sensing of Coastal Zone Salinity," *J. Coastal Res.* **13**(2), 363-372 (1997).

2. L. Klein and C. Swift, "An Improved Model for the Dielectric Constant of Sea Water at Microwave Frequencies," *IEEE J. Oceanic Engr.* **OE-2**(1), 104-111 (1977).

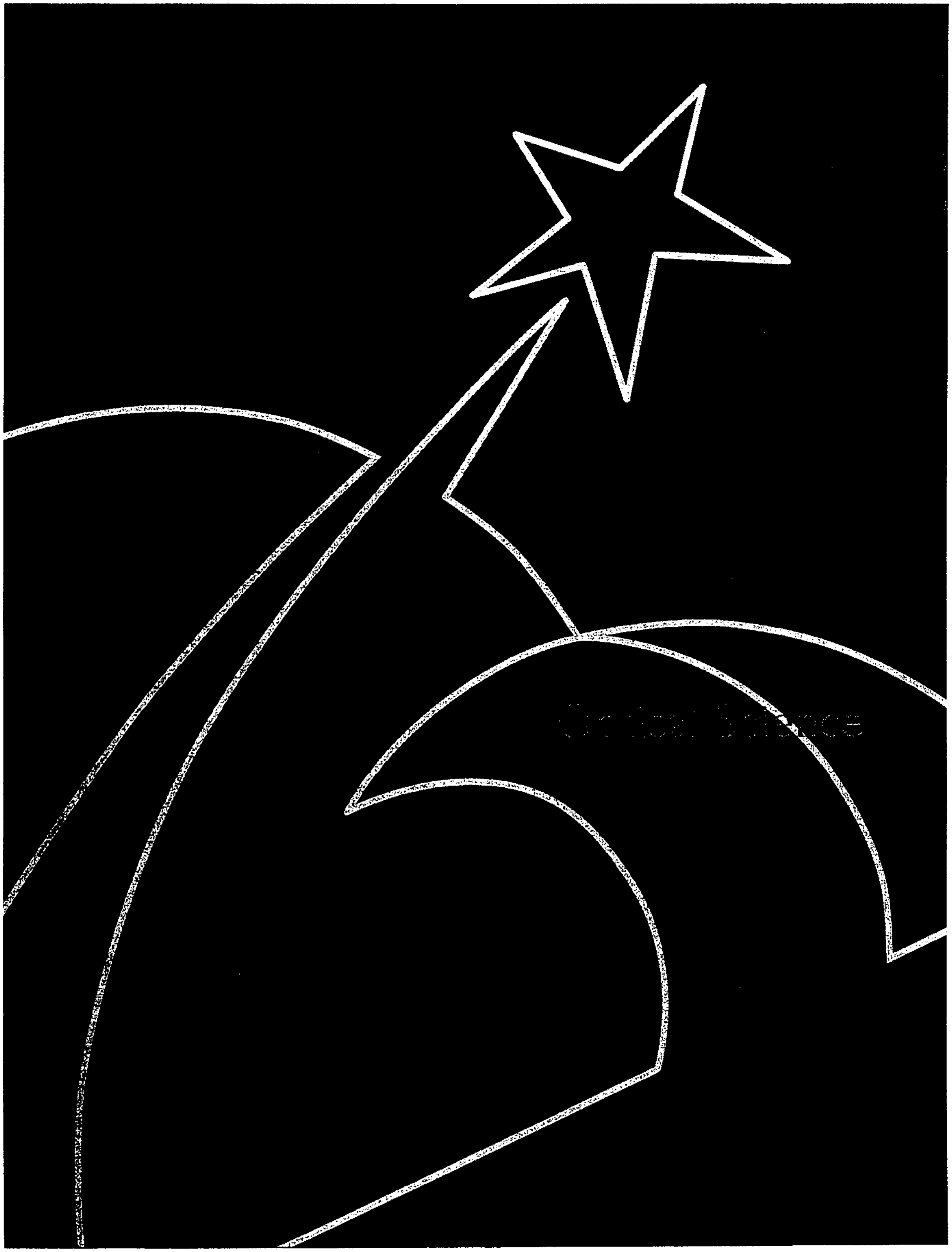

Ultrahigh-Speed Optical Communications Networks

I.N. Duling III
Optical Sciences Division

Everyone wants more bandwidth. People at home want more video channels (stereo, of course), videophones, and higher speed connection to the Internet. The Department of Defense wants instant access to the data being collected by sensors that might be onboard ships, satellites, planes, tanks, trucks, or men. All of this activity requires that massive amounts of information move as quickly as possible. Current state-of-the-art communication systems transport information at a rate of 10 Gb/s (10 billion bits each second). At the Naval Research Laboratory we are researching a communications network that can transport information at a rate of 100 Gb/s.

System Design: Since current electronics cannot operate faster than 10 Gb/s, the data are structured as 10 channels, each carrying 10 Gb/s of data. Bits, a one or a zero, are represented in the data stream by the presence or absence of a pulse of light. The pulses of a single channel are about 2 ps in duration, separated by 100 ps. As the channels are combined, the pulses of the nine other channels are placed between the pulses of the first channel. Once the bit stream is assembled, it can be transmitted onto the network. When it reaches its destination, a fast optical switch is used to separate the channels from each other. The transmission is considered error free if there is less than one error in every billion bits of information. At its best, the communications system at NRL operates with less than one error in every trillion bits of information.

To accomplish this, workers in the Optical Techniques Branch have pooled their expertise in a variety of areas. The source of the optical pulses must be extremely stable. Years of research into short pulse fiber lasers at NRL have resulted in a laser that produces the required 2 ps pulses at a 10 Gb/s repetition rate. High-speed lithium niobate modulators, fabricated at NRL, extract the data from the 100 Gb/s data stream so that they can be read by electronics operating at 10 Gb/s (the current state of the art). A low-noise, high-power optical receiver converts the optical pulse stream into the electrical signals that are the output of the communications system.

System Performance: The "eye" diagram in Fig. 1 shows the output data of the communications system testbed. The shape is produced by triggering an oscilloscope synchronously with the incoming data. By displaying all possible patterns of zeros and ones simultaneously, we can detect any pattern-dependent distortions that might occur on transmission. This is a sensitive way to observe noise in the system. As the noise increases, the open space in the middle of the pattern begins to close up until it is filled. The fact that the received eye is wide open indicates that there has been successful communication.

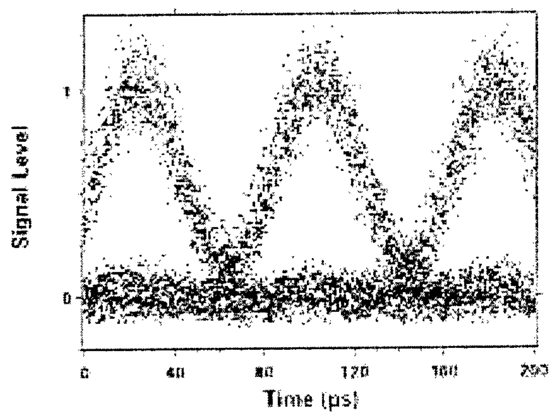

Fig. 1 — Eye diagram at the output of the 100 Gb/s communications link. The data shown are from one of the eight channels operating at 12.5 Gb/s. Seven similar channels were propagating with this one in the same fiber at the same wavelength.

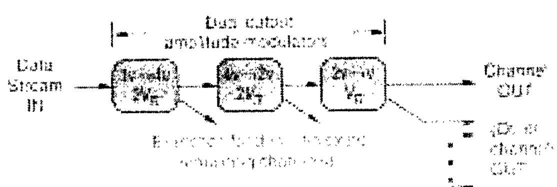

Fig. 2 — The channels are selected by a series of optical switches. Each switch opens and closes at half the rate of the preceding switch. In this way, with seven modulators, all eight channels could be separated at the same time.

The communications system uses a series of three high-speed switches to separate the channels in the 100 Gb/s data stream (Fig. 2). In this case, the system is operated with eight 12.5 Gb/s channels. Each switch is adjusted to extract every other pulse of the train that comes into it. The first switch takes in 100 Gb/s and puts out two streams of 50 Gb/s. The second takes one of those and puts out two streams of 25 Gb/s. The final stage

puts out two streams of 12.5 Gb/s, which are two of the original channels. With an entire tree structure of switches, all eight channels are obtained.

Time division multiplexed data of this sort are well suited for processing at the optical level, which means that all optical processing can be easily built into a network of this kind. Some of this work has resulted in patents and license requests and many collaborations between NRL and both government laboratories and universities.

[Sponsored by ONR] ◆

Flexible Organic Emissive Displays

Z.H. Kafafi,[1] G.M. Daly,[2] H. Murata,[3] and C.D. Merritt[1]
[1]*Optical Sciences Division*
[2]*ASEE Postdoctoral Fellow*
[3]*SFA, Inc.*

Flat-panel displays (FPD) will have a tremendous impact on current and future technologies for both commercial and military applications. Displays in general have become indispensable media for the delivery of information that combines text, graphics, still images, or video. With the advent of High Definition Television (HDTV) and the developing need for full-color, high-contrast, lightweight, and low-power displays, new technologies are required to replace the cathode ray tube (CRT). Traditionally, the CRT has been the main display technology for most commercial and military applications. However, due to engineering limitations, they are not suitable for flat panel displays. An emerging technology that addresses the needs of the FPD industry is emissive displays based on electroluminescence from molecular organic light-emitting diodes (MOLEDs). Displays based on organic materials have the additional advantage that they can be manufactured on plastic instead of on glass substrates. This provides the ultimate in thin, lightweight displays with the additional advantage that they can be molded into any shape or form (Fig. 3). This feature is particularly advantageous in some military applications (e.g., helmet-mounted, cockpit, submarine, and map displays). At NRL, we have developed MOLEDs on plastics while optimizing device configurations and materials. We have demonstrated that the MOLEDs made on plastics show superior luminous power efficiency compared to that exhibited by their analogs

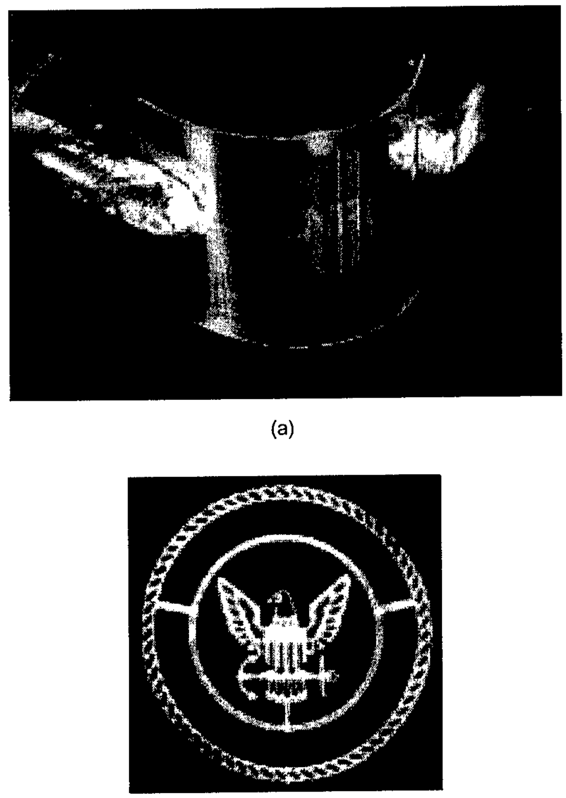

(a)

(b)

Fig. 3 — MOLEDs on polyester substrates: (a) bent ~75° and (b) with NRL eagle logo.

on glass substrates, despite the greater attenuation of light through the plastic substrates [1].

Diode Structure and Optimization: Figure 4 is a sketch of the MOLED thin-film device configuration along with the chemical structures of the materials used. Devices are made in a high vacuum thin-film deposition system equipped with thermal evaporation sources. The basic device structure consists of: a polyester substrate (display back-plane) coated with the transparent metal oxide indium-tin oxide (anode) used for the injection of holes; a 50-nm TPD (*N*,*N*'-diphenyl-*N*,*N*'-bis(3-methylphenyl)-1-1'-biphenyl-4,4'-diamine) hole transport layer; a 50-nm Alq_3 (tris(8-hydroxyquinoline)aluminum) electron transport/emissive layer; and a magnesium-silver (MgAg) cathode used for the injection of electrons. At the interface of the hole transport and electron transport layers, an emissive zone (~5 nm) is formed upon charge injection, where the electrons and holes recombine generating excited Alq_3 (Alq_3*)

molecules. Electroluminescence is observed when Alq_3^* in the singlet excited state radiatively relax to the ground state through the emission of a photon. Phenomenologically, MOLEDs differ from inorganic LEDs in that carrier transport occurs through a charge hopping mechanism. Following injection of holes or electrons at the respective electrode interface, radical cations or anions are formed, and conduction occurs through a series of charge transfer reactions that are driven by the applied field. In these devices, critical issues that affect the performance of the devices include barriers to carrier injection at each respective interface and electroluminescence quantum efficiency (number of photons emitted/number of electrons injected) of the chromophore.

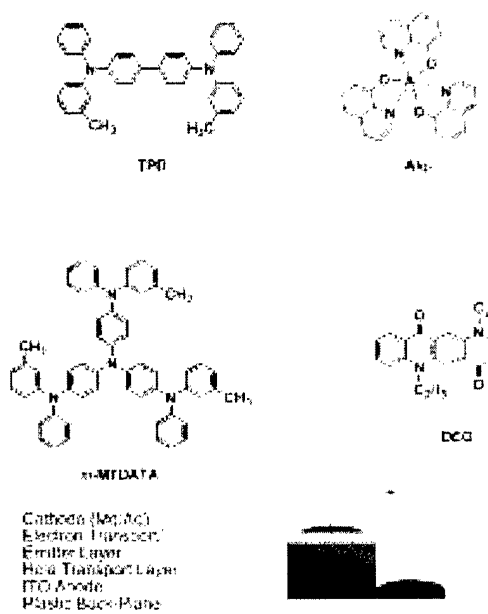

Fig. 4 — MOLED device configuration and organic thin film materials: Alq_3(tris(8-hydroxyquinoline)aluminum), TPD (*N,N'*-diphenyl-*N,N'*-bis(3-methylphenyl)-1-1'-biphenyl-4,4'-diamine), *m*-MTDATA (4,4',4"-tris(3-methylphenylphenylamino)-triphenylamine) and DEQ (diethylquinacridone).

Figure 5 shows an energy level diagram relative to the vacuum level (Energy = 0) for each respective device layer. For the molecular solids, the lower level corresponds to the solid state ionization potential (IP) and the upper level corresponds to the solid state electron affinity. The work functions of ITO and MgAg alloy are also shown in the diagram. At the ITO/TPD interface there is an energy barrier of ~0.8 eV for hole injection. To reduce the barrier to hole injection, a second hole transporter with a lower IP than that of TPD has been inserted between TPD and ITO. In this configuration, a 40-nm layer of *m*-MTDATA (4,4',4"-tris(3-methylphenylphenylamino)-triphenylamine) and a 10-nm layer of TPD is substituted for the 50-nm TPD layer. To evaluate the performance of the MOLEDs, we compare the luminous power efficiency and external quantum efficiency for the different device structures. The luminous power efficiency (lm/W) is defined as the ratio of the luminous flux (in lumens (lm)) from a Lambertian source to the electrical input power (W). The external quantum efficiency is a measure of the radiant light output per number of electrons injected (photons/electrons). At a current density of 100 A/m^2, MOLEDs on plastics with a single hole transport layer typically have an average luminous power efficiency of 1.5 lm/W, while those incorporating a double hole transport layer demonstrate a slightly higher average luminous power efficiency of 1.8 lm/W. The increase in luminous power efficiency has been attributed to the fact that *m*-MTDATA has an ionization potential of ~5.1 eV, intermediate between those of TPD and ITO, hence lowering the barrier to hole injection. This phenomenon is observed mainly as a voltage effect where at a given voltage, a higher current density is achieved.

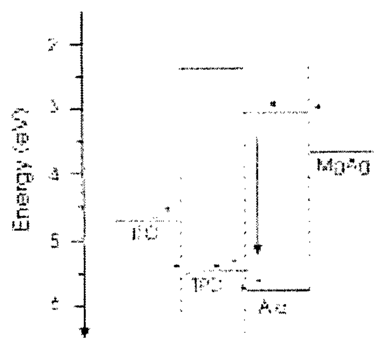

Fig. 5 — Energy level diagram (relative to vacuum) for materials used in a basic MOLED structure.

Major improvements in MOLED efficiency can be achieved by doping the emissive layer with a molecular compound that has a very high fluorescence quantum yield (80-100%). For example, we will use a substituted quinacridone, in particular diethyl quinacridone (DEQ), as a dopant in the electroluminescent host Alq_3. In this configuration, a 25-nm 1% molar DEQ in Alq_3 layer and 25-nm Alq_3 layer is substituted for the 50-nm Alq_3 layer.

For double hole transport layer MOLEDs on plastics, we note that the luminous power efficiency changed from 1.8 lm/W to 4.4 lm/W and the external quantum efficiency increased from 1.2% to 2.7% going from an undoped to a DEQ-doped Alq_3 layer.

MOLED Performance on Plastic vs Glass Substrates: Figure 6 compares the performance of an optimized device made on plastic vs glass substrates in terms of luminous power efficiency and external quantum yield. Devices made on plastics are more efficient than devices fabricated on glass. These results are surprising considering the bulk properties (sheet resistance and optical transparency) of the ITO on glass are superior to those of ITO on plastic substrates. The enhanced performance has been attributed to increased waveguiding in devices fabricated on glass substrates, which reduces the amount of light scattered in the forward direction [1]. The MOLEDs on plastics did not show appreciable reduction in performance after being bent (several times) around a 0.5-cm radius rod (Fig. 5). These results are promising in that highly efficient, low-power MOLED displays on flexible plastic substrates are a real and viable technology.

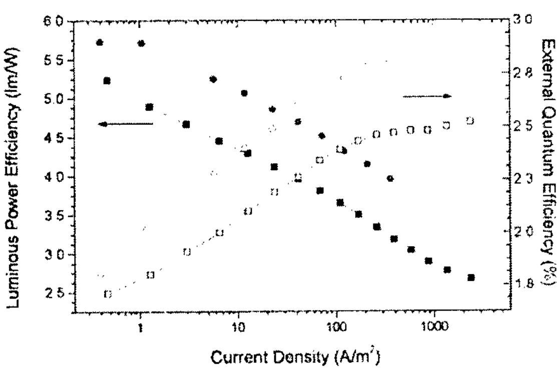

Fig. 6 — Plot of luminous power efficiency (solid objects) and external quantum efficiency (hollow objects) vs voltage for devices on polyester (●,O) and glass (■,□).

Future Directions: We are planning to develop new emitting and transport materials and incorporate them in novel and efficient device structures for the realization of full-color displays. Full-color displays can be achieved through individual color pixels (blue/green/red) or through several color-changing mechanisms, starting with a blue emitter. Challenges for plastic displays include improving thermal dissipation of heat to avoid deformation of the plastics, increasing operating temperature range, increasing device lifetime, and incorporating thin-film transistors for active matrix addressing schemes.

[Sponsored by ONR and DARPA]

Reference

1. G. M. Daly, H. Murata, C. D. Merritt, Z. H. Kafafi, H. Inada, and Y. Shirota, "Enhanced Performance of Molecular Organic Light-Emitting Diodes on Polyester Substrates," *Proc. SPIE* **3148**, p. 393-400, (1997). ◆

Laser Eye Protection

J.S. Shirk
Optical Sciences Division

A.W. Snow
Chemistry Division

Laser Threats: Laser systems are essential on a battlefield where they provide a critical technological edge to U.S. forces. However, the intense light from lasers can also lead to accidental eye injuries. A more sinister threat arises from rogue states and terrorists who know well that portable, easy-to-use lasers are obtainable on the open market. Some protection against single line threats is now available, but protection against common multi-wavelength and tunable lasers is more difficult since the wavelength cannot be predicted. The danger is even more severe if the victim is looking through a high optical gain device (binoculars, periscopes, gun sights) that concentrates a distant beam on the eye.

A collaborative effort between the Chemistry and Optical Sciences divisions at NRL in cooperation with personnel at the Patuxent River Naval Air Station, Wright-Patterson Air Force Base, the Army Research and Development Command (TARDEC), and several university researchers has been aimed at developing passive optical limiters. This has resulted in promising new materials for reverse saturable absorption/thermal hybrid optical limiters. Limiters using the new materials offer a way to minimize the potential for injuries to personnel or a disruption of their military mission.

Protection: Optical Limiters: An optical limiter has a high transmission at normal light intensities and a decreasing transmission for intense beams. This change in transmission limits the transmitted energy of a laser beam and thus protect eyes against intense flashes of light. Optical limiters typically take advantage of some nonlinear optical response in a material. Figure 7 illustrates an optical limiter. Except for the critical nonlinear element near the focal point, similar optics are found in binoculars and telescopes. The nonlinear element is designed to have an intensity-dependent absorption, refractive index and/or scattering coefficient. The operation of this element is akin to photochromic sunglasses, except the transmission change must occur in a few picoseconds to protect against a Q-switched laser pulse.

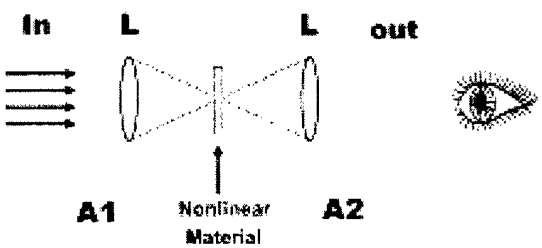

Fig. 7 — A typical optical limiter.

Recent Breakthroughs: Important breakthroughs in nonlinear materials for optical limiting have been made at NRL. Notable among these is the development of phthalocyanine materials that combine large nonlinear absorption and large nonlinear refraction coefficients. One of these materials was tested independently at the U.S. Army's ARDEC laboratory at Picatinny Arsenal, New Jersey, where it was found to have the lowest threshold and one of the best dynamic ranges of all the competing materials.

The new materials arose from a study of the mechanisms that determine the nonlinear optical properties of materials. This study explored the effect of high concentrations and high fluences where optical limiters typically operate. The left-hand side of Fig. 8 shows the pertinent molecular energy levels of a simple nonlinear absorber. When the ground state absorption coefficient σ_0 is much less than the excited state absorption coefficient, the absorbance σ_1 increases as the first excited state is populated by intense light. This effect provides limiting, but only over a restricted range of intensity. The transmission no longer falls after the maximum population in the first excited state is reached.

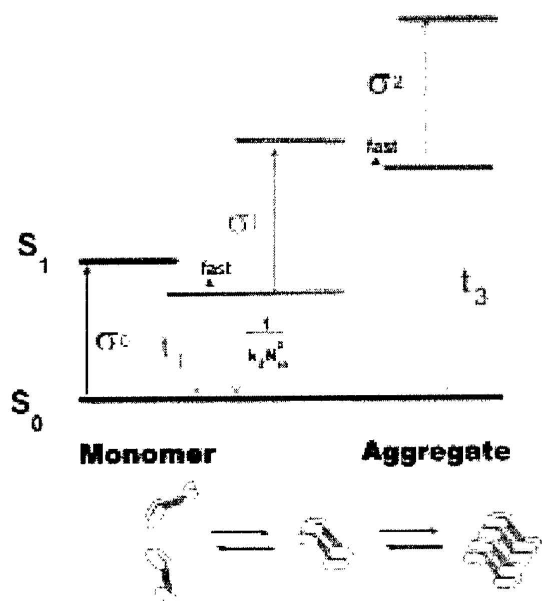

Fig. 8 — Energy levels giving nonlinear absorption. The new energy levels contributed by aggregate structures are on the right. Examples of specific aggregate structures are also shown.

Strategies for overcoming this saturation were developed at NRL. The best limiters use concentrated solutions or pure materials for the nonlinear element. Under these conditions, phthalocyanines can form ordered, stacked structures. Specific intermolecular interactions within these structures are crucial in determining the optical properties. These interactions depend critically on the size and structure of the aggregates. In particular, we found that long-lived, strongly absorbing, multiphoton states exist in specific aggregates. These states, shown on the right-hand side of Fig. 8, can extend the dynamic range of the limiter well beyond the initial saturation limit.

Taking advantage of these molecular processes required the synthesis of new molecular structures. New synthetic routes were developed at NRL to give control over the molecular and supramolecular structures that determine the nonlinear optical properties. For example, increasing the excited state lifetime can give a larger nonlinear absorption coefficient. Such suppression was achieved by surrounding the active chromophore with long

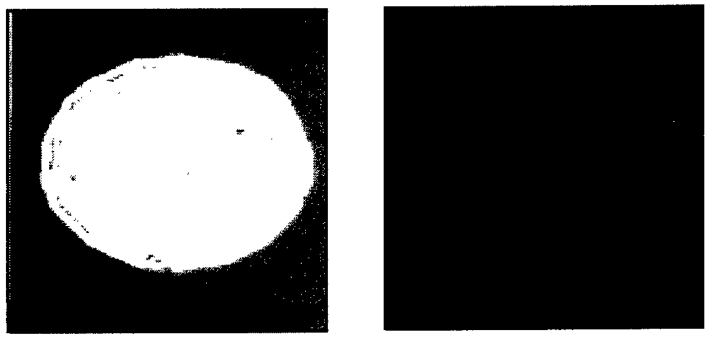

Fig. 9 — The spatial distribution of the intensity of a laser beam before (a) and after (b) an NRL limiter. The intensity scale of the output beam was expanded by a factor of 2.5 so it could be seen.

aliphatic substituents. These acted as "molecular insulation" to protect the excited state from deleterious interactions.

The long side chains that protect the excited state were simultaneously designed to endow the material with a large nonlinear refraction. Nonlinear refraction can make an important contribution to the limiting. With this nonlinearity, an incident laser beam induces a refractive index variation across the material and makes the nonlinear element a defocusing lens. The lens causes the laser beam to diverge so that aperture A2 (Fig. 7) removes a substantial fraction of the energy. Figure 9 illustrates this effect. On the left is a false-color image showing the intensity of the input beam to an NRL optical limiter. This beam has an intensity that can cause eye damage. On the right is an image of the intensity distribution in the output beam. The limiter has lowered the intensity to about one percent of the incident value. It has also dispersed this remaining light so that it is near the edges of the transmitted beam. This output spatial distribution is safer than the incident beam since it will not focus to a small spot on the retina.

Summary: Research at NRL and collaborating institutions has resulted in new and promising materials for reverse saturable absorption/thermal hybrid optical limiters. These materials can keep the energy transmitted through optical devices below the maximum permissible exposure (ANSI MPE) over a wide range of input energies. The limiters also alter the spatial distribution of the transmitted light to reduce the potential for subsequent damage. Currently, this level of protection is available in an optical system where there is an intermediate focus with a high optical gain. Suitable devices include, for example, periscopes, binoculars and gun sights.

[Sponsored by ONR and Joint Services Agile Program] ◆

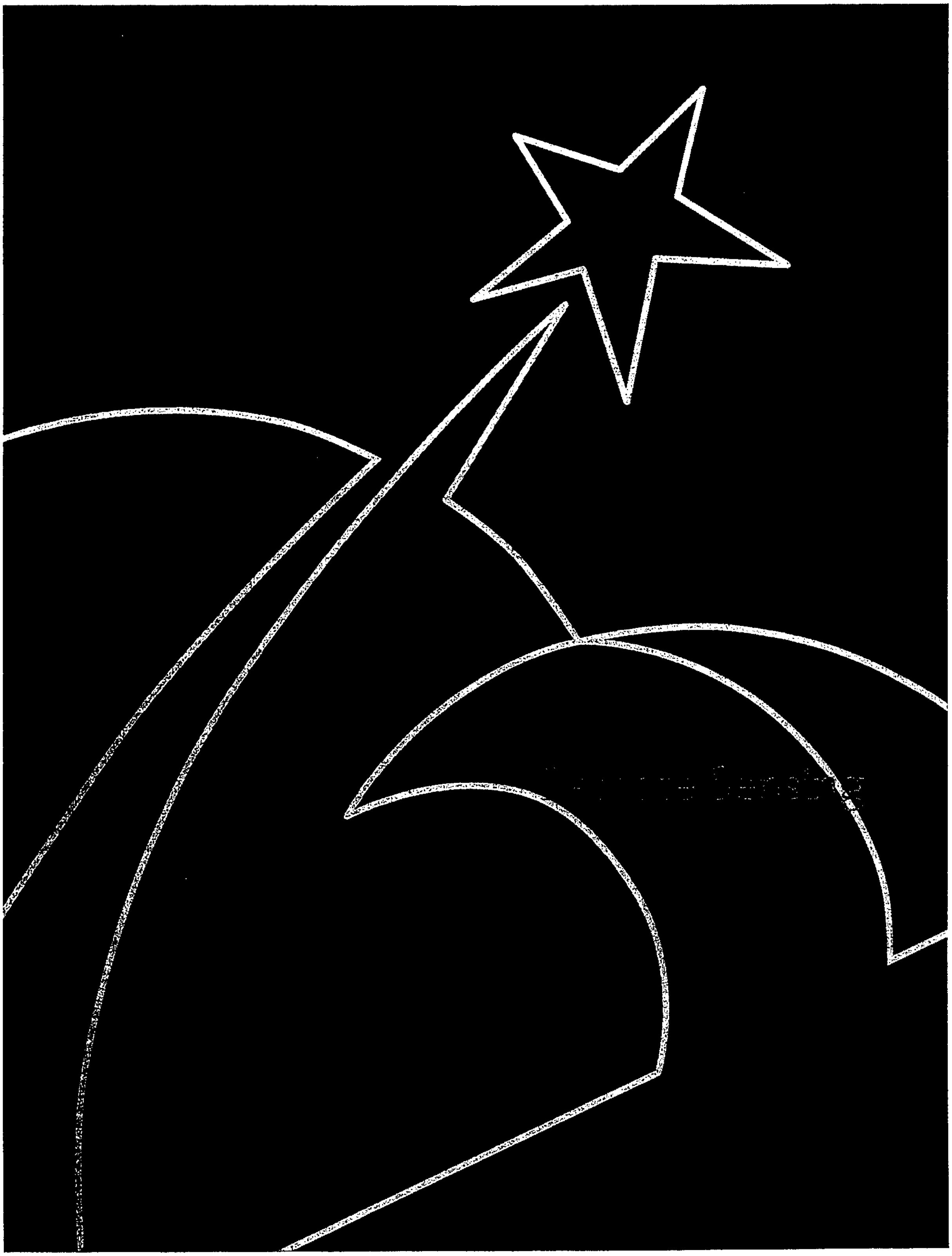

A Meteorological Re-analysis for the Study of Gulf War Illness

T.R. Holt, D.L. Westphal, S.W. Chang, N.L. Baker, T.F. Hogan, L.R. Brody, R.A. Godfrey, and J.S. Goerss
Marine Meteorology Division

D.J. Laws and C.W. Hines
Fleet Numerical Meteorology and Oceanography Center

Introduction: In March 1991 after the ground campaign of Operation Desert Storm, U.S. Army demolition teams destroyed ammunition bunkers and stacks of munitions at the Khamisiyah Ammunition Storage Area in southeastern Iraq. The U.S. Government now believes that the 122-mm rockets destroyed in at least one of the bunkers and in an excavated area known as "the Pit" were filled with chemical agents sarin and cyclosarin. It has been suggested that low-level exposure to these chemical agents, commonly known as nerve gas, could have led to the symptoms associated with Gulf War Syndrome or Gulf War Illness. Ongoing investigative studies of this possibility require a determination of the release rate and accurate atmospheric transport and dispersion modeling to assess the concentration of the gas relative to troop positions. This in turn requires an analysis of the complicated, time-dependent mesoscale structure of the atmosphere at frequent intervals. The analysis must be carried out for several days since the release may have continued for 36 or more hours after the initial detonation, and since even low concentrations of nerve agent far from Khamisiyah are of interest to epidemiologists. The Marine Meteorology Division, assisted by the Fleet Numerical Meteorology and Oceanography Center (FNMOC), has performed global and mesoscale re-analyses of the atmosphere in support of the study of this event.

The Re-analysis Procedure: The re-analysis is conducted with the Navy's state-of-the-art global and mesoscale analysis and prediction systems: the Navy Operational Global Atmospheric Prediction System (NOGAPS) [1] and the NRL Coupled Ocean/ Atmosphere Mesoscale Prediction System (COAMPS) [2]. A comprehensive set of observations has been collected and used in the re-analysis, including unclassified and declassified surface reports, ship and buoy reports, observations from pibal and rawinsonde, from aircraft, and retrievals from civilian and military satellites. The atmospheric conditions over southern Iraq, Kuwait, and northern Saudi Arabia are reconstructed using COAMPS at the spatial resolutions of 45, 15, and 5 km. In addition to a baseline re-analysis, perturbation analyses are also performed to estimate the atmospheric sensitivity to observational error and analysis error. These additional analyses suggest that the re-analysis has bounded the variability and that the actual atmospheric conditions are unlikely to differ significantly from the baseline re-analysis.

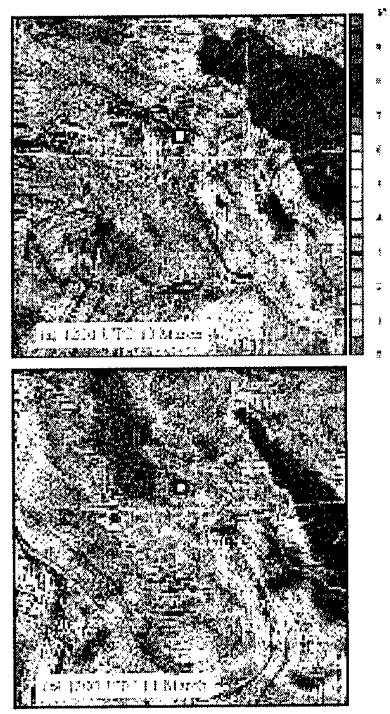

Fig. 1 — COAMPS 15-km mesh re-analysis of 10-m wind speed (shaded, contour interval of 1 m s-1) and streamlines valid 1200 UTC for the days indicated. Surface wind observations are plotted in white (full barb = 10 m s-1). The white box indicates the location of Khamisiyah.

Results: The re-analysis indicates that meteorological conditions at and up to 72 h after the time of the detonation (1200 UTC 10 March to 1200 UTC, 13 March 1991) are typical of a weather pattern that occurs after the passage of the regional, strong wind regime called the Shamal and are controlled by eastward propagating small-amplitude troughs and ridges. Figure 1 shows that mesoscale conditions over the Tigris-

Euphrates Valley are further modulated by diurnal variation in the local circulations between land, the Persian Gulf, and the Zagros mountains. Boundary layer winds at Khamisiyah from the north-northwest at the time of the detonation shift to west-northwest at night. On the second day, strong high pressure passes north of Khamisiyah and the winds strengthen and turn to the east-southeast. During the final day, the region is dominated by the approach and passage of a low-pressure system and the associated front, with the southeasterly winds veering to northwesterly.

A transport model for passive scalars [3], driven by COAMPS forecasts of variables such as winds, temperatures, and vertical mixing, is used to illustrate sensitivity of potential areas of contamination to the re-analyzed fields. The dosage pattern, computed from transport calculations based on various release scenarios and re-analyzed meteorological conditions for the 72-h period after the demolition, suggests that the mean path of the released chemical agents is southward from Khamisiyah initially, turning westward and eventually northwestward (Fig. 2). The curving branch to the southwest results from persistent anticyclonic conditions during the first 12 h of emission. The light, westerly winds over the next 12 h result in little transport of the gas out of the area. The wind then shifts rapidly to southeasterly and remains from that direction for the next 48 h. Thus, the final 12 h of the 36-h emission are in southeasterly winds, resulting in the northwest branch of the dosage pattern.

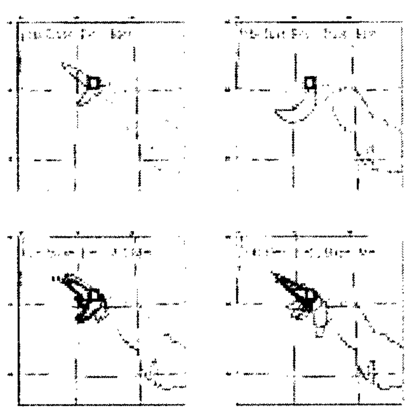

Fig. 2 — Simulated dosage patterns for 1200 UTC, 10 March to 1200 UTC 13 March 1991: (a) baseline emission and baseline re-analysis; (b) instantaneous release and baseline re-analysis; (c) baseline release and four perturbation re-analyses; and (d) location- and time-perturbation releases and baseline re-analysis.

The vertical distribution of the agent is controlled by boundary layer mixing. The simulated emission began at 1330 UTC, or 1630 local time, in the late afternoon. The gas released in the first few hours is immediately mixed throughout the kilometer depth of the boundary layer (Fig. 3(a)). After sunset, the boundary layer stabilizes and subsequent emissions are concentrated in the lowest few hundred meters in a process called fumigation (Fig. 3(b)). After sunrise the next day, the gas is again mixed throughout the boundary layer and surface concentrations decrease (not shown). Fumigation occurs again after sunset on 11 March in the southeasterly flow.

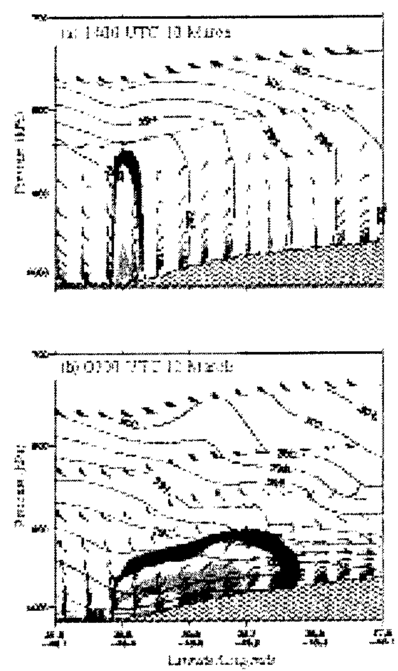

Fig. 3 — Cross section from 31.6N, 46.7E to 27.8N, 45.1E (NNE-SSW through Khamisiyah) of simulated gas concentration (arbitrary units, with two shaded contours per decade) for the baseline emission and baseline re-analysis. Also shown are potential temperature (contoured every 2 K) and wind speed and direction (wind barbs, with a full barb equal to 5 m s[-1]). (a) 1400 UTC, 10 March; (b) 0000 UTC, 11 March.

Conclusions: This study demonstrates the value of the re-analysis procedure for problems of interest to the Navy and the other armed services. A mesoscale prediction and data assimilation system embedded in and driven by a global system is a powerful method for obtaining meteorological

conditions and is essential for studies of continuous or instantaneous emissions of chemical or biological agents or other naturally occurring aerosols such as smoke and dust. An even more complete system, with a dispersion model embedded within COAMPS, is now being developed at NRL. This system will allow real-time, quantitative predictions of dosage and distribution of the agents of interest.

Because of the sensitivity of this topic, the NRL re-analyses have been reviewed by two impartial panels and were chosen over those of other providers as the most accurate and robust. Hence, NRL has been requested to provide re-analyses for other critical periods during the Gulf War. The effort was jointly supported by U.S. Navy SPAWAR, OATSD(NCB) and OSAGWI and could not have been accomplished without the computational resources, technical aid and expertise of FNMOC.

[Sponsored by SPAWAR, OATSD(NCB), OSAGWI]

References

1. T. Hogan and T. Rosmond, "The Description of the Navy Operational Global Atmospheric Predictions System's Spectral Forecast Model," *Mon. Wea. Rev.* **119**, 1786-1815 (1991).

2. R.M. Hodur, "The Naval Research Laboratory's Coupled Ocean/Atmosphere Mesoscale Prediction System (COAMPS)," *Mon. Wea. Rev.* **125**, 1414-1430 (1997).

3. O.B. Toon, R.P. Turco, D.L. Westphal, R. Malone, and M.S. Liu, "A Multidimensional Model for Aerosols: Description of Computational Analogs," *J. Atmos. Sci.* **45**, 2123-2143 (1988). ◆

Wide-Field Imaging of Low-Frequency Radio Interferometric Data

N.E. Kassim and R.S. Foster
Remote Sensing Division

T.J.W. Lazio and D.S. Briggs
National Research Council Associate

Introduction: High dynamic range images of far-field sources at very high frequency (VHF) radio frequencies can address a number of astrophysical and Department of Defense (DoD) applications. On the astrophysical side, such images can be used to study (1) the magnetohydrodynamics of the blast wave-ambient medium interaction in a supernova, including the acceleration of high-energy particles and the origin of cosmic rays; (2) the supernova mechanism and the possible means of providing asymmetric velocity kicks to the newborn neutron star; (3) the three-dimensional (3-D) spatial distribution of thermal and nonthermal emitting gas in the galaxy; and (4) the distribution and spatial spectrum of plasma density fluctuations responsible for interstellar scattering. Production of high dynamic range images requires compensation of phase fluctuations induced by the ionosphere. DoD applications of wide-field imaging and ionospheric compensation techniques include using high-frequency (HF) solar radar for predicting arrival times of Earthward-bound coronal mass ejections (CMEs) for geomagnetic storm prediction and characterizing and tracking naturally and artificially generated ionospheric waves at HF and VHF frequencies.

Methodology: The complexity of producing wide-field images at VHF radio frequencies has prevented routine imaging at the limiting sensitivity and angular resolution inherent in the data. Most radio arrays are intrinsically noncoplanar and the simple, 2-D Fourier inversion, which is commonly employed to derive an image from the measured interferometric visibility data, is inadequate. At frequencies above 1000 MHz, the phase errors introduced by the assumption of coplanarity are small, and high-resolution images are routinely produced with sensitivities at the thermal noise limit. At lower frequencies, the combination of noncoplanar arrays, an intrinsically larger field of view, and the increased space density of radio sources introduces errors, which have precluded achieving the desired thermal-noise-limited sensitivities. Algorithms to implement the required 3-D treatment are available; but the computational expense of applying them to real data has been prohibitive, and only low-resolution images have been produced until recently. We have been engaged in a program to demonstrate that, once adapted to operate efficiently within a powerful and parallel computing environment, these complex wide-field imaging algorithms can be employed to generate images of far-field radio emitters at high resolution and sensitivity in a routine manner.

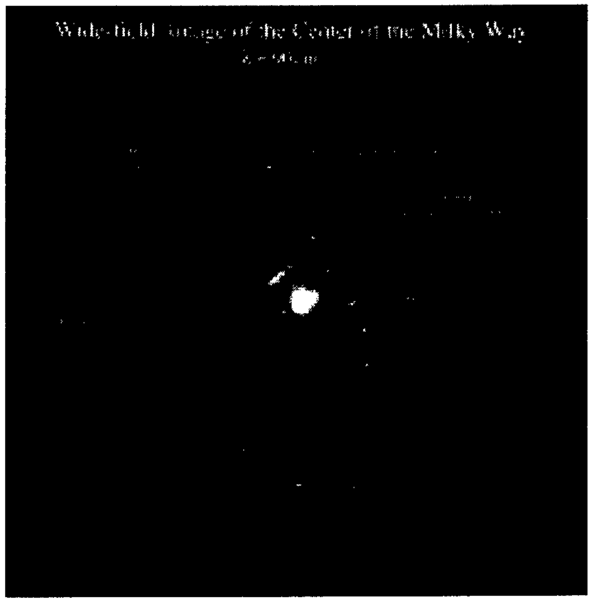

Fig. 4 — An image of the center of the Milky Way Galaxy at 330 MHz, produced on the ARL SGI PCA. This image is approximately 2° on a side. Prominent are a previously unknown supernova remnant, Sgr A, within which a 2 million solar-mass black hole is thought to reside; the massive star formation regions Sgr B1 and B2, the magnetic field-dominated structures of the Arc and threads; and other previously identified supernova remnants and regions of ionized hydrogen.

We have used the very large array (VLA) radio interferometer at the National Radio Astronomy Observatory near Socorro, New Mexico, to gather radio interferometric data at 330 MHz. The data were then processed through a serial version of a 3-D, wide-field imaging algorithm on the SGI Power Challenge Array at the Army Research Laboratory in Aberdeen, Maryland, and on the IBM SP2 at the Maui High Performance Computing Center in Maui, Hawaii.

The computational power provided by these machines is also enabling us to combat bandwidth smearing. The limiting factor on the resolution obtained at large angular distances from the phase center of an image has been the large bandwidth over which the data were averaged before being Fourier inverted. However, the intrinsic bandwidth of the data is much narrower and, if this narrower bandwidth can be preserved in the imaging, the result is a much more uniformly shaped synthesized beam over the entire 2.6° field of view (FOV).

Results: Figure 4 shows an example of recent work. This is a 330 MHz image of a 4-deg^2 region within the constellation Sagittarius, which includes the center of our galaxy, the Milky Way. With this map—the largest ever made of the galactic center at a uniform and high resolution—we have identified a bright, previously unknown supernova remnant. Also prominent are Sgr A, within which a 2 million solar-mass black hole (1 solar mass = 2×10^{30} kg) is thought to reside; massive star formation regions (Sgr B1 and B2); unusual magnetic field-dominated structures (the Arc and threads); and other previously identified supernova remnants and regions of ionized hydrogen.

The data used to produce this image are being combined with more recently acquired data to search for additional supernova remnants, radio pulsars, and radio transients. Identification of such objects would improve our understanding of (1) the star formation history, (2) the distribution of plasma turbulence, and (3) possibly the gravitational potential in the galactic center. In the course of observing the galactic center over the past decade, we have also assembled a unique database for the identification of radio transients, which will allow us to constrain the nature of the transient source population in the galactic center.

[Sponsored by NRL] ◆

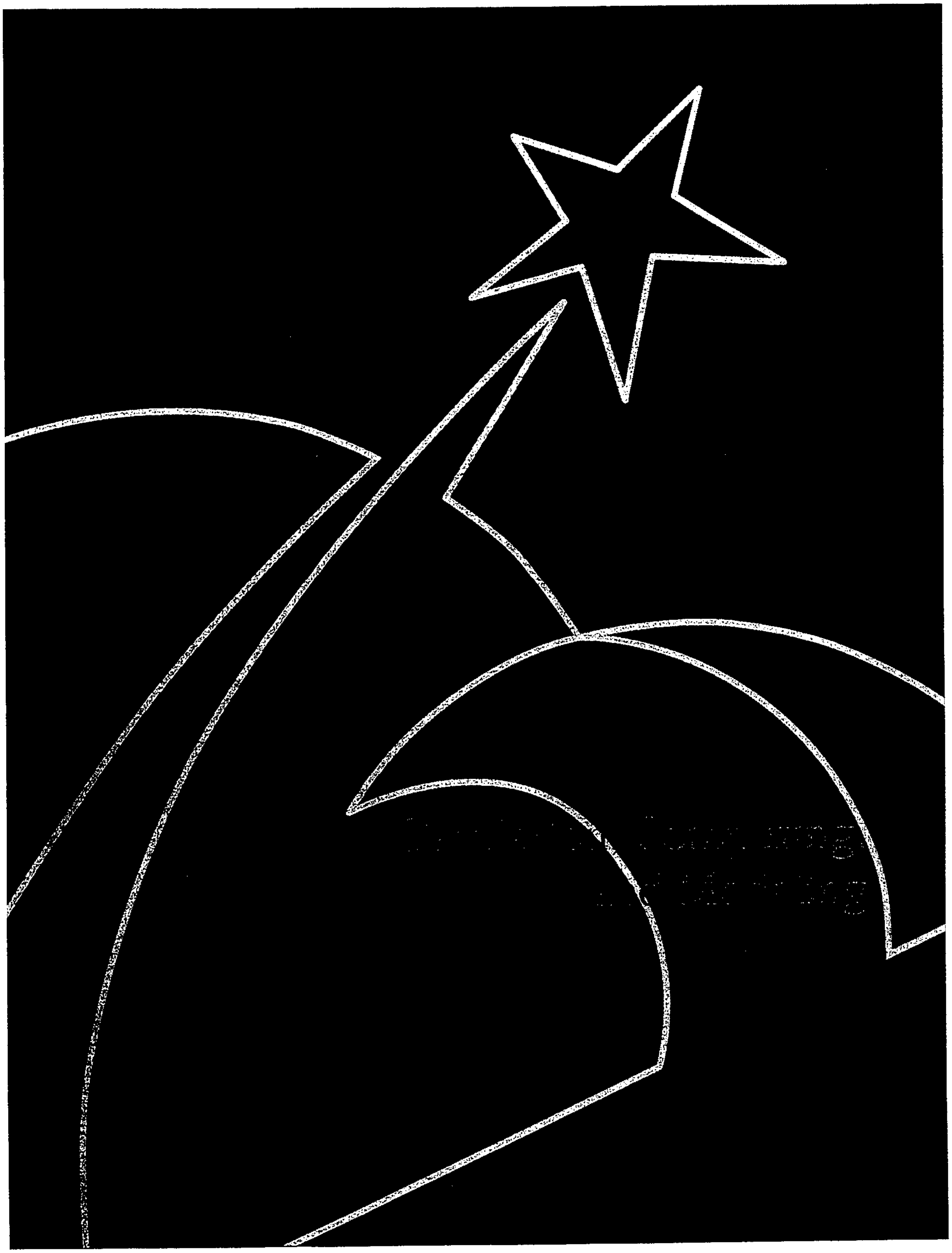

Reduction of Ship Radar Cross Section Using Measured and Calculated Signature Data

M.A. Busse and D.A. Zolnick
Radar Division

At the present time, U.S. Navy ship RCS (radar cross section) reduction is achieved through a combination of shaping and RAM (radar absorbing material) solutions. Unlike aircraft RCS reduction programs, the physical size and geometric complexity of Navy ships make exact RCS calculations impossible with existing computer technology. As a result, the Navy relies on a combination of high-speed (approximate) computer calculations and RCS measurements to direct its RCS reduction efforts. Because RCS calculations and measurements have both advantages and limitations, it is desirable to combine all available methods to achieve the most accurate results possible.

Signature Calculations: NRL has produced the RTS signature calculation and analysis system. The heart of this system is a RCS calculation engine that uses high-frequency RCS approximations to accurately compute the RCS of large/complex targets, including sea multipath, multiple bounce interactions, and blockage. The system can compute signatures for surfaces covered with RAM and for semitransparent surfaces. The RTS system also includes a workstation analysis tool called XRAT that can display target geometry and various signature information. Figure 1 shows a sample RTS computer model using XRAT. We use this model as an example for demonstrating the signature analysis process. The RTS system saves scattering information at each aspect angle so the user can identify the individual scattering components contributing to the overall target signature. The user can then select a feature from the calculated signature and interactively display the saved signature contributions for that aspect angle on the computer model with the levels color coded as shown in Fig. 1.

Signature Measurements: RCS reduction efforts on existing Navy ship classes can take advantage of full-scale at-sea testing. These measurements are typically conducted using a high-resolution imaging radar at a fixed point on shore, with the target ship turning one-half-mile diameter circles at a range of approximately 5-10 miles from the radar. These radars use varying waveforms to produce HRR (high range resolution) and ISAR (inverse synthetic aperture radar) data results. The target ships typically have radar reflectors (markers) attached at the bow and stern to aid in tracking.

HRR data are typically produced by using a chirp pulse and recording the returned energy at 512 frequencies. Performing an FFT (fast Fourier transform) on the returned data provides 512 bins of range resolution. The bandwidth of the pulse is adjusted so that the total range covers the maxi-

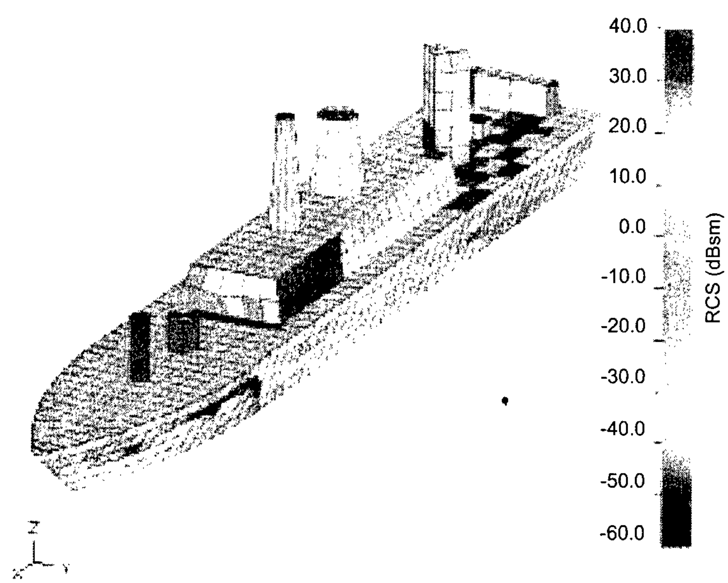

Fig. 1 — RTS computer model of generic ship target with RCS shown in dBsm.

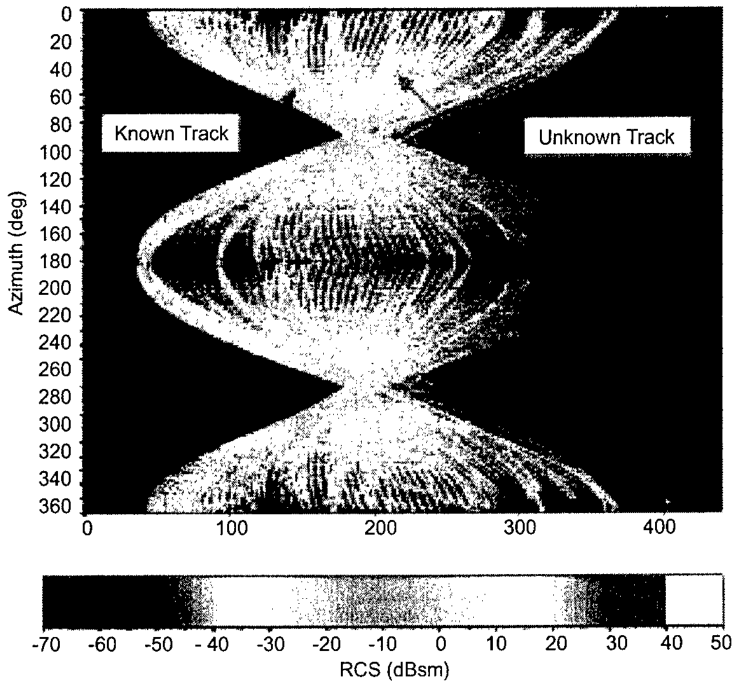

Fig. 2 — High range resolution RCS plot showing tracks used for determining scattering location.

mum downrange extent of the target. Figure 2 is an RTS-computed HRR plot. The radar illuminates from the left-hand edge of the plot, and the RCS is shown on the same color-coded scale used in Fig. 1. A full 360° rotation of the ship is shown in one plot. Individual features on the ship appear as nearly sinusoidal tracks on the HRR plot. The location of the ship feature that produces the track can be determined by measuring the distance from the unknown track to the location of a track corresponding to a known feature at multiple points on each track. Each measurement defines a plane perpendicular to the radar at the measured distance from the known feature. Each plane can be plotted as a line in a plan view of the computer model of the target. This produces a number of lines that should intersect in a very small region where the scattering originates. As an example of this process, the lines generated from the tracks in Fig. 2 are plotted on the computer model shown in Fig. 3. The cylinder on the fo'c'sle is used as a known feature, and plotted lines from the unkown track form a nice intersection at the small cone on the deckhouse, indicating that this is the source of the scattering. Note that the RCS level of the unknown track in Fig. 2 and the cone in Fig. 3 are the same. Because HRR data plots contain no information about the height of scattering, there is often ambiguity when attempting to identify scattering features. This previously described method is very useful in allowing an analyst to correlate HRR and calculated signature data.

ISAR images are produced by performing an FFT on multiple (typically 256) radar pulses. This processing produces Doppler frequency information that, because of the ship's rotation (due to constant turn rate and sea effects), provides cross-range resolution. ISAR images typically make the target appear warped due to the difference between downrange and cross-range resolutions. NRL has developed a technique for warping a computer model of the target based on motion telemetry information from the ship. This warped model is overlaid on the image to facilitate scattering location determination. ISAR data shares a limitation with HRR data in that it produces a two-dimensional image with 1° of geometric uncertainty. NRL is currently developing a method to warp the ISAR image such that it can be overlaid on the same display shown in Fig. 1 without distortion of the model. This will allow a user to correlate HRR, ISAR, and RTS data simultaneously on the same display.

Summary: By correlating signature results from various sources, an analyst can usually

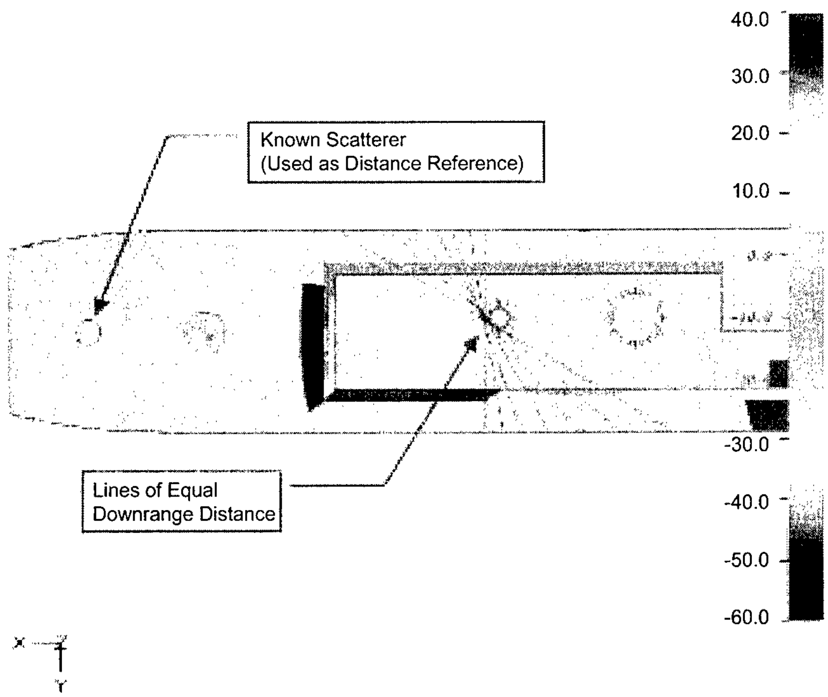

Fig. 3 — Plan view of computer model with lines of equal downrange distance plotted.

overcome the limitations of each individual data source and determine scattering mechanisms with a reasonable degree of confidence. When scattering mechanisms are identified, an analyst can use the RTS system to evaluate solutions by changing target geometry and/or adding RAM materials and computing the new target signature. This provides an analysis loop that can be used to methodically and reliably reduce ship signatures.

[Sponsored by NAVSEA] ◆

Prototype Cloud Simulation in a Flight Mission Rehearsal System

L.A. Hembree and S. Brand
Marine Meteorology Division

Over the past several years, the role of simulation within the Department of Defense (DoD) has been increasing. Currently, most modeling and simulation efforts include very little, if any, appropriate environmental information and environmental effects. Because efforts are now underway to increase the overall realism of simulations, opportunities exist to incorporate more realistic environmental information and effects into the simulations.

Clouds, in particular, play a critical role in the success or failure of tactical aircraft missions. The purpose of this article is to describe the prototype development for incorporating realistic clouds into a flight mission rehearsal system. To develop the prototype, NRL adapted and integrated several independently developed components. These included a realistic cloud model, rendering methodologies, and a flight mission rehearsal system. The prototype was the first time all three components had been integrated into a flight mission rehearsal system to provide scenes with realistic clouds.

Cloud Model: A means of realistically and quickly modeling clouds was required. The Cloud Scene Simulation Model (CSSM) was selected as the model to be used. CSSM was developed by The Analytical Sciences Corporation (TASC) under sponsorship from the Air Force Phillips Laboratory and the Defense Advanced Research Projects Agency (DARPA). CSSM uses readily available meteorological input data, such as wind, temperature, and moisture information (typically available from atmospheric soundings and surface observations or from numerical model output) and is relatively fast. The CSSM is a parametric model that takes advantage of several computationally efficient stochastic field generation algorithms to

synthesize the overall external structures and internal water density fields of a variety of cloud types. The model output consists of 3-D fields of cloud liquid water content.

Visualization Methodology: The visualization had to satisfy the following requirements: (1) the images had to be derived from 3-D cloud data such as that available from the CSSM; (2) visibility effects between any two points had to be realistic; (3) varying levels of data resolution to support varying graphics hardware fidelity and databases had to be accommodated; and (4) the methodology had to be relatively fast.

A geometric-primitive aggregation approach was chosen as the best rendering methodology. This approach, initially developed by Loral Inc., with funding from DARPA and NRL, groups many small graphic primitives together to provide a total cloud structure. It has the potential to produce a very accurate overall appearance. Each primitive has its own attribute settings. Therefore, transparency and lighting variations throughout the cloud can be accurately modeled. The visibility problem is solved with this technique by assigning the transparency value to the texture for each primitive based on its liquid water content value.

The Mission Rehearsal System: The PowerScene™ mission rehearsal system was chosen as the prototyping system. It was initially developed under sponsorship from the Naval Air Systems Command. Scenes are generated by using rectified satellite and photographic imagery as a texture on a digital terrain elevation database (DTED) obtained from the National Imagery and Mapping Agency (NIMA). The user can "fly" through the generated scene in a simulated autonomous flight mode using realistic stick and throttle controls, or a joystick. The autonomous flight mode is restricted by the flight dynamics of the simulated aircraft. In the simpler joystick-controlled viewing mode, these constraints are relaxed and permit the user to move arbitrarily around the simulation area, stopping, starting, and moving sideways as needed. In this manner, the user can become familiar with the target mission area and thus identify a preferred route and approach prior to the mission.

Results: Figure 4 shows how a typical scene appears in current mission rehearsal systems. The observation point is located above the China Lake, California, airport and is looking to the west-northwest. The irrigated fields at A are used as a reference point in the following figures. Figure 5 is the same scene with clouds added. The view is in the same direction as in Fig. 4, but the viewpoint is farther to the south-southeast. The clouds were generated using CSSM and the rendering methodology described. The China Lake airport is located just below B and is barely visible. The irrigated fields at A are not visible. Additional irrigated fields are located at C. Figure 6 is the same scene as in Fig. 5, but farther along the flight path near the base of the clouds. The irrigated fields at A are now visible, as is the airport. This shows how the visibility changes as the amount of clouds between the observer and an object changes.

Summary: The integration of the CSSM into PowerScene™ marks the first time that a realistic cloud model has been integrated into a flight mission rehearsal system, thus allowing the impact of clouds on mission effectiveness to be examined. Significant future enhancements could be achieved from both the computer science/visualization perspective as well as the meteorological perspective. The cloud rendering could be enhanced by reducing depth complexity and developing additional cloud textures. The meteorological challenges include developing the capability to derive fields from numerical weather prediction models for use as real-time inputs to the CSSM; developing a method to incorporate the horizontal inhomogeneity of cloud fields; and integrating a physically based model to transform cloud liquid water to transparency before rendering. These enhancements will provide the basis for an end-to-end

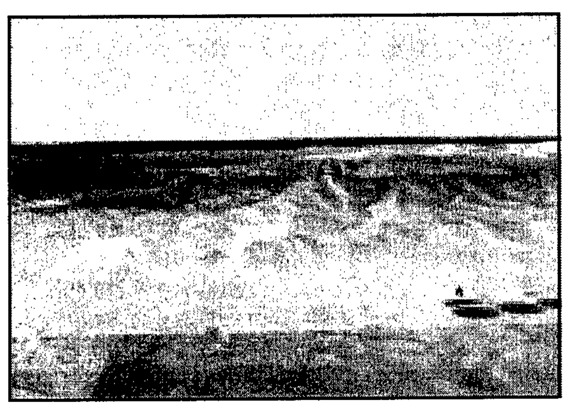

Fig. 4 — Normal rendering of scene without clouds. The view is from over the China Lake, California, airport looking west-northwest; DTED terrain rendered with photo imagery is used as texture. Irrigated fields at **A** are used as a reference point in Figs. 5 and 6.

Fig. 5 — Similar to Fig. 4, but with clouds incorporated. Figure 4 was looking in the same direction, but the airport **B** was below the view point. Point **A** is the location of the irrigated fields in Fig. 4.

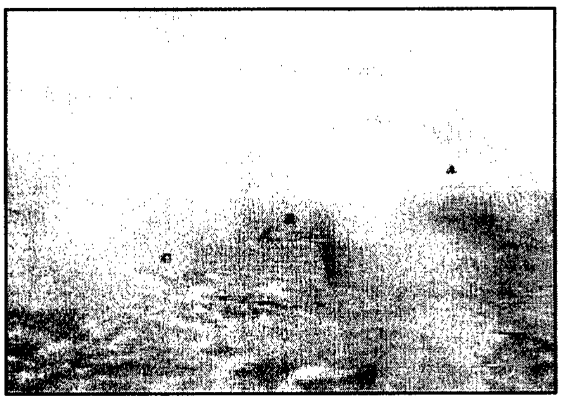

Fig. 6 — Same as in Fig. 5, but farther along the flight path near the base of the clouds. Points **A**, **B**, and **C** correspond to the same points in Fig. 5.

system for more realistic and efficient flight mission planning and rehearsal.

[Sponsored by ONR]

References

1. L. Hembree, S. Brand, W. Mayse, M. Cianciolo, and B. Soderberg, "Incorporation of a Cloud Simulation into a Flight Mission Rehearsal System: Prototype Demonstration," *Bull. Amer. Meteorol. Soc.* **78**(5), 815-822, (1997).

2. L. Hembree, S. Brand, W. Mayse, M. Cianciolo, and B. Soderberg, "Cloud Simulation for a Flight Mission Rehearsal System," *Proc. Seventh Conference on Aviation*, Long Beach, Calif., Feb. 1997, pp. 450-455.

◆

Enhanced Modeling of the Total Upper Atmospheric Density for Orbital Tracking

J.M. Picone,[1] J. Lean,[1] S. Thonnard,[1] R.R. Meier,[1] S.L. Coffey,[2] and A.E. Hedin[3]

[1]*E. O. Hulburt Center for Space Research*

[2]*Naval Center for Space Technology*

[3]*Universities Space Research Association, Washington, DC*

The largest source of error in software for precision tracking of objects in low Earth orbit (LEO) is uncertainty in estimating upper atmospheric drag. This is primarily due to the inaccuracy of present operational models for computing the total atmospheric density. The empirical models developed by Jacchia in the 1960s are now extrapolating data more than 30 years old to estimate present conditions. Under an exploratory development program aimed at significantly improving total density estimates, NRL scientists have exclusively acquired the technology for supporting and upgrading the Mass Spectrometer-Incoherent Scatter Radar (MSIS) model of upper atmospheric composition and temperature. MSIS is the standard model used by the scientific community. Unlike the Jacchia models, MSIS can be upgraded with new data from future multiyear, global remote sensing missions, beginning in 1998 with the launch of NRL's STP P91-1 mission on the Advanced Research and Global Observation Satellite (ARGOS). Here we discuss the future role of MSIS in precision orbit determination and the incorporation into MSIS of our new proxy (designated SOLEUV) for the solar extreme ultraviolet radiative flux, which is the primary driver of global upper atmospheric variability on time scales of a day or longer.

The Use of MSIS: MSIS (Fig. 7) forms the core of the NRL Ground Data Analysis Software (GDAS) supporting the Defense Meteorological Satellite Program's (DMSP) Special Sensor Ultraviolet Limb Imager (SSULI). SSULI is an operational system designed and built by NRL for measuring upper atmospheric composition. The first SSULI will fly aboard the DMSP S-16 satellite in the year 2000. The Air Force Space Command 55th Space Weather Squadron (SWS) will run the GDAS, using SSULI spectral data to compute an optimal scaling factor for the solar input (SOLEUV) to MSIS (and possibly one for the geomagnetic

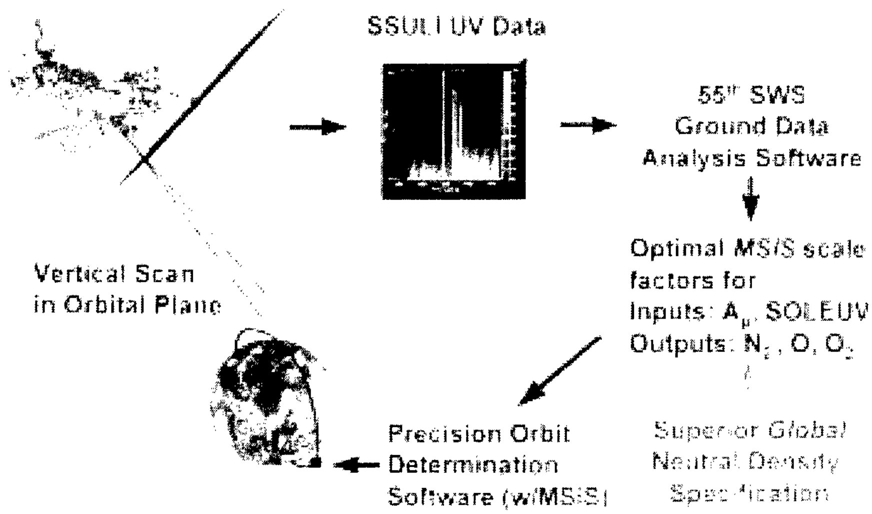

Fig. 7 — Beginning with DMSP S-16 in 2000, SSULI spectral data for each orbit (~100 min) will flow in near real time to the 55th Space Weather Squadron, which extracts optimal scaling factors for MSIS input(s) and the output composition. These factors may then be ingested directly into orbit determination software in which MSIS resides, providing a superior *global* density specification. The ARGOS/LORAAS system is identical to SSULI and will provide data for evaluating SSULI-enhanced MSIS products in the NCST Special Perturbations Space Object Catalog.

input A_p), along with optimal scaling factors for the output composition (N_2, O, and O_2 densities). Precision orbit determination software that includes MSIS can then ingest these factors directly to compute superior, near-real-time drag estimates for all LEO objects. We will test this system on the Naval Center for Space Technology's Special Perturbations Space Object Catalog (SPSOC), which now performs precision orbit determination on 7500 LEO objects using the unclassified observation sets from the Naval Space Command. In addition, ARGOS carries a direct copy of SSULI, known as LORAAS. The LORAAS data, along with the SPSOC, will provide a prototype simulation of the operational use of the SSULI-enhanced, MSIS density specification.

Reducing Global Systematic Error: The second major element of our work is the reduction of global systematic error in operational density models through the use of a faithful representation of the solar extreme ultraviolet (EUV) flux. Both the Jacchia and MSIS models presently represent the solar influence through its 10.7-cm radio flux ($F_{10.7}$), which is conveniently measured from the ground and provides a reliable long-term proxy for solar activity. However, because $F_{10.7}$ overemphasizes the solar coronal regime relative to the more important chromospheric EUV sources, we have developed a new full-disk solar chromospheric proxy (SOLEUV) for use in the MSIS model. SOLEUV draws on the following measures of solar activity: UARS SOLSTICE Magnesium (Mg) Index (May 1992 - present); NOAA Mg Index (November 1978 - May 1992); Helium 1083 nm equivalent width (1976 - November 1978); and the plage index plus smoothed $F_{10.7}$ (1949-1976). Figure 8 compares the SOLEUV and $F_{10.7}$ time series over several solar cycles; the different colors in the SOLEUV plot indicate contributions of its four components. Since both $F_{10.7}$ and SOLEUV are directly related to solar activity, the two time series show similar behavior over long time scales (solar cycle). However, SOLEUV provides a superior representation on time scales of days to months. Figure 9 illustrates these differences with a spectral power decomposition of each time series. We see, for example, that $F_{10.7}$ overemphasizes periods around 75 days and underemphasizes time scales around 13 days. Closer inspection reveals that SOLEUV and $F_{10.7}$ differ at most other time scales as well. Recent work by the Air Force Research Laboratory indicates that the Mg index used in SOLEUV can remove significant systematic errors that are present in existing empirical models. The availability of both the SPSOC and our SOLEUV proxy will permit a detailed evaluation of the resulting enhancement to MSIS when applied to precision orbit determination. The new SOLEUV proxy is also a standalone product with wider application to operational specification and forecasting of the near-Earth space environment.

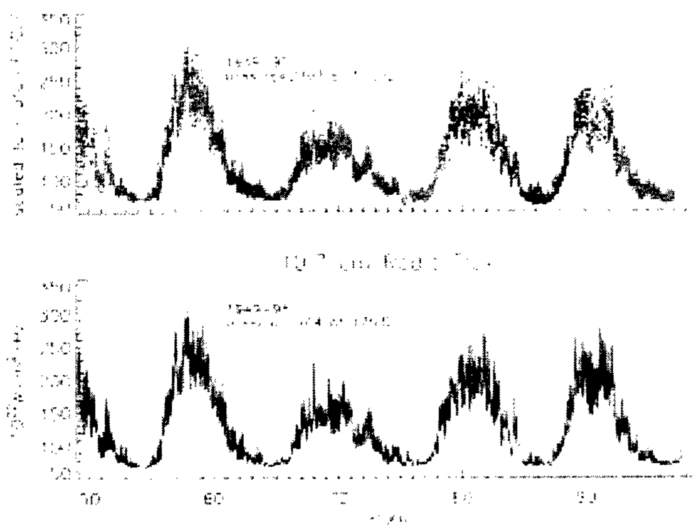

Fig. 8 — Comparison of time series: new NRL chromospheric proxy for the solar extreme ultraviolet flux (SOLEUV, top panel) vs $F_{10.7}$.

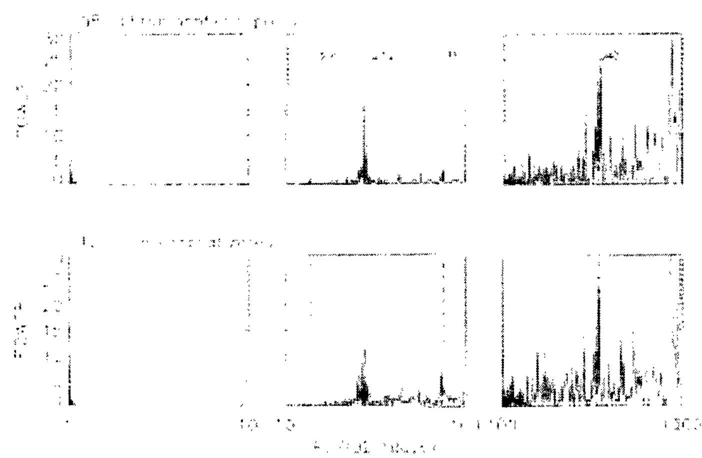

Fig. 9 — Comparison of power spectra as functions of time scale (in days): SOLEUV (top row) vs $F_{10.7}$ (dotted lines identify important spectral features).

Impact: Our work covers key facets of accurate density modeling and drag estimation for precision orbit determination. These include the state-of-the-art empirical density model; a superior solar EUV proxy to eliminate long-standing systematic errors in upper atmospheric models, testing of improved models in a high-performance, operationally consistent environment; and the assimilation of near-real-time, operational remote sensing data into the model to improve the global neutral density specification. The last aspect is a major issue of space environment forecasting, and our results should provide vital information on how to use operational data to develop superior global forecasts of various space environmental properties.

[Sponsored by ONR]

References

1. J.M. Picone, A.E. Hedin, S. Coffey, J. Lean, D.P. Drob, H. Neal, D.J. Melendez-Alvira, R.R. Meier, and J.T. Mariska, "The Naval Research Laboratory Program on Empirical Models of the Neutral Upper Atmosphere," *AAS 97-0632*, 1997 AAS/AIAA Astrodynamics Specialist Conference, Sun Valley, Idaho, August 4-7, 1997.

2. H. Neal and S. Coffey, "Maintaining the Space Object Catalog with Special Perturbations," *AAS 97-0687*, 1997 AAS/AIAA Astrodynamics Specialist Conference, Sun Valley, Idaho, August 4-7, 1997.

3. J.N. Bass, M.J. Kendra, J.M. Griffin, D.R. Larson, N. Ericson, and T. Killeen, "Computer-Efficient Models of Thermospheric Density and Composition: Application of Satellite Data in Near Real Time - Final Report," Report PL-TR-96-2150 (Phillips Laboratory, Hanscom AFB, Mass., 1996). ◆

Global Prediction of Gas Exchange Enhancement Due to Capillary Waves on the Ocean

J.R. Saylor
Remote Sensing Division

An understanding of how carbon dioxide and other gases cycle through the oceans and atmosphere is key to our ability to predict global warming. The oceans play an important role in this cycle because of their large capacity to absorb gases. Accordingly, an understanding of the physical processes that influence the transport of gas across the air/sea interface is critical to the development of climatological models.

One of the physical processes that affects transport is capillary waves. Our prior laboratory experiments have demonstrated that capillary waves having wavelengths λ on the order of several millimeters can increase the transport of dissolved gases by almost two orders of magnitude over that experienced by a flat surface. During these experiments, the water surface was completely covered with capillary waves. On the ocean, however, the degree of coverage by such waves is smaller, and the contribution of capillary waves to transport must correspondingly be reduced. In this work, the prevalence of capillary waves on the ocean surface is quantified using the wave height spectrum, $\phi(k)$, which quantifies the amount of energy possessed by waves as a function of their wave number k ($k = 2\pi/\lambda$). The range of capillary waves is divided into discrete bands of wave numbers Δk. Within each band, the prevalence of this band of waves on the ocean surface is quantified, and their contribution to the total amount of gas exchange is computed. By repeating this process for all capillary waves, a model for K_f (the contribution of capillary waves to the total gas exchange coefficient) is developed.

Model: When discussing gas transport, the total gas exchange coefficient k_{tot} is used. In this work, we break this coefficient down and identify the fraction that is attributable to capillary waves. Thus, we define K_f as

$$K_f = \frac{K_c}{K_{tot}}, \tag{1}$$

where K_c is the portion of K_{tot} due to capillary waves. K_f varies between 0 and 1. The model described here is for the transport of carbon dioxide, although other dissolved gases and heat could have been considered.

K_{tot} is modelled in the typical way, using data from wind/wave tunnel studies to relate the total gas exchange coefficient to wind speed [2].

K_c is computed using our prior experimental data for capillary waves [1], which is plotted in Fig. 10. As the figure indicates, K is a function of both the mean square slope $\overline{S^2}$ of the wave and λ (viz., wave number). $\overline{S^2}$ for a given band of wave numbers Δk on the ocean is computed by an appropriate integration of the wave height spectrum $\phi(k)$. By using this computed value for $\overline{S^2}$ and the data of Fig. 10, a value of K for the band Δk is obtained. Repeating this process over successive bands of capillary wave numbers, and then summing the values of K obtained, yields K_c. Inserting K_c and K_{tot} into Eq. (1) completes the model.

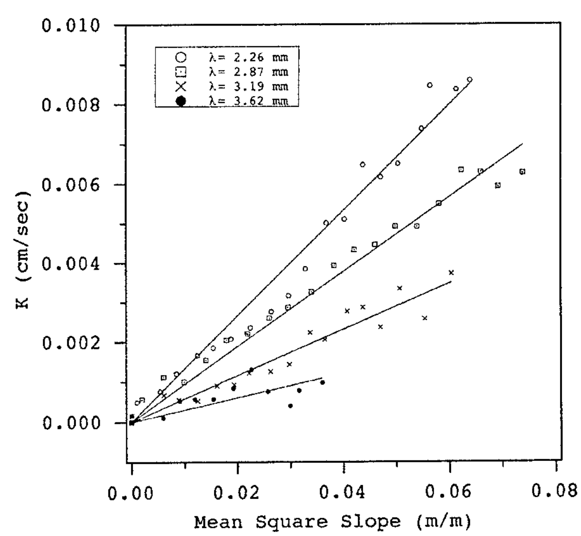

Fig. 10 — Plot of K for carbon dioxide vs mean square wave slope $\overline{S^2}$ for four different wavelengths. A linear curve fit is included for each data set.

Results: Because $\phi(k)$ is a function of wind speed, K_f is also wind-speed-dependent, and is plotted in Fig. 11. A peak value of $K_f = 0.044$ is attained at u = 13 m/s. Since u is the only input to the K_f model, remotely sensed wind speed data can be used to provide global maps of K_f. Global wind

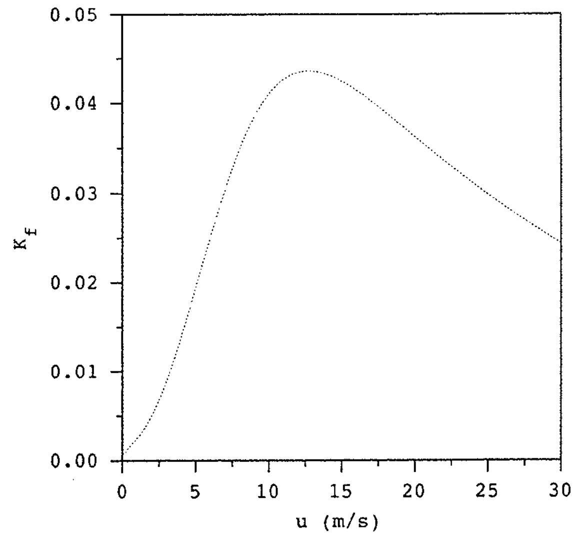

Fig. 11 — Plot of K_f vs wind speed u.

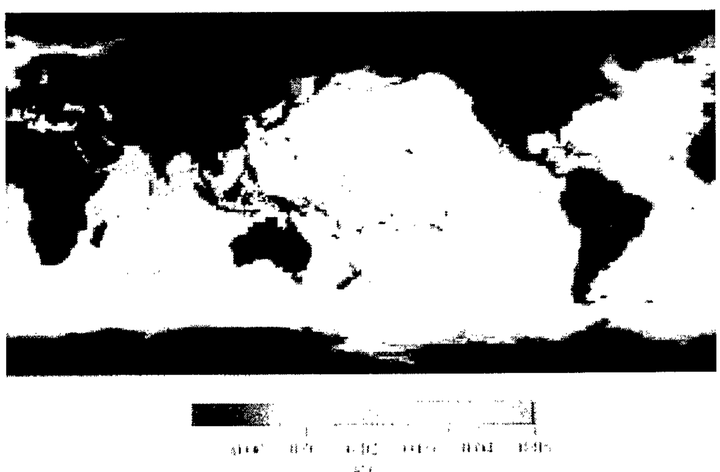

Fig. 12 — Map of K_f for the month of February 1997.

speed data were obtained from passive microwave radiometric measurements from the Defense Meteorological Satellite Program (DMSP) Special Sensor Microwave Imager (SSM/I). These measurements are provided in the form of wind speed maps where each location is a monthly averaged wind speed spanning the years 1988 to present. Using this wind speed data, a value for K_f is computed at each location on the globe, providing a map of K_f for each month. Figure 12 is an example of the resulting map for the month of February 1997.

Presenting the entire data set in the form of maps at each month for which data are available is impractical. Instead, in Fig. 13 plots of the global average value for K_f are presented as a function of month for 118 months. The blank region located roughly in the center of the plot corresponds to a period of instrument failure. This figure illustrates a small degree of monthly and yearly variability and gives an average value of ~0.03.

The data presented in Fig. 13 indicate that the predicted contribution of capillary waves to gas exchange on the ocean is small, not exceeding 4%,

which is somewhat surprising considering the very large enhancement of gas exchange that has been observed in the laboratory (e.g., Fig. 10). The reason for this is that existing models for the wave height spectrum $\phi(k)$ predict that millimeter-scale waves have very little energy on the ocean. It is noted, however, that actual measurements of wave height spectra at the wavelengths considered here have not been performed, and existing spectra are based on data obtained at longer wavelengths. Moreover, recent measurements performed at a resolution of $\lambda = 4$ mm indicate that measured wave height spectra are significantly larger than predicted by existing models [3]. Hence, more accurate wave height spectra might result in much larger values of K_f than those predicted here. These results suggest the need for higher resolution measurements of $\phi(k)$.

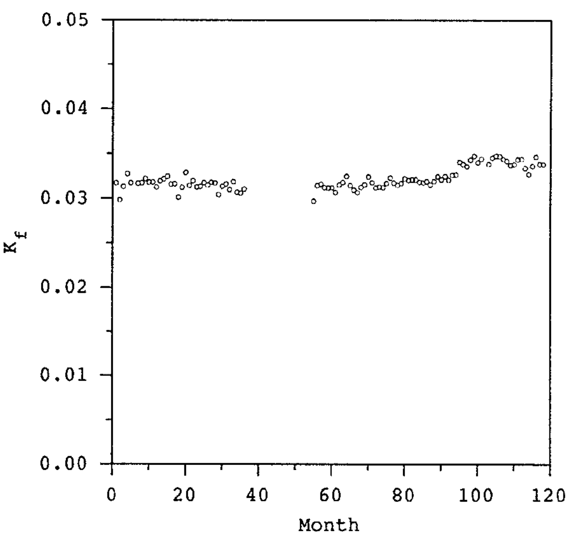

Fig. 13 — Plot of K_f averaged over the entire ocean surface of the globe, for each month. Month 1 corresponds to July 1987, and the last month (month 118) corresponds to April 1997.

Further evidence that capillary waves may play a much more important role than the predicted magnitudes of K_f indicate is presented in Fig. 14. As illustrated in Fig. 10, K increases as λ decreases. However, a decrease in wavelength also results in a decrease in $\phi(k)$. These competing trends suggest an optimum wavelength at which capillary waves contribute most to gas exchange. This is indeed the case, as illustrated in Fig. 14, where the product of ϕ and K is plotted as a function of wave number. This product is seen to have a peak at k = 1790 rads/m (λ = 3.5 mm) and that this peak is independent of wind speed. This result further demonstrates the importance of extending oceanic wave height measurements into the region of millimeter-scale capillary waves.

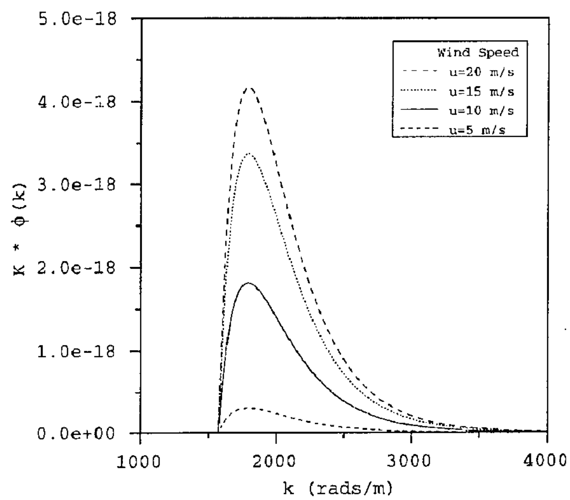

Fig. 14 — The product of K and $\phi(k)$.

Summary: A model was developed to estimate K_f, the contribution of capillary waves to the oceanic gas exchange coefficient. Global averages of K_f were estimated to be less than 4% in spite of the significant enhancement of gas exchange due to capillary waves that is observed in the laboratory. It is suggested that this small value for K_f is due to very small predicted values for $\phi(k)$, which are not supported by experimental measurements. Finally, it was shown that a peak in the contribution of capillary waves to the gas exchange coefficient occurs around λ = 3.5 mm, and is independent of wind speed.

Acknowledgments: Robert A. Handler provided significant input to the work presented herein. The author also thanks Geoffrey B. Smith, Richard I. Leighton, and Walter McKeowan for useful comments and discussions. Satellite data were obtained from the NOAA National Geophysical Data Center. The technical assistance of Ralph Ferraro (NOAA/NESDIS/ORA) is also acknowledged. Computational support was provided by the High Performance Computing Modernization Program (HPCMP).

A portion of this work was performed while the author held a National Research Council - Naval Research Laboratory Postdoctoral Research Associateship.

[Sponsored by ONR]

References

1. J.R. Saylor and R.A. Handler, "Gas Transport Across an Air/Water Interface Populated with Capillary Waves," *Phys. Fluids* **9**, 2529-2541 (1997).

2. F.J. Ocampo-Torres, M.A. Donelan, N. Merzi, and F. Jia, "Laboratory Measurements of Mass Transfer of Carbon Dioxide and Water Vapour for Smooth and Rough Flow Conditions," *Tellus* **46B**, 16-32 (1994).

3. P. A. Hwang, S. Atakturk, M. A. Sletten, and D.B. Trizna, "A Study of the Wavenumber Spectra of Short Water Waves in the Ocean," *J. Phys. Oceanog.* **26**, 1266-1285 (1996).

◆

Ultrawideband Electromagnetics and Signals

E.L. Mokole
Radar Division

In recent years, interest in developing ultrawideband (UWB) radar systems has increased. By its nature, the spectrum of a UWB signal and the passband of a UWB device encompass many of the conventional radio frequency bands. For the electromagnetics (EM) and signal processing associated with conventional radars, the signal spectra are assumed to be narrowband so that many quantities of interest are essentially constant over the pertinent frequencies. Equivalently, the absolute spectral bandwidth is small relative to the carrier frequency. For a UWB radar, however, the EM effects can vary considerably across different frequency bands, so that the EM and signal-processing theories relevant to UWB radar must account for the frequency dependence.

Background: To make the notion of UWB more concrete, define relative bandwidth B_R as $(B/f_c)100\%$, where B is the absolute bandwidth and f_c is the center frequency. A signal or system is narrowband (NB) if B_R is less than or equal to 1%, is wideband (WB) if B_R is greater than 1% and less than or equal to 25%, and is UWB if B_R exceeds 25% [1]. This definition is illustrated in Fig. 15 with plots of the power spectra for 100 cycles (B_R = 0.89%: NB), 10 cycles (B_R = 8.86%: WB), and 1 cycle (B_R = 104.36%: UWB) of the sine signal at carrier f_0.

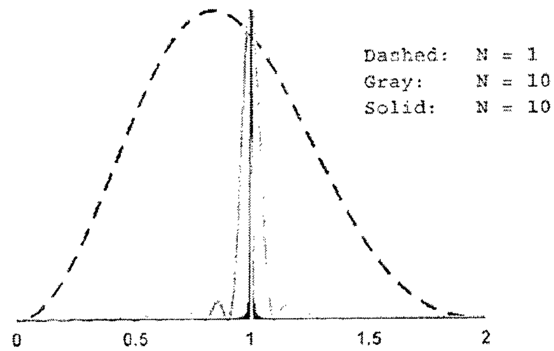

Fig. 15 — Normalized power spectra of 1 cycle (UWB), 10 cycles (WB), and 100 cycles (NB) of the sine function at carrier frequency f_0, where the horizontal axis is the normalized frequency f/f_0.

The major advantage of a UWB radar is the high-resolution capability that its bandwidth affords. Over the last four decades, UWB radars have been used for measuring the depth of ice and snow (1960), for detecting tunnels in Vietnam (1960s), for underground remote sensing (1970s), for locating buried cables and pipes of utility companies (1980s), and for detecting obscured objects in foliage (1990s). Currently, the DoD is interested in using UWB sensors to detect strategically relocatable targets like tanks and missile launchers beneath tree canopies and subsurface mines, bunkers, and unexploded ordnance. UWB technology is also used in automated highway systems.

Several issues are significant for UWB systems: (1) the bandwidth of UWB systems causes serious problems with radio frequency interference (RFI); (2) the theoretical underpinnings of UWB radar are largely nonexistent and are not well understood; (3) many conventional radiation parameters such as antenna pattern, mainbeam, and sidelobe are not appropriate for UWB antennas because they are defined for a single frequency; (4) most antennas distort UWB input signals because the transfer function of the antenna varies substantially over the signal spectrum; (5) the scattering from distributed targets is different for UWB signals, because the resolution is less than the target dimensions; and (6) instead of using the envelope of a signal to process and extract information, the RF waveform may be used for UWB signals.

The Radar Division has been conducting basic research to establish a theory for UWB radar. To date, research has focused on radiation, sea scatter,

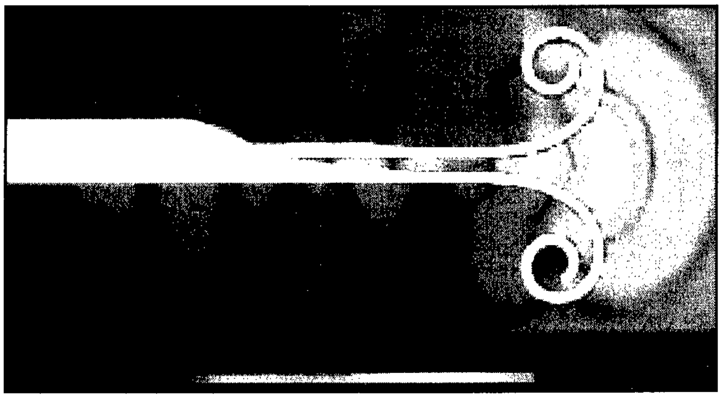

Fig. 16 — Time snapshot of the simulated magnitude of the radiated field of a balun-fed cornu flared horn. Red and violet indicate fields with the greatest and least magnitudes, respectively.

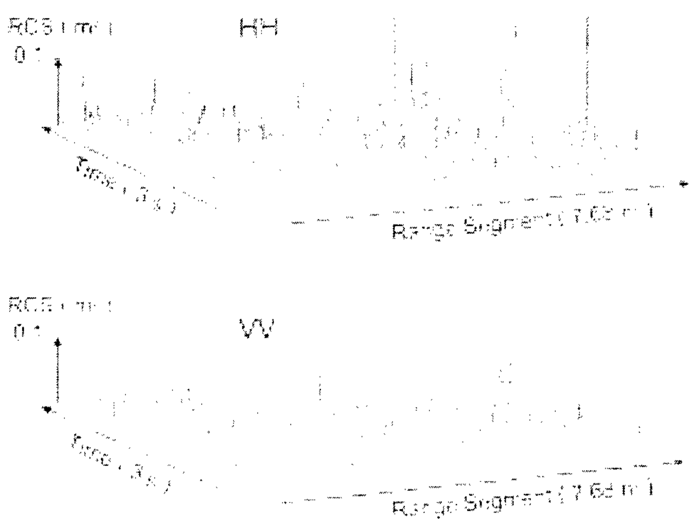

and signal processing. Accomplishments include an extensive analytical characterization of the wide-angle bicone antenna, the design of a significantly improved UWB flared-horn antenna, the development of two schemes for detecting spatially distributed, Doppler-shifted targets, and the development of the very high resolution microwave microscope (MWM), which is an experimental UWB measurement radar for sea scatter. Brief discussions of selected topics follow.

UWB Radiation: Broadband elements and time-delay scanning arrays that are excited by UWB signals have been studied. In particular, the wide-angle bicone has been shown to be UWB, and closed-form results for electrically small and large bicones have been derived. Time-domain and frequency-domain techniques have been developed for studying UWB radiation and, more specifically, for characterizing the effect of shaping on the behavior of an antenna. Numerical simulations with

these techniques have been used to develop novel UWB flared-horn elements, including curvature-based antennas like the cornu spiral. A performance improvement in terms of much lower transmission-line-voltage reflections is achieved by avoiding the sharp end discontinuities of many narrowband antennas. In particular, good simulated performance has been achieved for the balun-fed cornu flared horn (Fig. 16). This patent-pending antenna design avoids the late-time radiation induced by the traditional method of feeding flared horns from the side and lowers the voltage standing wave ratio (VSWR) by reducing end reflections through the cornu shape of the plates.

Microwave Microscope: To study the scatter of UWB signals from the sea at microwave frequencies, an experimental UWB measurement radar system, the microwave microscope (MWM), has been built. This system has a 50% relative bandwidth, operates at X-band (9.2 GHz) with 2 kW of peak power, and has demonstrated better than 2-cm (0.8-in) range resolution on external land and sea clutter. A camera is mounted on top of the radar platform and slaved to the radar boresight to provide optical ground truth of the surface. Because of the low power, typical measurements are taken at ranges less than 100 m. From November 1996 through March 1997, field measurements were performed at AUTEC, a deep-water ocean site in the Bahamas. Initial results are revealing significant differences in the character of the dual-polarized UWB return signals from the combination of large-scale and small-scale features that exist on the sea surface (Fig. 17). For conventional pulses, vertical polarization is more sensitive to the many small-scale features within the resolution cell, and horizontal polarization is more sensitive to the occasional large-scale feature. The net result is that the median return level for vertical polarization somewhat exceeds the median return level for horizontal polarization, even though the peak returns for horizontal polarization are usually greater. In contrast, with UWB pulses, horizontal polarization still produces large peak returns for the large-scale features, but the comparatively smaller size of the resolution cell now makes vertical polarization less sensitive to the fewer small-scale features. Consequently, the median returns for both UWB polarizations are comparable, and the peak returns for the horizontal UWB polarization are very dominant.

Summary: The major advantage of UWB radar is extremely wide bandwidth (ultrahigh resolution). Currently, such systems have limited application because extremely wide bandwidths also induce RFI. Moreover, UWB technology is not mature. Although the electromagnetic and signal processing theories pertaining to UWB radar require considerably more attention, inroads have been made by the UWB research program at NRL. For example, analytical approaches and numerical methods/assets have been developed for studying UWB radar, and the MWM provides ultrahigh-resolution insight into sea scatter.

[Sponsored by NRL and ONR]

Reference

1. S.N. Samaddar and E.L. Mokole, "Some Basic Properties of Antennas Associated with Ultrawideband Radiation," in *Ultra-Wideband Short-Pulse Electromagnetics 3*, C.E. Baum, L. Carin, and A.P. Stone, eds. (Plenum Press, New York, 1997), pp. 147-164.

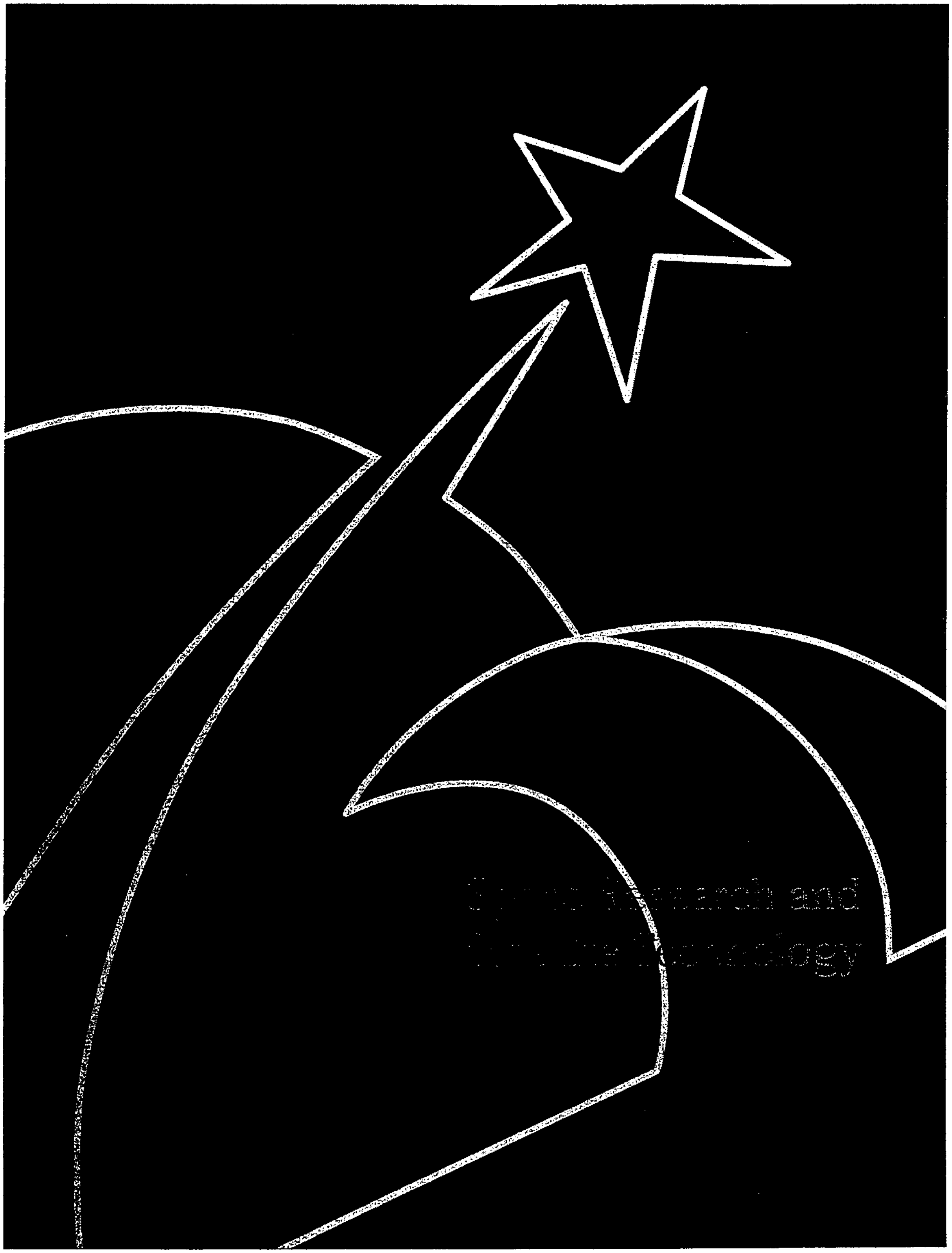
Space Research and

Satellite-to-Satellite Relative Navigation Using GPS Signal Simulators

P.W. Binning
Space Systems Development Department

Overview: The Orbit and Covariance Estimation Analysis (OCEAN) software, under development by the Astrodynamics and Space Applications Office, allows for relative positions to be estimated between two orbiting platforms while receiving signals from the Global Positioning System (GPS). There are a number of relative satellite missions being planned by the National Aeronautics and Space Administration (NASA); in addition, GPS will be used by NASA's Space Shuttles and on the International Space Station. In these applications, an accurate relative position would be useful for operations. The most accurate relative navigation algorithm will remove or model the common error sources between the two orbiting platforms.

A unique aspect of this research is the employment of a hardware simulation to model the GPS signal environment. It is also useful since there is a lack of abundant data from actual flight experiments. Signal simulators do have limitations, such as not being able to easily model GPS multipath effects.

GPS Relative Navigation: The Global Positioning System is a constellation consisting of 24 satellites. A user, such as another orbiting vehicle, receives signals from each GPS satellite from which a range may be determined. Because of clock biases in the GPS system, the ranges are not true ranges but are called *pseudoranges*. After receiving pseudoranges to a number of GPS satellites, the user's position is then determined since the locations of the GPS satellites are well-known. If two user vehicles are receiving pseudoranges from a sufficient number of GPS satellites, then a relative position may also be calculated.

The relative positions are determined by using a filter to remove measurement noise commonly associated with GPS. An Extended Kalman Filter, using a discrete backwards smoother, are the algorithms usually employed.

Three methods for determining the relative position are the Straight Difference Method (SDM), the Correlated Pseudorange Method (CPM), and the Single Difference Pseudorange Method (SDPM). The SDM subtracts the independently determined positions of each user vehicle to form the relative position. The CPM correlates the errors in the Kalman filter between the two user vehicles. In this case, the relative position is still found by subtracting the two absolute positions. On the other hand, the SDPM actually subtracts the two pseudoranges to form a relative measurement. This measurement is then used to directly find the relative state.

Simulation Hardware: A Northern Telecom (NT) STR2760 GPS Signal Simulator generates the GPS signals in a laboratory to simulate an orbiting GPS receiver. The simulator is configured and controlled for the desired user orbit through a DEC ALPHA workstation. An Allan Osborne TurboRogue GPS receiver is connected to the STR2760 to make the desired pseudorange measurements. Figure 1 shows the STR2760 configuration.

Two orbit scenarios are generated to obtain a nominal spacecraft separation distance of 50 km. The receiver measurements are transferred to the DEC workstation at the conclusion of the simulation and processed through the OCEAN software. The true relative position of the simulated spacecraft and the locations of the GPS satellites are retrieved from the NT software. The true position and computed position are differenced to determine the error in the estimate.

Results: Figure 2 graphically shows the relative position errors from the three different

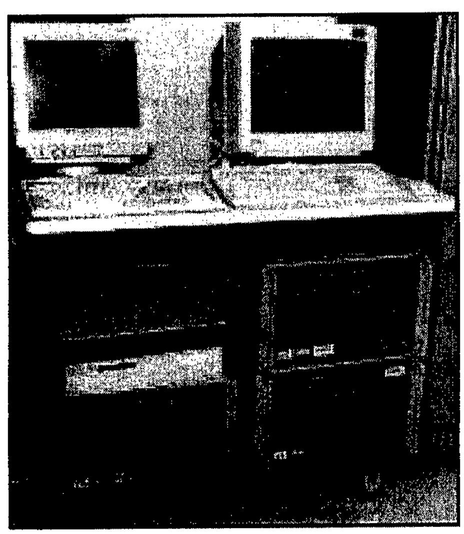

Fig. 1 — Northern Telecom STR2760 GPS signal simulator setup.

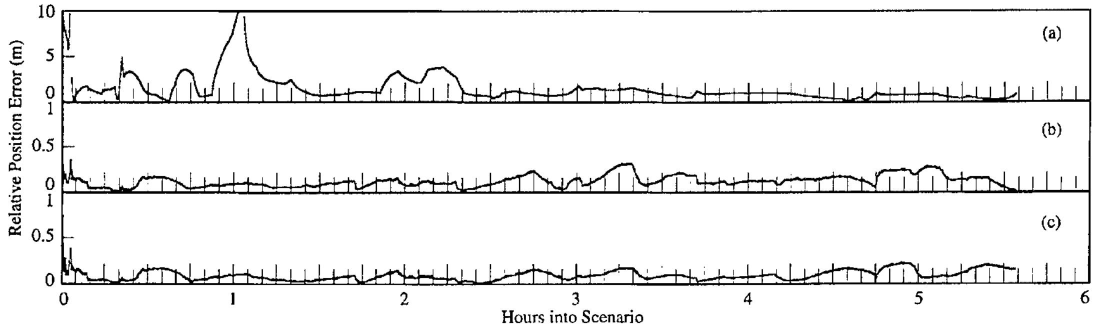

Fig. 2 — Relative satellite-to-satellite position errors from the (a) Straight Difference Method (SDM), (b) Correlated Pseudorange Method (CPM), and (c) Single Difference Pseudorange Method (SDPM).

methods. The SDM has a relative root-mean-square (rms) error of 137.95 cm. The CPM and SDPM show relative rms errors of 7.62 cm and 7.17 cm, respectively.

Conclusions: The OCEAN filter/smoother shows considerable promise for use in satellite-to-satellite relative navigation experiments. Relative position errors below 10 cm are achievable when using the most accurate algorithms. The study is continuing by examining the effect of multipath on the relative position.

[Sponsored by Secretary of the Air Force (SAF/MBMB-AFOY)]

References

1. P.W. Binning, "Absolute and Relative Satellite to Satellite Navigation Using GPS," Ph.D. Thesis, University of Colorado, Boulder, Colo. (1997).

2. P.W. Binning and I. Galysh, "Satellite to Satellite Relative Navigation Using GPS Pseudoranges," Proceedings of ION National Technical Meeting, Jan. 14-16, 1997, Institute of Navigation, Santa Monica, Calif., pp. 407-415. ◆

Prediction of Geomagnetic Storms: Space Weather Forecasting

J. Chen and S. Slinker
Plasma Physics Division

Introduction: "Space weather" refers to the state of the magnetosphere and the ionosphere, a plasma-filled region of space surrounding the Earth. Under disturbed space weather conditions, satellite- and ground-based technological systems (e.g., communications networks, electric power grids, and satellites) can suffer deleterious effects. Such systems are particularly vulnerable during severe geomagnetic storms, disturbances in the electric and magnetic fields of the ionosphere. Large storms are relatively infrequent but, when they occur, they can stress the susceptible systems for prolonged periods of time over large geographic areas. Secure operation of systems can still be maintained and hazards can be minimized if the occurrence, duration, and severity of impending storms can be accurately predicted in a timely manner. Thus, space weather forecasting is important for protecting national assets in both the commercial and military sectors. This task is being carried out by the Space Environment Center (SEC) of the National Oceanic and Atmospheric Administration (NOAA) and the U.S. Air Force (USAF).

The state of the magnetosphere is determined by the solar wind, a continuous stream of tenuous (typically a few particles per cubic centimeter) magnetized plasma emanating from the Sun, impinging on the Earth's magnetosphere. Large geomagnetic storms are caused by solar wind structures having long durations (several hours to a few days) of strong (> 10 nT) southward interplanetary magnetic field (IMF). Here, 1 nT = 10^{-5} G. These geoeffective structures (those effective in causing geomagnetic disturbances) are the results of eruptions at the Sun such as coronal mass ejections (CMEs). Figure 3 schematically depicts the plasma connection between the Sun and the Earth. Accurate forecasts of large storms are difficult to achieve because (1) the interplanetary medium is not known accurately at any given time, and (2) the propagation of solar disturbances to the Earth and the resulting magnetic field polarity and

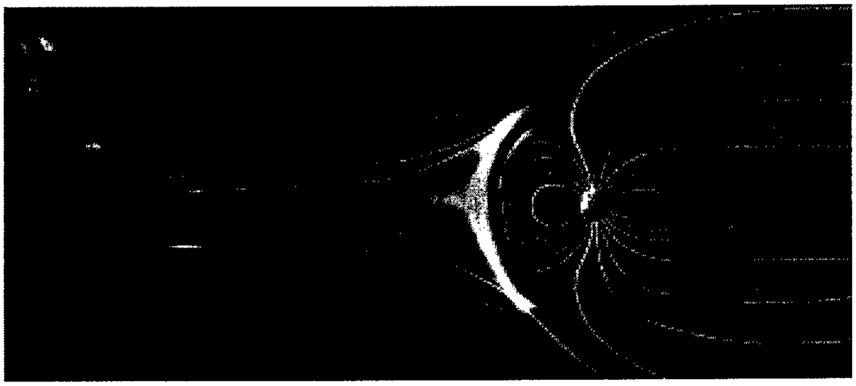

Fig. 3 — The Sun continually sends out the solar wind, a low-density plasma with a few particles per cubic centimeter and fluctuating magnetic field of approximately 5 nT to 50 nT near the Earth. Its speed ranges from 400-600 km/s to 800 km/s in some "magnetic clouds," a 1 astronomical unit consequence of solar eruptions. In such structures, the magnetic field can be strongly southward for long periods of time (several hours to a day or two), amplitudes of 20 nT to 30 nT.

strength are not well understood. A recent study shows that during 1987-1993, approximately 70% to 80% of storms were missed (false negatives) and 70% to 80% of predicted storms did not occur (false positives) [1].

A Method of Predicting Geomagnetic Storms in Real Time: The geoeffective solar wind features are well documented: (1) long durations (> several hours) of and (2) strongly southward IMF (10 nT to 30 nT). These features are very distinct from the typical "background" solar wind. Figures 4(a) and 4(b) show the B_y and B_z components of the IMF measured by the magnetometer onboard the IMP 8 satellite. This is a classic interplanetary magnetic cloud, which advected past the satellite at about 700 km/s. Until $T = 6$ h (after 17:00 universal time (UT), January 13, 1988), the IMF fluctuates with small amplitudes. The magnetic cloud is characterized by long durations of unipolar solar wind. The southward IMF, $B_z < 0$, begins at about $T = 22{:}00$ UT and lasts for approximately 19 h, reaching $B_z = -20$ nT. This southward IMF part of the cloud caused a strong geomagnetic storm that lasted more than one day. The severity of storms is usually measured by the Dst index, which is the hourly average of the deviations in the magnetic field from the quiet-time values as measured by several ground stations distributed around the Earth. Thus, Dst = 0 means no disturbance, and the more negative Dst is the more severe the storm is. The storm caused by this magnetic cloud attained minimum Dst = –150 nT, a rather significant storm, as shown in Fig. 4(f).

Notice that the magnetic cloud is strikingly different from the typical fluctuating solar wind. This is because the magnetic cloud is a magnetically organized structure (see 1995 NRL Review, p. 209). We take advantage of this fact to estimate the magnetic field profile of the entire structure after sampling only the leading edge. The dashed curve in Fig. 4(b) is the profile of B_z estimated at the time indicated by the diamond using only the data available at that time. We have found that typically the first 10% to 20% of a structure can allow us to estimate the remaining structure accurately [2]. Thus, noting that it is these long-duration B_z solar wind events that drive large geomagnetic storms, we see that this technique can allow us to predict the magnetic field properties of geoeffective solar wind structures many hours in advance. Figures 4(c) and 4(d) show the estimated duration (τ') and the maximum B_z (B'_{zm}) of the unipolar solar wind intervals being encountered. A detailed comparison shows that these estimates are remarkably accurate.

Prediction of Large Geomagnetic Storms: Using the estimated values of τ' and B'_{zm}, we apply a Bayesian classification technique to predict whether a solar wind event being analyzed will prove to be geoeffective according to specific criteria: if a solar wind event leads to a storm with Dst < –80 nT for 2 h or longer, then it is deemed geoeffective. The probability P_1 that a solar wind structure is geoeffective is calculated by using Bayes theorem (Fig. 4(e)). The dashed line means that the solar wind event has northward ($B_z > 0$) IMF and is

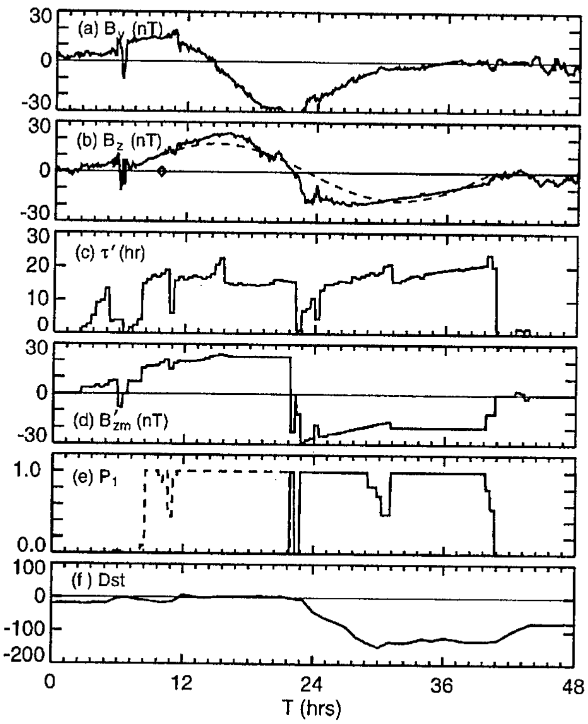

Fig. 4 — An interplanetary magnetic cloud encountered by the IMP 8 satellite on January 13-14, 1988. Time T is shown in hours after 17:00 UT, 13 January 1988; (a) B_y component of the IMF; (b) B_z (north-south) component of the IMF, with $B_z > 0$ pointing northward; (c) predicted duration of event; (d) predicted maximum of B_z; (e) predicted probability that a solar wind event being examined is geoeffective; and (f) observed Dst index.

nongeoeffective but will be followed by a geoeffective ($B_z < 0$) solar wind event of comparable duration and B_z magnitude. This probability is accurately determined to be nearly unity for this event. After B_z turns southward, the method correctly calculates the probability that the solar wind is geoeffective to be nearly unity, as represented by the solid line. Since we know that the onset of a storm roughly coincides with the southward turning of B_z, the estimated B_z profile (dashed curve, Fig. 4(b)) allows us to predict at $T = 9.6$ h, (diamond, Fig. 4(b)) that a geomagnetic storm exceeding the specified threshold will occur around $T = 24{:}00$ UT. Comparing with the measured Dst values shown in Fig. 4(f), we see that the prediction made at the indicated time (diamond) is quite accurate for the approximately 30-h period that follows.

Summary: A technologically advanced nation critically depends on its ability to maintain an uninterrupted supply of energy and communications networks for all of its essential functions for both the civilian and military sectors. During the last two decades, there has been rapid miniaturization of electronic components and integration of systems over increasingly large geographic areas using conducting cables and metallic pipelines. During large geomagnetic storms, the electric power grids, ground-based and space-based communications networks, and the operation of satellites can be disrupted for prolonged periods of time. Secure operation of such systems can still be maintained and hazards can be minimized if large storms can be predicted accurately and in a timely manner. The prediction technique can be used in real-time storm prediction if there is real-time solar wind data from upstream of the Earth. Currently, we are testing the method using the solar wind data from the WIND satellite station at the L1 libration point, approximately 200 Earth radii toward the Sun.

[Sponsored by ONR]

References

1. J.A. Joselyn, "Geomagnetic Activity Forecasting: The State-of-the-Art," *Rev. Geophys.* **33**, 383 (1995).

2. J. Chen, P.J. Cargill, and P.J. Palmadesso, "Predicting Solar Wind Structures and Their Geoeffectiveness," *J. Geophys. Res.* **102**, 14701 (1997).

◆

A Theory of Slow Solar Wind Acceleration

R.B. Dahlburg,[1] J.T. Karpen,[2] G. Einaudi,[3] and P. Boncinelli[4]
[1]*Laboratory for Computational Physics and Fluid Dynamics*
[2]*Space Science Division*
[3]*Berkeley Research Associates and University of Pisa*
[4]*University of Florence*

Background: Energetic particles stream continuously from the Sun in the form of a solar wind, which comes in two flavors: a fast (over 600 km/s), steady component, and a slower (about 300 km/s), highly variable component. The existence and energy source of the fast wind, which streams out from the Sun along open field lines, can be explained in part by a mechanism proposed 40 years ago [1]. The slow wind, however, has remained more mysterious. Recent radio scintillation and ultraviolet observations have revealed that the slow solar wind comes from streamers, which are ray-like dense structures located just above the "helmets" formed by closed magnetic loops in the inner corona [2]. Observations by NRL's Large Angle and Spectrometric Coronagraph (LASCO) instrument, a set of coronagraphs currently onboard the Solar and Heliospheric Observatory (SOHO) (a joint NASA-ESA spacecraft), also indicate the existence of dense clumps of ionized gas or "plasmoids," which apparently originate at the base of streamers and are carried outward by the slow wind [3]. Taken together, these data demonstrate that the slow solar wind reaches its maximum speed within about 10 to 30 solar radii from the Sun's surface while plasmoids are being torn out of the streamer's magnetic field.

Model and Simulation: Based on these observations, we have developed and tested a new model for the acceleration of the slow component of the solar wind [4]. The initial configuration, shown in Fig. 5, consists of a reversing magnetic field, reproducing the basic magnetic conditions in a streamer above a coronal helmet, and centered within a broader wake flow, reproducing the shift from fast to slow solar wind as one enters the streamer. We then shake this system and follow its complex behavior by use of numerical simulations. The time-dependent evolution of this numerical

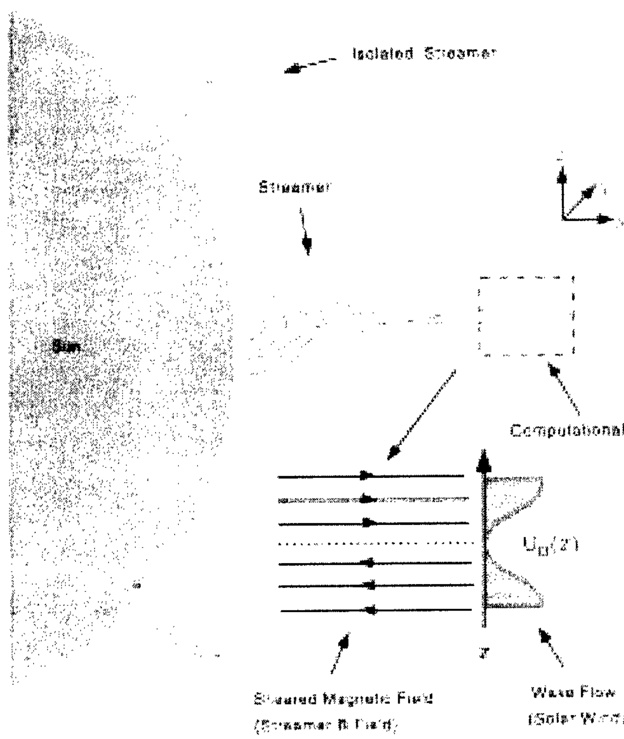

Fig. 5 — Definition sketch for the slow solar wind model.

model represents the evolution of the solar wind as it travels outward from the Sun in the vicinity of a coronal streamer. We find that the inner part of the wake flow is accelerated by evolving instabilities that pull energy out of the faster portions of the flow and deposit it within the slowest region. This process yields a final speed in the core of the wake of about one-half to three-quarters the maximum velocity at the edges of the wake—the same speed ratio as is measured for the slow-to-fast components of the solar wind. Figure 6 shows the time-dependent development of this acceleration. In addition, the reversing magnetic field can tear and reconnect, leading to the formation of plasmoids, which travel along with the background flow. The increased variability of the slow component arises as the magnetized wake transitions to turbulence, as seen in Fig. 7. The system transitions from ordered one- and two-dimensional states to a turbulent three-dimensional state.

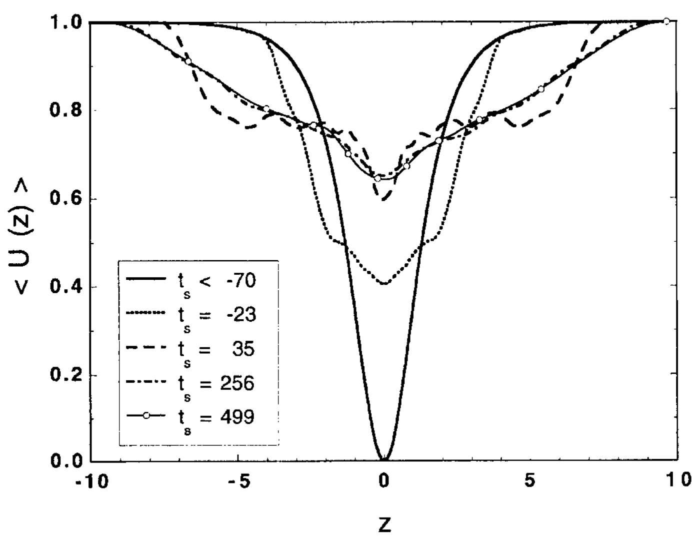

Fig. 6 — Streamwise velocity (U) averaged in the streamwise (x) and spanwise (y) directions as a function of the cross-stream direction (z) at different times (t_s) in a typical numerical simulation. The increase in the average U at z = 0 is understood to mimic the acceleration of the slow component of the solar wind.

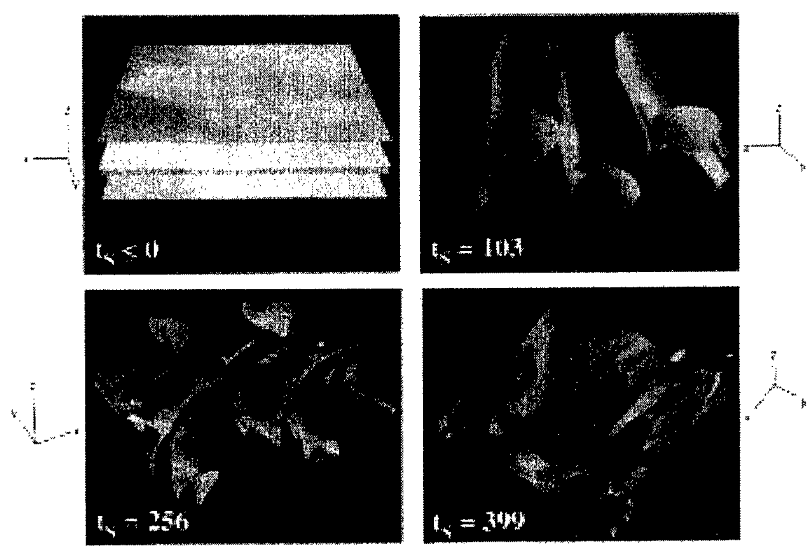

Fig. 7 — Vorticity isosurfaces at selected times during a 3-D numerical simulation, illustrating the transition to turbulence in the magnetized wake model of the slow solar wind. The isosurfaces are chosen to have one-half the maximum vorticity magnitude.

Implications: The basic philosophy of our new model is easy to express—*the fast solar wind accelerates the slow wind.* The success of our theory at matching several observed features of the slow solar wind indicates that no separate physical mechanism is required to explain the acceleration of this component and the production of plasmoids. For example, our theory predicts that plasmoid speeds should increase with distance from the Sun and then level off at 50 to 75% of the fast wind speed near the streamer, a feature that fits well with recent NRL LASCO observations [3].

[Sponsored by NASA, ONR and Agenzia Spatiale Italiana]

References

1. E.N. Parker, "Dynamics of the Interplanetary Gas and Magnetc Fields," *Astrophys. J.* **128**, 664 (1958).

2. S.R. Habbal, et al., "Origins of the Slow and the Ubiquitous Fast Solar Wind," *Astrophys. J.* **489**, L103 (1997).

3. N.R. Sheeley, et al., "Measurements of Flow Speed in the Corona Between 2 and 30 R," *Astrophys. J.* **484**, 472 (1997).

4. G. Einaudi, P. Boncinelli, R.B. Dahlburg, and J.T. Karpen, "Formation of the Slow Solar Wind in a Coronal Streamer," submitted to *J. Geophys. Res.* (1997).

Attitude Determination Using GPS and Smart Structures

A. Bosse, G. Creamer, G. Kirby, R. Weber, and S. Fisher
Spacecraft Engineering Department

Introduction: Experimental results are presented that validate the use of the Global Positioning System (GPS) for determining the orientation or attitude of a large, flexible spacecraft. GPS attitude determination represents a low-cost alternative to star cameras, Earth sensors, and Sun sensors and is suitable for a wide range of Navy space missions requiring arc-min-level attitude knowledge. Attitude is estimated using differential carrier phase measurements from multiple GPS antennas located on the spacecraft, and the resolution of this estimate improves linearly as the baseline (distance between antennas) is increased. The objective of this test was to achieve arc-min-level attitude accuracy, which requires a baseline of at least 5 m; therefore, one of the four GPS antennas was placed at the end of a long, flexible boom attached to a rigid platform. Both for ground testing and on-orbit operation, this antenna will move due to thermal cycling and vibration-induced jitter. Employing strain sensors bonded to the boom, the motion of the GPS antenna is monitored in real time, and a correction is applied in software to the resulting attitude estimate.

Flexible Spacecraft Simulator: Figure 8 shows the spacecraft simulator employed for this experiment. It is located at the NRL Maryland Point Observatory, which is located in a radio-quiet area of southern Maryland. The main component is a rigid platform that has onboard batteries for power, three reaction wheels, two 2-axis rate gyros, and three GPS antennas. The platform sits atop a hemispherical air bearing that enables it to rotate without friction a full 360° in the horizontal plane and ±30° in any vertical plane. Attached to the platform is a 5-m long carbon fiber composite tube, which has 24 strain gauges bonded along its length and a single GPS antenna located at its tip. Signal processing is accomplished using an Ashtec ADU-2 GPS unit housing four 12-channel receivers and a dSPACE, Inc., 32-channel data acquisition board with digital signal processor, both connected to a 133 MHz Pentium computer.

Fig. 8 — Flexible spacecraft simulator located at NRL Maryland Point Observatory.

Smart Structures Metrology System: The metrology system used to estimate the boom-mounted antenna lateral displacements uses two lines of 12 strain sensors each along the length of the boom, located 90° apart around the circumference. Optimal sensor locations were determined from sensor noise levels and numerical simulations of strains and antenna displacements. The motion of the antenna is determined from the measured axial strains using a strain-to-displacement mapping matrix. The algorithm that generates the mapping matrix assumes linear curvature over each segment of the boom as defined by two adjacent strain sensors. Double integration of the curvature and enforcement of displacement and slope continuity at the endpoints of adjacent segments yields the necessary mapping matrix.

GPS Signal Processing: Platform attitude determination is accomplished using double differencing of carrier phase signals from each of the four GPS antennas and each of the GPS satellites in the field of view (FOV). A long 6.3-m baseline and a short 1.6-m baseline, defined by each pair of diametrically opposed antennas, are utilized to determine the attitude. Prior to each test, these baselines are surveyed to determine their nominal vector components in the platform body-fixed frame. A least-squares estimate of these same vectors is then obtained in an Earth-fixed reference frame at a 1 Hz sample rate during each test. Simultaneously, a displacement correction from the metrology system is applied to the nominal baseline vector for the long baseline to compensate for antenna motion. Knowledge of the two baseline vectors defined in both the platform frame and the navigation frame is sufficient to determine platform heading about the vertical axis, pitch about the short baseline, and roll about the long baseline.

Results: Figures 9 and 10 show experimental results of platform attitude and boom-mounted antenna displacements for the integrated GPS/Smart Structures system. During testing, the platform was stationary and the boom was initially restrained. Approximately halfway through each test the boom restraint was removed. Figure 9 presents two tests, one that does not incorporate

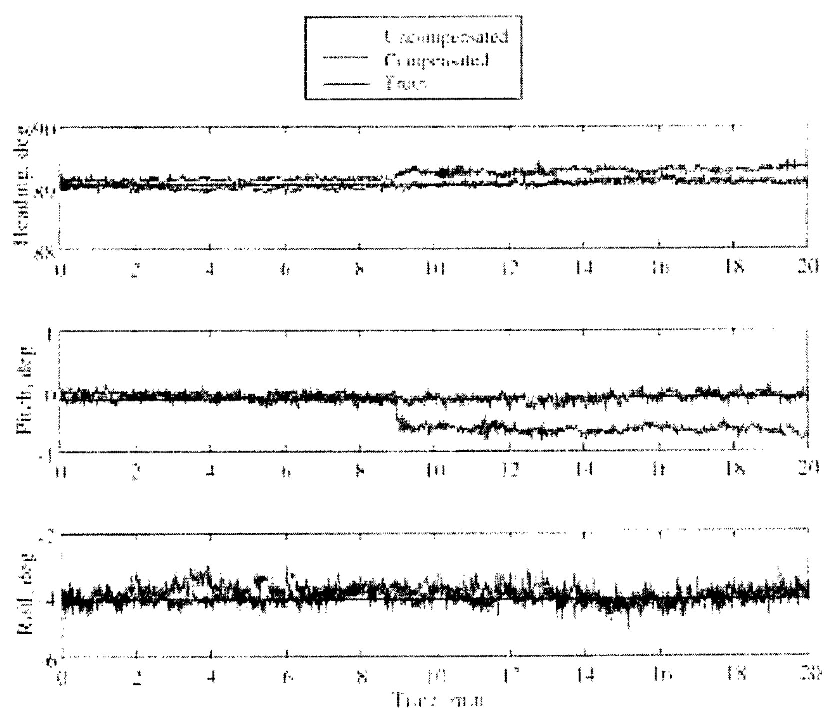

Fig. 9 — GPS attitude estimates.

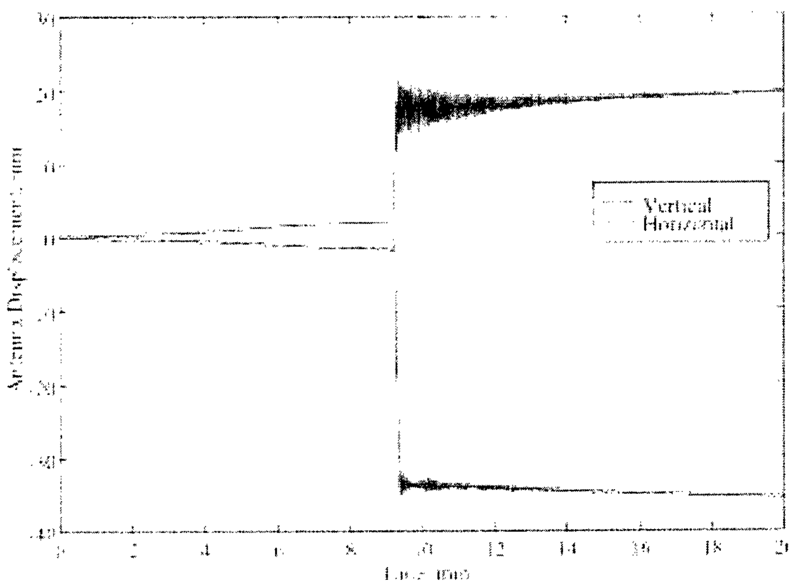

Fig. 10 — Lateral displacements of boom-mounted antenna.

antenna motion compensation and one that does. For the compensated system, the standard deviations in heading, pitch, and roll are 3.7, 4.7, and 20.7 arc-min, respectively. The advantage of the long baseline for heading and pitch is clearly demonstrated. Although not shown, a Kalman filter solution, combining the GPS attitude and the rate gyro signals, yields additional noise reduction of up to 50%. Estimated lateral displacements of the boom-mounted antenna for the compensated test are provided in Fig. 10, where it is clear that both static and dynamic motion ensued upon removal of the boom restraint. Although no truth measurement was available for the boom motion, the compensated GPS attitude performance indicates the accuracy is better than 5 mm.

Conclusions: Test results demonstrate that an integrated GPS/Smart Structures architecture for attitude determination of large, flexible spacecraft represents an ideal marriage of two useful technologies. Long baselines enhance GPS attitude resolution, whereas Smart Structures technology provides the required baseline metrology information. Future plans include the study and practical implementation of a Smart Structures metrology system for space-based radio-frequency and optical interferometers.

[Sponsored by National Reconnaissance Office] ◆

Advanced Thermal Control Technology Development at NRL

K. Cheung
Spacecraft Engineering Department

T. Hoang and J. Kim
TTH Research, Inc.

Introduction: Advances in electronic components have, in the past, resulted in higher performance devices that require more power and are packaged into smaller "boxes." Providing for the thermal controls of such devices is becoming more challenging. The importance of thermal control systems (TCS) in the development of advanced electronics is evident in the supercomputer industry, where more patents have been filed for thermal control than for electronic innovations. For spacecraft, the same trend in electronics has an even more severe thermal impact because of no convection heat transfer to air (vacuum), the need for high reliability in space (passive operation with no moving parts that can fail), and the need to minimize weight and power requirements for thermal components. To meet these needs for its future Department of Defense (DoD) spacecraft programs, NRL has been conducting an extensive research and development (R&D) program to realize the needed advanced thermal control

technologies. In particular, the capillary pumped loop (CPL) has been the focus of our development efforts. The CPL is a passive two-phase (usually liquid and vapor anhydrous ammonia) heat transport device, with no moving parts. It has an order of magnitude greater heat transport capability than any existing thermal control device. In addition, it has the ability to provide precise control of component temperatures and can passively pump its working fluid against gravity to allow full testability on-ground. Waste heat from electronics is collected at the evaporator and rejected at the condenser to a radiator through vaporization and condensation of the fluid. Fluid circulation is provided by capillary (surface tension) forces developed at the vapor-liquid interfaces inside small porous channels of a porous wick material located in the evaporator. The reservoir provides management of excess liquid in the loop.

Despite the enormous benefits, the CPL is not currently available for use due to severe functional limitations and design measures required to avoid failure. The problem is caused by vapor presence on the liquid side of the wick inside the evaporator. Vapor in the liquid side will form bubbles that can block the flow of liquid though the wick and essentially shut down the circulation of the fluid and the transport of the heat through the system (deprime). Elaborate schemes that are often lengthy and complex are necessary to assure proper placement of liquid and vapor in the loop. Complex and costly design measures are also required to suppress vapor bubble presence and/or growth inside the liquid side of the wick. To fully realize the potential of CPL technology and make it available for use by spacecraft designers, several distinct NRL-developed concepts are being investigated. These concepts include the advanced-capillary pumped loop (A-CPL), electrohydrodynamics (EHD) assisted CPL, and organic-inorganic hybrid solgel wick materials.

Advanced-Capillary Pumped Loop Development: When heat is first applied to the CPL evaporator, transient pressure fluctuations across the wick can inject vapor bubbles into the liquid side of the wick. Bubbles can also form at any time due to heat leak through the wick and also be carried into the evaporator by the returning liquid from the condenser. To prevent bubbles in the liquid side from blocking flow to the wick and causing deprime, the advanced-capillary pumped loop (A-CPL) uses a secondary loop that is plumbed into the evaporator liquid volume to "flush" the bubbles from the evaporator into the reservoir [1]. Figure 11 illustrates a schematic of the A-CPL system. The wick in the evaporator provides for the circulation of the working fluid in the main loop, which is essentially identical to a regular CPL. The mass-flow rate for the main heat transport is depicted in Fig. 11 as m_R. The secondary loop uses another wick that is located inside the reservoir to circulate the fluid in the secondary loop. Whenever flushing of the bubbles inside the evaporator is needed, heat is applied to the reservoir wick section, which then generates additional vapor flow (m_V). Vapor generated in the reservoir flows into the primary loop and is reliquefied in the condenser. The additional liquid flowing into the evaporator will purge vapor

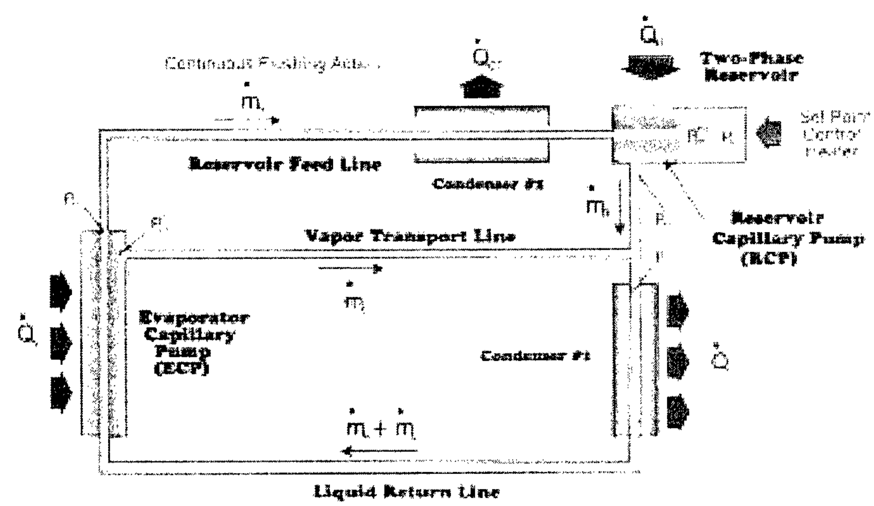

Fig. 11— Schematic of the advanced-capillary pumped loop (A-CPL).

bubbles out of the evaporator liquid side and carry them into the reservoir. The wick in the reservoir can never deprime since the reservoir is sized to always contain some liquid.

A two-evaporator A-CPL testbed was designed, fabricated, and tested. To facilitate flow visualization, the test loop used transparent Teflon tubing for all transport lines, and R-134a was selected as the working fluid. Start-up tests were performed to experimentally verify (1) the ability of start-up with a partially flooded loop condition, (2) the effectiveness of the vapor bubble flushing action generated by the secondary loop, and (3) the feasibility of the A-CPL concept in a multiple evaporator system. In a typical start-up test, heat was applied to the evaporator shortly after engaging the secondary loop, even though bubbles were present inside the evaporator. The lengthy and complex start-up procedure required by the conventional CPL system was not needed. After start-up, the secondary loop was "deactivated" by turning off the power supply to the reservoir wick heater. Heater power to the evaporator was cycled to make sure that the secondary loop successfully removed all bubbles from the evaporator liquid side. All start-up tests were successful. The A-CPL concept was also proven to be feasible in multiple evaporator systems, with the secondary loop successfully removing bubbles from both evaporators in the testbed simultaneously. For the loop tested, it was found that a minimum of 60 W of heat was necessary for the secondary loop to generate enough fluid flow to flush out all the vapor bubbles in the evaporator. Below this, the generated flow will not be able to overcome the buoyancy effects in a 1-g environment that makes the vapor bubbles preferentially stay on the top portion of the tubing and fittings.

Electrohydrodynamics (EHD)-Assisted CPL Development: Electrohydrodynamics (EHD) uses fluid motions induced by an electrostatic field to augment energy and mass transports. NRL has teamed with the University of Maryland, and they have formed a consortium of government and private organizations to jointly develop EHD technology for use in CPL systems to augment the evaporator to make it more bubble tolerant. Figure 12 is a schematic of a proof-of-concept test loop. Inside the EHD-assisted CPL evaporator, a cylindrical wire mesh electrode is mounted against the inside surface of the wick (liquid side). Such arrangement will give the highest electric field intensity near the electrode and the lowest one at the center of the liquid volume. Consequently, liquid will be extracted and pulled into the inner wick surface, while any vapor bubbles inside the core will be "pushed" toward the center of the

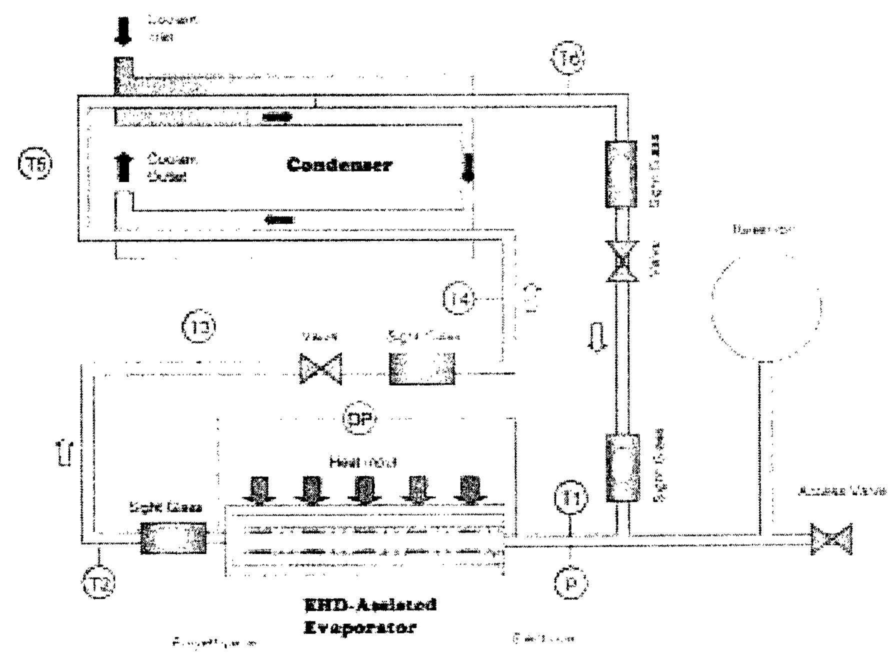

Fig. 12 — Schematic of the electrohydrodynamics (EHD)-assisted capillary pumped loop (CPL) testbed.

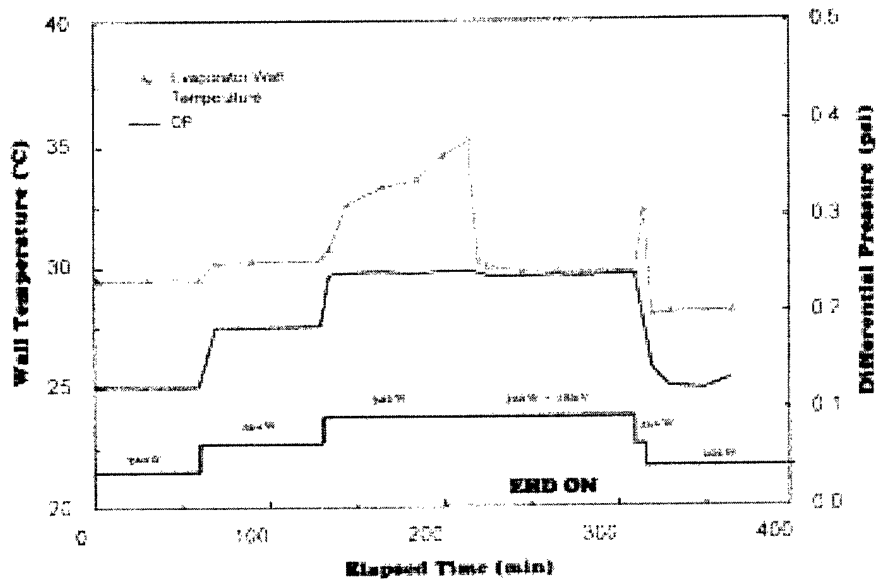

Fig. 13 — Deprime recovery of the electrohydrodynamics (EHD)-assisted capillary pumped loop (CPL) evaporator.

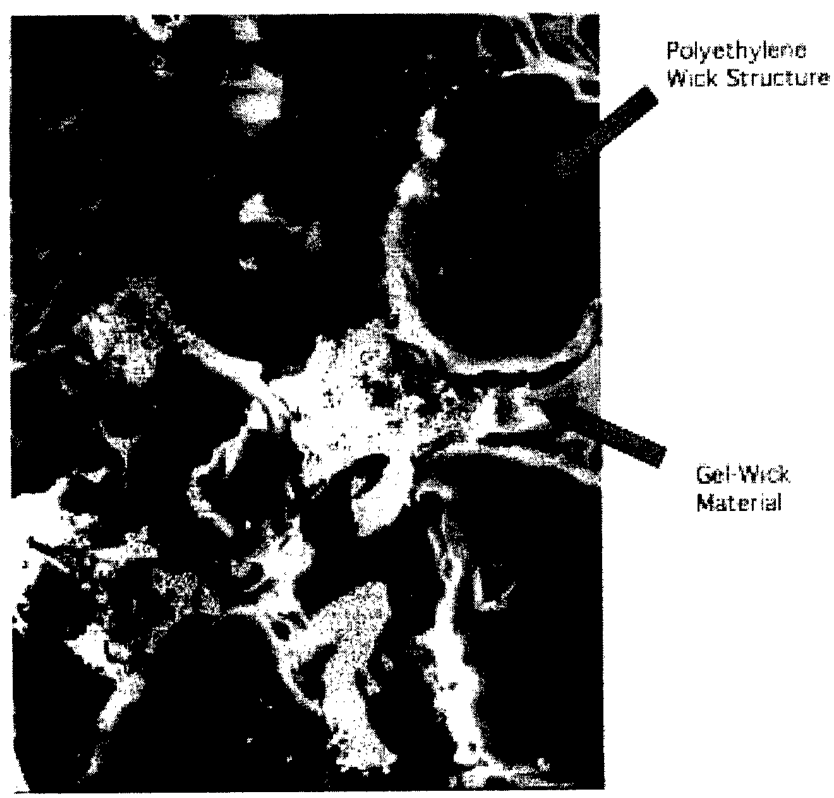

Fig. 14 — SEM of the solgel filled polyethylene wick.

Table 1 — Physical Properties of the Solgel Wick Samples

Sample	Bulk Density (g/cm^3)	Apparent Density (g/cm^3)	Porosity %	Pore Size (mm)	Swelling (% Volume)
Polyethylene	0.65	0.88	27	15 to 20	0
R20	0.33	1.15	71	3 to 5	2
R30D	0.28	1.20	77	10 to 35	3
R50	0.53	1.18	55	0.2 to 0.5	2

liquid volume and away from the wick. Therefore, under the EHD effect, blockage of return liquid caused by the presence of vapor bubbles will be minimized, realizing an increased vapor tolerant CPL evaporator. Unlike the conventional CPL evaporator, a strong secondary circulation dominates inside the liquid volume of the EHD-assisted CPL evaporator as a combined result of EHD-induced convection and EHD-interfacial effects. The enhanced energy transport and flow momentum will also isothermalize the liquid volume, helping to collapse and break down any existing vapor bubbles.

Figure 13 depicts a successful deprime recovery on a typical experimental run with R-134a as the working fluid. The evaporator is intentionally powered to 300 W, slightly over its transport capacity. As a result, the evaporator wall temperature continues to rise, signifying a depriming condition. When the EHD is turned on, the evaporator wall temperature drops instantaneously and then stabilizes itself. It is important to note that the power consumption required for EHD is extremely low, often less than a fraction of watt.

Organic-Inorganic Hybrid Wick Materials Development: The porous wick material inside the evaporator provides for the circulation of the working fluid, therefore, it is the single most important component of a CPL. Existing wicks have either low performance or high thermal conductivity, both of which are detrimental to CPL. It is desirable to develop a wick material that has small pore size, high porosity, high permeability, and low thermal conductivity. However, there is no single component material system that satisfies all of these demanding features. NRL's Spacecraft Engineering Department and Materials Science and Technology Division are currently developing an organically modified ceramic porous material by solgel processing to offer optimum wick properties. This inorganic-organic hybrid is synthesized by a two-step reaction of hydrolysis and polymerization, resulting in a homogeneous material with nanoscale distribution of organics and inorganics. The solution chemicals and drying process can be tailored to have an optimized hybrid porous material for CPL application.

Bulk and apparent densities of three samples, along with those of a polyethylene wick sample, are tabulated in the table. Sample R20, which was prepared by reacting the organic and inorganic components in the hot bath for 20 min and was catalyzed with only one acid, had a bulk density of 0.33 g/cm^3 and above 70% porosity. Sample R30D, which was in the hot bath for 30 min and was catalyzed with two acids, had a bulk density of 0.28 g/cm^3 and porosity of 77%. Sample R50 was prepared at a temperature 20° lower than the other two samples. It was reacted at that temperature for 50 min and was catalyzed with one acid. This sample had a bulk density of 0.53 g/cm^3 and porosity of 55%. Scanning electron microscopy of these samples show a fine microstructure with mesopores ranging between 0.2 μm to 0.5 μm. Samples R20 and R30D, which were prepared at higher temperature, had coarser morphology than R50. The pore sizes in these samples ranged from 3 μm to 10 μm. All gel wick samples have much finer structure than the polyethylene, with sample R50 having submicron pores.

However, all these samples are found to be too fragile for CPL evaporator integration. A concept of curing gel-solution inside a rigid polyethylene wick is currently being pursued to improve the overall structural integrity. Figure 14

shows a scanning electron microscopy (SEM) picture of a gel-filled polyethylene wick sample. Its pore size, porosity, and permeability are comparable to conventional high-performance metal wicks but with much lower thermal conductivity and mass density. These features can significantly reduce evaporator volume/weight and minimize the reverse heat flow associated with metal wicks.

Summary: CPL thermal control system is one of the enabling technologies for the next generation of DoD spacecraft. Tolerance to vapor bubbles inside its evaporator is needed to realize viable CPL systems. NRL is leading the R&D efforts within DoD to develop this needed capability. The A-CPL, the EHD-assisted CPL, and the solgel wick concepts have been successfully demonstrated through prototype builds and tests to provide a CPL with vapor bubble tolerance while simultaneously increasing its performance. Space flight demonstrations are planned in the near future to qualify these technologies.

[Sponsored by NSTP and NRO]

Reference

1. T. Hoang, K. Cheung, and J. Kim, "Design and Test of a Proof-of-Concept Advanced Capillary Pumped Loop," SAE Paper No. 972326, July 1997. ◆

New Views of the Sun

R.A. Howard, G.E. Brueckner, and D.J. Michels
Space Sciences Division

Plasma emissions from the Sun—the solar wind—constantly bathe the Earth, affecting many aspects of the terrestrial environment. Understanding those emissions, how and why they form, how they propagate into interplanetary space including Earth, is a primary objective for researchers in the Space Sciences Division. With the launch of the Solar and Heliospheric Observatory (SOHO) on 2 December 1995, we are obtaining new views of the Sun and the solar corona, a tenuous region of hot, ionized gas and magnetic field surrounding the Sun. During the last two years, the Sun has been at the minimum of its activity cycle, but we are observing many new and unexpected results of solar activity.

The Experiments: The SOHO satellite program is a joint effort between the European Space Agency (ESA) and the National Aeronautics and Space Administration (NASA) and carries twelve experiments from many countries to study the Sun in a coordinated way. Five months after launch, it arrived into an orbit about the L1 Lagrangian point, 1.6 G m toward the Sun along the Sun-Earth line. The L1 point is where the gravitational and orbital forces balance. An advantage of this orbit is continuous sunlight. Not only is this good for the science, but the thermal stability of the satellite is excellent since it does not have the day/night cycle common in low-Earth orbits.

Naval Research Laboratory (NRL) provided hardware for two of the experiments. Those experiments are the Large Angle and Spectrometric Coronagraph (LASCO) for which G.E. Brueckner is the principal investigator and the Extreme-ultraviolet Imaging Telescope (EIT) for which J.-P. Delaboudiniere, of the Institute d'Astrophysique Spatiale in France, is the principal investigator. Both experiments were conceived and built by large consortia of investigators in the U.S. and various countries and many contractors.

LASCO is a collection of three coronagraphic telescopes that together image the solar corona in visible light from 70,000 km above the surface of the sun to 22 M km or one-seventh of the distance between the Sun and Earth. The images are the type that would be obtained during a full eclipse of the Sun by the Moon but, by going outside the Earth's atmosphere, we are able to create this artificial eclipse continuously and also observe much farther away from the Sun than is even possible during an eclipse. The EIT is a single telescope with four reflective multilayer mirror segments that image the Sun in four narrow wavelength bands in the extreme ultraviolet, 17-30 nm.

Science Objective: Together LASCO and EIT provide information on coronal structures including electron density, Doppler velocity, and ion temperatures. But they also are providing unprecedented images of the solar environment. Figure 15 shows the solar corona viewed against the background of the Milky Way. The simple radial coronal streamers record the slow outflowing plasma contrast to the curved, Sun-grazing comet just before it impacted the Sun. LASCO has discovered over 30 Sun-grazing comets, some of which may have impacted the Sun, but all of which were dark after their perihelion. The NRL

SOLWIND coronagraph observed the first Sun-grazing comet to impact the Sun in August 1979.

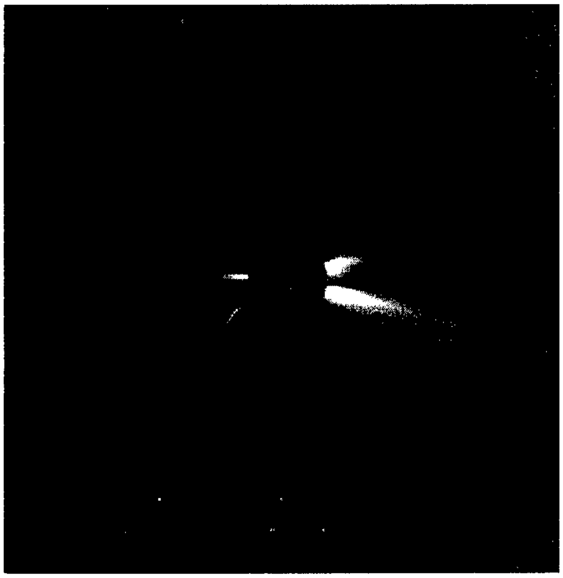

Fig. 15 — The solar corona from 3.7 to 32 solar radii as observed from the SOHO/LASCO experiment on December 22, 1996, in visible light. The small circle in the center of the image indicates the size and position of the Sun behind the occulting disk. The stars and the Milky Way can be seen in the background. The radial structures emanating from the occulting disk are coronal streamers, regions of enhanced electron density. The curved structure on the left of the occulter is a Sun-grazing comet on a path toward the Sun.

The sensitivity of the experiments is far greater than previous experiments of this type, partly through the use of charge coupled device (CCD) technologies for the detectors. The ultraviolet sensitization was derived in part from the results of a joint effort with the Electronics Division and its Microelectronics Processing Facility. For example, the signal-to-noise ratio (SNR) is about 700:1 compared to about 50:1 for previous coronagraphs.

Puffs in the Wind: One of the unexpected results of the increased sensitivity is the observation of outflow along the coronal streamers. The streamers have been thought of as quiescent uniform structures that map the otherwise unobserved coronal magnetic field. However, examining the images returned from LASCO and EIT as time-lapse movies, we see continuous outflow from the solar surface out to the edge of the field at 32 solar radii. This outflow was measured by Neil Sheeley and colleagues and was found to confirm the theoretical prediction in 1966 for the speed profile of the slow solar wind. This analysis established the sonic point, where the speed of the outflowing material exceeds the speed of sound and becomes supersonic, to be at about 5 solar radii.

CMEs: A striking manifestations of solar activity is the coronal mass ejection (CME) (Fig. 16). During a CME, large amounts (e.g., 10^{14} g to 10^{17} g) of coronal gas and magnetic field are thrown out from the Sun. This phenomena, discovered by the NRL coronagraph on the OSO-7 satellite in 1971, is now believed to be one of the causes of enhanced geomagnetic activity. This enhanced activity can sometimes cause disastrous outages of power systems. Prior to SOHO, we had expected that this period of the minimum of the solar activity cycle would be producing relatively small CMEs at a rate of about 1 every 5 days. But we have been observing them at the rate of more than 1 every 2 days, and most of them are much larger than expected. SOHO has also discovered a global effect of CMEs. When a CME

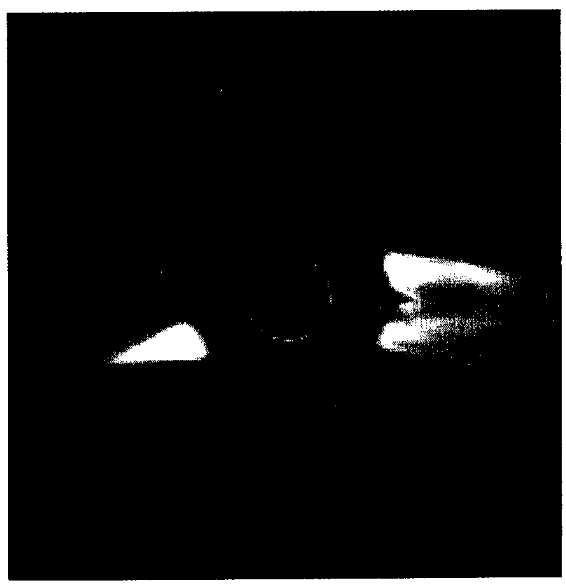

Fig. 16 — A coronal mass ejection (CME) as it is leaving the west limb of the Sun on November 1, 1997. CMEs are occurring every two days during the minimum of the solar activity cycle and will occur more frequently in a few years. They are large-scale expulsions of mass and magnetic field. In this image, the field of view of this LASCO telescope ranges from 2 to 6 solar radii. The CME is interpreted as the eruption of a twisted magnetic flux rope being viewed end on. The dark region behind the bright front is probably where the magnetic field is highest and the density is lowest.

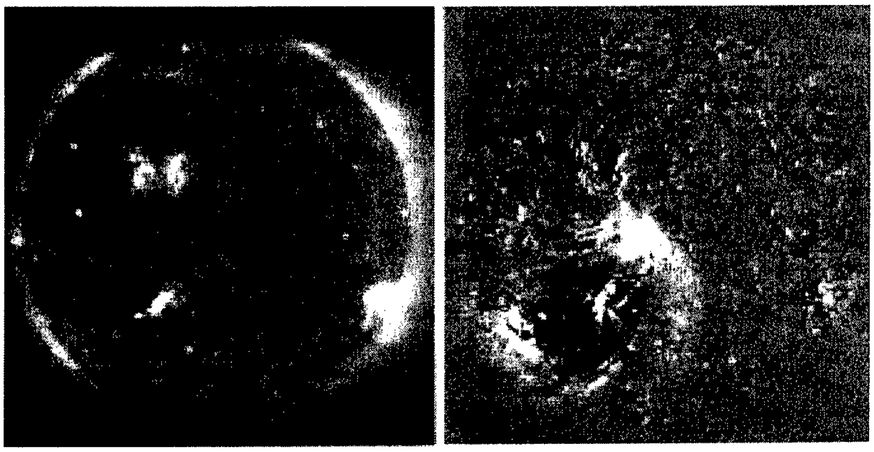

(A) 1997/04/07 14:12 UT (B) 1997/04/07 14:12 UT minus 14:00 UT

Fig. 17 — An image of the ultraviolet corona from the Extreme-ultraviolet Imaging Telescope (EIT) experiment in the light of Fe XII (11 times ionized iron) at 19.5 nm. The left image is a direct image, and the right image is the difference from the image taken 12 min earlier. Here we see a disturbance emanating from the site of a flare in the southeast part of the solar disk. In the right-hand image, dark means that the Fe emission is depleted relative to the earlier time, and white means that the emission is enhanced relative to the earlier time.

is launched, the disturbance is frequently accompanied by ejecta at the opposite limb of the Sun. This implies that a disturbance has traveled quickly around the Sun and a destabilization in some other region. Figure 17 shows an example of such a traveling disturbance.

Space Weather: The event in Fig. 17 was accompanied by a halo CME. This type of CME, first observed by NRL in 1979, is indicative of a CME that is either heading toward or away from the Earth. This ambiguity is due to the symmetry of the Thomson scattering process. However, the EIT instrument identifies the source region on the solar disk, thus removing the ambiguity. Of the many CMEs that have occurred since launch, over a dozen events have been identified as being directed toward Earth. In almost all cases, a major geomagnetic storm occurred a few days later. A storm occurs when the ejected plasma reaches the Earth. Typical transit times are about 80 h. While we don't know what the range of effects will be, simply knowing when the storm will be occurring represents a major advance in our understanding of space weather.

Summary: SOHO is proving to be an advanced observatory to study the Sun. We have shown that not only are CMEs occurring more frequently, but the entire corona is evolving on all time scales and at all temperatures available to us. This will affect our concepts of solar cycle evolution. In addition, the observations of the major CMEs that are heading toward Earth is providing, for the first time, a direct link between geomagnetic storms and the causative solar event. For more information and to see the state of the Sun in real time, visit our web page at http://lasco-www.nrl.navy.mil.

[Sponsored by NASA and ONR]

References

1. G.E. Brueckner, "The Large Angle Spectrometric Coronagraph (LASCO)," *Solar Phys.* **162,** 357 (1995).

2. J.P. Delaboudiniere, "EIT: Extreme-ultraviolet Imaging Telescope for the SOHO Mission," *Solar Phys.* **162,** 391 (1995).

3. R.A. Howard, "Observations of CMEs from SOHO/LASCO," in *Coronal Mass Ejections,* N.U. Crooker, J.A. Joselyn, and J. Feynman, eds. (American Geophysical Union, Washington, D.C., 1997), p. 17.

4. N.R. Sheeley, Jr., "Measurements of Flow Speeds in the Corona Between 2 and 30 R," *Astrophys. J.* **484**, 472 (1997).

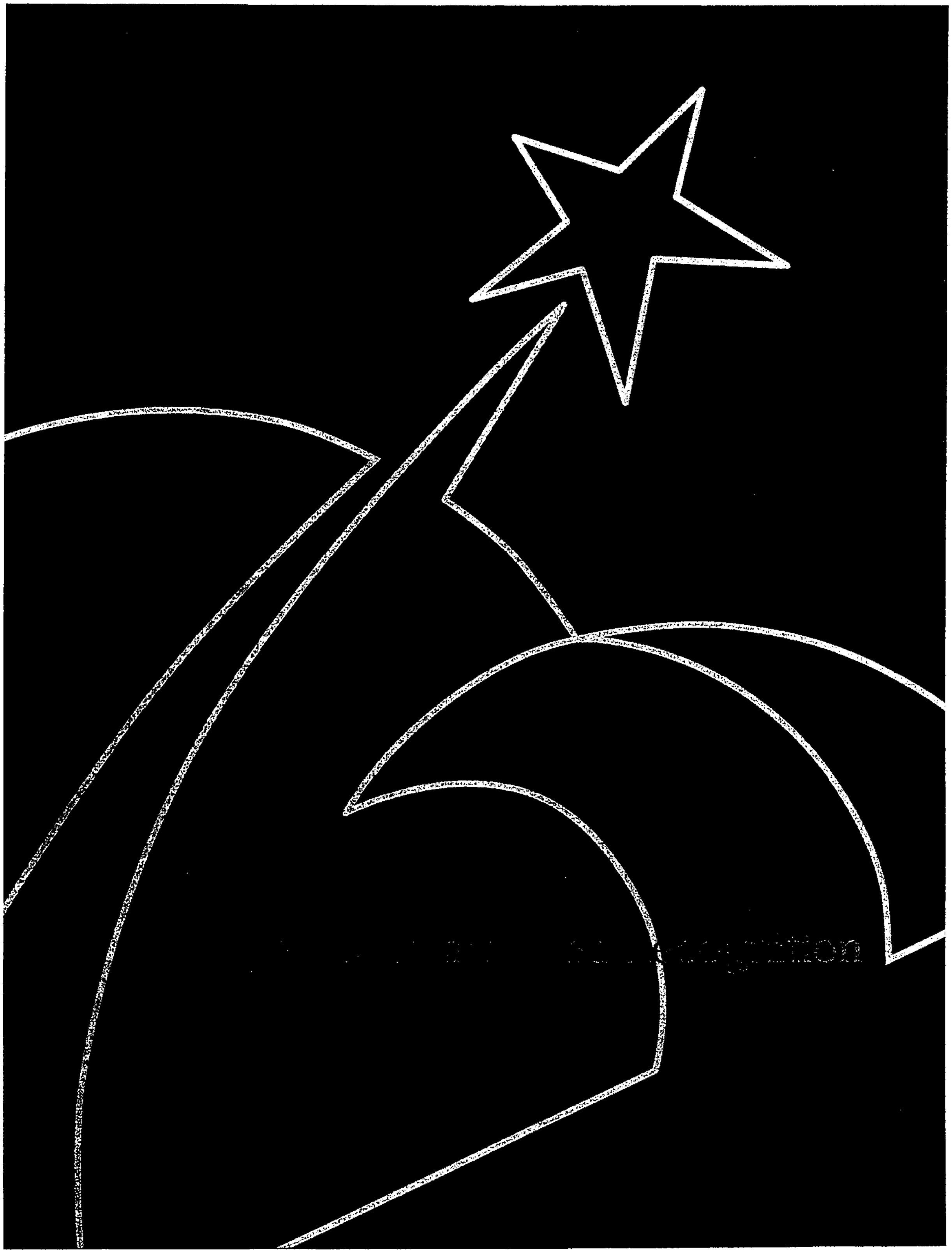

Special Awards and Recognition

NRL is proud of its many distinguished scientists, engineers, and support staff. Here we feature some who have received awards from prestigious institutions, the Department of the Navy, and NRL.

Dr. Eric Hartwig
Ocean and Atmospheric Science and Technology Directorate

PRESIDENTIAL RANK OF MERITORIOUS EXECUTIVE IN THE SENIOR EXECUTIVE SERVICE (SES)

This award was presented by The Honorable John Dalton, Secretary of the Navy. A letter of citation reads, "A Presidential Rank Award is among the highest honors a public employee may receive. It is a recognition of your sustained, outstanding achievements which have brought great credit, not only upon yourself, but the entire Department of the Navy. Your accomplishments have contributed in large measure to our ability to provide for the national security in the most efficient and effective manner." The nomination credits Dr. Hartwig, a national leader in ocean sciences, with setting the course for national ocean sciences programs.

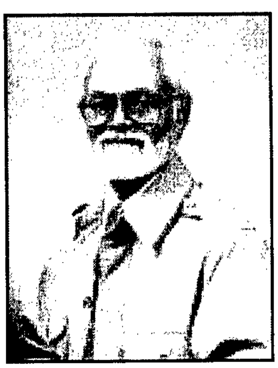

Dr. David Griscom
Optical Sciences Division

SIGMA XI 1997 PURE SCIENCE AWARD

Dr. Griscom was cited for "advancements in the physics of radiation-induced defects in technologically relevant glasses and diffusion of knowledge through critical literature reviews." His work has centered on radiation hardening of fiber-optics for monitoring fusion reactor plasmas and image guides for remote viewing of fission reactors. Recently, he has initiated a Department of Energy (DoE)-sponsored program to study radiation-induced decomposition of glasses for nuclear waste disposal.

Dr. Dennis Hardy
Navy Technology Center for Safety and Survivability

SIGMA XI 1997 APPLIED SCIENCE AWARD

Dr. Hardy was cited for "original and ingenious work on Navy fuels chemistry in advancing the state of analytical methods and quality control." His scientific and technical contributions have been widely recognized within and beyond the fuels chemistry community.

Dr. Frances Ligler
Center for Bio/Molecular Science and Engineering

THE WOMEN IN SCIENCE AND ENGINEERING (WISE) 1997 SCIENTIFIC ACHIEVEMENT AWARD

This award is presented to a Federally employed woman scientist who has made significant contributions to science and who has either encouraged young women to pursue science and engineering careers or assisted other women scientists or engineers in advancing their careers. Dr. Ligler is recognized for her biosensor projects—the flow immunosensor and the fiber-optic biosensor—which have received widespread academic, government, and industrial attention. In addition, Dr. Ligler organized and leads the Women's Science and Technology Network, which developed a mentor program to improve the performance of all NRL scientists and engineers and instituted a workshop series for the professional advancement of senior female professionals.

Ms. Carolyn Thomas
Technical Information Division

WOMEN OF COLOR TECHNOLOGY AWARD

The *U.S. Black Engineer and Information Technology* and *Hispanic Engineer and Information Technology* magazines cited Ms. Thomas for her "outstanding accomplishments and technological innovations and the positive light in which she portrays all women, but in paticular women of color, breaking stereotypes and serving as a role model." Ms. Thomas has been involved with NRL's library automation since 1972, developing applications to support the library acquisition processes, implementing an online library system in the early 1980s, replacing the traditional, and then standard, "card catalog" with the online system, and serving as a key member of the InfoVision/2000 Steering Committee. While a member of this committee during 1996, she worked on the development of a vision and plan for a 21st-century information infrastructure for NRL.

Ms. Laurie Stackpole
Technical Information Division

INFORMATION TODAY AWARD FOR INNOVATIONS IN TECHNOLOGY

Ms. Stackpole, chief librarian of the Ruth H. Hooker Research Library and Technical Information Center, was recognized by the Special Library Association for "her exceptional use and application of technology in a special library setting." She is recognized for the Library's innovative joint ventures with publishers, such as the American Physical Society and Elsevier Science, and for the emphasis she has placed on developing a 21st-century information infrastructure for NRL.

FEDERAL LIBRARIANS ROUND TABLE (FLRT) AWARD

This award recognizes leadership or special achievement in the promotion of library and information science in the federal community. Ms. Stackpole was recognized "for her leadership in designing, developing, and implementing technologies that underpin the digital library. Ms. Stackpole has empowered end users through desktop access to the full content of journals, reports, and other library resources."

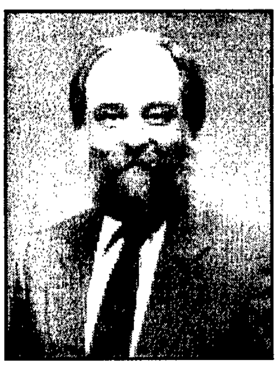

Dr. Gary Prinz
Materials Science and Technology Division

1996 E.O. HULBURT SCIENCE AWARD

The E.O. Hulburt Science Award is the highest civilian honor awarded for scientific achievement by the Naval Research Laboratory. Dr. Prinz was cited for "his inspirational research investigations of metallic single crystalline magnetic thin and ultrathin film problems employing a wide variety of magnetic, surface physics, and spin-sensitive techniques; for his outstanding insight into the growth and physical properties of such magnetic thin film systems; and for his enthusiastic and influential efforts in bringing the standards of surface science to bear on the investigation of magnetic films and multilayers, thus greatly enhancing our understanding of their behavior."

Mr. Peter Wilhelm
Naval Center for Space Technology

ROGER L. EASTON AWARD FOR EXCELLENCE IN ENGINEERING ACHIEVEMENT

Mr. Wilhelm is the first recipient of the Roger L. Easton Award, the highest civilian award presented by the Naval Research Laboratory for engineering achievement. He was cited for "exceptional technical expertise, outstanding management, and zealous dedication to excellence in support of Navy and national space program....Mr. Wilhelm has provided technical and managerial leadership for each of the scientific and support satellites launched by the Navy. His technical achievements in high-performance, long-life satellites, multiple satellite launching systems, passive and active gravity gradient stabilization systems, low power-low weight electronics, station-keeping microthrusters, and solid-state memory systems have been critical to maintaining the United States' superiority in space." Mr. Wilhelm was also elected to the National Academy of Engineering. He was cited for his career contributions to the U.S. space program.

Ms. Susan Bales
Director of the Naval Science Assistance Program (NSAP)

NAVY SUPERIOR CIVILIAN SERVICE AWARD

Ms. Bales was cited for her "outstanding leadership, technical expertise, and unselfish dedication as [Naval Science Assistance Program] NSAP director." According to the citation, "Ms. Bales' vision in utilizing state-of-the-art information collection and distribution technologies enabled development of a Global Tactical Technical Information Center for NSAP/ Office of Naval Research (ONR) providing a 'near real time' window to the technology 'needs and hot spots' of the major Naval Operational Force Commands."

Mr. George Stimak
Deputy Director of the Naval Science Assistance Program (NSAP)

NAVY MERITORIOUS CIVILIAN SERVICE AWARD

Mr. Stimak was cited for his service as the acting director of the [Naval Science Assistance Program] NSAP in which he "displayed an unprecedented level of support for NSAP and the operational commands where the NSAP science and technical advisers are assigned, by appraising their requirements on major issues impacting science and technology and research development." The citation reads, "Mr. Stimak was the key to greatly improved coordination between the Office of Naval Research, the Naval Research Laboratory, and the Surface Warfare Center communities and the operational fleet they are supporting."

Mr. Brian Sweeney
Optical Science Division

NAVY MERITORIOUS CIVILIAN SERVICE AWARD

Mr. Sweeney, who received this award for work in high-speed optical communications, is recognized for "his substantial contributions as the program's principal investigator. In this capacity, Mr. Sweeney personally conducted key research and directed the efforts of three staff scientists. In addition, he monitored the work of research and development contracts totaling $4 million. Mr. Sweeney was responsible for defining the requirements and specifications that enabled the successful development of hardware that met the sponsor's operational needs. The work done by Mr. Sweeney has helped to establish NRL as a leader in the application of high-speed network technology for C^4I and C^2W within the Department of Defense."

Dr. Robert Brady
Chemistry Division

NAVY MERITORIOUS CIVILIAN SERVICE AWARD

According to the citation, "Dr. Brady successfully developed numerous organic surface coatings now used on ships of the United States Navy. His work is characterized by a comprehensive view of the chemistry of materials, insight in recognizing opportunities for performance enhancement, and creativity in devising practical solutions for critical operational needs. His basic research generates fundamental knowledge of organic and polymer chemistry, which is relevant to naval requirements. Dr. Brady is commended for elevating the Navy's competence in materials chemistry and producing advanced coatings that extend the performance and endurance of the Fleet."

Dr. Ted Tsui
Marine Meteorology Division

NAVY MERITORIOUS CIVILIAN SERVICE AWARD

According to the citation, "Dr. Tsui provided critical research direction and administrative oversight during an extremely dynamic period in the history of the division. His exceptional leadership resulted in the successful transition of numerous meteorological support systems to operations, including a new state-of-the-art mesoscale analysis and forecast system, the Coupled Ocean/Atmosphere Mesoscale Prediction System, and a tropical cyclone forecast aid—the Automated Tropical Cyclone Forecasting System."

Mr. Francis Campbell
Condensed Matter and Radiation Sciences Division

NAVY MERITORIOUS CIVILIAN SERVICE AWARD

Mr. Campbell was cited for "ingenious and intensive work focused on increasing the reliability of many Navy systems. During his 35 years at the Laboratory, his span of investigations have ranged from radar camouflaging materials, to laser hardening of solar cells, and to probing the phenomena of aging in the dielectric materials of electrical systems. His most important contribution was unraveling the mystery of the unexpectedly high number of electrical system failures and electrical fires on Naval aircraft during their operation. As a result of his investigations, critical redesign of electrical systems has been implemented by the Navy, resulting in the reduction of these incidents and increasing the operational reliability of Naval aircraft."

Mr. George Kowalski
Space Science Division

NAVY MERITORIOUS CIVILIAN SERVICE AWARD

Mr. Kowalski was cited for his work as project manager for NRL's Large Angle Spectrometric Coronagraph (LASCO)/Extreme Ultraviolet Imaging Telescope (EIT). He was recognized for the "critical project direction and management oversight that led to the successful construction and deployment of this space instrumentation package...outstanding organizational ability [that] allowed the construction of this complex multinational suite of instruments to be completed on time and within the available resources...[and] successful management of the LASCO/EIT program [which] will long be remembered as a major accomplishment."

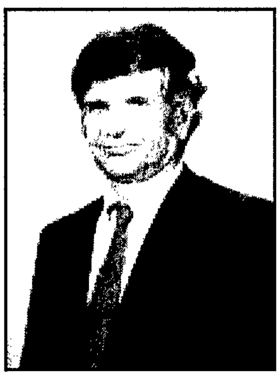

Mr. Joseph Thomason
Radar Division

NAVY MERITORIOUS CIVILIAN SERVICE AWARD

Mr. Thomason was cited for his "personal contributions and leadership in the field of High-Frequency Over-the-Horizon (HF OTH) radar technology and development, ... which has provided the Navy with a true wide-area surveillance capability (millions of square miles) that provides early warning to the battle group both in the open ocean and in the littoral regions. Furthermore, this sensor has seen extensive and successful application in the drug interdiction effort as the most cost-effective sensor for area sureveillance."

Dr. William Waltman
Remote Sensing Division

NAVY MERITORIOUS CIVILIAN SERVICE AWARD

Dr. Waltman was cited for his "fundamental contributions to a large number of highly successful scientific experiments conducted by NRL in the fields of radio astronomy and atmospheric science." As chief engineer on the Orbiting Ozone and Aerosol Monitor (OOAM) space experiment, the space-based Millimeter-wave Atmospheric Sounder (MAS) experiment, the ground-based Water Vapor Millimeter-wave Spectrometer (WVMS) system, the Independent Range Interferometer System (IRIS) program, and consulting engineer for the Gusty Badger and other classified programs, Dr. Waltman has gone well beyond his normal responsibilities to ensure the success of the projects.

Ms. Wilberena Cosby
Contracting Division

COMMANDING OFFICER'S AWARD FOR ACHIEVEMENT IN THE FIELD OF EQUAL EMPLOYMENT OPPORTUNITY (SUPERVISORY)

Ms. Cosby was cited for her "constant dedication of assisting NRL in achieving its EEO goals, her unwavering support of branch employees in their overall development, and her promotion of NRL to the community." Ms. Cosby has been promoting EEO inside and outside of NRL for many years. She strongly supports and takes advantage of the Upward Mobility Program, Cooperative Education Program, and other hiring authorities to include candidates from minority groups.

Ms. Cindy Hartman
Supply Division

COMMANDING OFFICER'S AWARD FOR ACHIEVEMENT IN THE FIELD OF EQUAL EMPLOYMENT OPPORTUNITY (SUPERVISORY)

Ms. Hartman was cited for her "outstanding work in hiring, promoting, and developing female, disabled, and minority employees. Through her personal example and leadership skills, she sets the standard for achieving an open, equitable, supportive, and representative work place which fosters activities to achieve that end." Ms. Hartman encourages and promotes employee participation in the NRL Mentor Program and in NRL's school partnership efforts.

Ms. Leona Cole
Marine Geosciences Division

COMMANDING OFFICER'S AWARD FOR EXCELLENCE IN SECRETARIAL SUPPORT

Ms. Cole was recognized for her "continuous performance in an outstanding manner, her ability to train and lead young inexperienced personnel in office automation techniques and her support for the international Coastal Benthic Boundary Layer (CBBL) program and The Technical Cooperation Program (TCCP)." Dr. Herbert Eppert, Jr., head of the Marine Geosciences Division, noted, "To say that Ms. Cole has been a 'vital asset' to her branch is a tremendous understatement—not only is she an incredibly productive performer always willing to take on additional requests, but she is extremely well organized and...she consistently typifies the very best of the qualities that make NRL strong."

The Scientific Team
(Left to right) Dr. Russell Howard, Dr. Kenneth Dere, Dr. Dennis Socker, Dr. Donald Michels, and Dr. Clarence Korendyke; (Not shown) Dr. Guenter Brueckner and Dr. J. Daniel Moses.

The Engineering/Technical Team
(Left to right) Mr. Donald Conroy, Mr. Benjamin Au, Ms. Linda Gould, Ms. Elizabeth Kegley, Ms. Nancy Linder, Ms. Mary Teufel, Mr. Randall Waymire, Mr. J. Allen Oliver, and Mr. David Roberts; (Not shown) Mr. George Kowalski, Mr. Donald Lilley, and Mr. Thomas Spears.

NAVY AWARD OF MERIT FOR GROUP ACHIEVEMENT

Space Science Division

The LASCO/EIT Team received this award for their work on the Large Angle and Spectrometric Coronagraph (LASCO) and the Extreme-ultraviolet Imaging Telescope (EIT) experiments, which were developed for and launched on the European Space Agency's Solar and Heliospheric satellite (SOHO). The **scientific team** was cited for "significantly advancing the observation of the solar corona by developing an exciting scientific concept and carrying out the development of the state-of-the-art LASCO and EIT experiments to observe the solar atmosphere with unprecedented sensitivity and resolution." The **engineering/technical team** was cited for "a sustained high level of effort in the development of the state-of-the-art LASCO and EIT experiments."

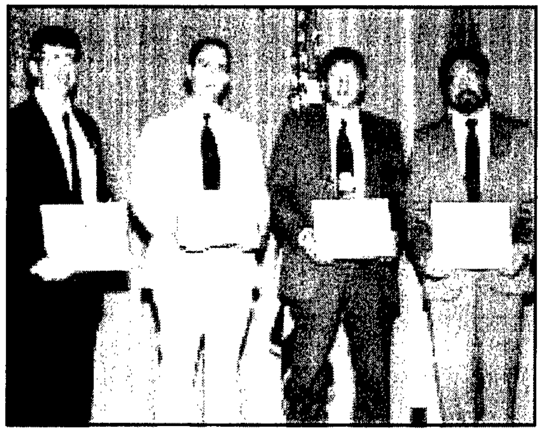

NRL AWARD OF MERIT FOR GROUP ACHIEVEMENT

Optical Sciences Division

(Left to right) Mr. Brian Sweeney, Mr. Russell Rhodes, Dr. Keith Williams, and Mr. Carl Villarruel.

The team members are recognized for their substantial contributions to high-speed optical communications. The research team has been instrumental in laying the groundwork for a program that will have a major impact in the Command, Control, Communications, Computers, and Intelligence (C^4I) and Command and Control Warfare (C^2W) environments

NRL AWARD OF MERIT FOR GROUP ACHIEVEMENT

Chemistry Division

(Left to right) Dr. Joel Miller, Dr. James Yesinowski, Dr. Kenneth Mcgrath, and Dr. Al Garraway.

The team received this award for the development of Nuclear Quadruple Resonance (NQR) as a pratical method of detecting explosives and narcotics. The team identified and solved many of the technical issues that have enabled this technology to move from the laboratory, where it had been considered a rather impractical curiosity, into the field. This technology will indeed make life more difficult for the prospective terrorist and provide a further degree of security to the traveling public.

NAVY AWARD OF MERIT FOR GROUP ACHIEVEMENT AND SPECIAL ACT AWARD

Naval Center for Space Technology

(Left to right, front row) Mr. Charlie Bird, Mr. Chris Garner, Mr. Bob Patterson, Mr. Chris Butkiewicz, Mr. Mike Hurley, Mr. Bob Haynes, Ms. Moira Stanton, Mr. Mike Zedd, and Mr. Bob Circle; (Back row) Dr. Shannon Coffey, Mr. Dave Golder, Mr. John Traylor, Mr. Bernie Kelm, Ms. Amey Peltzer, Mr. Bill Purdy, Mr. Robert Towsley, Dr. Charmaine Gilbreath, and CAPT Bruce Buckley, NRL's Commanding Officer; (Not shown) Mr. Fred Domer, Mr. Ron Mader, Ms. Anne Clement, and Mr. Steve Gates.

The Tether Physics and Survivability Experiment (TiPS) team was cited for "significant contributions leading to the success of the [TiPS] program and the advancement of tether technology." The recipients of this award provided the scientific engineering and management expertise to successfully design, build, test, integrate, and operate the TiPS spacecraft.

NRL'S AWARD FOR EXCELLENCE IN MISSION SUPPORT

Technical Information Division

(Left to right) Mr. W.F. Rettenmaier, Mr. Rod Atkinson, Ms. Carolyn Thomas, Mr. Murray Bradley, and Ms.Patricia Ames

This award was presented to the Library Management Team of the Ruth H. Hooker Library and Technical Information Center for accomplishments in planning and implementing a program of Web-based digital library services that provides the NRL research community with ready access through the Library's Info Web information system and gateway to scientific and technical information previously available only to walk-in users. The work of the team capitalized on the network infrastructure and software tools already available throughout the organization, to provide NRL and Office of Naval Research (ONR) personnel with the ability to use their desktop computers to access the virtual library.

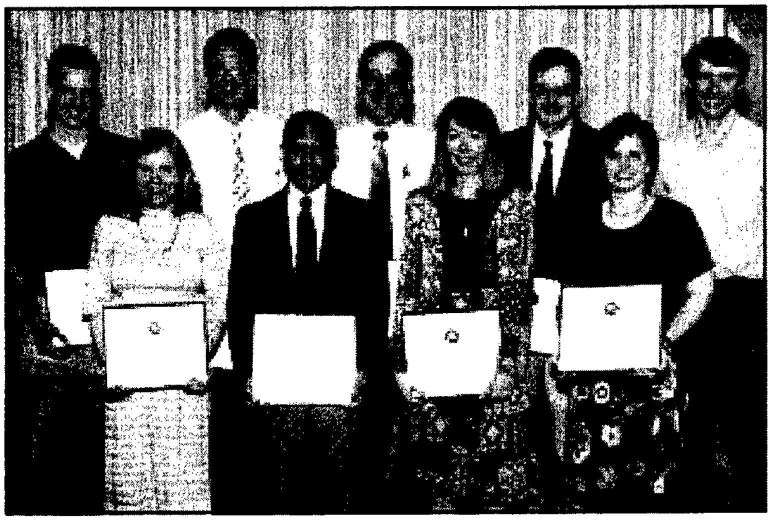

THE *1997 NRL REVIEW* ARTICLE AWARDS

(Left to right) Mr. Edward Ashton, Dr. Elizabeth Dobisz, Mr. William Purdy, Mr. Richard Siquig, Dr. John Spencer, Dr. Ruth Preller, Mr. Richard Allard, Ms. Pamela Posey, and Dr. Christie Marrian.

Awards for *NRL Review* articles recognize authors who submit outstanding research articles for this scientific publication. The articles are judged on the relevance of the work to the Navy and DoD, readability to the college-graduate level, clearness and conciseness of writing, and the effective use of graphics that are interesting and informative. The following awards were presented for articles that appeared in the *1997 NRL Review.*

FEATURED RESEARCH ARTICLE

"*Modeling the Dispersion of Radioactive Contaminants in the Arctic,*" R.H. Preller and P.G. Posey (Oceanography Division)

DIRECTORATE AWARDS FOR SCIENTIFIC ARTICLES

Systems Directorate: "*Detection of Subpixel Targets in Multispectral Imagery,*" E.A. Ashton (Optical Sciences Division)

Materials Science and Component Technology Directorate: "*Nano-Precision Lithography for Nanoelectronics,*" E.A. Dobisz, C.R.K. Marrian, and M.C. Peckerar (Electronics Science and Technology Division)

Ocean and Atmospheric Science and Technology Directorate: "*The Master Environmental Library (MEL),*" R.A. Siquig, R.A. Allard, and J.H. Spencer (Marine Meteorology, Oceanography, and Remote Sensing Divisions, respectively)

Naval Center for Space Technology: "*The Tether Physics and Survivability Spacecraft (TiPS),*" S.L. Coffey, W.E. Purdy, and W.J. Barnds (Spacecraft Engineering Department)

Alan Berman Research Publication and Edison Patent Awards

The Annual Research Publication Awards Program was established in 1968 to recognize the authors of the best NRL publications each year. These awards not only honor individuals for superior scientific accomplishments in the field of naval research but also seek to promote continued excellence in research and in its documentation. In 1982, the name of this award was changed to the Alan Berman Research Publication Award, in honor of its founder.

There were 275 separate publications submitted by the divisions in 1997 to be considered for recognition. Of those considered, 37 were selected. These selected publications represent 179 authors, each of whom received a publication awards certificate, a bronze paperweight, and a booklet listing the publications that were chosen for special recognition. In addition, NRL authors share in their respective division's monetary award.

The winning papers and their respective authors are listed below by their research units. Non-Laboratory coauthors are indicated by an asterisk.

NRL also recognizes patents as part of its annual publication awards program. The NRL Edison Patent Award was established in January 1991 to recognize NRL employees for outstanding patents issued to NRL by the U.S. Patent and Trademark Office during the preceding calendar year. The award recognizes significant NRL contributions to science and engineering as demonstrated by the patent process that are perceived to have the greatest potential benefit to the country. Of the 14 patents considered for 1997, 3 were selected, representing 7 inventors. They are listed under the NRL Edison Patent Awards.

Systems Directorate

Magneto-Percolation Materials for LO Applications
Jonas K. Lodge, Scott L. Browning, Peter F. Loschialpo, and John H. Schelleng

Radar Division

Time-Domain Fields Exterior to a Two-Dimensional FDTD Space
Mark Kragalott, Michael S. Kluskens, and William P. Pala

Improved AEGIS AN/SPY-1 Cancellation Using Transmitter Equalization
Michael S. Steiner, Michael F. Walder, and Ben H. Cantrell

Information Technology Division

Voice Processing Techniques for C^4I Applications
George S. Kang, Lawrence J. Fransen, Thomas M. Moran, and David A. Heide

A Recommended Error Control Architecture for ATM Networks with Wireless Links
Dennis N. McGregor and J. Bibb Cain*

Optical Sciences Division

High Performance Fiber Optic Accelerometer
Sandeep T. Vohra, Alan Tveten, Anthony Dandridge, and Bruce A. Danver*

High Performance Photonic Analog-digital Converter
Michael Y. Frankel, Jin U. Kang, and Ronald Esman

Tactical Electronic Warfare Division

A Fuzzy Logic Multisensor Association Algorithm: Theory and Simulation
James F. Smith III

A Modeling Approach for Infrared Electronic Warfare Simulation in Maritime Environments
Suzanne C. Hiser, Robert Gover, Allen J. Goldberg, and Lee B. Peters*

Chemistry Division

Interaction of Ammonia with Hydrogen on A1(111)
John N. Russell, Jr., Victor M. Bermudez, and Chung Sook Kim

Virtual Environment Firefighting/Ship Familiarization Feasibility Tests
Frederick W. Williams, Patricia A. Tatem, John P. Farley, David L. Tate, Linda Sibert, Tony King, Donald H. Hewitt,* Charles W. Siegmann III,* Jennifer T. Wong,* and Terrance A. Toomey*

Materials Science and Technology Division

Structural Inhomogeneities Observed in $YBa_2CU_3O_{7-\delta}$ Crystals with Optimal Transport Properties
Valerie M. Browning, Michael S. Osofsky, Earl F. Skelton, Syed B. Qadri, J.Z. Hu,* L.W. Finger,* and P. Caubet*

Enhanced Carrier Lifetimes and Suppression of Midgap States in GaAs at a Magnetic Metal Interface
Berend T. Jonker, Orest J. Glembocki, Ronald T. Holm, and Robert J. Wagner

Laboratory for Computational Physics and Fluid Dynamics

Magnetic Flux Tube Tunneling
Russell B. Dahlburg, Spiro K. Antiochos, and David Norton*

A Theory of Deflagration-to-Detonation Transition in Unconfined Flames
Alexei M. Khokhlov, Elaine S. Oran, and J. Craig Wheeler*

Condensed Matter and Radiation Sciences Division

Ferromagnetic Spin Fluctuation Induced Superconductivity in Sr_2RuO_4
David J. Singh and Igor I. Mazin*

Evidence for Modification of theSuperconducting Order Parameter in $YBa_2Cu_3O_{7-\delta}$ Films by Injection of a Spin Polarized Current
Douglas B. Chrisey, James S. Horwitz, Michael S. Osofsky, Robert J. Soulen, Jr., Mark B. Johnson, Jeffrey M. Pond, B. Woodfield,* Jefferson Byers,* George M. Daly, Paul C. Dorsey,* and R.C.Y. Auyeung*

Plasma Physics Division

Reflective Probing of the Electrical Conductivity of Hot Aluminum in the Solid, Liquid and Plasma Phases
Andrew N. Mostovych and Yung Chan*

Plasma Wakefield Generation and Electron Acceleration in a Self-Modulated Laser Wakefield Accelerator Experiment
Antonio Ting, Charles Manka, Eric Esarey, Phillip Sprangle, Richard Hubbard, H. Rayvon Burris, Richard P. Fischer, Christopher I. Moore, Karl Krushelnick,* and Michael Baine*

Electronics Science and Technology Division

Experimental Demonstration of a W-band Gyroklystron Amplifier
Monica Blank, Bruce G. Danly, Baruch Levush, P.E. Latham,* and Dean E. Pershing*

Nuclear Spectroscopy in Single Quantum Dots: Nanoscopic Raman Scattering and Nuclear Magnetic Resonance
Daniel Gammon, Eric S. Snow, Thomas A. Kennedy, D. Scott Katzer, Doewon Park, and Steve W. Brown*

Center for Bio/Molecular Science and Engineering

Diffusion and Transfer of Antibody Proteins from a Sugar-Based Hydrogel
Michael A. Markowitz, David C. Turner, Bruce P. Gaber, and Brett D. Martin

Application of a Portable Immunosensor to Detect the Explosives TNT and RDX in Groundwater Samples
Anne W. Kusterbeck, John C. Bart, Karen E. Hoffman,* Angela M. Wilkins,* and Linda L. Judd*

Acoustics Division

Inversion of Bottom/Subbottom Statistical Parameters from Acoustic Backscatter Data
Altan Turgut

The Role of the Environment in Active Sonar Performance
Roger C. Gauss and John R. Preston*

Remote Sensing Division

Multipath EM Scattering from Breaking Ocean Waves at Grazing Incidence
Mark A. Sletten and James C. West*

Multichannel Optical Aperture Synthesis Imaging of
ζ^1 Ursae Majoris with the Navy Prototype Optical Interferometer
J. Thomas Armstrong, David Mozurkewich, Thomas A. Pauls, Lee J. Rickard,
James A. Benson,* Donald J. Hutter,* Nicholas M. Elias II,* Phillip F. Bowers,*
Ken Johnston,* Arsen R. Hajian,* Christian A. Hummel* Nathaniel M. White,*
David Black,* and Craig S. Denison*

Oceanography Division

The Interaction of Southwest Monsoon Upwelling,
Advection and Primary Production in the Northwest Arabian Sea
Timothy R. Keen, John C. Kindle, and David K. Young

The Contribution of the Global Thermohaline Circulation
to the Pacific to Indian Ocean Throughflow via Indonesia
Jay F. Shriver and Harley E. Hurlburt

Marine Geosciences Division

Observations on Attenuation and Shear-Wave Velocity
in Fine-Grained, Marine Sediments
Frederick A. Bowles

Marine Meteorology Division

The Naval Research Laboratory's Coupled Ocean/Atmosphere
Mesoscale Prediction System (COAMPS)
Richard M. Hodur

Stratus and Fog Products Using GOES-8-9 3.9-μm Data
Thomas F. Lee, Joseph F. Turk, and Kim A. Richardson

Space Science Division

Implications of Satellite OH Observations for Middle Atmospheric H_2O and Ozone
Michael E. Summers, Robert R. Conway, David E. Siskind, Michael H. Stevens,
D. Offermann,* M. Riese,* P. Preusse,* D.F. Strobel,* and J.M. Russell III*

EIT and LASCO Observations of the Initiation of a Coronal Mass Ejection
Kenneth P. Dere, Guenter E. Brueckner, Russell A. Howard, Clarence M. Korendyke,
Donald J. Michels, J. Daniel Moses, Dennis G. Socker, M.J. Kooman,* R.W. Kreplin,*
N.E. Moulton,* O.C. St. Cyr,* J.P. Delaboudiniere,* G.E. Artzner,* J. Brunaud,*
A.H. Gabriel,* J.F. Hochedez,* F. Millier,* X.Y. Song,* J.P. Chauvineau,* J.P. Marioge,*
J.M. Defise,* C. Jamar,* P. Rochus,* R.C. Catura,* J.R. Lemen,* J.B. Gurman,*
W. Neupert,* F. Clette,* P. Cugnon,* E.L. Van Dessel,* P.L. Lamy,* A. Llebaria,*
R. Schwenn,* and G.M. Simnett*

Space Systems Development Department

Calibrating the Naval Space Surveillance Fence Using
Simultaneous Satellite Laser Ranging Data
G. Charmaine Gilbreath, Paul W. Schumacher, Jr.,* Edward D. Lydick,*
Mark A. Davis,* and John M. Anderson*

Spacecraft Engineering Department

Adaptive Filters for Real-Time System Identification and Control
Shalom Fisher, Tae W. Lim,* and Albert Bosse*

Experiments in Tether Dynamics Planned for ATEx's Flight
Michael F. Zedd

NRL Edison (Patent) Awards

Method and Apparatus for Detecting Target Species Having Quadropolar Muclei by Stochastic Nuclear Quadrupole Resonance
Allen N. Garroway, Joel B. Miller, David B. Zax,* and Ming-Yuan Liao*
CHEMISTRY DIVISION

Ultra High Density, Non-Volatile Ferromagnetic Random Access Memory
Gary A. Prinz
MATERIALS SCIENCE AND TECHNOLOGY DIVISION

All-Optical, Rapid Readout, Fiber-Coupled Thermoluminescent Dosimeter System
Alan L. Huston and Brian L. Justus
OPTICAL SCIENCES DIVISION

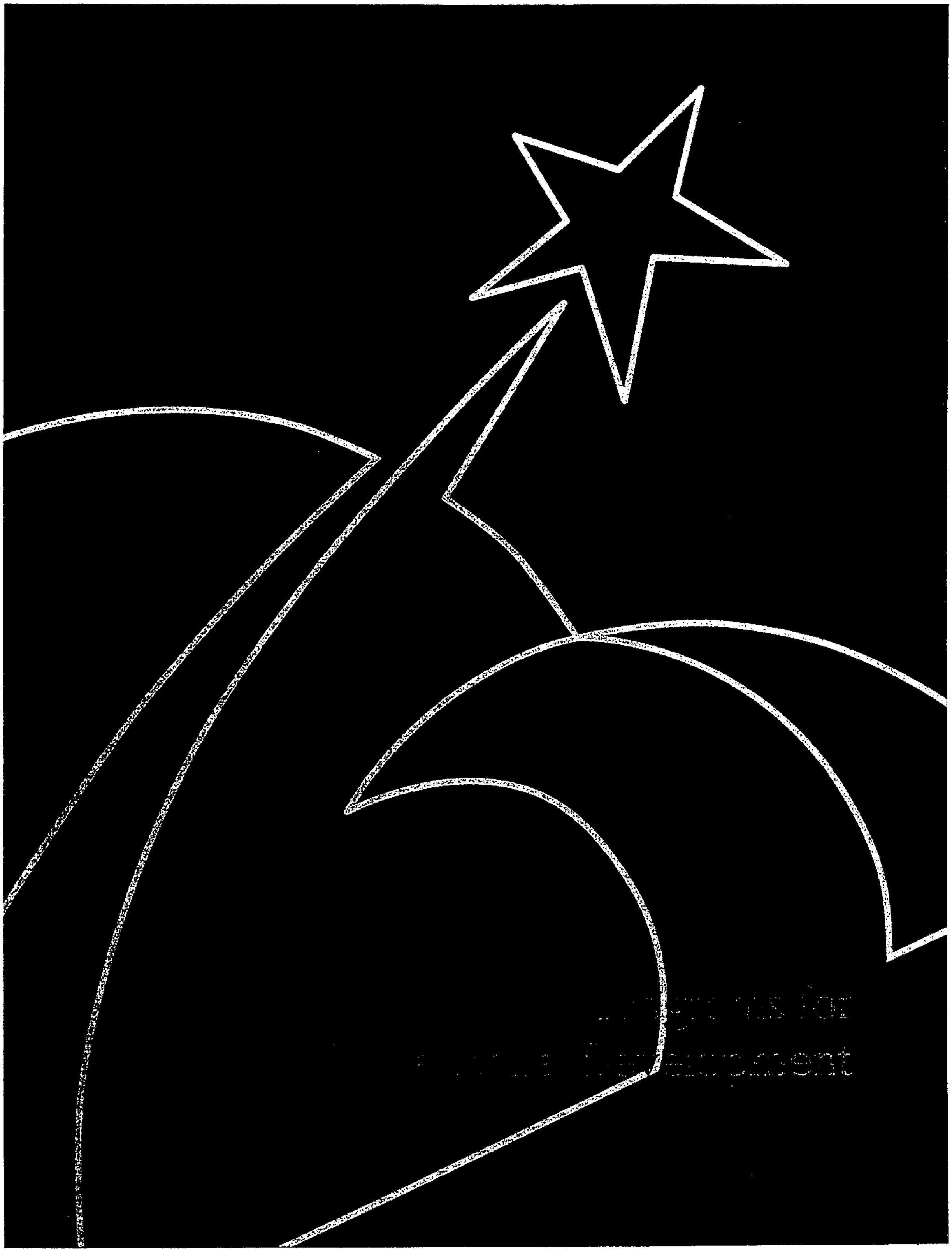
for

Programs for NRL Employees

During 1997, under the auspices of the Employee Development Branch, NRL employees participated in 4445 individual training events. Many of these were presented as either videotaped or on-site instructed courses on diverse technical subjects, management techniques, and enhancement of such personal skills as efficient use of time, speed reading, memory improvement, and interpersonal communications. Courses are also available by means of computer-based training (CBT) and live television, for monitoring nationwide.

One common study procedure is for employees to work full time at the Laboratory while taking job-related scientific courses at universities and schools in the Washington area. The training ranges from a single course to full graduate and postgraduate programs. Tuition for training is paid by NRL. The formal programs offered by NRL are described here.

GRADUATE PROGRAMS

• The **Advanced Graduate Research Program** (formerly the Sabbatical Study Program, which began in 1964) enables selected professional employees to devote full time to research or pursue work in their own or a related field for 1 year at an institution or research facility of their choice without the loss of regular salary, leave, or fringe benefits. NRL pays all educational costs, travel, and moving expenses for the employee and dependents. Criteria for eligibility include professional stature consistent with the applicant's opportunities and experience, a satisfactory program of study, and acceptance by the facility selected by the applicant. The program is open to paraprofessional employees (and above) who have completed 6 years of Federal Service, 4 of which are at NRL.

• The **Edison Memorial Graduate Training Program** enables employees to pursue advanced studies in their fields at local universities. Participants in this program work 24 hours each workweek and pursue their studies during the other 16 hours. The criteria for eligibility include a minimum of 1 year of service at NRL, a bachelor's or master's degree in an appropriate field, and professional standing in keeping with the candidate's opportunities and experience.

• To be eligible for the **Select Graduate Training Program**, employees must have a college degree in an appropriate field and must have demonstrated ability and aptitude for advanced training. Students accepted in this program devote a full academic year to graduate study. While attending school, they receive one-half of their salary, and NRL pays for tuition and laboratory expenses.

• The **Naval Postgraduate School** (NPS), located in Monterey, California, provides graduate programs to enhance the technical preparation of Naval officers and civilian employees who serve the Navy in the fields of science, engineering, operations analysis, and management. It awards a master of arts degree in national security affairs and a master of science degree in many technical disciplines.

NRL employees desiring to pursue graduate studies at NPS may apply for a maximum of six quarters away from NRL, with thesis work accomplished at NRL. Specific programs are described in the NPS catalog. Participants will continue to receive full pay and benefits during the period of study.

Ms. Joan Gardner, of the Marine Geosciences Division, is currently participating in the Edison Memorial Graduate Training Program at George Washington University, Washington, DC.

• In addition to NRL and university offerings, application may be made to a number of noteworthy programs and fellowships. Examples of such opportunities are the **Alfred P. Sloan Fellows Program, Brookings Institute Advanced Study Program**, the **Fellowship in Congressional Operations**, and the **Women's Executive Leadership Program**. These and other programs are announced from time to time, as schedules are published.

• Research conducted at NRL may be used as **thesis material for an advanced degree**. This original research is supervised by a qualified employee of NRL who is approved by the graduate school. The candidate should have completed the required course work and should have satisfied the language, residence, and other requirements of the graduate school from which the degree is sought. NRL provides space, research facilities, and supervision but leaves decisions on academic policy to the cooperating schools.

CONTINUING EDUCATION

• Local colleges and universities offer **undergraduate and graduate courses** at NRL for employees interested in improving their skills and keeping abreast of current developments in their fields. These courses are also available at many other DoD installations in the Washington, D.C. area.

• The Employee Development Branch at NRL offers **short courses** to all employees in a number of fields of interest including technical subjects, computer operation, supervisory and management techniques, and clerical/secretarial skills. Laboratory employees may attend these courses at nongovernment facilities as well. Interagency courses in management, personnel, finance, supervisory development, and clerical skills are also available.

For further information on any of the above programs, contact the Employee Development Branch (Code 1840) at (202) 767-2956.

TECHNOLOGY TRANSFER

• The **Office of Research and Technology Applications Program** (ORTA) ensures the full use of the results of the Nation's federal investment in research and development by transferring federally owned or originated technology to state and local governments and the private sector. (Contact Dr. Richard Rein, Code 1004, at (202) 767-7230).

Dr. Verne Jacobs, of the Condensed Matter and Radiation Sciences Division, is currently participating in the Advanced Graduate Program. For the first nine months, he will attend the University of Maryland, Institute for Plasma Research. He will complete the program at the Hebrew University of Jerusalem, Israel, Racah Institute of Physics.

TECHNOLOGY BASE

• The **Navy Science Assistance Program** (NSAP) establishes an information loop between the Fleet and the R&D shore establishments to expedite technology transfer to the user. The program addresses operational problems, focuses resources to solve specific technical problems, and develops a nucleus of senior scientific personnel familiar with the impact of current research and system performance on military operations. The program also provides 2-year science advisor positions in the Fleet. NRL is a participant of this ONR program.

• The **Scientist-to-Sea Program** (STSP) provides increased opportunities for Navy R&D laboratory/center personnel to go to sea to gain first-hand insight into operational factors affecting system design, performance, and operations on a variety of ships. NRL is a participant of this NSAP-ONR program.

For further information on these and other Technology Base Programs, contact Dr. Stephen Sacks, Code 5006, at (202) 767-3666.

PROFESSIONAL DEVELOPMENT

NRL has several programs, professional society chapters, and informal clubs that enhance the professional growth of employees. Some of these are listed below.

• The **Counseling Referral Service** (C/RS) helps employees to achieve optimal job performance through counseling and resolution of problems such as family, stress and anxiety, behavioral,

NRL scientists (left to right) Dale Linne von Berg, Celia Merzbacher (Optical Sciences Division), Mike Livingston and Joy Cheung (Radar Division) aboard the USS *Vicksburg* (CG-69) as part of the Scientist-to-Sea Program. The Scientist-to-Sea Program provides an opportunity for participants to experience the Fleet Navy in action.

emotional, and alcohol- or drug-related problems that may adversely impact job performance.

C/RS provides confidential assessments and short-term counseling, training workshops, and referrals to additional resources in the community. (Contact Ms. Eileen Long-Farias at (202) 767-6857.)

• A chartered chapter of **Women in Science and Engineering** (WISE) was established at NRL in 1983. Informal luncheons and seminars are scheduled to inform scientists and engineers of women's research at NRL and to provide an informal environment for members to practice their presentations. WISE also sponsors a colloquium series to feature outstanding women scientists. (Contact Dr. Wendy Fuller-Mora at (202) 767- 6207 or Dr. Debra Rolison at (202) 767-3617.

• **Sigma Xi**, the scientific research society, encourages and acknowledges original investigation in pure and applied science. As an honor society for research scientists, individuals who have demonstrated the ability to perform original research are elected to membership in local chapters. The NRL Edison Chapter, comprising approximately 600 members, recognizes original research by presenting awards annually in pure and applied science to outstanding NRL staff members. The chapter also sponsors lectures at NRL on a wide range of scientific topics for the entire NRL community. These lectures are delivered by scientists from all over the nation and the world. The highlight of the Sigma Xi lecture series is the Edison Memorial Lecture, traditionally featuring a distinguished scientist. (Contact Dr. Wendy Fuller-Mora at (202) 767-6207, Dr. Robert Pellenbarg at (202) 767-2479, or Mr. Paul Bey, Jr. at (202) 404-6029.

• The **NRL Mentor Program** was established to provide an innovative approach to professional and career training and an environment for personal and professional growth. It is open to permanent NRL employees in all job series and at all sites. Mentorees are matched with successful, experienced colleagues with more technical and/or managerial experience who can provide them with the knowledge and skills needed to maximize their contribution to the success of their immediate organization, to NRL, to the Navy, and to their chosen career fields. The ultimate goal of the program is to increase job productivity, creativity, and satisfaction through better communication, understanding, and training. NRL Instruction 12400.1 established the NRL Mentor Program, and it provides the policy and procedures for the program. (Contact Ms. Natalie Gibbs at (202) 767-3034.)

• The Charlotte Moore-Sitterly Chapter of **Federally Employed Women, Inc.** (FEW) was chartered at NRL in 1993. FEW is an international organization of federally employed women and men whose purpose is to eliminate sex discrimination and sexual harassment and enhance career opportunities for women in government. FEW works closely with other Federal agencies and organizations, including the Office of Personnel

Management, Equal Employment Opportunity Commission, and Federal Women's Program subcommittees. (Contact Dr. Jeanie Osburn at (202) 767-3885.)

• Employees interested in developing effective self-expression, listening, thinking, and leadership potential are invited to join either of two NRL chapters of **Toastmasters International**. Members of these clubs, who possess diverse career backgrounds and talents, meet three times a month in an effort to learn to communicate not by rules but by practice in an atmosphere of understanding and helpful fellowship. NRL's Commanding Officer and Director of Research endorse Toastmasters, and the Employee Development Branch pays for membership and educational materials for those NRL employees whose supervisors see a need for their active training in public speaking or communication skills. (Contact Kathleen Parrish at (202) 767-2782.)

• An agreement between NRL-SSC and **Mississippi's Alliance for Minority Participation** places students whose background and interests match the Laboratory's field of research with NRL mentors in a 10-week research environment. Together with accomplished senior researchers and faculty advisors, students plan, develop, and conduct a summer research project to include challenging, hands-on experiences with research equipment and principles of modern research. (Contact Ms. Linda Ladner at (601) 688-4754.)

After eight weeks of using communications skills taught in speechcraft, an intense communications course sponsored by Toastmasters International, these NRLers are confidently expressing their enthusiasm for mastering many new techniques in listening, thinking, and speaking.

EQUAL EMPLOYMENT OPPORTUNITY (EEO) PROGRAMS

Equal employment opportunity is a fundamental NRL policy for all persons, regardless of race, color, sex, religion, national origin, age, or physical/mental handicap. The EEO Office is a service organization whose major functions include promoting and practicing affirmative employment efforts, counseling employees in an effort to resolve employee/management conflicts, processing formal discrimination complaints, providing EEO training, and advising and providing guidance to employees on EEO policy. Additionally, the EEO Office is responsible for the management of the following special emphasis programs:

• The **African-American Employment Program (AAEP)**
• The **American-Indian/Alaskan-Native Employment Program (AI/ANEP)**
• The **Asian-American/Pacific Islander Employment Program (AA-PIEP)**
• The **Federal Women's Program (FWP)**
• The **Hispanic Employment Program (HEP)**
• The **Individuals with Disabilities Program (IWDP)**

Each of these programs has responsibility to identify pertinent areas of concern regarding recruitment, selection, advancement, and retention of employees. They also encourage NRL's population to heighten their sensitivities to others around them as well as to achieve their maximum potential by sponsoring special training and awareness programs throughout the year. (Contact the EEO Office at (202) 767-2486 for additional information on any of its programs or services.)

OTHER ACTIVITIES

• The **Community Outreach Program** traditionally has used its extensive resources to foster programs that provide benefits to students and other community citizens. Volunteer employees assist with and judge science fairs, give lectures, tutor, mentor, coach, and serve as classroom resource teachers. The program also sponsors Black History Month art and essay contests for local schools, student tours of NRL, a student Toastmasters Youth Leadership Program, an annual holiday party for neighborhood children, an

NRL's Equal Employment Opportunity Office and each of the EEO subcommittees hosted the 2nd Annual Cultural Extravaganza on the Mall. The extravaganza brought together cultural cuisine, music, and dancing in celebration of this year's theme, "Unity Through Diversity."

annual collection for Children's Hospital, and other programs that support the local community. Also through this program, NRL has active partnerships with four District of Columbia and three Aberdeen, Maryland, public schools. (Contact Mr. Dom Panciarelli at (202) 767-2541.)

• Other programs that enhance the development of NRL employees include four computer user groups (**IBM PC**, **Mac**, **NeXT**, and **Sun**) and the **Amateur Radio Club**. The **Recreation Club** encourages the wide interest of sports for employees with its many facilities and programs, such as a six-lane heated indoor pool; basketball and volleyball court; weight room with qualified consultant, by appointment; table tennis; hot tub and sauna; five martial arts disciplines; aerobics, ranging from low-low to high and step classes; swimming lessons; water walking and exercise; swing dance sessions; softball and basketball leagues; and specialized sports clubs (running, skiing, swimming, biking, and golfing). Sportswear, NRL paraphernalia, discount tickets to amusement parks, and film-developing services are available at the Rec Club office. The **Showboaters**, a nonprofit drama group that presents live theater for the enjoyment of NRL and the community, performs two major productions each year in addition to occasional performances at Laboratory functions and benefits for local charities. Although based at NRL, membership in Showboaters is not limited to NRL employees.

NRL's Community Outreach Program volunteers hosted students from Aberdeen Middle School and Hillsdale Elementary School to visit the Naval Center for Space Technology's Payload Checkout Facility. Both schools are NRL partner schools under the DoD Personal Excellence Partnership Program.

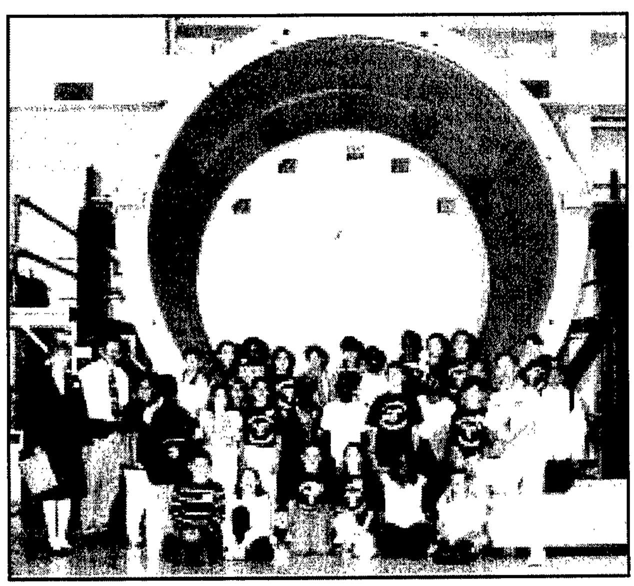

Programs for Non-NRL Employees

Several programs have been established for non-NRL professionals. These programs encourage and support the participation of visiting scientists and engineers in research of interest to the Laboratory. Some of the programs may serve as stepping-stones to federal careers in science and technology. Their objective is to enhance the quality of the Laboratory's research activities through working associations and interchanges with highly capable scientists and engineers and to provide opportunities for outside scientists and engineers to work in the Navy laboratory environment. Along with enhancing the Laboratory's research, these programs acquaint participants with Navy capabilities and concerns.

RECENT PH.D., FACULTY MEMBER, AND COLLEGE GRADUATE PROGRAMS

• The **National Research Council (NRC)/ NRL Cooperative Research Associateship Program** selects associates who conduct research at NRL in their chosen fields in collaboration with NRL scientists and engineers. The tenure period is 2 years.

• The American Society for Engineering Education (ASEE) administers the NRL/ASEE **Postdoctoral Fellowship Program** that aims to increase the involvement of highly trained scientists and engineers in disciplines necessary to meet the evolving needs of naval technology. Appointments are for 1 year (renewable for a second and sometimes a third year). These competitive appointments are made jointly by NRL and ASEE.

• **The Consortium for Oceanographic Research Education (CORE) Postdoctoral Fellowship Program** is administered in much the same manner as the above two programs. However, this program is focused on selecting associates with advanced degrees in the oceanic and atmospheric environmental sciences. The purpose of this program is to recruit scientists and engineers in these specialized areas.

• The American Society for Engineering Education also administers the Navy/ASEE **Summer Faculty Research and Sabbatical Leave Program** for university faculty members to work for 10 weeks (or longer, for those eligible for sabbatical leave) with professional peers in participating Navy laboratories on research of mutual interest.

• **The NRL/United States Naval Academy (USNA) Cooperative Program for Scientific Interchange** allows faculty members of the U.S. Naval Academy to participate in NRL research. This collaboration benefits the Academy by providing the opportunity for USNA faculty members to work on research of a more practical or applied nature. In turn, NRL's research program is strengthened by the available scientific and engineering expertise of the USNA faculty.

• The **National Defense Science and Engineering Graduate Fellowship Program** helps U.S. citizens obtain advanced training in disciplines of science and engineering critical to the U.S. Navy. The 3-year program awards fellowships to recent outstanding graduates to support their study and research leading to doctoral degrees in specified disciplines such as electrical engineering, computer sciences, material sciences, applied physics, and ocean engineering. Award recipients are encouraged to continue their study and research in a Navy laboratory during the summer.

For further information about the above six programs, contact Ms. Lesley Renfro at (202) 404-7450.

PROFESSIONAL APPOINTMENTS

• **Faculty Member Appointments** use the special skills and abilities of faculty members for short periods to fill positions of a scientific, engineering, professional, or analytical nature.

• **Consultants and experts** are employed because they are outstanding in their fields of

specialization or because they possess ability of a rare nature and could not normally be employed as regular civil servants.

• **Intergovernmental Personnel Act Appointments** temporarily assign personnel from state or local governments or educational institutions to the Federal Government (or vice versa) to improve public services rendered by all levels of government.

STUDENT PROGRAMS

The student programs are tailored to the undergraduate and graduate students to provide employment opportunities and work experience in naval research. These programs are designed to attract applicants for student and full professional employment in fields such as engineers, physicists, mathematicians, and computer scientists. The student employment programs are designed to help students and the educational institutions gain a better understanding of NRL's research, its challenges, and its opportunities. The employment programs for college students include the following:

• The **Student Career Experience Program** (formerly known as Cooperative Education Program) employs students in study-related occupations. The program is conducted in accordance with a planned schedule and a working agreement among NRL, the educational institution, and the student. Primary focus is on the pursuit of bachelors degrees in engineering, computer science, or the physical sciences.

• The **Student Temporary Employment Program (STEP)** enables students to earn a salary while continuing their studies and offers them valuable work experience.

• The **Summer Employment Program** employs students for the summer in paraprofessional and technician positions in engineering, physical sciences, computer sciences, and mathematics.

• The **Student Volunteer Program** helps students gain valuable experience by allowing them to voluntarily perform educationally related work at NRL.

For additional information on these undergraduate and graduate college student programs, contact the Staffing Branch, Code 1810 at (202) 767-8313.

HIGH SCHOOL PROGRAMS

• The **DoD Science & Engineering Apprentice Program** (SEAP) employs high school juniors, seniors, and college students to serve for 8 weeks as junior research associates. The college students must have participated in SEAP during high school. Under the direction of a mentor, students gain a better understanding of research, its challenges, and its opportunities through participation in scientific programs. Criteria for eligibility are based on science and mathematics courses completed and grades achieved; scientific motivation, curiosity, and capacity for sustained hard work; a desire for a technical career; teacher recommendations; and achievement test scores. The NRL Program is the lead program and the largest in DoD.

For additional information, contact the Employee Development Branch (Code 1840) at (202) 767-2956.

Kary Oetjen and Samuel Pinansky, SEAP students, discuss their progress in extending and generalizing computer models for electromagnetic wave scattering from the ionosphere. Both students were mentored by Dr. Arthur K. Jordan within the Remote Sensing Division.

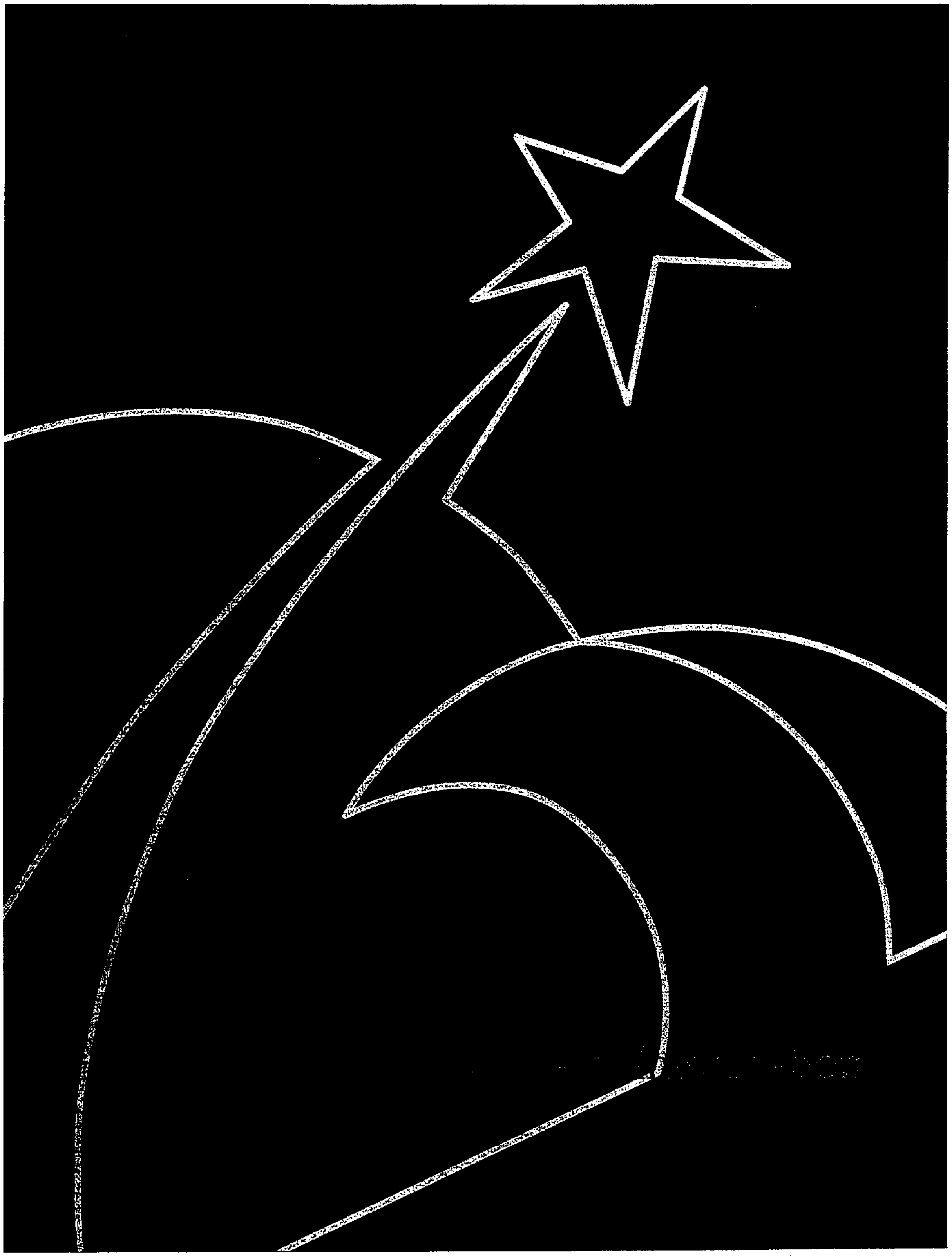

Technical Output

The Navy continues to be a pioneer in initiating new developments and a leader in applying these advancements to military requirements. The primary method of informing the scientific and engineering community of the advances made at NRL is through the Laboratory's technical output — reports, articles in scientific journals, contributions to books, papers presented to scientific societies and topical conferences, patents, and inventions.

The figures for calendar year 1997 presented below represent the output of NRL facilities in Washington, D.C.; Bay St. Louis, Mississippi; and Monterey, California.

In addition to the output listed, NRL scientists made more than 1430 oral presentations during 1997.

A complete listing of the publications by NRL authors appears in the *Bibliography of NRL Publications*, a separate annual publication.

Type of Contribution	Unclassified	Classified	Total
Articles in periodicals, chapters in books, and papers in published proceedings	1119	0	1119
NRL Formal Reports	19	17	36
NRL Memorandum Reports	116	14	130
Books	3	0	3
Patents granted			62
Statutory Invention Registrations (SIRs)			5

*This is a provisional total based on information available to the Ruth H. Hooker Research Library and Technical Information Center on January 9, 1998. Additional publications carrying a 1997 publication date are anticipated.

Technology Transfer at NRL

There are many ways for private companies to benefit from the technical resources of NRL. Some of these include: (1) entering into Cooperative Research and Development Agreements (CRADAs), (2) obtaining licenses for Navy-owned patents, and (3) consulting with NRL scientists and engineers.

Entering into a CRADA is an excellent way for U.S. companies to gain access to commercially important NRL research and development (R&D) technology. Authorized under the Federal Technology Transfer Act of 1986, a CRADA is an agreement between one or more federal laboratories and one or more nonfederal parties, such as private companies. Designed to encourage and facilitate cooperative R&D, CRADAs can involve research in any area that is consistent with NRL's mission.

Additionally, the Federal Government can license its own inventions. NRL has developed many new technologies and processes in areas as diverse as advanced materials, chemistry, biotechnology, optics, ocean and atmospheric sciences, and electronics. NRL currently has over 500 patents available for license in these fields.

As the Navy's corporate laboratory, NRL draws on the powerful resources of an interdisciplinary combination of scientific expertise and modern facilities. NRL's technical staff is recruited from all disciplines of engineering and the physical sciences and is available to work with private companies to help them solve their technical problems. Many of the staff have received the Award for Excellence in Technology Transfer from the Federal Laboratory Consortium (FLC). This award recognizes employees who have accomplished outstanding work in the process of transferring laboratory-developed technology.

During 1997, new products have been introduced from NRL technology by the private sector. For instance, NRL's patents, "Mode Matched Combination Taper Fiber Optic Probe" and "Waveguide Binding Sensor for Use with Assays" were licensed by Research International and are used to make sensing probes for the portable fiber optic biosensor. This instrument detects biological warfare agents, toxins and explosives in the field.

NRL and Keithley Instruments signed a CRADA this year to further the development of laser-heated thermoluminescent glass materials invented by researchers in the Optical Sciences Division. These materials have enabled the use of improved optical methods for thermoluminescence dosimetry of ionizing radiation. In particular, remote sensing of radiation can be performed using a novel fiber-optic coupled instrument, shown in the schematic, that has been constructed using the new thermoluminescent glass material. This remote dosimeter has applications in medicine, as a real-time in-vivo monitor of the dose received by patients during radiotherapy procedures, and in the environment, as a monitor of environmental contamination due to leakage of radioactive wastes from aging waste storage sites.

For additional information, contact NRL's Technology Transfer Office, 4555 Overlook Ave., S.W., Washington, DC 20375-5320, or call (202) 767-7230; e-mail: techtransfer@nrl.navy.mil; URL: http://infonext.nrl.navy.mil/~techtran/.

NRL has developed a fiber-optic-coupled dosimeter for remote sensing of ionizing radiation. This all-optical dosimeter can perform in situ, real-time measurements of radiation doses in hazardous or inaccessible areas.

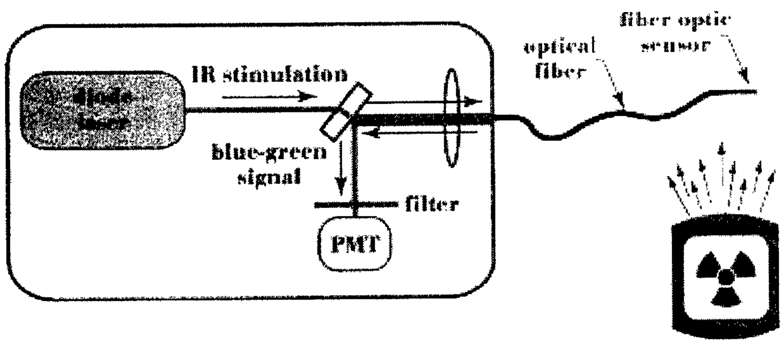

Key Personnel

Area Code (202) unless otherwise listed
Personnel Locator - 767-3200
DSN-297 or 754

Code	Office		Phone Number
	EXECUTIVE DIRECTORATE		
1000	Commanding Officer	CAPT B.W. Buckley, USN	767-3403
1000.1	Inspector General	CAPT R.E. Leonard, USN	767-3621
1001	Director of Research	Dr. T. Coffey	767-3301
1001.1	Scientific Staff Assistant	Mr. D. DeYoung	767-2880
1002	Chief Staff Officer	CAPT R.E. Leonard, USN	767-3621
1004	Head, Technology Transfer	Dr. R. Rein	767-7230
1006	Head, Office of Program Administration and Policy Development	Ms. L. McDonald	767-3091
1200	Head, Command Support Division	Mr. J.C. Payne	767-3048
1220	Head, Security	Dr. J.T. Miller	767-0793
1230	Public Affairs Officer	Mr. R. Thompson (Acting)	767-2541
1240	Head, Safety Branch	Mr. K.J. King	767-2232
1400	Head, Military Support Division	CDR R. Francisco, USN	767-2271
1600	Officer-in-Charge, Flight Support Detachment	CDR D.R. Dowell, USN	301-342-3751
1800	Director, Human Resources Office	Ms. B.A. Duffield	767-3421
1803	Deputy EEO Officer	Ms. D. Erwin	767-2486
3204	Deputy for Small Business	Ms. L. Byrne	767-6263
	BUSINESS OPERATIONS DIRECTORATE		
3000	Associate Director of Research	Mr. R.E. Doak	767-2371
3008	Office of Counsel	Ms. H.J. Halper	767-2244
3030	Head, Management Information Systems Staff	Mr. R.L. Guest	767-2030
3200	Head, Contracting Division	Mr. J.C. Ely	767-5227
3300	Comptroller, Financial Management Division	Mr. D. Therning	767-3405
3400	Supply Officer	Ms. C. Hartman	767-3446
3500	Director, Research and Development Services Division	Mr. S. Harrison	767-3697
	SYSTEMS DIRECTORATE		
5000	Associate Director of Research	Dr. R.A. LeFande	767-3324
5200	Head, Technical Information Division	Mr. P.H. Imhof	767-2187
5300	Superintendent, Radar Division	Dr. G.V. Trunk (Acting)	767-2573
5500	Superintendent, Information Technology Division	Dr. R.P. Shumaker	767-2903
5600	Superintendent, Optical Sciences Division	Dr. T.G. Giallorenzi	767-3171
5700	Superintendent, Tactical Electronic Warfare Division	Dr. J.A. Montgomery	767-6278
	MATERIALS SCIENCE AND COMPONENT TECHNOLOGY DIRECTORATE		
6000	Associate Director of Research	Dr. B.B. Rath	767-3566
6030	Head, Laboratory for Structure of Matter	Dr. J. Karle	767-2665
6100	Superintendent, Chemistry Division	Dr. J.S. Murday	767-3026
6300	Superintendent, Materials Science & Technology Division	Dr. D.U. Gubser	767-2926
6400	Director, Lab. for Computational Physics and Fluid Dynamics	Dr. J.P. Boris	767-3055
6600	Superintendent, Condensed Matter & Radiation Sciences Division	Dr. D.J. Nagel	767-2931
6700	Superintendent, Plasma Physics Division	Dr. S. Ossakow	767-2723
6800	Superintendent, Electronics Science & Technology Division	Dr. G.M. Borsuk	767-3525
6900	Director, Center for Bio/Molecular Science and Engineering	Dr. J.M. Schnur	404-6000
	OCEAN AND ATMOSPHERIC SCIENCE AND TECHNOLOGY DIRECTORATE		
7000	Associate Director of Research	Dr. E.O. Hartwig	404-8690
7030	Head, Office of Research Support Services	Mr. G. Bower	601-688-4010
7100	Superintendent, Acoustics Division	Dr. E.R. Franchi	767-3482
7200	Superintendent, Remote Sensing Division	Dr. P. Schwartz	767-3391
7300	Superintendent, Oceanography Division	Dr. W.B. Moseley	601-688-4670
7400	Superintendent, Marine Geosciences Division	Dr. H.C. Eppert, Jr.	601-688-4650
7500	Superintendent, Marine Meteorology Division	Dr. P.E. Merilees	408-656-4721
7600	Superintendent, Space Science Division	Dr. H. Gursky	767-6343
	NAVAL CENTER FOR SPACE TECHNOLOGY		
8000	Director	Mr. P.G. Wilhelm	767-6547
8100	Superintendent, Space Systems Development Department	Mr. R.E. Eisenhauer	767-0410
8200	Superintendent, Spacecraft Engineering Department	Mr. H.E. Senasack, Jr.	767-6411

Employment Opportunities for Entry-Level and Experienced Personnel

The *NRL Review* illustrates some of the exciting science and engineering carried out at the Naval Research Laboratory, as well as the potential for new personnel. In this regard, NRL offers a wide variety of challenging positions that involve the full range of work, from basic and applied research to equipment development. The nature of the research and development conducted at NRL requires professionals with experience. Typically there is a continuing need for electronics, mechanical, aerospace, ceramic and materials engineers, metallurgists, computer scientists, and oceanographers with bachelor's and/or advanced degrees and physical and computer scientists with Ph.D. degrees. Opportunities exist in the areas described below:

Ceramic Engineers and Materials Scientists/ Engineers. These employees are recruited to work on materials, microstructure characterization, electronic ceramics, solid-state physics, fiber optics, electro-optics, microelectronics, fracture mechanics, vacuum science, laser physics technology, and radio frequency/microwave/millimeter wave/ infrared technology.

Electronics Engineers and Computer Scientists. These employees may work in the areas of communications systems, electromagnetic scattering, electronics instrumentation, electronic warfare systems, radio frequency/microwave/ millimeter wave/infrared technology, radar systems, laser physics technology, radio-wave propagation, electron device technology, spacecraft design, artificial intelligence, information processing, signal processing, plasma physics, vacuum science, microelectronics, electro-optics, fiber optics, solid state, software engineering, computer design/architecture, ocean acoustics, stress analysis, and expert systems.

Mechanical Engineers. These employees may be assigned to spacecraft design, remote sensing, propulsion, experimental fluid mechanics, experimental structural mechanics, solid mechanics, elastic/plastic fracture mechanics, materials, finite-element methods, nondestructive evaluation, characterization of fracture resistance of structural alloys, combustion, and CAD/CAM.

Chemists. Chemists are recruited to work in the areas of combustion, polymer science, bioengineering and molecular engineering, surface science, materials, fiber optics, electro-optics, microelectronics, electron-device technology, and laser physics.

Physicists. Physics graduates may concentrate on such fields as materials, solid-state physics, fiber optics, electro-optics, microelectronics, vacuum science, plasma physics, fluid mechanics, signal processing, ocean acoustics, information processing, artificial intelligence, electron-device technology, radio-wave propagation, laser physics, ultraviolet/X-ray/gamma-ray technology, electronic warfare, electromagnetic interaction, communications systems, radio frequency/microwave/millimeter wave/infrared technology, and computational physics.

Oceanographers, Meteorologists, and Marine Geophysicists. These employees work in the areas of ocean dynamics, air-sea interaction, upper-ocean dynamics, oceanographic bio-optical modeling, oceanic and atmospheric numerical modeling and prediction, artificial intelligence applications for satellite analyses, benthic processes, aerogeophysics, marine sedimentary processes, and advanced mapping techniques. Oceanographers and marine geophysicists are located in Washington, D.C., and the Stennis Space Center,

Bay St. Louis, Mississippi. Meteorologists are located in Washington, D.C., and Monterey, California.

APPLICATION AND INFORMATION

Interested applicants should submit an Application for Federal Employment (SF-171), an Optional Application for Federal Employment (OF-612), or a resume. The OF-612 and SF-171 can be obtained from local Office of Personnel Management and Human Resource Offices of federal agencies.

Direct inquiries to:

Naval Research Laboratory
Human Resources Office, Code 1810 RV
Washington, DC 20375-5324
(202) 767-3030

Location of NRL in the Capital Area

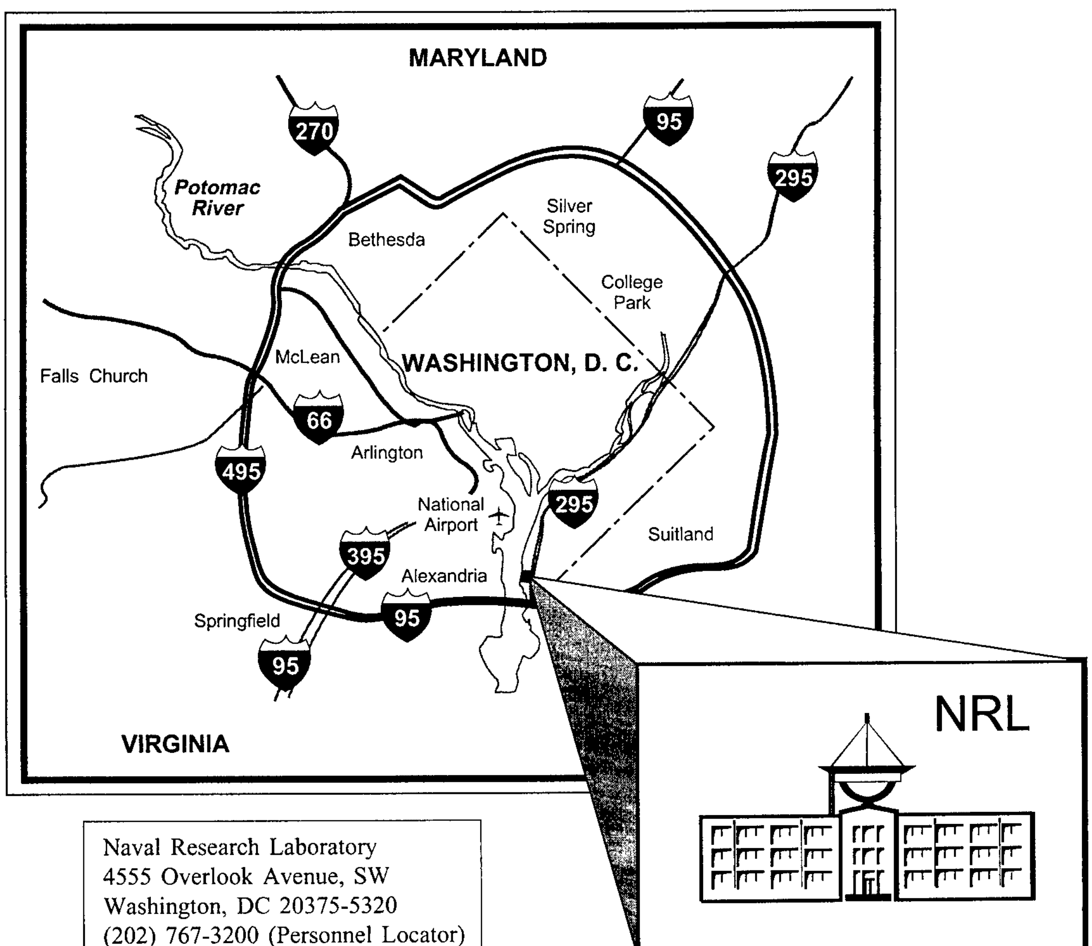

Naval Research Laboratory
4555 Overlook Avenue, SW
Washington, DC 20375-5320
(202) 767-3200 (Personnel Locator)

Contributions by Divisions, Laboratories, and Departments

Subject Index

Author Index

NRL Review Staff

Senior Science Editor:	*Dr. John D. Bultman*
TID Editor:	*Jonna Atkinson*
Assistant TID Editor:	*Patricia Staffieri*
TID Consultants:	*Kathleen Parrish and Timothy Calderwood*
Head, TID:	*Peter H. Imhof*

Computerized composition and design: *Jonna Atkinson, Donna Gloystein, Judy Kogok, and Jan Morrow*

Editorial assistance: *Marsha Bray, Maureen Long, and Saul Oresky*

Graphic support: *Jonna Atkinson, Suzanne Guillimineau, and Jan Morrow*

Historical update: *Dr. David van Keuren*

Photographic production: *Richard Bussey, Gayle Fullerton, James Marshall, and Michael Savell*

Production assistance: *Rosie Bankert, Diltricia Montgomery, Leona Sprankel, and Paul Sweeney*

Distribution: *Barbara Jolliffe*

REVIEWED AND APPROVED
NRL/PU/5230--98-350
April 1998

Bruce W. Buckley
Captain, USN
Commanding Officer

Quick Reference Telephone Numbers

	NRL Washington	NRL-SSC	NRL-Monterey	NRL CBD
Hotline	(202) 767-6543	(601) 688-5001	(408) 656-4721	(202) 767-6543
Personnel Locator	(202) 767-3200	(601) 688-3390	(408) 656-4731	(410) 257-4000
DSN	297- or 754-	485	878	—
Direct-in-Dialing	767- or 404-	688	656	257
Public Affairs	(202) 767-2541	(601) 688-5328	(408) 656-4708	—

Additional telephone numbers are listed on page 239.